8-3-2006

Kinematics of the Narrow-Line Regions in the Seyfert Galaxies NGC 4151 and NGC 1068

Varendra Das

Recommended Citation

Das, Varendra, "Kinematics of the Narrow-Line Regions in the Seyfert Galaxies NGC 4151 and NGC 1068." Dissertation, Georgia State University, 2006.
https://scholarworks.gsu.edu/phy_astr_diss/8

Kinematics of the Narrow-Line Regions in the Seyfert Galaxies NGC 4151 and NGC 1068

by

Varendra Das

Under the Direction of D. Michael Crenshaw

Abstract

We present a study of high-resolution long-slit spectra of the narrow-line regions (NLRs) of NGC 4151 (a Seyfert 1 galaxy) and NGC 1068 (a Seyfert 2 galaxy) obtained with the Space Telescope Imaging Spectrograph (STIS) aboard the *Hubble Space Telescope* (*HST*). The spectra were retrieved from the Multimission Archive at Space Telescope (MAST) and were obtained from five and seven orbits of *HST* time resulting in five and seven parallel slit configurations at position angles of 52° and 38° for NGC 4151 and NGC 1068 respectively. The spectra have a spatial resolution of $0\farcs2$ across and $0\farcs1$ along each slit. Observations of [O III] emission from the NLRs were made using the medium resolution G430M grating aboard *HST*. The spectral resolving power of the grating, $R = \frac{\lambda}{\Delta\lambda} \simeq 9000$, resulted in the detection of multiple kinematic components of the [O III] emission line gas along each slit. Radial velocities of the components were measured using a Gaussian fitting procedure.

Biconical outflow models were generated to match the data and for comparison to previous models done with lower dispersion observations. The general trend is an increase in radial velocity roughly proportional to distance from the nucleus, followed by a linear decrease after roughly 100 pc. This is similar to that seen in other Seyfert galaxies, indicating common acceleration and deceleration mechanisms. The full-width at half-maximum (FWHM) of the emission lines reaches a maximum of 1000 $\mathrm{km\,s^{-1}}$ near the nucleus, and generally decreases with increasing distance to about 100 $\mathrm{km\,s^{-1}}$ in the extended narrow-line region (ENLR), starting at about 400 pc from the nucleus. In addition to the bright emission knots, which generally fit our model, there are faint high velocity clouds that do not fit the biconical outflow pattern of our kinematic model.

A comparison of our observations with high-resolution radio maps shows that the kinematics of the faint NLR clouds may be affected by the radio lobes that comprise the inner jet. However, the bright NLR clouds show a smooth transition across the radio knots in radial velocity and velocity dispersion plots and remain essentially undisturbed in their vicinity, indicating that the radio jet is not the principal driving force on the outflowing NLR clouds.

A dynamical model was developed for NGC 1068; it includes forces of radiation pressure, gravity, and drag due an ambient medium, simultaneously acting on the NLR clouds. The velocity profile from this model was too steep to fit the data, which show a more slowly increasing velocity profile. Gravity alone was not able

to slow down the clouds but with the drag forces included, the clouds could slow down, reaching systemic velocities at distances that depend on the column densities of the NLR gas and density of the intercloud medium. A biconical model using the geometric parameters from our kinematic fit, and the velocity law from the dynamic fit, was used to match the data. The resulting dynamic model represented a poor fit to the data, indicating the need for additional dynamical considerations.

Index Words: Seyfert galaxies, NGC 4151, NGC 1068, AGN, NLR, Kinematics, Dynamics, Bicones, Unified Models

Kinematics of the Narrow-Line Regions in the Seyfert Galaxies NGC 4151 and NGC 1068

by

Varendra Das

A Dissertation Presented in Partial Fulfillment of Requirements for the Degree of

Doctor of Philosophy

in the College of Arts and Sciences

Georgia State University

2006

Kinematics of the Narrow-Line Regions in the Seyfert Galaxies NGC 4151 and NGC 1068

by

Varendra Das

Major Professor:	D. Michael Crenshaw
Committee:	Nikolaus Dietz Douglas R. Gies Steven B. Kraemer H. Richard Miller Paul J. Wiita

Electronic Version Approved:

Office of Graduate Studies
College of Arts & Sciences
Georgia State University
August 2006

Dedication

This dissertation is dedicated to my late grandfather who taught me to be curious, without which of course, I would not have been studying this mysterious yet fascinating science called astronomy. I dedicate this dissertation also to my parents, whose sole purpose in life is to make me happy, which is a rather unlikely feat of course, since they spoiled me a long, long time ago...

Acknowledgments

I wish to extend my sincere gratitude and appreciation to the multitudes of people who helped make this dissertation possible. Special thanks go to my adviser, D. Michael Crenshaw, who read my numerous drafts and made many critical corrections, suggestions, and improvements to finally make sense of the chaos. Many thanks go to my committee members, Nikolaus Dietz, Douglas R. Gies, Steven B. Kraemer, H. Richard Miller, and Paul J. Wiita, for helpful criticism, support and guidance. Gratitude goes out to Rajesh Deo, a fellow graduate and colleague, who unfortunately had to endure numerous questions about the intricate world of Linux. I would like to acknowledge with much appreciation the entire faculty in the Department of Physics and Astronomy for accepting me into the Astronomy Program and giving me the opportunity to earn my doctorate at Georgia State University. I would like to thank them also for providing an atmosphere of cheerfulness and camaraderie which made my work much easier over the years. As for the other graduate students in the department at GSU, it's going to be hard to find such a bunch of friendly, lively, and delightful students anywhere else and I am surely going to miss them.

Contents

Acknowledgments . . . . **v**

Tables . . . . **x**

Figures . . . . **xi**

Abbreviations and Acronyms . . . . **xvi**

1 Introduction **1**

1.1 The Discovery of Seyfert Galaxies 3

1.2 The AGN Zoo 5

1.3 The Classification of Seyfert Galaxies 7

1.4 The Components of Seyfert Galaxies 8

1.5 Unification of Seyfert Galaxies 9

1.6 The NLR of Seyfert Galaxies 12

1.6.1 Ionization of the NLR 13

1.6.2 Kinematics and Dynamics of the NLR 14

2 Observations **22**

2.1 *HST* Observations of NGC 4151 22

2.2 Radio Maps of NGC 4151 29

2.3 *HST* Observations of NGC 1068 31

2.4 Radio Maps of NGC 1068 40

2.5 STIS Data Reduction 42

3 Analysis 43

3.1 STIS Spectroscopic Analysis 43

3.1.1 Separating the Components 46

3.1.2 Measuring the Velocities 47

3.1.3 Errors 48

3.2 Radio Analysis: NGC 4151 49

3.2.1 The Location of the SMBH 49

3.2.2 Aligning the Radio and [O III] Maps 51

3.3 Radio Analysis: NGC 1068 54

3.3.1 The Location of the SMBH 54

3.3.2 Aligning the Radio and [O III] Maps 55

4 Measurements 59

4.1 Graphical Results for NGC 4151 60

4.2 Graphical Results for NGC 1068 71

5 Models 82

5.1 General Assumptions 82

5.2 Explanation of Model Parameters 83

5.3 Constructing the Models 86

5.3.1 Mapping Velocities on the Bicone 86

5.3.2 Finding Radial Velocities 90

5.4 Extraction of Slits 96

5.5 Fitting the Models to Data 100

6 Kinematic Results 104

6.1 Methodology 105

6.2 The Final Fits for NGC 4151 116

6.3 Backflow in NGC 4151 123

6.4 The Final Fits for NGC 1068 126

6.5 Effects of the Radio Jet 135

  6.5.1 Inclination Effects 135

  6.5.2 Interaction with the Radio Jet in NGC 4151 137

  6.5.3 Interaction with the Radio Jet in NGC 1068 141

7 Dynamics of the NLR of NGC 1068 146

7.1 Building the Mass Profile for NGC 1068 147

  7.1.1 The Black Hole Mass 147

  7.1.2 The Bulge Mass 148

  7.1.3 The Nuclear Stellar Cluster Mass 150

7.2 Dynamics Based on Gravity 152

  7.2.1 Rotation 153

  7.2.2 Escape and Infall Velocity 155

  7.2.3 Gravitational Drag 156

7.3 Radiation-Gravity Formalism 158

  7.3.1 Building the Velocity Equation 159

  7.3.2 Physical Constraints on the NLR of NGC 1068 160

  7.3.3 Radiation and Gravity Results 162

7.4 Radiation, Gravity, and Drag Forces 165

  7.4.1 Deceleration due to Drag 165

  7.4.2 Constraints on Cloud and Medium Densities for NGC 1068 . . 167

  7.4.3 Radiation, Gravity and Drag Results 168

  7.4.4 Dynamical Fit 173

  7.4.5 Remarks on Accelerating the Clouds 173

  7.4.6 Remarks on Decelerating the Clouds 175

8 Discussion 176

8.1 Kinematic Results and Implications 177

8.2 The Radio Jet Interaction and Implications 181

8.3 Dynamics of the NLR and Implications 182

8.4 Future Studies 185

References 187

Tables

2.1 Observational Parameters for NGC 4151. 23
2.2 Observational Parameters for NGC 1068. 32

5.1 Definition of Model Parameters. 85
5.2 Parameters used to generate Figure 5.2. 87
5.3 Parameters used to generate Figure 5.13. 101

6.1 Parameters used to generate the first run model for NGC 4151. . . . 107
6.2 Parameters used to generate the second run model for NGC 4151. . . 108
6.3 Parameters used to generate the third run model for NGC 4151. . . . 110
6.4 Parameters used to generate the fourth run model for NGC 4151. . . 111
6.5 Parameters used to generate the fifth run model for NGC 4151. . . . 112
6.6 Model with the largest possible inclination for NGC 4151. 114
6.7 Model with the smallest possible inclination for NGC 4151. 115
6.8 Best-fit parameters and their errors for NGC 4151. 116
6.9 Best-fit parameters and their errors for NGC 1068. 127

7.1 Parameters used to generate the drag model shown in Figure 7.13. . . 174

Figures

1.1 Components of a Seyfert 10

2.1 [O III] image of the NLR of NGC 4151 24
2.2 Spectral image of slit 1 for NGC 4151 25
2.3 Spectral images of slits 2 and 3 for NGC 4151 27
2.4 Spectral images of slits 4 and 5 for NGC 4151 28
2.5 The radio map of NGC 4151 29
2.6 The radio map of NGC 4151 30
2.7 [O III] image of NGC 1068 33
2.8 Slits on top the [O III] image of NGC 1068 34
2.9 Spectral images of slits 1 and 2 for NGC 1068 36
2.10 Spectral images of slits 3 and 4 for NGC 1068 37
2.11 Spectral images of slits 5 and 6 for NGC 1068 38
2.12 Spectral images of slits 7 and 8 for NGC 1068 39
2.13 Radio map for NGC 1068 40
2.14 Radio map for NGC 1068 showing slits 41

3.1 Multicomponent fits of spectra from slit 1 of NGC 4151 45
3.2 Cartoon of spectra showing separation criteria 47
3.3 Radio map of NGC 4151 showing the labeled components 50
3.4 Radio map of NGC 4151 overlaid on the [O III] map 51

3.5 Radio map of NGC 4151 overlaid with slits on the [O III] map 53
3.6 Radio map of NGC 1068 with slits overlaid 55
3.7 Radio map of NGC 1068 overlaid on the [O III] map 57
3.8 Radio map of NGC 1068 overlaid with slits on the [O III] map 58

4.1 Radial velocity, FWHM, and flux of slit 1 of NGC 4151 63
4.2 Radial velocity, FWHM, and flux of slit 2 of NGC 4151 64
4.3 Radial velocity, FWHM, and flux of slit 3 of NGC 4151 65
4.4 Radial velocity, FWHM, and flux of slit 4 of NGC 4151 66
4.5 Radial velocity, FWHM, and flux of slit 5 of NGC 4151 67
4.6 Comparison of our velocities and those of Hutchings et al. (1999) . . 68
4.7 The radio intensity of slits 1 and 2 of NGC 4151 69
4.8 The radio intensities of slits 3–5 of NGC 4151 70
4.9 Radial velocity, FWHM, and flux of slit 1 of NGC 1068 72
4.10 Radial velocity, FWHM, and flux of slit 2 of NGC 1068 73
4.11 Radial velocity, FWHM, and flux of slit 3 of NGC 1068 74
4.12 Radial velocity, FWHM, and flux of slit 4 of NGC 1068 75
4.13 Radial velocity, FWHM, and flux of slit 5 of NGC 1068 76
4.14 Radial velocity, FWHM, and flux of slit 6 of NGC 1068 77
4.15 Radial velocity, FWHM, and flux of slit 7 of NGC 1068 78
4.16 Radial velocity, FWHM, and flux of slit 8 of NGC 1068 79
4.17 The radio intensities of slits 3 and 4 of NGC 1068 80
4.18 The radio intensities of slits 5 and 8 of NGC 1068 81

5.1 Model parameters used to generate bicone 84
5.2 The velocity map on the first quadrant of the bicone 88

5.3 The velocity map on the top half of the bicone 89
5.4 The coordinate system used 91
5.5 Front and back half of radial velocity map on the bicone 92
5.6 Front and back half of an inclined radial velocity map 93
5.7 Complete front and back half of a bicone model showing radial velocity 95
5.8 Radial velocity map on an inclined bicone 96
5.9 An example slit for extraction 97
5.10 An example extracted slit 98
5.11 Model radial velocity plots of the extracted slit 99
5.12 Conventional model radial velocity plot of extracted slit 100
5.13 Example figure of a bad fit 102

6.1 First run of the model for NGC 4151, slit 1 107
6.2 Second run of the model for NGC 4151, slit 1 108
6.3 Third run of the model for NGC 4151, slit 1 110
6.4 Fourth run of the model for NGC 4151, slit 1 111
6.5 Fifth run of the model for NGC 4151, slit 1 112
6.6 Model errors for NGC 4151, slit 1 (largest possible inclination) . . . 114
6.7 Model errors for NGC 4151, slit 1 (smallest possible inclination) . . . 115
6.8 The final model representation of NGC 4151 117
6.9 The fit for NGC 4151: slit 1 120
6.10 The fit for NGC 4151: slits 2 and 3 121
6.11 The fit for NGC 4151: slits 4 and 5 122
6.12 Possible flow patterns of the rogue clouds of NGC 4151 124
6.13 The final model representation of NGC 1068 127
6.14 The fit for NGC 1068: slits 1 and 2 130

6.15 The fit for NGC 1068: slits 3 and 4 131

6.16 The fit for NGC 1068: slits 5 and 6 132

6.17 The fit for NGC 1068: slits 7 and 8 133

6.18 The NLR with respect to host galaxy of NGC 1068 134

6.19 The NLR with respect to host galaxy of NGC 4151 134

6.20 The uneven radial velocity splitting in NGC 4151 seen in projection . 135

6.21 The near even velocity splitting in NGC 1068 seen by an observer . . 137

6.22 Jet/cloud comparison for NGC 4151: slits 1 and 2 139

6.23 Jet/cloud comparison for NGC 4151: slits 3 and 4 140

6.24 Jet/cloud comparison for NGC 4151: slit 5 141

6.25 Jet/cloud comparison for NGC 1068: slits 3 and 4 143

6.26 Jet/cloud comparison for NGC 1068: slits 5 and 8 144

6.27 Cartoon showing the lateral radio expansion driving the faint clouds . 145

7.1 Mass profile of NGC 1068 153

7.2 Rotation curves of the NLR of NGC 1068 154

7.3 Escape velocity curves of the NLR of NGC 1068 155

7.4 Velocity curves after a launch at 140 pc with 1000 km $\mathrm{s}^{-1}$and 300 km s^{-1}157

7.5 Velocity profiles with several force multipliers for NGC 1068 162

7.6 Velocity profiles with several lower force multipliers for NGC 1068 . . 163

7.7 Velocity profiles with several launch radii for NGC 1068 164

7.8 Drag velocity profiles with force multiplier 500 for NGC 1068 169

7.9 Drag velocity profiles with force multiplier 6000 for NGC 1068 170

7.10 Drag velocity profiles with force multiplier 500 and $r_1 = 10$ pc 171

7.11 Drag velocity profiles with force multiplier 6000 and $r_1 = 10$ pc . . . 172

7.12 Drag velocity profiles with force multiplier 6000 and $r_1 = 20$ pc . . . 172

7.13 Model of slit 4 with drag forces in NGC 1068 174

Abbreviations and Acronyms

AGN	Active Galactic Nuclei
BLR	broad-line region
BLRG	broad-line radio galaxy
CCD	Charged Coupled Device
Co-I	Co-Investigator
CPU	central processing unit
ENLR	extended narrow-line region
FOC	Faint Object Camera
FR-I	Fanaroff-Riley class I
FR-II	Fanaroff-Riley class II
FWHM	full-width at half-maximum
$\mathbf{H_2 0}$	Water
HST	*Hubble Space Telescope*
IDL	Interactive Data Language
IR	infrared
LINERs	low ionization emission-line regions
LOS	line-of-sight

MAST	Multimission Archive at Space Telescope
MERLIN	Multi-Element Radio Linked Interferometer Network
NASA	National Aeronautic and Space Administration
NLR	narrow-line region
NLRG	narrow-line radio galaxy
O III	doubly ionized oxygen
pc	parsecs
PI	Principal Investigator
QSO	quasi-stellar object
quasars	quasi-stellar radio sources
RAM	random access memory
SED	spectral energy distribution
SMBH	supermassive black hole
STIS	Space Telescope Imaging Spectrograph
UV	ultraviolet
VLA	Very Large Array
VLBA	Very Long Baseline Array
WFPC2	Wide Field Planetary Camera 2
3CR	Third Cambridge Revised Catalog
3C	Third Cambridge Catalog
3D	three dimensional

– 1 –

Introduction

The following presentation is based on the study of two well-known and well-studied galaxies, NGC 4151 and NGC 1068. These two galaxies are part of a general class of galaxies now known as Seyferts, named after their discoverer, Carl K. Seyfert. The Seyfert class is again only a part of a much larger collection of objects known as Active Galactic Nuclei (AGN), which are galaxies that have very energetic central regions that normally outshines the rest of the galaxy. Since Seyfert galaxies are the nearest and brightest AGN, they played a crucial role in establishing the foundation upon which basic ideas of general classification schemes of AGN emerged. The need for such classification schemes is most pressing today, with the appearance of a 'zoo' of different AGN types, and the demand for such a classification scheme stems from the accepted norm that 'the simplest theory is normally the best one'. A general classification system for AGN is highly desirable because of the numerous classes that exist and because the list of properties that distinguish between the classes is large and growing. The properties that separate the classes of AGN to date includes luminosity levels, radio power, detection or absence of broad or narrow emission lines, detection or absence of low- or high-ionization emission lines, the amount of variability and polarization, brightness in the infrared (IR), ultraviolet (UV), or X-ray bands, continuum brightness relative to emission or absorption lines, etc. What is needed is a set of fundamental parameters that would predetermine what properties the AGN should have. An example of a scientific movement that strides for simplicity in understanding a broad range of phenomenon is the classification of stars. The wealth of information from stellar spectra would be overwhelming had it not been for the simple Hertzsprung–Russell classification that placed stars within a two-dimensional framework of temperature and luminosity that is governed by simple astrophysical laws. In the AGN field, the same type of simplification is sought after so as to unite all classes of AGN.

The present study focuses on the kinematics and dynamics of the NLR of Seyfert galaxies and their implications within the current unification picture of Seyfert galaxies. Because Seyferts are nearby and their NLRs are resolvable with modern ground- and space-based telescopes, they are also very important in understanding the physics involved in the AGN process. The various classes of AGN are summarized below, starting with the most studied active galaxies, the Seyferts. The NLR is then discussed briefly since most of this study is concentrated on the morphological, kinematical, and dynamical nature of this region. The ultimate questions that we are attempting to answer are: (i) What mechanism drives the NLR gas? (ii) What mechanism slows down the gas? (iii) What are the implications of the kinematics of the NLR for the unified model of Seyfert galaxies?

A general outline of this dissertation is as follows. This chapter gives a brief overview of the history of Seyfert galaxies, and their relation to the more general class of active galaxies. We then discuss studies done previously on the NLRs of NGC 4151, NGC 1068, and other Seyfert galaxies. The observational aspects of this study are presented in Chapter 2 and the analysis of the data follows in Chapter 3. Measurements of the data are presented in Chapter 4 and kinematical models are developed to fit the data in Chapter 5. The kinematical fits to the data are presented in Chapter 6 and dynamical considerations are added to discuss important implications in Chapter 7. Finally, a discussion that summarizes important results and conclusions and what they mean for the NLR of Seyfert galaxies and AGN in general, is presented in Chapter 8.

1.1 The Discovery of Seyfert Galaxies

Seyfert galaxies are a special class of AGN that require attention in this dissertation, since we are studying two well known Seyfert galaxies, NGC 4151 and NGC 1068. The first hint of galaxies being active took place early in the 20th century. At the time, galaxies other than our own Milky Way were referred to as ‘spiral nebulae’. (Fath 1908) first reported unusual bright emission lines in the spectrum of NGC 1068, although most of his spectra from other spiral nebulae show absorption lines produced by the combined light of the stars in that system. Later in 1917 hydrogen emission lines and other lines seen in gaseous nebulae were discovered in NGC 1068 by Slipher

(1917). He noted that the lines appear broader than expected. In the following year, Campbell & Paddock (1918) noted broad "nebulium" lines in NGC 4151, in which they stated that "the character of the spectrum resembles that of the spiral nebula NGC 1068". In 1926, Hubble measured and reported more of the unknown nebular emission lines in NGC 1068, NGC 4151 and other galaxies, with the same broad features (Hubble 1926). After the Great Debate in 1920 between Harlow Shapley and Heber D. Curtis, the 'spiral nebulae' from which the nebular lines were coming from were eventually understood to be whole galaxies, outside of the Milky Way; however, the nature of the 'nebular lines' were still not known until 1928, when Bowen (1928) identified them as strong forbidden lines of O II, O III, and N II. More nebular lines were discovered and eventually identified as weak forbidden lines of S II, S III, Ne III, Ne IV, Ne V, Ar V, and Cl III (Bowen 1936). In 1943, Carl K. Seyfert (Seyfert 1943) reported that a small percentage of galaxies have very bright nuclei that are the sources of the unusually broad emission lines produced by atoms in a wide range of ionization states, and that these nuclei are stellar (point-like) in appearance. Today these objects are known as Seyfert galaxies, and they comprise only 1–2% of all bright spiral galaxies. About 90% of the Seyfert galaxies that are resolvable by telescopes are spiral galaxies, mostly of type Sb or SBb (Carroll & Ostlie 1996).

1.2 The AGN Zoo

In the 1950s, numerous radio sources were identified with giant ellipticals in the optical, whose spectra often showed Seyfert-like emission lines (Baade & Minkowski 1954). These came to be known as Radio Galaxies, and analogous to Seyfert 1 and 2 galaxies, they are further subdivided into broad-line radio galaxies (BLRGs) and narrow-line radio galaxies (NLRGs), based on the presence or absence of the broad emission lines (Osterbrock et al. 1975).

A systemic search for radio loud objects led to the discovery of another class of AGN, quasars, short for quasi stellar radio sources (Schmidt 1963). These are stellar-like objects with emission lines at large redshifts that are sometimes surrounded by faint wisps of a halo; these halos are often resolved into a distant parent galaxy. The differences between quasars and radio galaxies are that the radio galaxies are usually hosted by giant ellipticals, most of which have relatively small redshifts, whereas the hosts of quasars are fuzzy, with predominantly large redshifts. Searches for star-like objects with UV excesses like quasars led to the discovery of a large number of objects that have spectra very similar to quasars; in fact they were "radio-quiet" quasars. These were given the name quasi-stellar objects, or QSOs, to distinguish them from the radio-loud quasars. The QSOs have spectra similar to those of BLRGs and Seyfert 1 galaxies, with bright power-law continua and broad emission lines, but are much more luminous, making them a whole new class of AGN.

BL Lac objects are somewhat similar to quasars due to their point-like radio emission, but they show few or even no spectroscopic emission lines. Their continua are normally featureless, highly variable, and highly polarized (Visvanathan 1969). Similar objects with strong emission lines are classified as optically violently variable objects (OVVs), and all-together these two groups are collectively labeled as blazars, another AGN class.

LINERs, short for Low Ionization Nuclear Emission-Line Regions, are a low-luminosity class of AGN with strong low-ionization emission lines, first identified by Heckman (1980). The emission lines [O I] $\lambda 6300$ and [N II] $\lambda\lambda 6548, 6583$ are strong and detectable in a large number of spiral galaxies, which make LINERs very common (Ho et al. 1994). Some LINERs are considered low-luminosity Seyfert galaxies, but the relationship between LINERs and AGN is still not completely clear (Peterson 1997).

Most AGNs are bright in radio wavelengths, and typically show one or two narrow beams of energetic particles ejected in opposite directions away from the center. These ‘radio jets’ are typically weak in Seyfert galaxies, and only extend out to a few hundred parsecs, compared to the large-scale radio ejections seen in other AGN. Blazars are thought to have one of their relativistic jets pointed directly toward the Earth.

1.3 The Classification of Seyfert Galaxies

The Seyfert class of objects was divided into two groups when it was discovered that their spectra did not quite match, at least in the optical. The distinction between the two types is based largely in part on a detailed study of 71 Seyfert galaxies carried out by Khachikian & Weedman (1974). The Seyfert 1 galaxies are those whose hydrogen Balmer and other permitted lines are broader than their forbidden lines, whereas the Seyfert 2 galaxies have comparable line widths for both permitted and forbidden lines. The Seyfert 2 emission lines have FWHM $\leq 500\ \mathrm{km\,s^{-1}}$. Seyfert 1 galaxies have these "narrow" permitted and forbidden emission lines, and in addition they have broad permitted lines (1000–8000 $\mathrm{km\,s^{-1}}$ FWHM). The widths of all of these lines are attributed to Doppler broadening. The fact that there are no observations to date of broad forbidden lines indicate that the broad lines in Seyfert 1s originate close to the nucleus, in a compact (≤ 1 pc) broad-line region (BLR) with high densities that collisionally de-excite the low-transition probability states that give rise to the forbidden lines. The forbidden lines on the other hand, arise from a ≤ 1 kpc NLR of lower densities. The BLR seems to be absent or hidden in the Seyfert 2s. The great luminosity of Seyfert 1s arises from a featureless continuum, whereas in the Seyfert 2s, the continuum is significantly less luminous, and usually dominated by stellar light in the optical. Normal H II galaxies with bright stellar cores typically have FWHM of $\leq 200\ \mathrm{km\,s^{-1}}$, so the 'narrow lines' in Seyfert galaxies are narrow only relative to the broad lines. Another good measurement of distinction is the [O III]/Hβ ratio, which is very high in Seyfert 2s and implies a different ionizing source for the Seyfert 2s than in the H II galaxies. The nearest bright Seyfert 1 and 2 galaxies are NGC 4151 and NGC 1068, respectively.

1.4 The Components of Seyfert Galaxies

Seyfert galaxies are good representatives of the AGN class. The various components that define the morphology of Seyferts are also present in other galaxies to some degree. The current picture of an AGN can hence be understood by considering a typical Seyfert galaxy. Starting from the inner regions of the galaxy, its center consists of an engine that is the powerhouse of the AGN. It is commonly believed that in the centers of all AGN lies a supermassive black hole (SMBH) with a mass of 10^6–10^8 $M_\odot$ for Seyfert galaxies. Normal galaxies are thought to have "inactive" SMBHs. An accretion disk that is the originator of the intense radiation field, often outshining all of the stars combined in the host galaxy, surrounds the SMBH. Feeling the brunt of the radiation field is the BLR, with a size of a few light days. The BLR is an environment of dense ($n_H = 10^9$–10^{12} cm^{-3}) ionized clouds of gas that is responsible for the high-velocity emission lines that we see. Beyond the BLR and extending out to at least a few hundred parsecs is the NLR, a less dense ($n_H \leq 10^6$ cm^{-3}) region of ionized clouds (or 'knots') that emits the narrow, permitted and forbidden, lower-velocity emission lines seen in optical and UV spectra of this region. Frequently enclosed within, and sometimes extending out to comparable distances as the NLR, or even beyond, are two collimated, relativistic beams of plasma that make up the radio jets, although these are much weaker in Seyfert galaxies than in radio galaxies or quasars. In some AGN, beyond the NLR is the ENLR, an ionized region of gas that intercepts radiation and whose motion is similar to the rest of the host galaxy on scales of kpc. In cases where the host can be resolved or seen in the glare of the nucleus, the parent galaxies can be anything from dwarf ellipticals to giant core dominated (cD) galaxies, although in the case of Seyferts they tend to be spirals. A cartoon showing the various major components in a Seyfert galaxy is shown in Figure 1.1.

1.5 Unification of Seyfert Galaxies

In the past there have been a number of attempts to unify the different classes of AGN with as few fundamental physical parameters as possible. The broad consensus is that there are fewer intrinsic differences among AGN than are observed, and the wide variety of AGN phenomena that are seen in the various classes are due to a small number of physical differences and, to a large extent, on apparent differences due to orientation effects. The origin of this broad unification scheme stems from the observation of Seyfert galaxies, in particular Seyfert 2 galaxies, where there was interest in the missing broad emission lines and strong non-thermal continuum in an otherwise identical spectrum between Seyfert 1 and 2 galaxies. It has been suggested that Seyfert 1 and 2 galaxies are physically the same, but that the BLR in Seyfert

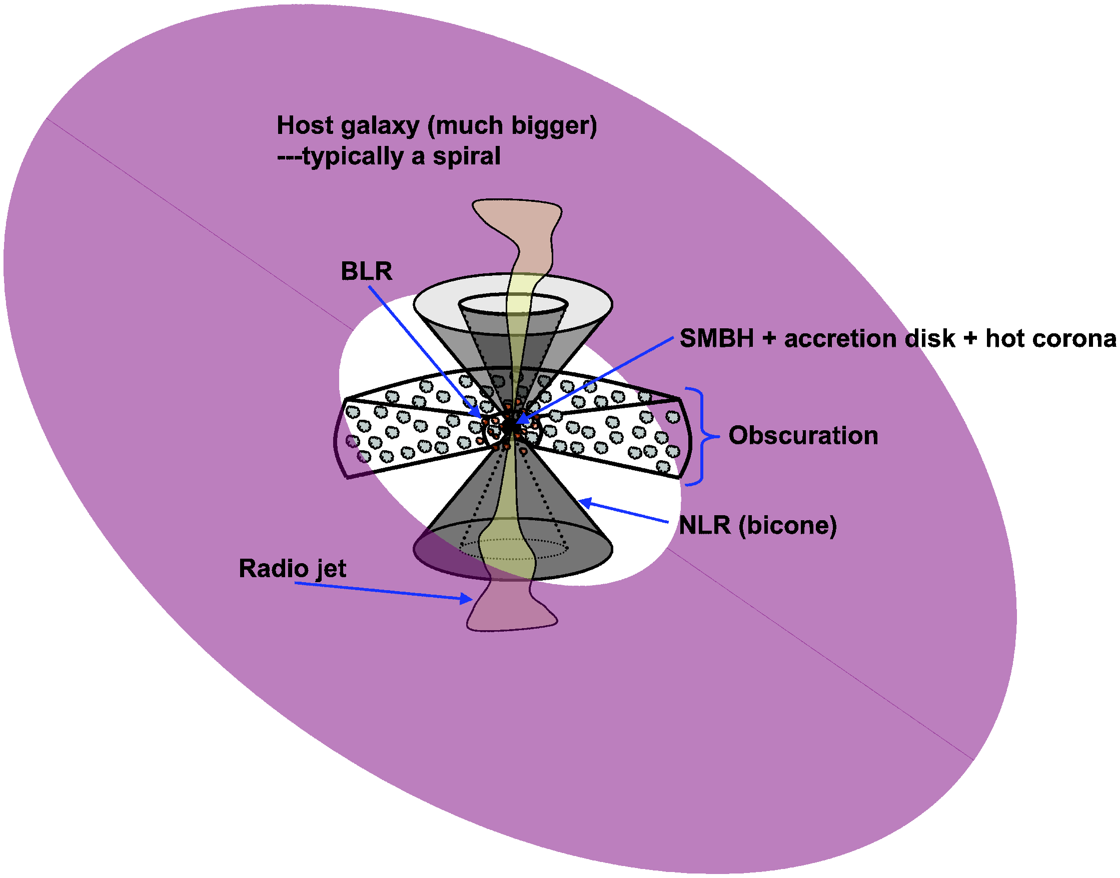

Figure 1.1: Picture of a Seyfert galaxy showing the major components.

2 galaxies is obscured from view by a thick dusty torus surrounding the nucleus (Osterbrock 1978) as illustrated in Figure 1.1. There have been modifications to the morphological nature of the torus over the years; for example, the latest claim is that the torus consists of clumpy, dusty clouds that are continuously ablating off the accretion disk, rather than a static, smooth toroidal structure (Elitzur & Shlosman 2006). But the overall picture remains that Seyfert galaxies viewed face-on relative to the torus are of type 1, whereas those that are viewed edge-on are of type 2, and that the fraction of the sky blocked by the torus determines the relative numbers of type 1 and 2 sources.

The main observational evidence for the unified model came in a paper by Antonucci & Miller (1985), where they discovered weak broad emission lines in the polarization spectrum of the Seyfert 2 galaxy NGC 1068. Antonucci & Miller proposed that the polarized broad lines were due to reflection by dust or electrons of the nuclear light that is hidden from our line-of-sight (LOS) by an optically thick source. The simplest geometry for this dusty source of obscuration is a torus. A second argument that strengthened the unification of Seyfert 1 and 2 galaxies is that the polarization of type 1 galaxies tends to be parallel to the jet axis, whereas the polarization of type 2 galaxies tends to be perpendicular to the jet axis (Antonucci 1983). Antonucci explained that Seyfert 2 galaxies therefore have to be oriented approximately edge-on with their jet axes perpendicular to the LOS, with the torus blocking any radiation coming directly from the BLR. Thirdly, the observed continuum flux of Seyfert 2 galaxies cannot produce the emission-line fluxes that we see (Kinney et al. 1991; Mulchaey et al. 1994), which indicates that the source of the continuum is being blocked in these type of galaxies. This missing radiation is not a problem for Seyfert 1s, which again indicates it arises from an orientation effect. Fourthly, observations of strong mid-IR continuum flux from hot dust in the centers of Seyfert 2s support the presence of a dusty torus near the continuum source (Storchi-Bergmann et al. 1992; Murayama et al. 2000; Rhee & Larkin 2000, 2005). Finally, narrow-band images of the emission lines from the NLRs of Seyferts often reveal biconical structures, supposedly produced by the collimation of radiation by the obscuring torus (Pogge 1988;

Tadhunter & Tsvetanov 1989; Evans et al. 1991; Kriss et al. 1992; Evans et al. 1993; Wilson et al. 1993; Arribas et al. 1996; Schmitt & Kinney 1996; Schmitt et al. 2006). Since then, it was realized that the same unification might apply to BLRGs and NLRGs, which are the radio-loud analogues to Seyfert 1 and 2 galaxies respectively. In addition, the Blazar class of AGN is thought to be viewed with the line-of-sight very close to the jet axis, the only orientation that could explain the 'beamed' radiation effect that results in the ultra-luminous appearance of these objects and the apparent superluminal motion of many of their radio components. Seyfert galaxies are therefore the backbone upon which current unification schemes are based, mainly because they are relatively nearby and bright, and hence the most intensely studied AGN in the sky.

1.6 The NLR of Seyfert Galaxies

The NLR in Seyfert galaxies presents an interesting component for study because it is the only component that can be spatially resolved in the optical. *HST* images of the NLR have for the first time distinguished their structures, which have resulted in the advancement in understanding of the physical processes in the NLR. Photoionization studies have helped us understand the physical conditions in the NLR gas such as its ionization state, abundances, densities, etc. (e.g., Kraemer & Crenshaw 2000b). However there are still important questions that remain mostly unanswered to this day. Firstly, what drives the NLR gas? It is thought by some that the NLR is largely ionized and driven laterally away from the jet axis by the radio jet (Pedlar et al. 1989; Taylor et al. 1992; Axon et al. 1998; Capetti et al. 1999), while others claim that the NLR gas is being ionized and driven in outflow by the central engine (Hutchings et al. 1999; Crenshaw et al. 2000; Ruiz et al. 2001; Crenshaw & Kraemer 2000b). Another mystery that remains to be explained is the velocity behavior and confinement of the NLR gas, which flows to large distances without breaking apart. The answers to these questions will shed considerable light on the dynamical processes at work in the nuclei of Seyferts in particular and AGN in general. It is with these questions in mind that we have undertaken this dissertation. We will attempt to answer some of the questions in the remaining sections and in the chapters to follow.

1.6.1 Ionization of the NLR

The ionization mechanism of the NLR of Seyfert galaxies has been scrutinized intensely over the past few decades. The two leading mechanisms were photoionization (see Koski 1978; Ferland & Osterbrock 1986, and references therein) and shock ionization (see Dopita & Sutherland 1995, and references therein). Photoionization was suggested as the dominant source of energy to produce the emission lines seen in the NLR as early as 1964 (Greenstein & Schmidt 1964; Oke 1965), where it was shown that shocks would not suffice to produce continuous energy in a small region over large timescales. Models by Osterbrock & Parker (1966) showed that photoionization can account for both high and low ionization emission lines seen in QSOs.

Recently, studies have shown that most of the emission lines seen in the NLR can be accounted for by assuming a central ionization source illuminating a multi-component gas (Kraemer et al. 2000; Kraemer & Crenshaw 2000a; Groves et al. 2004, and references therein), although an additional localized source of ionization which may be due to shocks was detected in NGC 1068 at the point where the NLR gas decelerates. Mundell et al. (2003) showed that the misalignment of the radio jet and NLR in NGC 4151 supports photoionization of the NLR by the AGN as the dominant excitation mechanism, but that enhanced optical emission observed in a few clouds bounding the radio jet might be shock related. Since it is now generally accepted that photoionization is the dominant source of ionization of the NLR gas, with shocks possibly contributing in localized regions, we will focus this dissertation on the kinematics and dynamics of the NLR, to gain more insight into the acceleration, and possibly deceleration, mechanisms of the gas.

1.6.2 Kinematics and Dynamics of the NLR

1.6.2.1 Ground Based Studies

Ground-based studies of the NLR of Seyfert galaxies have been limited to spatial resolutions of $\geq$ 50 pc for even the most nearby ones (Kaiser et al. 2000, and references therein). These studies have relied primarily upon spatially integrated line profiles to understand the dynamics of the NLR (Schulz 1990; Veilleux 1991). The problem with these ground based studies is that the emission-line profiles of the NLR gas can be explained by many different types of dynamical models, such as infall, rotation and outflows (Vrtilek 1983; Krolik & Vrtilek 1984; Vrtilek 1985). The first evidence for radial outflow in the NLR was presented in a ground-based study by Walker (1968). Later, Bell & Seaquist (1980) and Heckman et al. (1981) claimed that general outflow is required to map the motions of the NLR clouds but that tangential motions with some random component is possible. Heckman et al. (1981) analyzed and presented measurements of spatially integrated line profiles with spectral resolution $\sim 130\ \mathrm{km\,s^{-1}}$ for a sample of 27 Seyfert galaxies. They found that the blue asymmetries seen in the line profiles of [O III] can be explained by either infall or outflow depending on the location of the dust in the NLR. In the outflow scenario, the receding gas on the far side will be preferentially hidden from the observer by intervening dust, hence the blue asymmetry in the line profiles. However, if the dust is located primarily within the clouds, and the clouds are in infall, then the far side will be viewed preferentially by an observer, again resulting in the blue asymmetry seen in the line profiles. Heckman et al. (1981) argued for outflow because infalling clouds would have a difficult time losing angular momentum and reaching high velocities in an axisymmetric disk system. Krolik & Vrtilek (1984) modeled the motion of the NLR gas by assuming that the gas is embedded in a hot sparse medium, which drags the clouds in outflow. They also managed to replicate the blue asymmetry seen in the line profiles. Subsequent studies provided mounting evidence for outflows of the NLR gas. Mathews & Veilleux (1989) argued strongly for gas outflow, based upon stability requirements of the constituents clouds. Cecil et al. (1990) were able to isolate kinematic subsystems from the line profiles of NGC 1068, and they modeled the kinematics of the gas based upon accelerated gas outflow due to a high-speed thermal wind.

1.6.2.2 Space Based Studies

With the launch of *HST* and its high angular resolution ($\sim 0\overset{\prime\prime}{.}1$), the NLR of Seyfert galaxies has received considerable attention. With the limited long-slit capability of the Faint Object Camera (FOC), and later the expanded capability of STIS, detailed constraints on the kinematics of the NLR in Seyfert and other galaxies became possible. In turn, these kinematic studies provide good diagnostics upon which dynamical analyses can be based. In the following section we summarize previous kinematic and dynamic studies of the NLR.

The structure of the NLR resembles a biconical geometry and such a geometry was expected from a simple unified model, due to collimation by a thick torus (Antonucci & Miller 1985). Both Schulz (1990) and Evans et al. (1993) have modeled the NLR of NGC 4151 and found it to be consistent with a biconical geometry. In an *HST* study done on a sample of Seyfert 1 and 2 galaxies, Schmitt & Kinney (1996) compared both Seyfert types to study their NLR morphologies, and found triangular structures in most of their Seyfert 2s, and circular structures in most of their Seyfert 1s, consistent with the unified model and biconical structure for the NLR (see also Schmitt et al.

2003a,b). Veilleux et al. (2001) modeled the inner regions of the Seyfert galaxy NGC 2992, and found that the ionized gas can be fitted with a biconical structure.

The biconical geometry seems to be ubiquitous in the NLR of Seyfert galaxies, and two competing theories have emerged to explain the kinematics of the NLR gas. One line of studies suggests that the flow of the NLR gas is laterally away from the bicone/radio jet axis, which could be due to the radio jet's hot expanding cocoon. The other theory is that of radial outflow of the gas, due for example, to accelerated line driving by intense radiation from the central engine. In the next discussion, we explain some of the work done by researchers in these two areas, and in this dissertation we intend to shed more light on the nature of the driving mechanism of the NLR gas.

Lateral Flow Models - Based on FOC long-slit spectra, several authors suggest that the NLR clouds are accelerated by interactions between a radio jet and the ISM, such that clouds are carried away laterally from the radio jet axis by an expanding cocoon of shocked gas (Axon et al. 1998; Capetti et al. 1999; Winge et al. 1999, and references therein). In Capetti et al. (1999), long slit FOC spectra were taken perpendicular to the radio jet of Mrk 3. They found that in some slits, the [O III] emission line velocities split into two systems separated by several hundreds of $\mathrm{km\,s^{-1}}$ apart on either side of the jet. One of the systems is receding and the other one is approaching relative to the host systemic velocity, which Capetti et al. interpreted as expansion of gas away from the jet. In Axon et al. (1998) the same splitting of velocities across a radio jet was observed in NGC 1068 and also interpreted as expansion of the gas away from the radio jet. The jet-driven models suggest that the lateral expansion of the shocked cocoon will produce both blueshifted and redshifted velocities with approximately equal magnitudes along the jet/bicone axis at each location in the NLR, regardless of axis orientation. A clear representation of this picture is shown in Figure 6 in Nelson et al. (2000). Because of the excellent radio data we obtained, we will test these scenarios for possible radio jet and NLR cloud interactions in later chapters.

Radial Flow Models - Biconical outflow modeling of the NLR using STIS data was previously done by our group for NGC 1068 (Seyfert 2), Mrk 3 (Seyfert 2), NGC 4151 (Seyfert 1), and by other researchers (see for example Hutchings et al. 1998, 1999; Kaiser et al. 2000; Nelson et al. 2000; Cecil et al. 2002, and references therein). The NLR of NGC 1068 was modeled by Crenshaw & Kraemer (2000b) with data taken with the G430L grating of STIS. The radial velocity measurements were made using the bright [O III] λ5007 emission line with a $0\farcs1$ wide slit at position angle 202°. Acceleration of the gas to $\sim$ 100 pc and subsequent deceleration back to systemic velocity was inferred. Their model consisted of a simple biconical outflow geometry which is evacuated along the axis and tilted slightly out of the plane of the sky to match the amplitudes of blueshifted and redshifted clouds. Blueshifted and redshifted clouds were observed in both the northeast and southwest parts of the bicone, which could explain the "line-splitting" observed by Axon et al. (1998).

The NLR of Mrk 3 was modeled by Ruiz et al. (2001) using a combination of STIS medium resolution slitless and low resolution long slit data. A similar geometric/kinematic model matched the data well. Clouds were seen to accelerate close to the nucleus, then decelerate back to systemic velocity, a trend which is seen in other Seyfert galaxies. In an analysis of 10 Seyfert galaxies, Ruiz et al. (2005) studied the kinematics of the NLR using slitless spectroscopy at high spectral resolution. Each was observed with the STIS 1024x1024 pixel CCD detector through an open aperture ($52'' \times 52''$) and dispersed with the G430M grating. A high resolving power of ~ 9000 allowed velocity measurements down to ~ 33 km s^{-1} in the vicinity of the [O III] λ5007 line. Each target was observed during a single *HST* orbit. Although modeling was not done, the tell-tale signs of acceleration and deceleration of the gas seemed to be present in almost all of their Seyfert galaxies. In all the above papers, the observations and models indicate that the dominant accelerating mechanism emanates from within tens of parsecs from the central engine and that the acceleration is radial rather than lateral from the radio jet axis.

In Crenshaw et al. (2000), the NLR of NGC 4151 was similarly modeled with two slit positions, each $0\farcs1$ wide, at position angles 221° and 70°. The axis of the bicone was tilted to match the blueshifted and redshifted clouds, which contrary to NGC 1068, occurred exclusively in the southwest and northeast cones, respectively. With an inclination of the bicone axis with respect to the plane of the sky of 40°, they found that the models fit the data reasonably well.

In the first truly dynamical model of the NLR based on *HST* kinematics, Everett & Murray (2006) attempted to fit the NLR velocities in NGC 4151, based on measurements done by Das et al. (2005, see also §4.1). They tested an isothermal Parker wind model which assumes thermally expanding winds (Parker 1965). By assuming a spherical cloud geometry, they let the Parker wind drag along the embedded NLR clouds. As the Parker wind accelerates by thermal expansion and slowly loses heat by adiabatic cooling, the clouds are also accelerated to high speeds. They then let the Parker wind ram into a low density ambient medium to slow the velocity of the wind, and hence the clouds, back down to the systemic velocity. The model explains the velocity profile of the NLR of NGC 4151, but suffers from the fact that an isothermal wind cannot be sustained out to large distances. Also, the mass profile of the SMBH plus galaxy, which determines the temperature profile for their model, is not exactly known for NGC 4151. Hence while their model was not successful on physical grounds, it is worth noting its relative success in matching the NLR kinematics.

Cecil et al. (2002) analyzed several complexes and knots of gas that cover the entire NLR of NGC 1068 using long-slit STIS observations. These were sampled into radial velocity profiles, with some knots showing radial velocities as high as -3200 km s^{-1}. Simple biconical outflow models were overlaid on their [O III] spectral images for all slit positions, and velocities were compared. They also overplotted model velocities where the gas is allowed to expand away from the radio jet axis. They suggest that a higher maximum velocity than was found in Crenshaw & Kraemer (2000b) was required to better match the blue wing of the northeast cone. The red wing was not matched. The lateral expansion model also predicted larger velocities for the red wings than the data showed. They suggest that the redshifted bright emission seen in the northeast cone is caused by the clouds being pushed into the galactic disk by the expansion of the radio lobe, and that these clouds are most likely dragged along the galactic disk. This may explain the clouds' lower velocities. The blueshifted clouds are accelerated away from the galaxy and suffer no such fate, and hence their higher velocities. They also suggest that the high-velocity knots in the northeast can be explained by ablation of massive infalling dusty clouds.

We have remeasured the Cecil et al. (2002) observations of NGC 1068 as part of this dissertation, specifically for testing simple velocity models by separating the multiple emission components seen along the slit. Also we wanted to make detailed comparison between the NLR clouds and the radio knots to look for any disturbances in the clouds' velocities that would prove or disprove the lateral expansion flow model of the radio jet. Our initial study of the kinematics in NGC 1068, using the dataset of Cecil et al. (2002), was published in Das et al. (2006). Our other large dataset comes from our long-slit observations of NGC 4151, which were first published in Das et al. (2005).

– 2 –

Observations

2.1 *HST* Observations of NGC 4151

We obtained a total of five long-slit STIS spectra from the archives of MAST. These observations were taken by J. Hutchings (PI on proposal ID 8473) on 2000 July 02 with five orbits of *HST* time and we analyzed them in collaboration with the PI and Co-Is on the proposal. The slits were aligned in the sky in a parallel configuration at position angle of $57\overset{\circ}{.}8$ (rotation of the slit from N to E), and co-align well with the long axis of the NLR of NGC 4151 shown in Figure 2.1. In each orbit of *HST*, there were a total of three exposures per slit with a total of $\sim$ 40 minutes of integration for slit 1 and $\sim$ 48 minutes for the remaining slits. Each slit position was observed with an angular width of $0\overset{''}{.}2$ and an angular height of $52''$, and the entire light path through the STIS apparatus and medium resolution G430M grating restricted the wavelength dispersion to $\Delta\lambda = 0.28$ Å pixel^{-1}, resulting in a spectral resolving power of R=$\lambda/\Delta\lambda \approx 9000$ in the optical. The grating peaked at 4961 Å and transmitted light from a bandpass of 4820–5100 Å, which included the redshifted Hβ λ4861 line and the [O III] $\lambda\lambda$ 4959, 5007 emission lines as well. For our measurements, we used the [O III] lines because they are bright, with λ5007 being brighter than λ4959. The angular resolution of the STIS CCD is $0''.1$ pixel^{-1}, but the data from each slit were oversampled at $0''.05$ pixel^{-1} and saved onto a grid of 1024x1024 pixels. Each slit position therefore resulted in 1024 spectra, some of which were very noisy.

We used a systemic redshifted velocity of 997 km s^{-1}, based on H I observations of the outer regions of the host galaxy (Pedlar et al. 1992). A Hubble constant of 75 km s^{-1} Mpc^{-1} gives us a distance of 13.3 Mpc to NGC 4151, with $0''.1$ corresponding to a projected linear distance of 6.4 pc on the sky. The observational parameters for NGC 4151 are shown in Table 2.1.

Table 2.1: Observational Parameters for NGC 4151.

Slit position	Dataset	Date	Start time	Exp time (s)
1	O5KT01010	2000-07-02	03:01:00	2379
2	O5KT01020	2000-07-02	04:29:00	2865
3	O5KT01030	2000-07-02	06:06:00	2865
4	O5KT01040	2000-07-02	07:42:00	2865
5	O5KT01050	2000-07-02	09:19:00	2865

The top panel of Figure 2.1 shows an [O III] image of the inner $4''$ of the NLR of NGC 4151 as it would appear in the sky. The image shows the clumpy nature of the emission-line clouds and the approximate biconical shape of the region. The bright spot in the center corresponds to the continuum and [O III] peak and was used as a reference point to center the slits. The slit placements and orientation are shown in the bottom panel of the image. Slit 1 was centered on the optical continuum peak, where the SMBH presumably resides, and the remaining slits were taken at

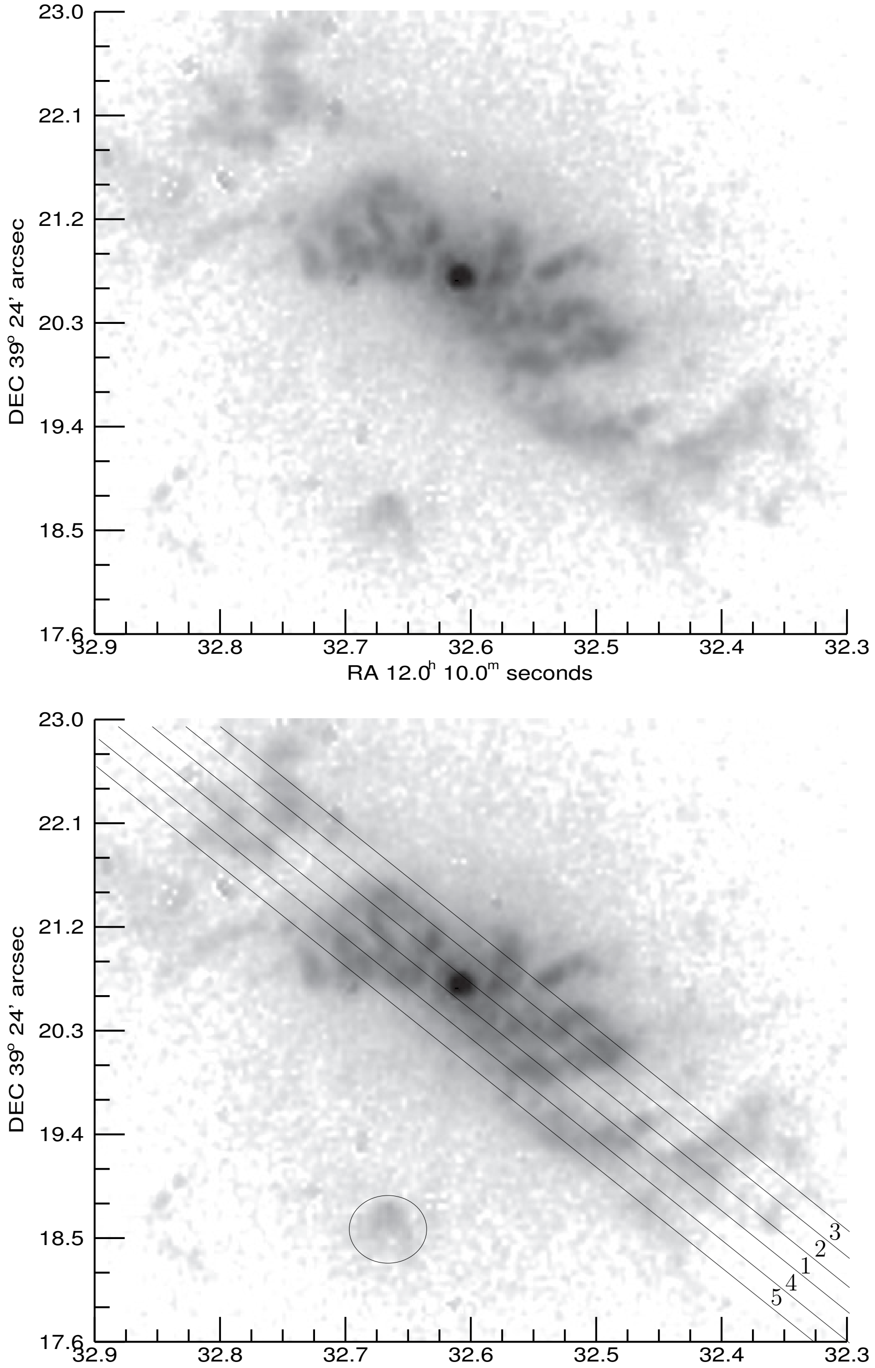

Figure 2.1: Top: WFPC2 [O III] image of the NLR of NGC 4151 showing the clumpy nature of the clouds and the bright continuum peak where the SMBH lies.
Bottom: Same image showing the placement of the five slits by STIS. The circle encloses an artifact produced by WFPC2. North is up and east is to the left.

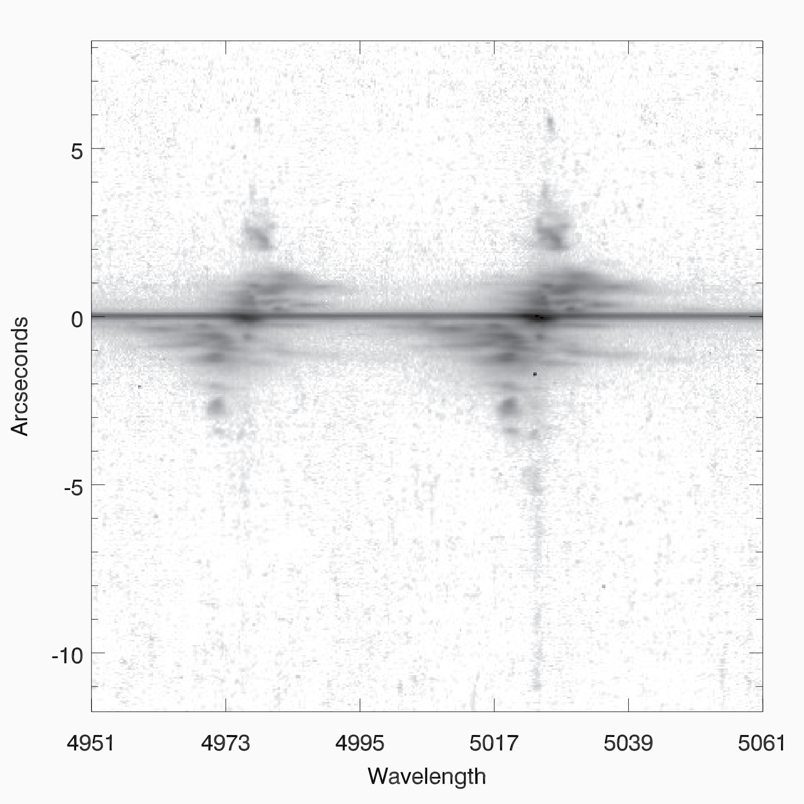

Figure 2.2: Spectral image of slit 1 of the NLR of NGC 4151 showing the two [O III] emission lines $\lambda\lambda$ 4959, 5007. Northeast is up in this image.

0″.2 and 0″.4 on either side, parallel to slit 1. This [O III] image was taken by Holland Ford on 1995 January 22 (Proposal ID: 5124) with the Wide Field Planetary Camera 2 (WFPC2) camera aboard *HST*. The narrow band filter F502N was used with 260 seconds of exposure to allow passage of the [O III] λ5007 emission line. One can see in this image that most of the emission comes from within 2″ of the bright central knot, although [O III] emission can be traced as far as 6″ on either side. The slits are approximately aligned with the long axis of the NLR for this galaxy. Later we will see that the kinematic major axis of the NLR is also along this orientation.

Figure 2.2 shows a fully reduced STIS spectral image of the twin [O III] emission lines, as they appeared through slit 1 (the data reduction is described in §2.5). The image is shown without the redshift correction of the host galaxy. The bright horizontal line through the image is the optical continuum emission produced by the nucleus. The top of the image corresponds to the northeast direction and the horizontal scale is in wavelength. Both [O III] lines clearly show an overall trend, in that the majority of clouds in the upper region are receding or redshifted and those clouds in the bottom part of the image are approaching or blueshifted with respect to the host galaxy. Close to the nucleus, within $\sim 2''$, the clouds tend to have high velocity dispersions. One can see at some positions multiple knots of [O III] gas at different wavelengths, indicating the presence of multiple clumps of gas along the line of sight, at different distances and velocities from the observer. The same kinds of patterns can be seen in Figures 2.3–2.4, with the exception of the bright continuum that is shown in Figure 2.2 (slit 1). In all the slits, the position measured along the vertical is with respect to this bright continuum; so for slits 2–5, which do not intercept this continuum, the position along each slit was measured with respect to the same pixel location in the dispersion direction that correspond to the continuum in slit 1.

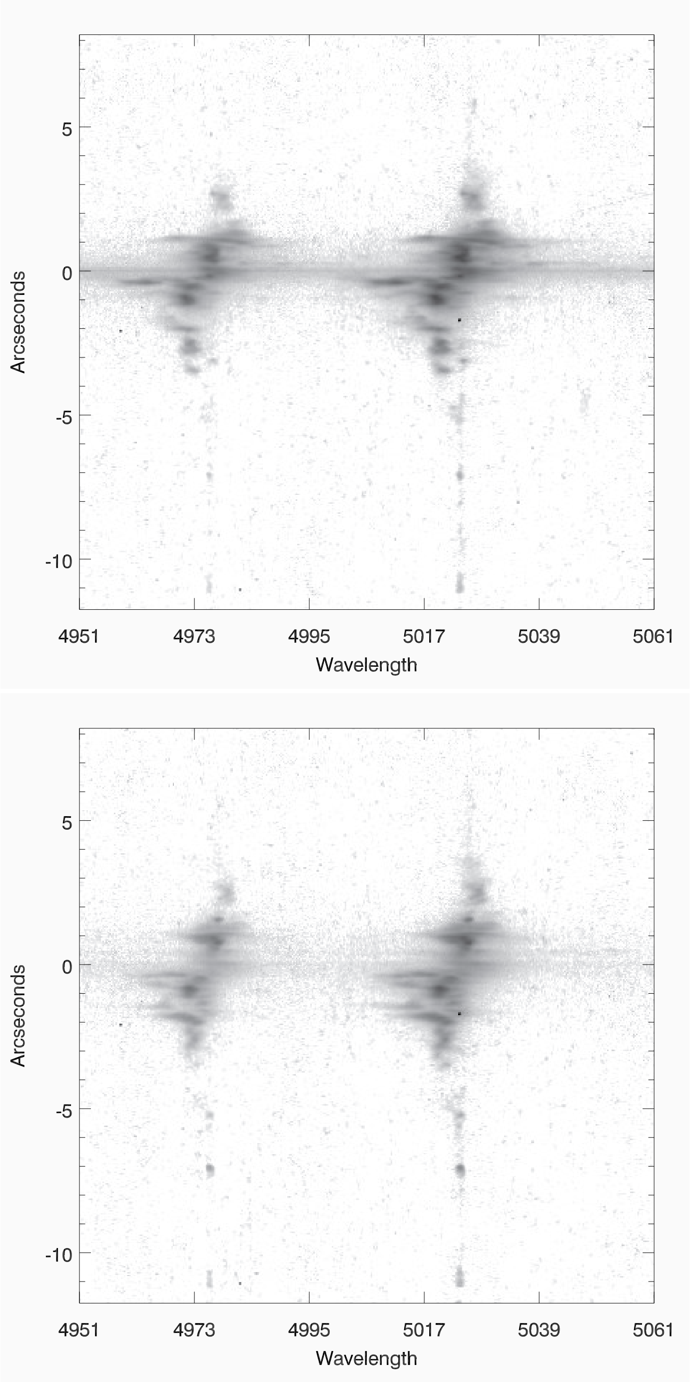

Figure 2.3: Spectral images of slits 2 (top) and 3 (bottom) of the NLR of NGC 4151 showing the two [O III] emission lines. Northeast is up in this image.

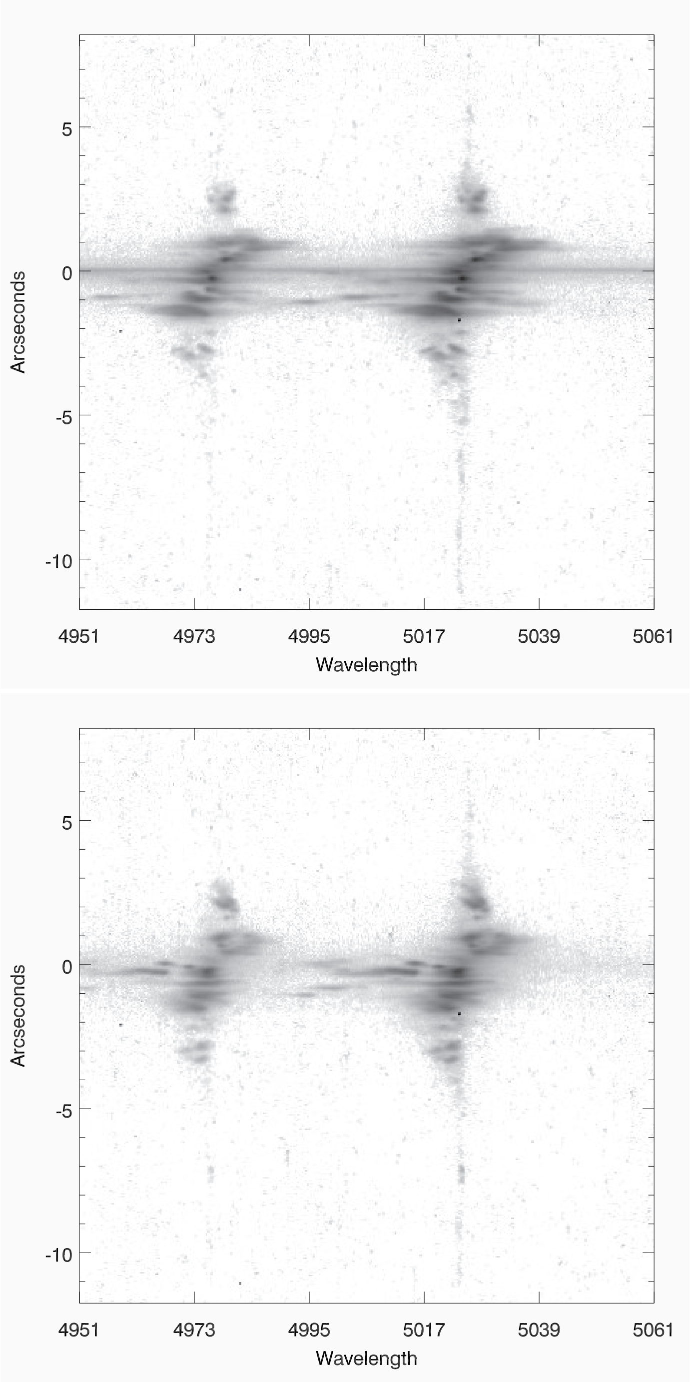

Figure 2.4: Spectral images of slits 4 (top) and 5 (bottom) of the NLR of NGC 4151 showing the two [O III] emission lines. Northeast is up in this image.

2.2 Radio Maps of NGC 4151

As part of the study we obtained the high resolution radio map of the radio jet of NGC 4151 from Mundell et al. (2003) shown in Figure 2.5. The map was taken with the 10-element Very Long Baseline Array (VLBA) plus the 27 antennas of the Very Large Array (VLA) and covers a region of 3$''$.2 (210 pc) along the jet axis. The radio map was imaged in λ21 cm continuum radio emission, which corresponds to a frequency of 1.4 GHz, and has an angular scale of 0$''$.014 pixel^{-1}. Our STIS slit positions projected on to the radio map are shown in Figure 2.6. The second brightest radio knot in slit 1 (known as radio knot D) is where the SMBH supposedly resides. This

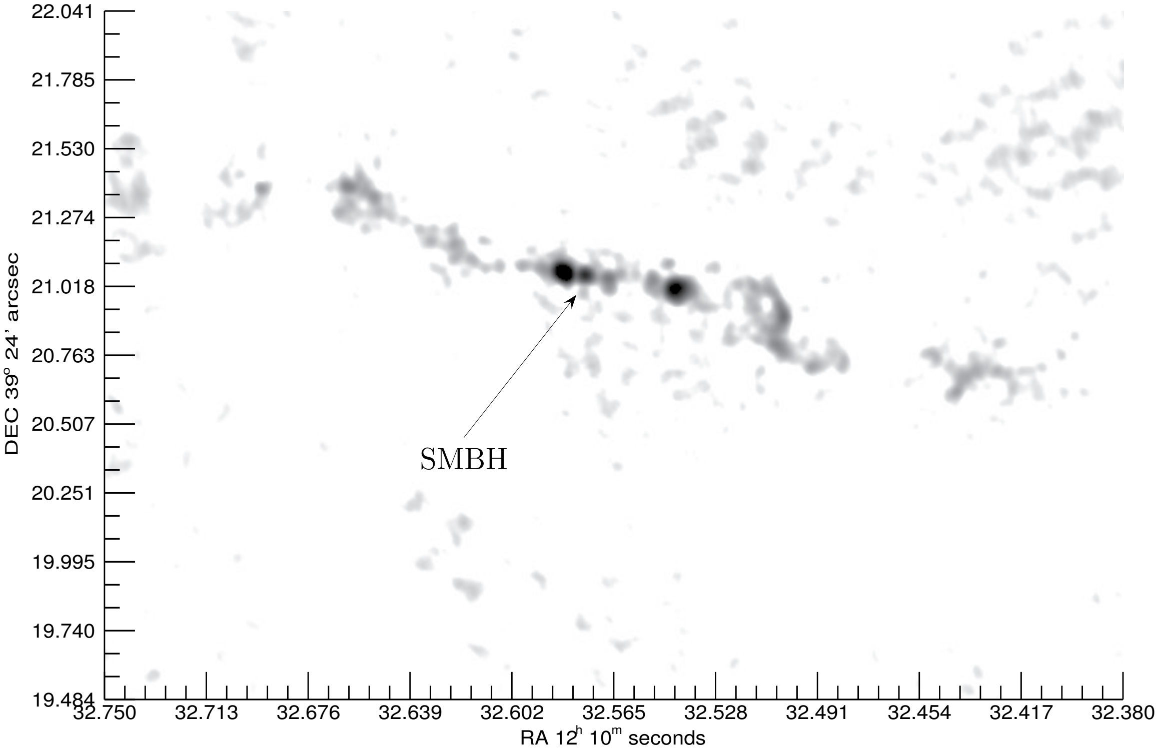

Figure 2.5: The radio map of NGC 4151 showing the knotty structure of the jet and the location of the supermassive black hole. North is up and east is to the left.

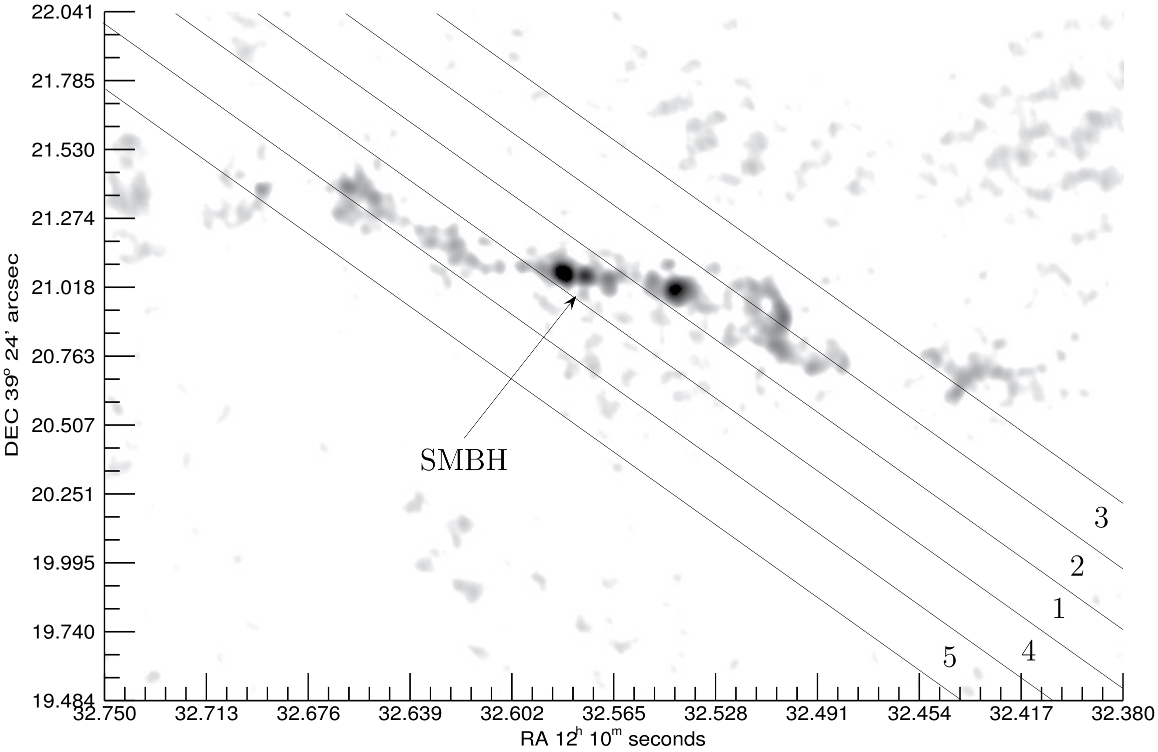

Figure 2.6: The radio map of NGC 4151 showing the positions of the STIS slits relative to the jet axis. North is up and east is to the left.

argument was based on the structure of the radio continuum emission and the distribution of the H I absorption lines (Mundell et al. 2003). For more detailed information concerning the radio map, see Mundell et al. (2003), and references therein.

The radio jet does not align particularly well with the slits and the NLR long axis as shown in Figure 2.6. The radio jet intersects all five slits and is at almost 90° in position angle in the sky. Because NGC 4151 is a Seyfert 1 galaxy, its inclination in the sky, together with the different position angles among the axes of the NLR, the radio jet, and the slits, makes testing for jet-cloud interactions between the radio knots and the NLR clouds difficult but not impossible.

2.3 *HST* Observations of NGC 1068

Observations of NGC 1068 were taken on 1999 September, 1999 October, and 2000 September by Cecil et al. (2002). They used STIS aboard *HST* to obtain spectra with the G430M grating, at a spectral resolution of $\lambda/\Delta\lambda \approx 9000$ and a spatial resolution of $0\farcs1$ along and $0\farcs2$ across each slit. Due to complications with guide stars, the observing time was split into two parts, one year apart, which resulted in a total of seven parallel long slit spectra at position angle 38°. Slits 1–5 were taken in 1999, and slits 6–7 were taken the following year. Slits 5 and 6 overlapped the same region of the sky, except for an offset of 17 pixels ($0\farcs85$) in the cross-dispersion direction. Slit 7 was also offset by the same amount relative to the first five slits. Each observation had a spectral coverage of 4820–5100 Å, to obtain maps of the [O III] and Hβ profiles. An additional observation included in this study (slit 8) was taken with the G430M grating of STIS by R. Antonucci (PI) in 2000 January at position angle of 10°. Three separate observations were obtained at the same slit location to correct for cosmic ray hits and other artifacts. The data from all the slit locations were binned in the dispersion direction by a factor of two and recorded with resolution $0\farcs05$ pixel^{-1} onto a 1024x534 wide grid. Each row represents one spectrum, and each slit therefore yields 1024 spectra, a few hundred of which were too noisy to be useful.

We used a systemic redshifted velocity of NGC 1068 of 1148 km s^{-1}, based on H I observations by Brinks et al. (1997), and a distance to NGC 1068 of 14.4 Mpc (Bland-Hawthorn et al. 1997), based on a Hubble constant of $\mathrm{H_0} = 75$ km s^{-1} Mpc^{-1},

Table 2.2: Observational Parameters for NGC 1068.

Slit position	Dataset	Date	Start time	Exp time (s)
1	O56502010	1999-10-02	07:57:00	2585
2	O56502020	1999-10-02	09:29:00	2775
3	O56502030	1999-10-02	11:06:00	2775
4	O56502040	1999-10-02	12:43:00	2775
5	O56502050	1999-10-02	14:19:00	2772
6	O56503010	2000-09-22	02:48:00	2294
7	O56503020	2000-09-22	04:15:00	2853
8[a]	O5LJ01050	2000-01-14	05:33:00	800
8[a]	O5LJ01060	2000-01-14	05:48:00	846
8[a]	O5LJ01070	2000-01-14	06:04:00	960

[a] these were added to comprise slit 8

and including a correction for Virgocentric infall. Therefore $0''.1$ corresponds to 7.2 pc. The observational parameters for NGC 1068 are shown in Table 2.2 (for more details see Cecil et al. 2002).

Figure 2.7 shows an [O III] image of the NLR of NGC 1068 as it would appear in the sky, while Figure 2.8 shows the same image but with the slit placement of Cecil et al. (2002) on top. The [O III] image was separately taken by William B. Sparks on 1994 January 10 (Proposal ID: 5578) with the FOC aboard *HST*. The narrow band filter, F501N, was used with 1196 seconds of exposure to reveal one of the two narrow forbidden [O III] emission lines, namely λ5007. The slit positions cover an area of 86.4 pc across and a few thousand pc along the slits. However, the brightest emission is seen only within a few hundred parsecs of the SMBH. Roughly 90% of this NLR emission is covered by the slits, with some emission seen outside of slits 1 and 7. Slit

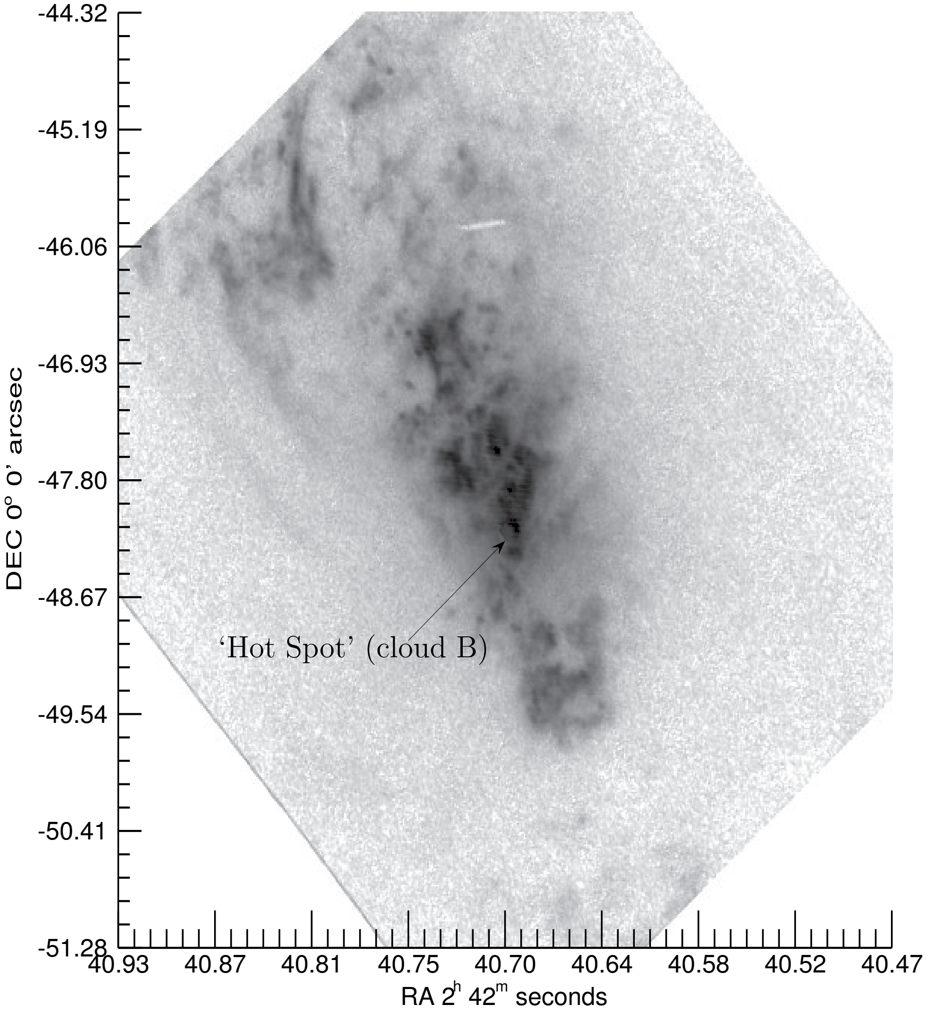

Figure 2.7: [O III] image of the NLR of NGC 1068 showing the clumpy structure of the clouds and the position of the continuum hot spot. We applied a sigma-filter to remove the reseaux intrinsically placed on the image. The reseaux are placed for alignment purposes on all FOC images. North is up and east is to the left.

positions 1–7 can be seen to be a few degrees off from the general orientation of the NLR long axis of NGC 1068.

Figures 2.9–2.12 show fully reduced STIS spectral images of the twin [O III] emission lines, $\lambda\lambda 4959, 5007$, as they appeared through slits 1–8 respectively. The images are shown without the redshift correction of the host galaxy. The bright horizontal

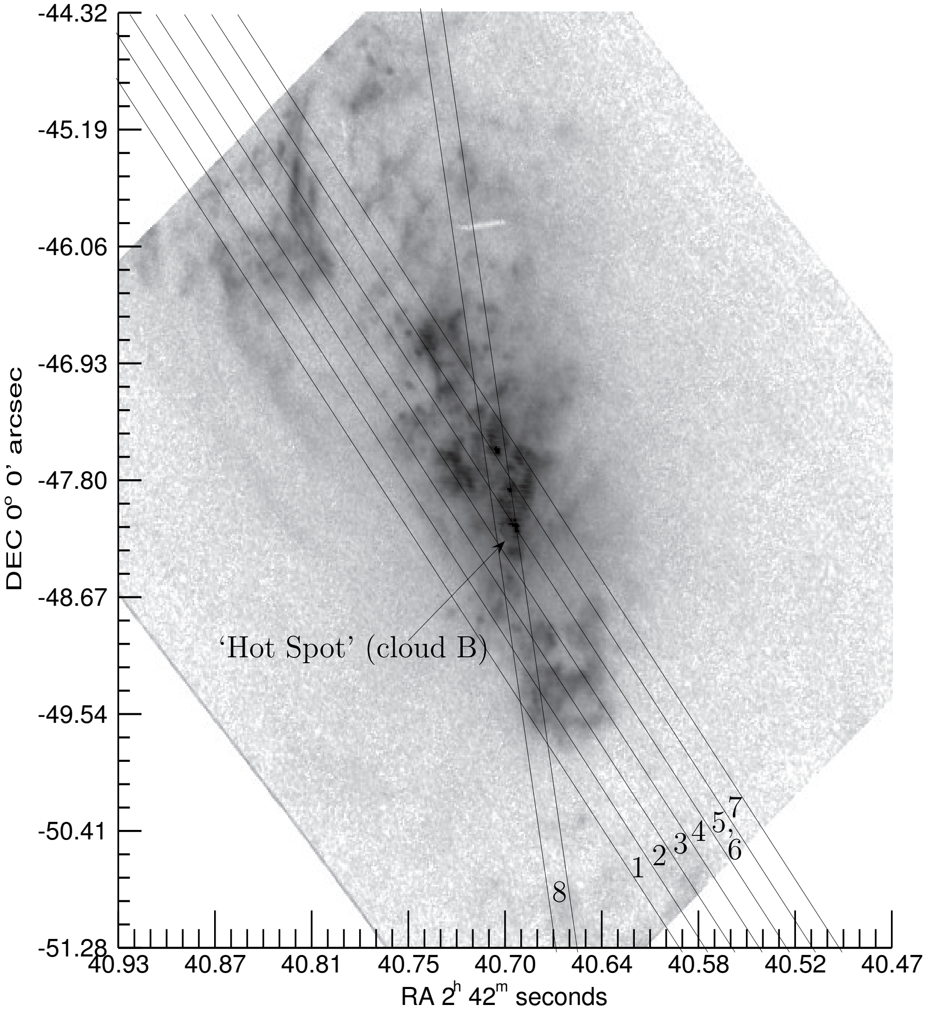

Figure 2.8: Same image as in Figure 2.7 showing the placement of the slits by STIS.

line through the spectral image of slit 4 is the optical continuum emission produced by nuclear light scattering off of electrons (Crenshaw & Kraemer 2000a), sometimes called the "hot spot". The hidden nucleus of NGC 1068 is then 0.″13 south of this optical hot spot according to precision astrometric studies by Capetti et al. (1997) (see §3.3.2 for more details). The less intense but broader dark band across all the images is produced by continuum emission from the massive stellar cluster that is present ∼ 100 pc on either side of the nucleus. The [O III] lines seen in the images show an overall trend in the northeast, of increasing redshifts and blueshifts up to a distance of $\sim 2''$. In the southwest however, there are fewer clouds and such trends are not clear. As in the case for NGC 4151, within $\sim 2''$ of the nucleus, the clouds appear highly dispersed in velocity, and one can see in the northeast multiple knots of [O III] gas at different wavelengths, indicating the presence of multiple clumps of gas along the line of sight, at different distances and velocities from the observer. The bright continuum line seen in slit 4 is also shown in slit 8, since this slit also intercepts the continuum hot-spot. In all the slits, the position measured along the vertical is with respect to this bright continuum. For slits 1–3 and 5–7, which do not intercept this continuum, the position along each slit was measured with respect to the same pixel location in the dispersion direction that corresponds to the continuum in slit 4.

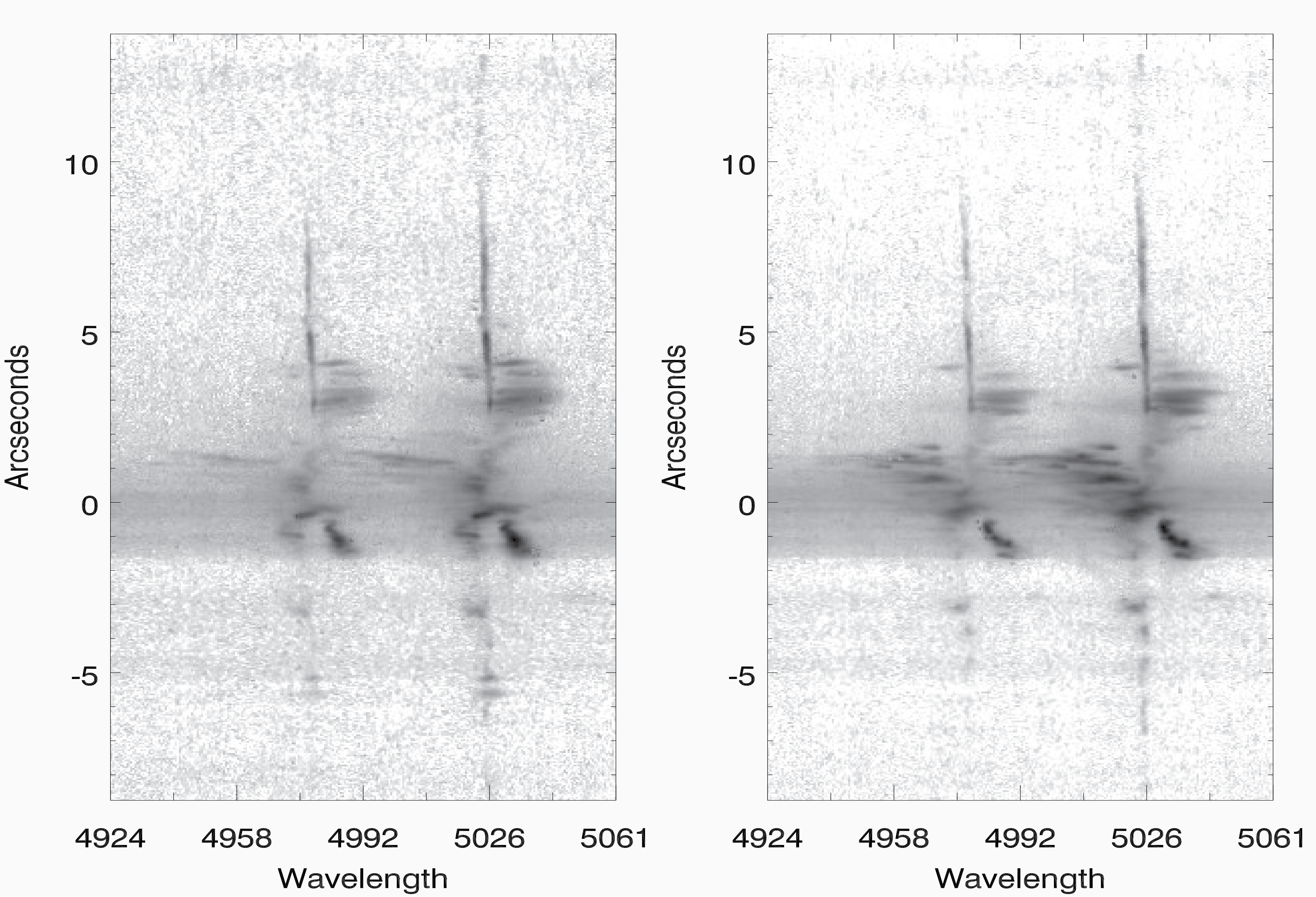

Figure 2.9: Spectral images of slits 1 (left) and 2 (right) of the NLR of NGC 1068 showing the two [O III] emission lines, $\lambda\lambda 4959, 5007$. Northeast is to the top of these images.

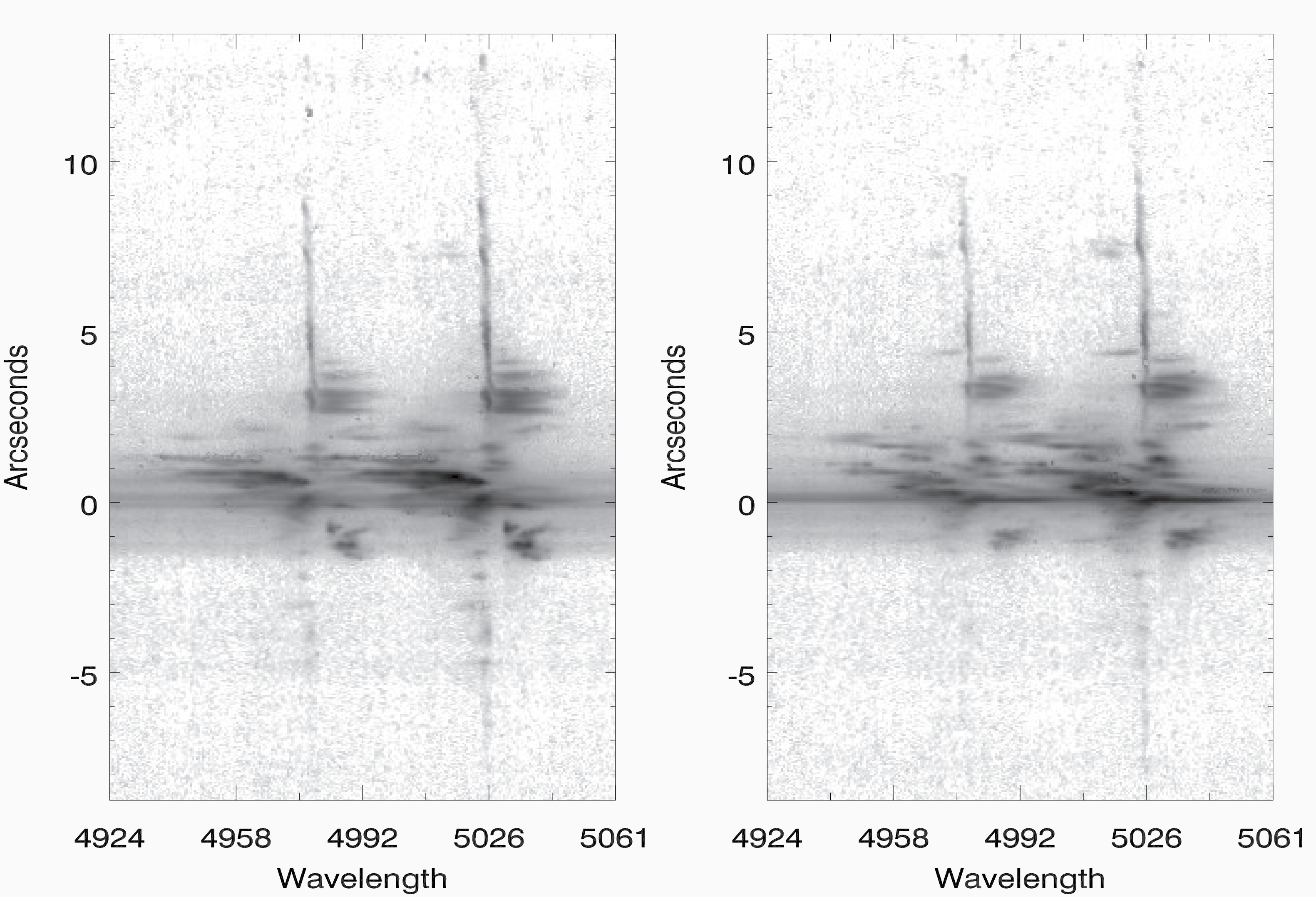

Figure 2.10: Spectral images of slits 3 (left) and 4 (right) of the NLR of NGC 1068 showing the two [O III] emission lines, $\lambda\lambda 4959, 5007$. Northeast is to the top of these images.

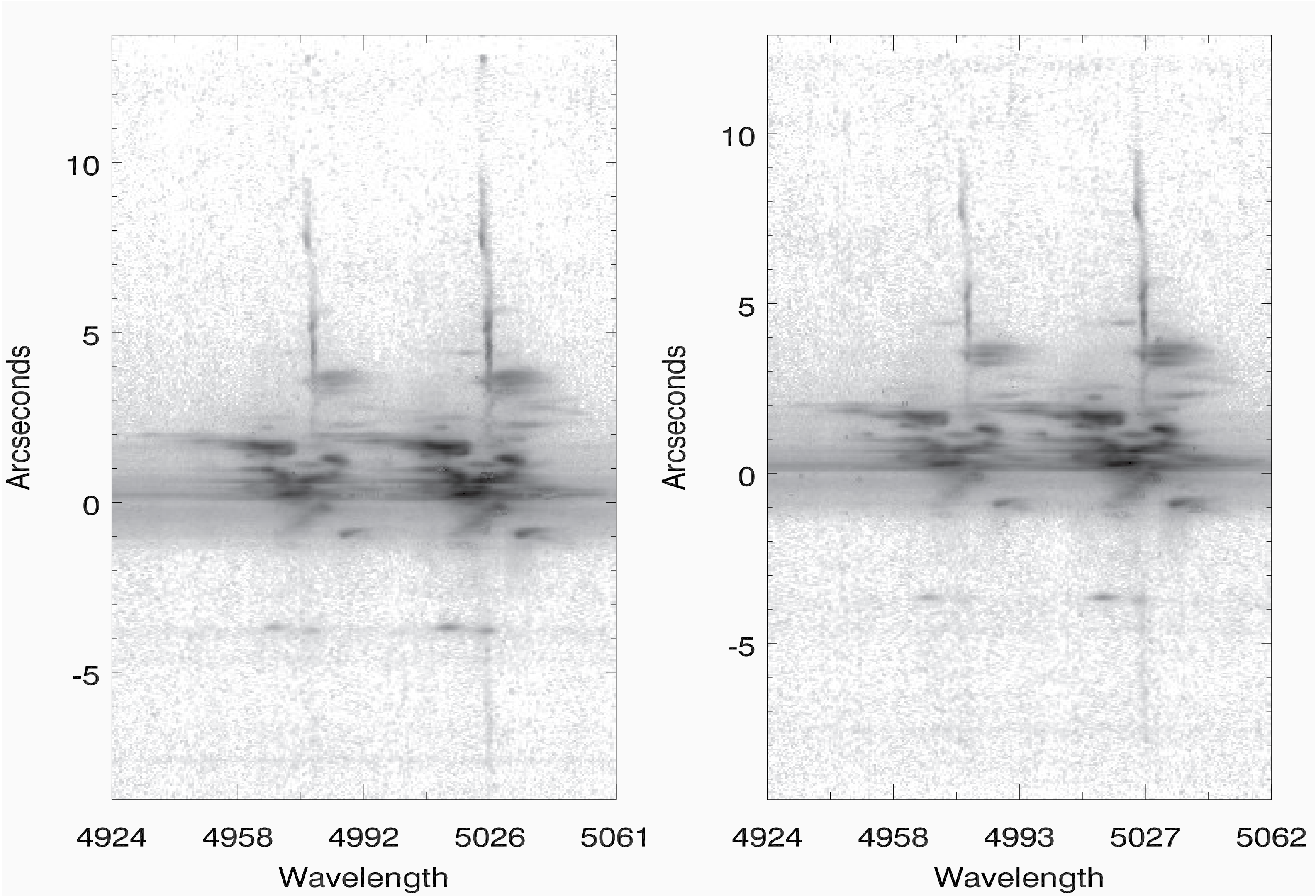

Figure 2.11: Spectral images of slits 5 (left) and 6 (right) of the NLR of NGC 1068 showing the two [O III] emission lines, $\lambda\lambda 4959, 5007$. Northeast is to the top of these images.

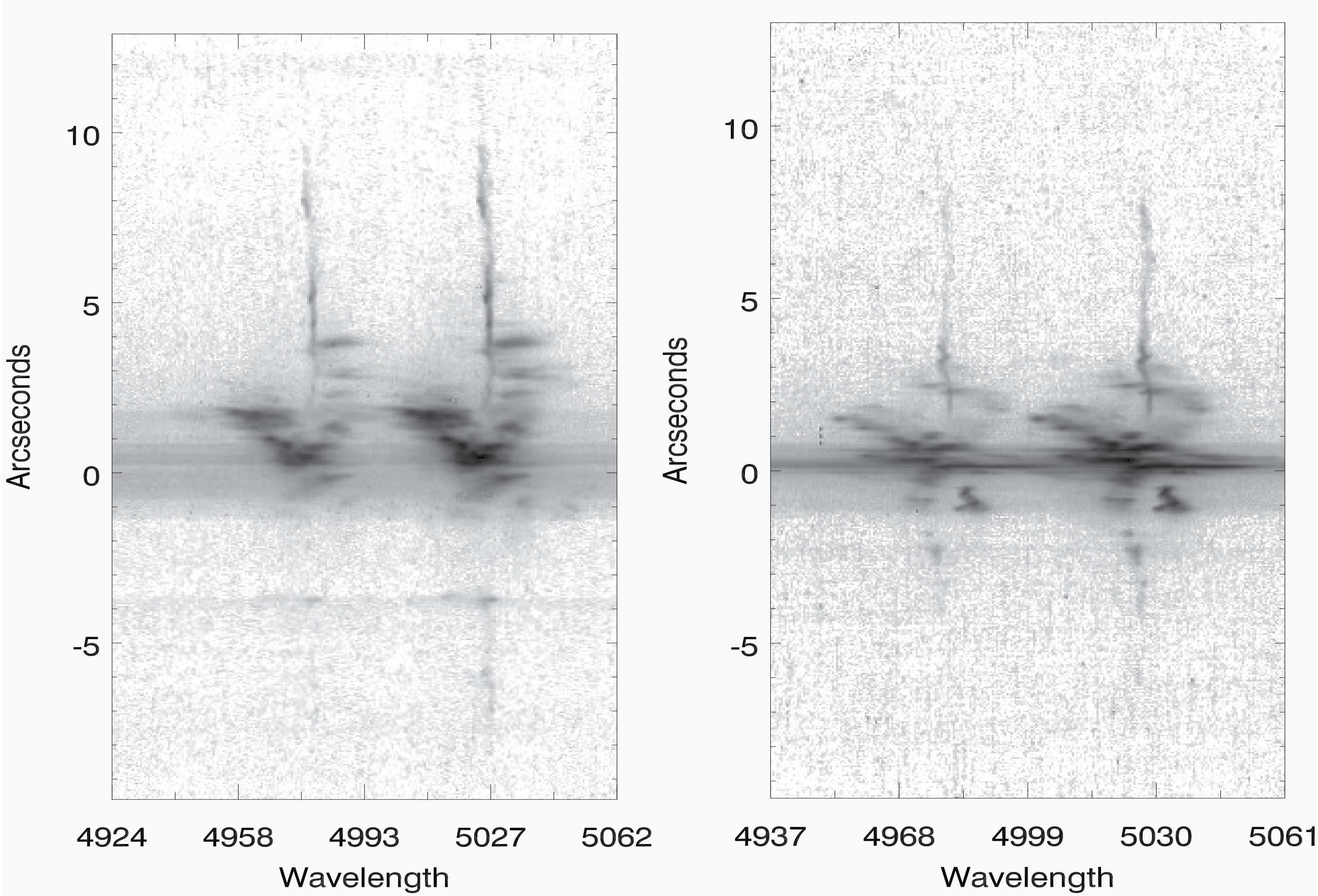

Figure 2.12: Spectral images of slits 7 (left) and 8 (right) of the NLR of NGC 1068 showing the two [O III] emission lines, $\lambda\lambda 4959, 5007$. Northeast is to the top of these images.

2.4 Radio Maps of NGC 1068

We obtained the high-resolution radio map of the NLR of NGC 1068 that is shown in Figure 2.13 from Jack Gallimore. The map was taken with the six-antenna Multi-Element Radio Linked Interferometer Network (MERLIN) array on 1998 January 2. The map covers a region of about $1''.5$ (210pc) along the jet axis and has an angular scale of $0''.014$ pixel^{-1}. The dark parts of the radio map represent compact radio sources. The SMBH supposedly resides at Gallimore's knot S1 in the figure. This

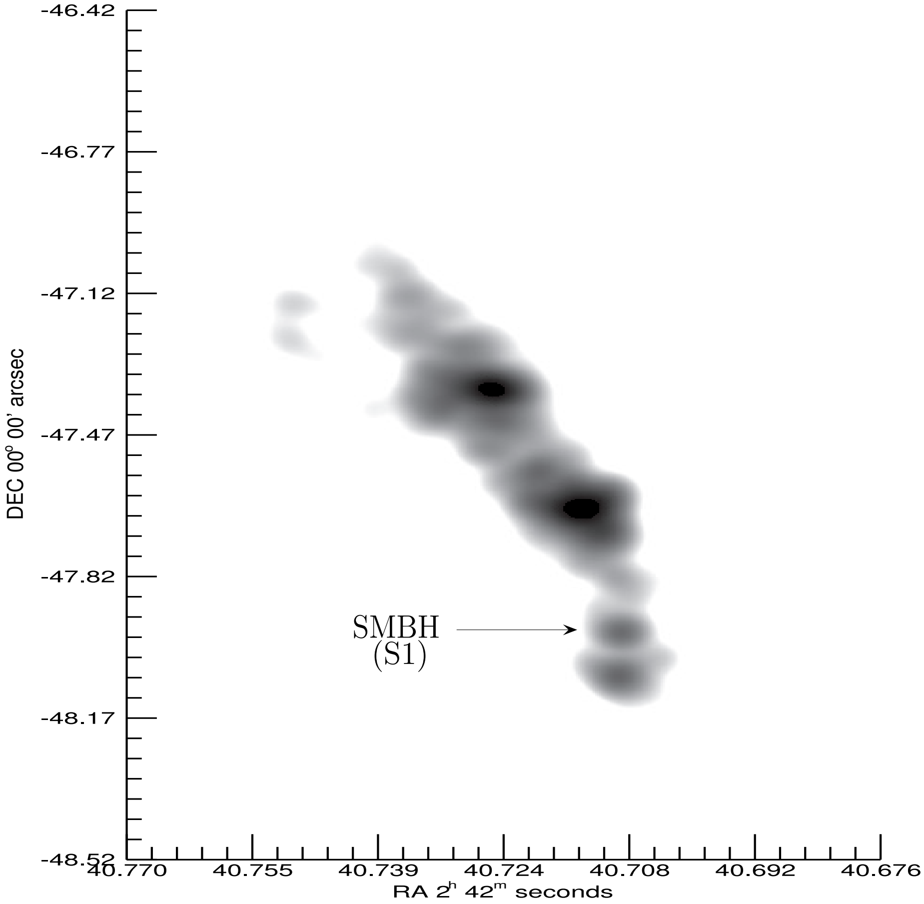

Figure 2.13: 5 GHz radio map showing the jet orientation and the location of the SMBH in NGC 1068. North is up and east is to the left.

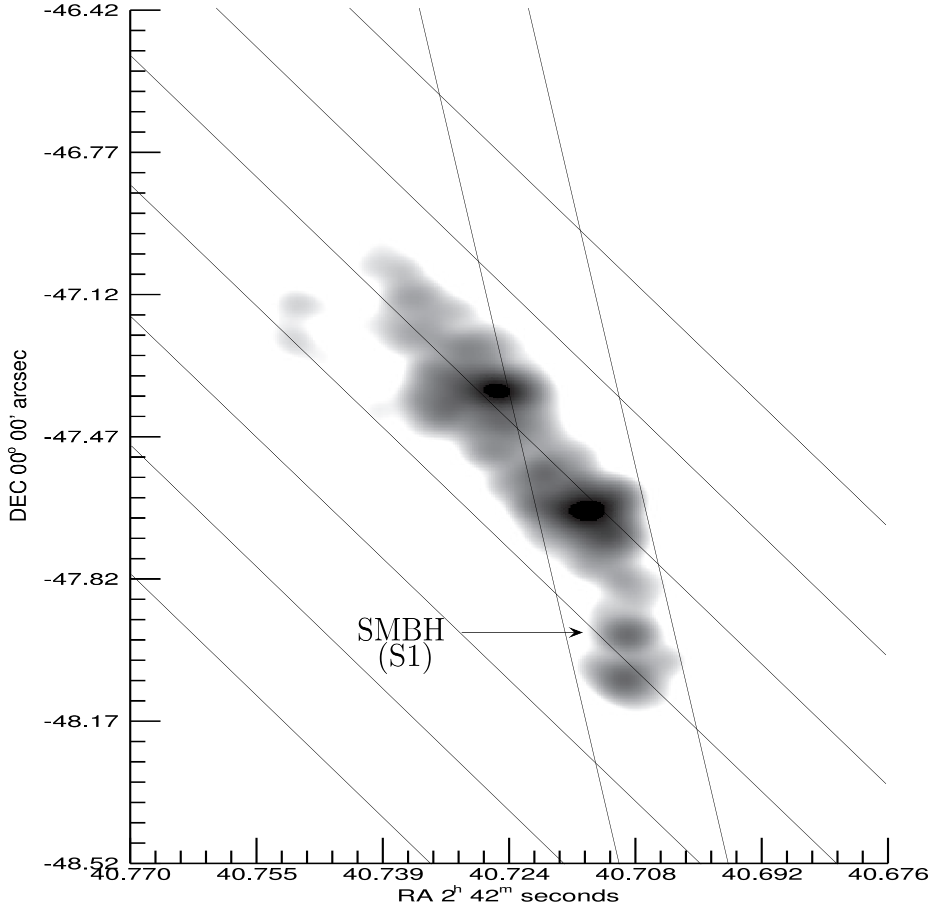

Figure 2.14: Same image as in 2.13 showing the positions of the slits relative to the jet axis.

argument was based on nuclear H_20 maser studies by Gallimore et al. (2001) where they argued that measurements of the 22 GHz H_20 maser spectrum showed redshifted and blueshifted emission on opposite sides of S1. This radio map was imaged at a frequency of 5 GHz. For more detailed information concerning the radio map, see Gallimore et al. (2004), and references therein. Figure 2.14 shows that the radio jet in NGC 1068 aligns well with the NLR long axis (as indicated by the slits). This will prove to be very useful in comparing the positions of the radio flux and the kinematics of the NLR clouds to test for jet/cloud interactions. Most of the radio jet intersects

3 of our parallel slit positions, but the bottom part of the jet is bent from position angle ~ 38° at one of the bright knots, out of alignment with the slits. However Antonucci's slit, positioned at 10° in the sky, nicely aligns with the rest of the radio emission after the bend.

2.5 STIS Data Reduction

For both NGC 4151 and NGC 1068 we used the Interactive Data Language (IDL) software developed at NASA's Goddard Space Flight Center for the STIS Instrument Definition Team to reduce the spectra. The bias and dark rate were subtracted from each spectral image, which were then flat-fielded. Cosmic-ray hits were identified and removed from observations by comparing multiple images obtained during each orbit. Hot or warm pixels identified in long sky exposures were replaced by interpolation in the dispersion direction. Wavelength calibration exposures obtained after each observation were used to correct the wavelength scale for zero-point shifts. The spectra were geometrically rectified and flux-calibrated to produce a constant wavelength along each slit column and fluxes in units of $\mathrm{ergs\,s^{-1}\,cm^{-2}\,\AA^{-1}}$ per cross dispersion pixel. No sky background was subtracted from the spectra, because it was due primarily to the host galaxy and varied across the image. The lack of background subtraction had no effect on the analysis of the spectra.

– 3 –

Analysis

3.1 STIS Spectroscopic Analysis

Observations from each slit were analysed in the same manner for both galaxies. The analysis that follows explains the procedure we used to extract velocity and other information from a long-slit observation. The same procedure will therefore apply to every slit position in our sample, for both galaxies. Each slit gives a spectral image (figures shown in Chapter 2) that contains one spectrum per cross-dispersion pixel along the slit, centered around the two bright Doppler-shifted [O III] emission lines and the fainter Hβ emission line (not shown in the images). Due to the relatively high resolution of the dispersion, we detected multiple components of [O III] emission at many positions along the slit, representing different velocity shifts. Close to the SMBH we detected mostly three kinematic components in both emission lines $\lambda\lambda4959, 5007$, and sometimes four components were detected in NGC 4151's spectra. In NGC 1068, we detected mostly three components, but in Antonucci's slit 8, sometimes four, five or even six kinematic components were detected. We used the brighter of the two [O III] emission lines ($\lambda5007$) and fitted each detected component with a local continuum and multiple Gaussians. Noisy spectra, roughly those $\geq 6''$

on either side of the nucleus, were not fit. An example of such a fitting technique is shown in Figure 3.1, which depicts a progression of spectra from slit 1 of NGC 4151, illustrating how the components fluctuate with position.

The analysis described in Figure 3.1 will be applicable to all slits because the spectra contained in it are representative of our combined set of spectra for all slits in both galaxies. Therefore this figure needs to be explained in detail. The figure itself shows the changing fluxes per component, and the appearance and disappearance of certain components. These plots represent spectra taken from slit 1 of NGC 4151 and range in distance from $0\farcs3$ (a) to $0\farcs55$ (f), in increments of $0\farcs05$, going away from the nucleus in the northeast direction. In (a), there are two distinct kinematic components of $\lambda5007$ emission, which we fit with two Gaussians using the programming language of IDL[1]. Going from (a) to (b), a third component emerges. A possible fourth component emerges in (c), but was not measured by our fitting routine. The second component shrinks in (c), and disappears in (d), while the fourth component grows stronger from (c) to (d) and is now detected and labeled '2'. This new second component grows stronger while the third shrinks and disappears from (d) through (f). Since our measurements along a slit are oversampling a resolution element ($0\farcs1$) by only a factor of two, the appearance of the same components in multiple rows along the slit indicates that we are obtaining multiple measurements of spatially-resolved knots, the brightest of which can be seen in Figures 2.1 and 2.7. These knots must be $\geq$ 10 pc in size, since our resolution is roughly 10 pc for NGC 4151 and NGC 1068.

---

[1] All programs were written in IDL version 6.1

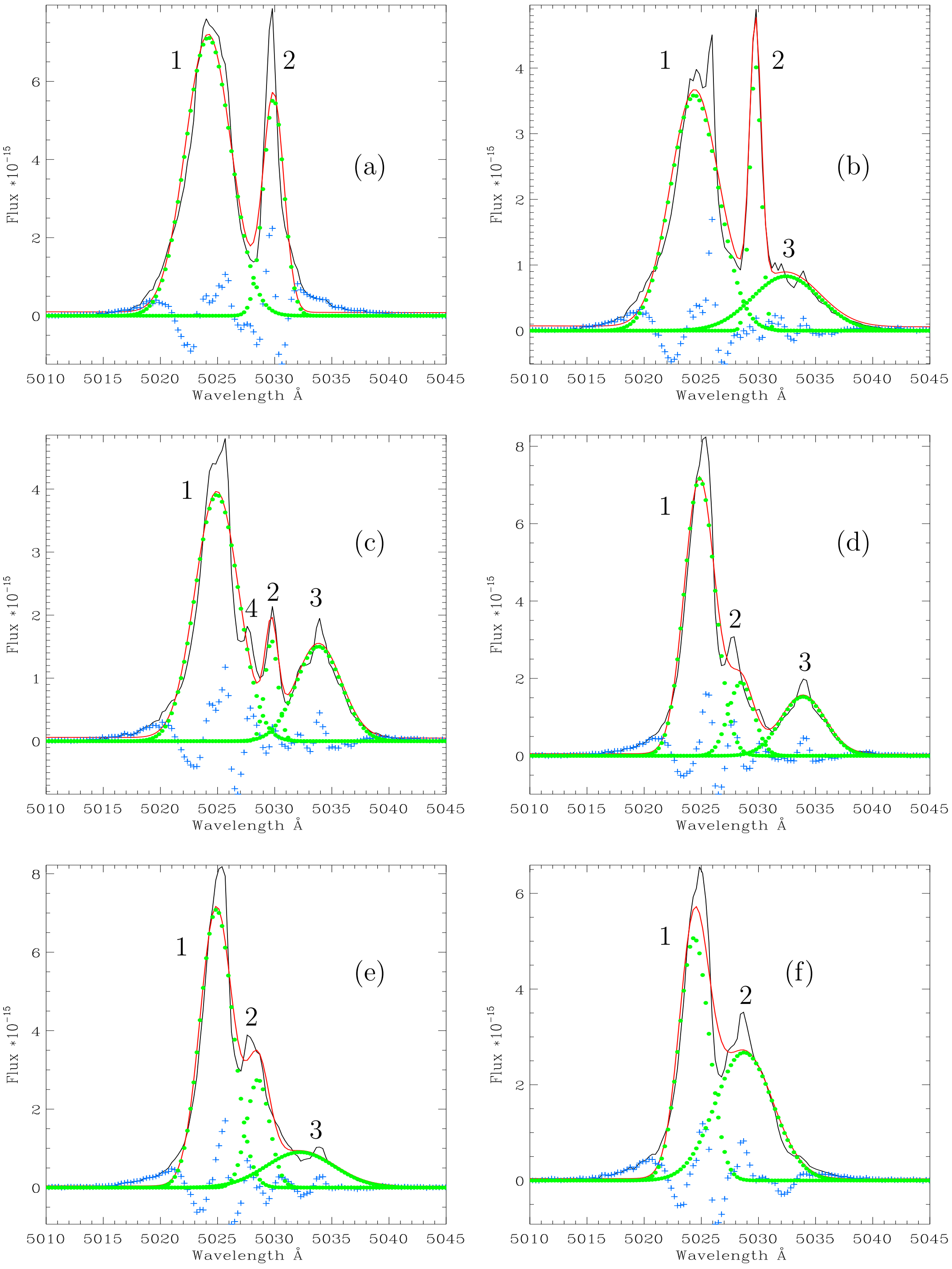

Figure 3.1: NGC 4151 spectra from slit 1 showing the multicomponent Gaussian fits. The black curves are the spectra, the green dotted curves are the individual fits per component, the red curves are the total fits, and the blue curves are the errors in the fits. The plots, ordered (a)–(f), are from positions in the northeast separated by 0.″05, increasing in distance away from the nucleus.

3.1.1 Separating the Components

For comparative purposes, we separated the different components seen in Figure 3.1 by relative intensities and labeled them in different colors. For example, components 1, 2, and 3 would be labeled with red, blue, and black respectively; later, the velocities of the components are plotted in those colors to differentiate them. If we detected more than three components, we labeled the brightest one red, the next brightest one blue, and the rest black (see §4 for more details). The colors assigned to the different components after separation should not be confused with the colors assigned to the Gaussian fits in Figure 3.1.

The separation of the different components by relative fluxes provides us with information about the different velocity structure superposed along the LOS. Consider the cartoon in Figure 3.2 showing a progression of spectra from (a)–(f), representing measurements across a few clouds for example. The components are ordered 1, 2, and 3 going from left to right, and the colors that we assign are marked below each component. Notice that in (b), the second component is labeled black and the third component is labeled blue. The relative nature of our separation criteria is made clear in (c)–(f); with only two components detected, they are labeled red and blue, and when we have detected only one component, we labeled those red. In cases such as (b), components 2 and 3 have exchanged colors. Such cases of mixing components are only detected occasionally and are easily identified in our plots.

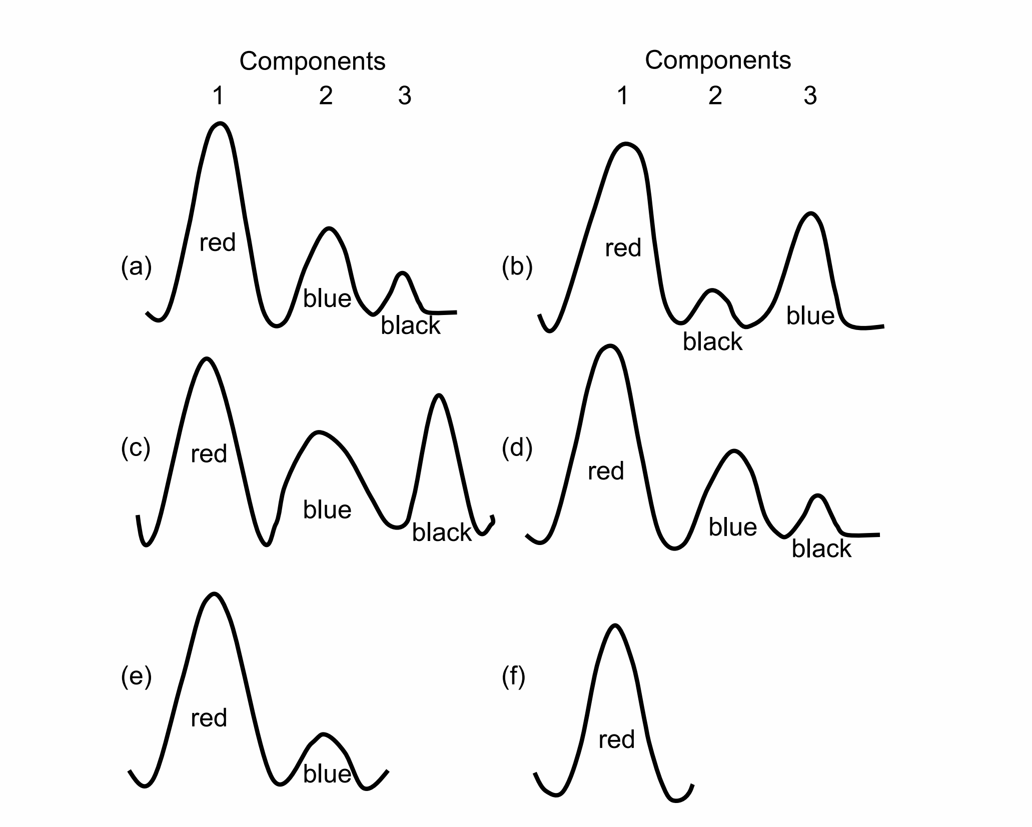

Figure 3.2: Multiple components in a progression of spectra and how we separate them according to flux. The components are assigned the indicated colors after separation. In (b) there is more flux under the last line; hence the color blue is assigned.

3.1.2 Measuring the Velocities

The central peaks of the Gaussians give us the central wavelengths from which we used the Doppler formula to find radial velocities for each component. The radial velocities are found as follows:

$$\frac{\lambda_c - \lambda_{lab}}{\lambda_{lab}} = \frac{v}{c}, \tag{3.1}$$

where λ_c is the center wavelength measured from the Gaussian fit and λ_{lab} is the rest wavelength of the ${}^1D_2 \rightarrow {}^3P_2$ transition from [O III], which is 5006.8 Å. Equation 3.1

is then rearranged to find v, and the intrinsic redshifted velocities of the galaxies are subtracted from v to find the corrected velocity relative to the SMBH.

$$v_{corrected} = v - v_{galaxy}, \tag{3.2}$$

where v_{galaxy} is 997 $\mathrm{km\,s^{-1}}$ (Pedlar et al. 1992) and 1197 $\mathrm{km\,s^{-1}}$ (Brinks et al. 1997) for NGC 4151 and NGC 1068, respectively.

3.1.3 Errors

There are three sources of uncertainty in the above velocity measurements. The first results from the fact that the [O III] emission lines are not perfect Gaussians as shown in Figure 3.1. By actually measuring the centroid of a line for a number a spectra, we found that our Gaussian fitting routine introduced a maximum fitting error of 0.75 Å in the centroid. The second error comes from the fact that clouds that were observed in the $0\farcs2$ wide slit are uncertain in their position in the dispersion direction by half of this amount. This is because the light from the clouds is dispersed in the direction of the slit width and hence all information about the clouds' position in that direction is lost. We calculated that a $0\farcs1$ offset would contribute an error of 0.56 Å. Noise introduced the third error. Various noisy spectra were measured several times with different starting parameters, and the wavelength shifts were found to fluctuate by no more than 0.30 Å. These errors were then converted to velocities and added in quadrature to produce a total maximum error of ± 60 $\mathrm{km\,s^{-1}}$. We also varied the continuum placement for randomly selected spectra but found that this did not shift the central wavelength significantly. The FWHM was also recorded by our IDL routine, as was the flux under the lines. These are displayed in various plots in Chapter 4.

3.2 Radio Analysis: NGC 4151

The radio map from Mundell had to be processed before we could compare co-spatial positions of radio flux and [O III] clouds. In addition, the [O III] images and the radio maps had to be aligned properly before any comparison could be made. This alignment is based on various studies regarding the astrometry of the SMBH in the optical and radio.

3.2.1 The Location of the SMBH

For NGC 4151, the position of the SMBH on the [O III] map was easily determined by the center of the brightest cloud. Due to the Seyfert 1 nature of this galaxy, the bright continuum seen in the optical marks the position of the SMBH. The [O III] peak is also co-spatial with the continuum peak. For the radio map we rely on recent studies of Mundell et al. (2003). Earlier low resolution studies by Carral et al. (1990) identified the brightest radio knot, C4, to be associated with the AGN (see Figure 3.3). They claim that the C4 knot shows a relatively flat spectral index, $\alpha_{18}^{2} = -0.4$, between 18 and 2 cm wavelengths, as compared to $\alpha_{18}^{2} \simeq -0.6$ to -0.7 for the rest of the radio knots. They argued that the flat spectral index and the high T_B of the central component is consistent with synchrotron self-absorption associated with an AGN. Higher

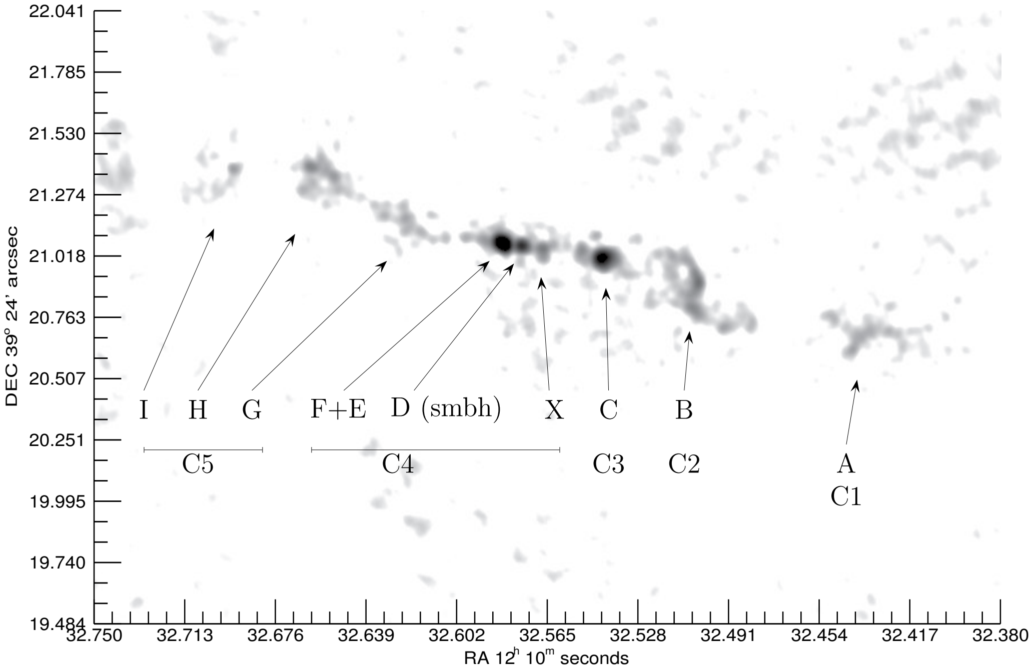

Figure 3.3: Radio map of NGC 4151 showing the various knots and how they were labeled depending on the map's resolution. The C1–C5 labeling scheme was done by Carral et al. (1990) and Mundell et al. (1995) in lower resolution studies. The high resolution studies by Mundell et al. (2003) identified more subcomponents and the knots are labeled A–I, and X, a new component. Other gray areas that look like radio emission are mostly noise.

resolution studies by Pedlar et al. (1993) revealed a small 150 mas radio 'jet' extending westward from knot C4 directly towards the adjacent knot C3; this is further evidence that C4 contains the nucleus and C3 is a compact knot in the jet. With still higher resolution, Mundell et al. (2003) resolved radio knot C4 into a number of subcomponents labeled F+E, D, and X. They argued that the radio jet appears very well collimated in the vicinity of D, with significant deviations at E in the east and C in the west due to interactions with dense clouds. They argued that the similar shape and opposing directions of E and C suggest that the AGN lies somewhere between the two knots. They pointed out that the greater flux density at F+E suggests that the AGN is located closer to F+E than to C, and finally that the continuum structure of component D shows a high degree of collimation that resembles radio core-jet structures seen in higher power AGN such as radio loud quasars. The SMBH is therefore placed at D.

3.2.2 Aligning the Radio and [O III] Maps

Figure 3.4 shows the high resolution image of the radio jet in NGC 4151 overlaid on

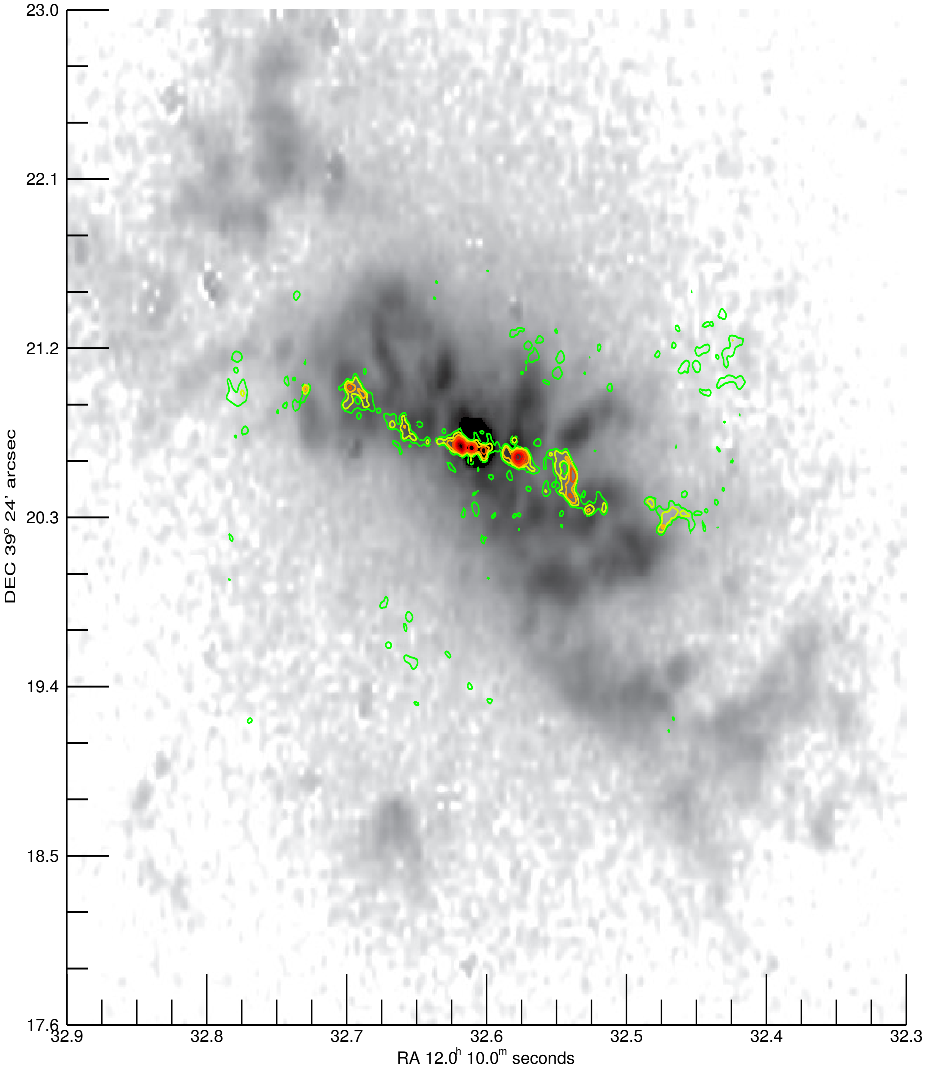

Figure 3.4: Radio map of NGC 4151 in color overlaid on a WFPC2 [O III] image showing alignment of the radio map with respect to the [O III] map.

the F501N narrow band WFPC2 image by Holland Ford. We resampled the images to have the same pixel scale and rotated the [O III] image to place north on top similar to the radio map. We then aligned the images based on the position of the SMBH in both. The peak of the optical nuclear emission in the [O III] image was aligned with the peak of the radio emission in component D. A reliable comparison of the location of the optical emitting clouds and the radio jet knots is now possible. Slits were overlaid on the images to match the STIS slit placements on the sky. Slit 1 was centered on the [O III] hot spot and the rest of the slits were placed at parallel offsets at $0''.2$ on either side of slit 1, as shown in Figure 3.5. This gives us the slits that intersect the radio region. The radio fluxes were then extracted from regions between the boundaries of each slit. The extracted radio intensities were then summed across the width of each slit to find the total intensity along the slit. Plots were then made of the radio intensity and the radial velocity data against position along each slit to compare and search for any radio disturbance of the [O III] data. These plots are presented in the next chapter.

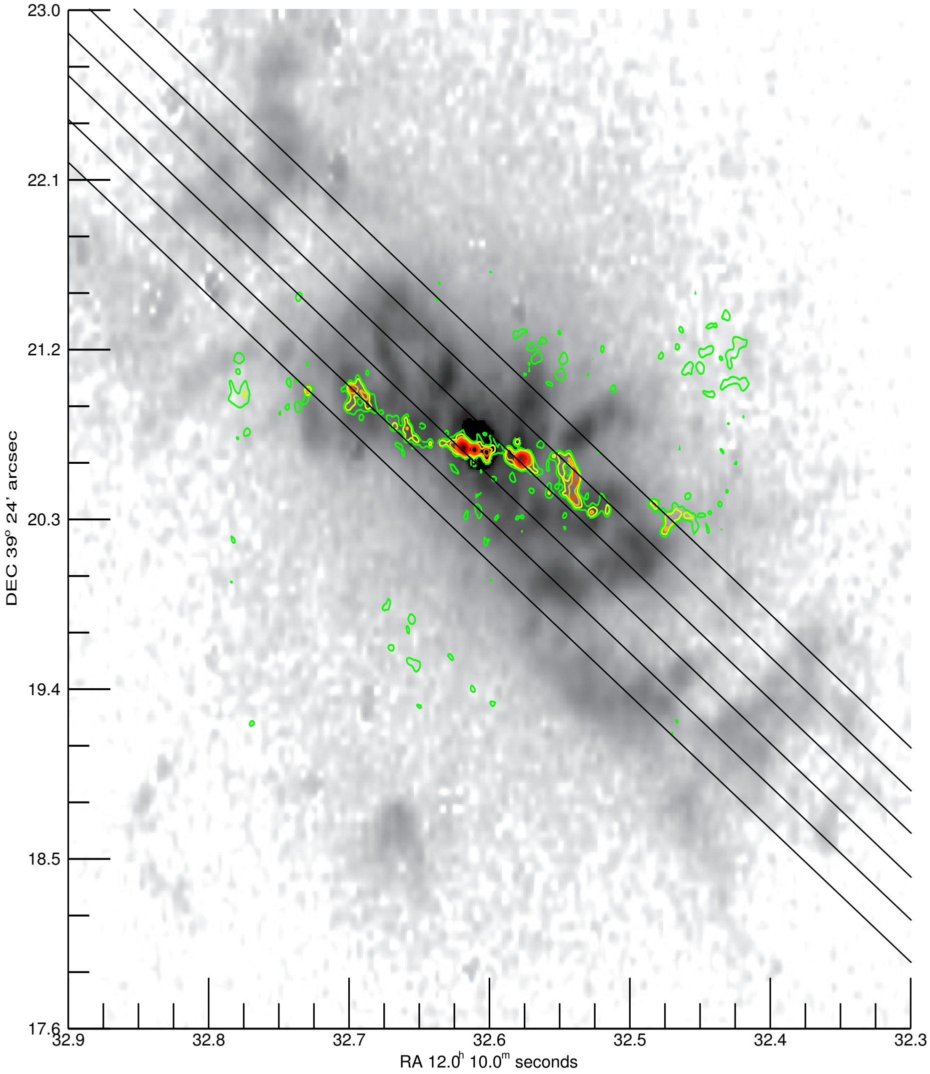

Figure 3.5: Radio map of NGC 4151 in color overlaid on a WFPC2 [O III] image showing alignment of the radio map with respect to the [O III] map and with respect to the slits used for radio flux extraction.

3.3 Radio Analysis: NGC 1068

The case of finding the SMBH in NGC 1068 is complicated by the fact that this galaxy is a Seyfert 2, hence the nucleus is hidden from view, at least in the optical wavelengths. The bright emission seen in Figure 2.7 is not where the SMBH resides, but is electron scattered light (Crenshaw & Kraemer 2000a). In order to align properly the radio and [O III] maps, we used precision *HST* astrometric studies from Capetti et al. (1997), coupled with accurate radio astrometric studies from Muxlow et al. (1996), which were altogether nicely summarized by Galliano et al. (2003).

3.3.1 The Location of the SMBH

The location of the SMBH was finally settled on radio knot S1 (see Figure 3.6), after much debate. At S1 the integrated radio spectrum is flat above 5 GHz and attenuated below 5 GHz, with no detection at 1.4 GHz and 1.7 GHz (Gallimore et al. 1996a,b, 1997; Muxlow et al. 1996). This attenuation most likely results from free-free absorption (Gallimore et al. 2004), and models of X-ray-irradiated molecular tori do predict such high free-free opacity (Krolik & Lepp 1989; Neufeld et al. 1994). This, coupled with the nuclear H_20 masers orbiting S1 (Claussen & Lo 1986; Gallimore et al. 2001), appears to be consistent with S1 marking the location of the SMBH. Muxlow et al. (1996) reported the position of S1 at α=$02^h42^m40\overset{s}{.}7098$, δ=$-00°00'47\overset{''}{.}938$ (J2000), with astrometric precision of 20 mas.

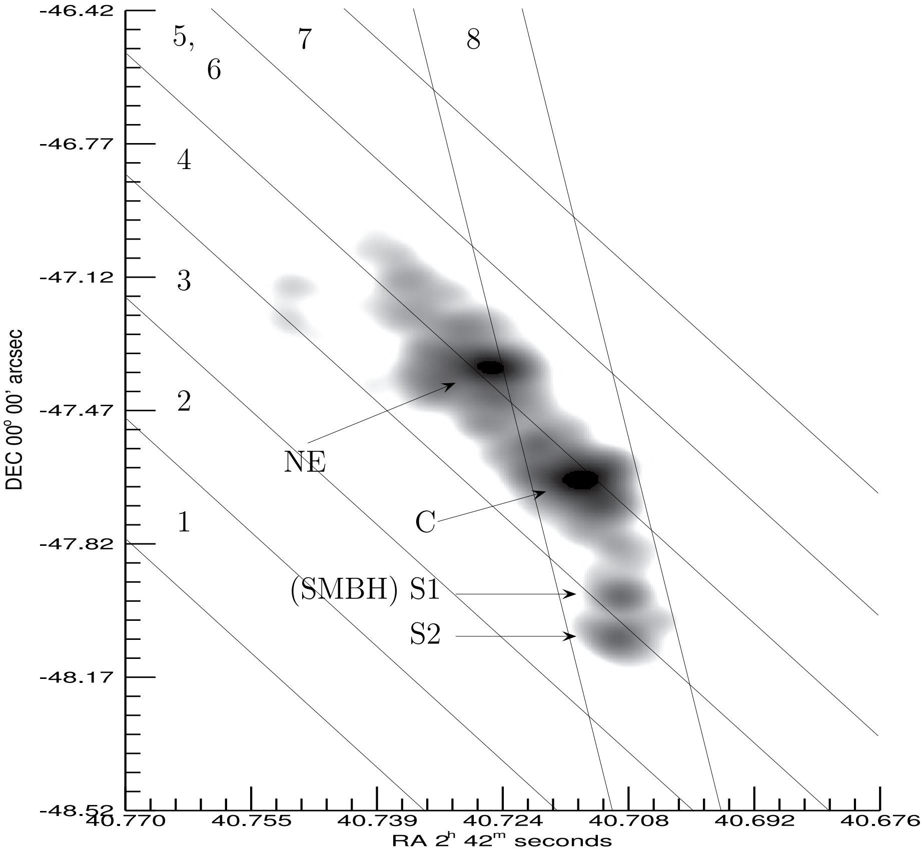

Figure 3.6: Radio map of NGC 1068 with the bright knots and slits labeled and showing the alignment of the slits with respect to the radio jet.

3.3.2 Aligning the Radio and [O III] Maps

Previously, *HST* UV and optical NLR images with 0″.1 resolution were obtained by Evans et al. (1991) and Macchetto et al. (1994), but these were not precise in their registration since *HST* images could only be positioned with ±0″.5 accuracy. Capetti et al. (1997) obtained for the first time a high accuracy alignment of the optical and radio emission from NGC 1068 with ±0″.08 precision, based on astrometric stars in the field of view Lattanzi et al. (1997), to obtain accurate absolute astrometry for *HST* images. Capetti et al. (1997) found that the optical continuum peak was located at α=$02^h42^m40\overset{s}{.}711$, δ=$-00°00'47\overset{''}{.}81$, which is $0\overset{''}{.}13$ North and $0\overset{''}{.}02$ East of S1. They also found that the optical continuum emission corresponds to the position of NLR cloud B shown in Figure 2.7.

With this registration, it was then easy to align the radio and [O III] maps. The radio map was first scaled down to match the resolution of the [O III] image. The [O III] image was counter-rotated by the WFPC2 orientation offset to bring the image to its true position angle in the sky. We then overlaid the radio map onto the [O III] map based on the positions of the SMBH and the 'hot spot'. Figure 3.7 shows the radio map in colored contours overlaid on the FOC image. With alignment in place we overlaid slits on the maps that correspond to ones placed by STIS in the sky, by using the continuum hot spot as a guide. Slit 4 was centered on the hot spot and placed at position angle 38°. The rest of the slits 5–7 and 1–3 were placed at parallel offsets of $0\overset{''}{.}2$ on either side of slit 4, as was originally done by STIS. This gives us the positions of the slits that intersect the radio map, as shown in Figure 3.8. The boundaries of the intersecting slits are then used to extract regions along slits 3, 4, 5, and 8 from the radio map. These slits were summed across their widths to find the total radio intensities along each slit. The radio intensities and the [O III] data were then plotted against position for each slit and compared for any [O III] disturbance, as was similarly done for the radio and [O III] maps of NGC 4151. These results are presented in Chapter 4.

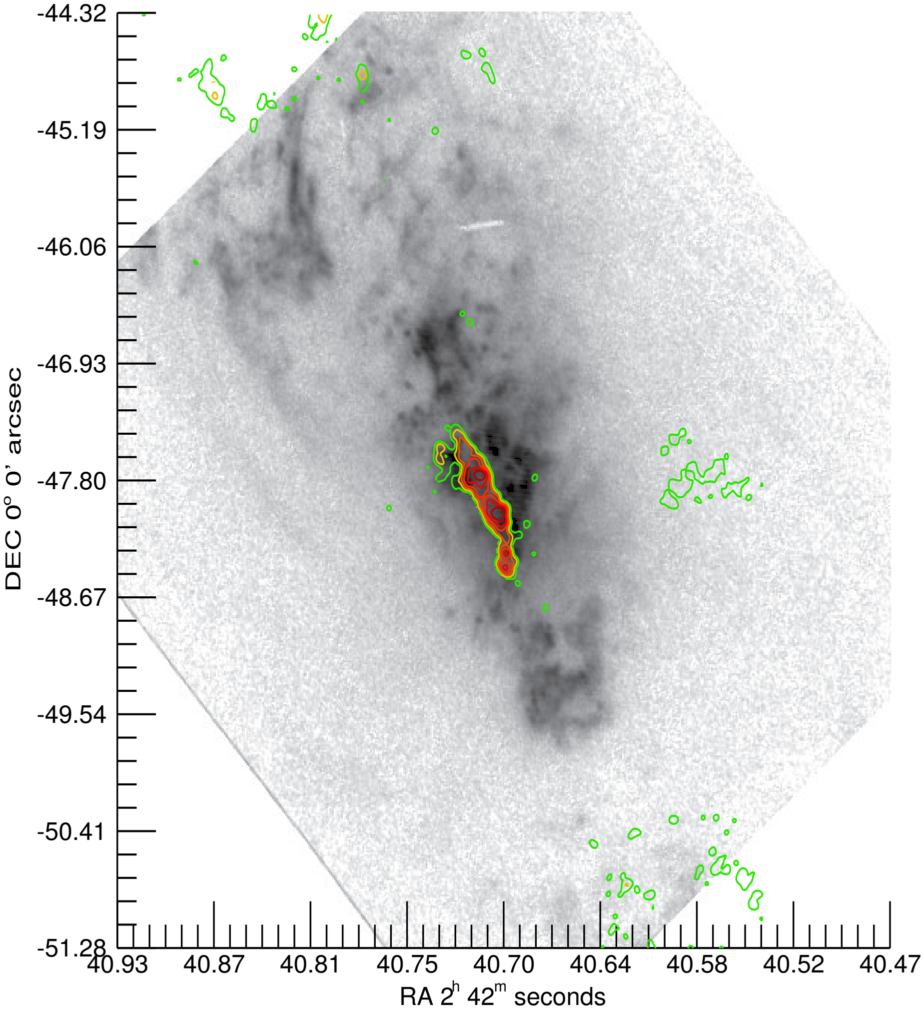

Figure 3.7: Radio map of NGC 1068 in color overlaid on a FOC [O III] image showing alignment of the radio map with respect to the [O III] map.

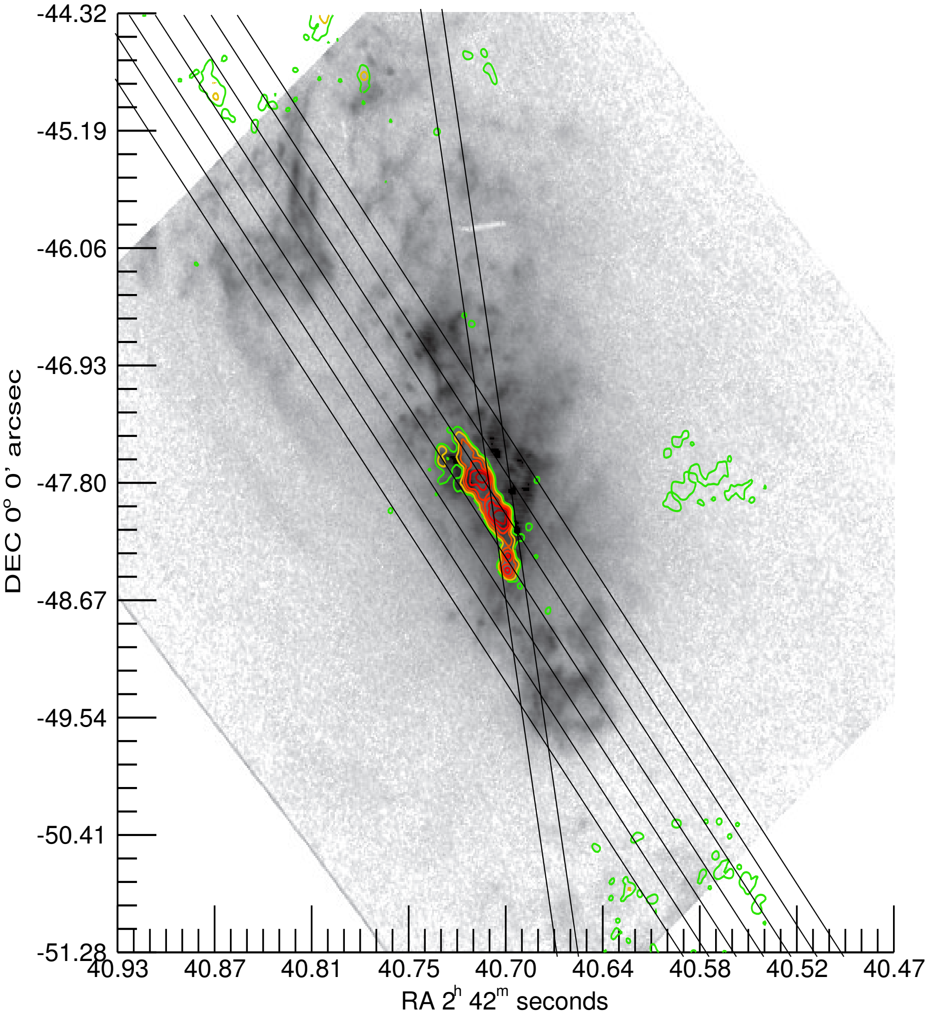

Figure 3.8: Radio map of NGC 1068 in color overlaid on an FOC [O III] image showing alignment of the radio map with respect to the [O III] map and with respect to the slits used for radio flux extraction.

– 4 –

Measurements

In the last chapter we analyzed and extracted the relevant velocity information from the 5 observed slit positions for NGC 4151 and the 8 slit positions for NGC 1068. The extracted velocities per slit are the key data upon which we based our models, and they therefore need to be presented and understood with care. In all the slits, the velocities measured were radial, i.e. along the LOS toward or away from the observer, and the various colors represent different [O III] kinematic components as explained in the previous chapter. The positions in the various plots are measured in arcseconds with respect to the nucleus. The general placement of the slits for both galaxies are in the northeast-southwest orientation, so we assigned positive positions going toward the northeast, and negative positions going toward the southwest.

We processed the radio maps of the NLR for both galaxies and carefully aligned them with the [O III] maps, as discussed in the previous chapter. We then extracted intensities through slits from the radio maps and plotted them alongside radial velocities to look for any radio disturbance on the NLR clouds. We present all relevant plots in this chapter and discuss them without interpretation. In the next chapter, we build kinematic models to match the data.

4.1 Graphical Results for NGC 4151

Figures 4.1–4.5 show the kinematic components in plots of radial velocities, FWHM, and fluxes as functions of projected position along the slit on either side of the nucleus of NGC 4151. Negative positions corresponds to the southwest direction. Note that the points tend to clump together, reflecting the ability of STIS to resolve the clouds, which appear to be a few tenths of arcseconds across in the images. In the upper plots, the brightest emission line clouds at each position in the northeast are redshifted, while those in the southwest are blueshifted, relative to the host galaxy. The highest velocities occur closer to the nucleus and velocities as high as 800 $\mathrm{km\,s^{-1}}$ can be seen in approach and recession. The highest velocities can be seen in blueshift in slits 4 and 5, at ~ -1500 $\mathrm{km\,s^{-1}}$. The general trend seen in all slits is an increase in radial velocity from near zero at the nucleus to a maximum redshift or blueshift within $\sim 1''$ of the nucleus, especially for the bright knots. Between $\sim 2''$ to $\sim 4''$ the velocities reduce from about 200 $\mathrm{km\,s^{-1}}$ to 100 $\mathrm{km\,s^{-1}}$ and at distances of about $4''$ or more from the nucleus, the radial velocities tend to taper off to ≤ 100 $\mathrm{km\,s^{-1}}$, presumably reflecting the ENLR rotational velocities. The medium flux clouds generally show the same pattern as the bright ones except in slits 1 and 4 where they are not confined to only blueshifts in the southwest. Also in slits 2 and 5, the medium flux clouds show some blueshifts in the northeast, in addition to the general trend mentioned above. The low flux clouds also follow similar patterns as do the bright clouds except in slits 1 and 4 where one can see additional flow patterns opposite to that of the bright clouds.

The FWHM in the middle plots show a range of widths at each position, but a decreasing average width with distance from the nucleus at all flux levels. Note that the measured FWHM has not been corrected for instrumental resolution, which is $\sim$ 30 $\mathrm{km\,s^{-1}}$ FWHM. In the bottom plots, all three components show a strong decrease in flux with distance and significant structure that corresponds to the emission line knots. At $\sim 2''$ all the components show a secondary peak in their fluxes. There is also a secondary peak at $\sim -3''$ in all the slits except slit 3. In the extreme southwestern bicone, we detect several low-flux, zero-velocity knots in all the slits except slit 4; these seem disconnected from the rest of the NLR and likely represent the ENLR.

Hutchings et al. (1999) found a number of low-flux, high velocity clouds in NGC 4151 using a combination of WFPC2 and STIS images and STIS slitless spectra. Some of these faint clouds did not fit into the general picture of biconical outflow (e.g. redshifts were detected in the southwest where blueshifts dominate). To check for consistency, we identified Hutchings et al.'s clouds in our data and compared our velocities with theirs. Our measurements are closely correlated over a wide range of velocities, as shown in Figure 4.6. Also shown on top of the figure are the letters of various high velocity knots, labeled according to Hutchings et al.'s scheme. The positions of Knots E and J in Hutchings et al.'s image should have placed them in our slits 1 and 5 respectively, but they were not found in our data. On average, the difference between Hutchings et al.'s velocity and ours is 134 $\mathrm{km\,s^{-1}}$, but there is no significant systemic offset. In addition to these knots, we found many more high velocity low and medium emission knots, which can be seen in the velocity plots of Figures 4.1–4.5.

The extracted radio intensities along their respective slits are plotted in Figure 4.7 and Figure 4.8. The peaks in the radio intensities correspond to the bright compact radio knots seen in Figure 3.3, and the radio intensities in all the plots are normalized to the brightest radio knot in slit 1. Slits 1 and 2 contain the brightest radio knots but the radio emission in slits 3 and 4 are only slightly above the background. The radio emission in slit 5 is too noisy to be of any use.

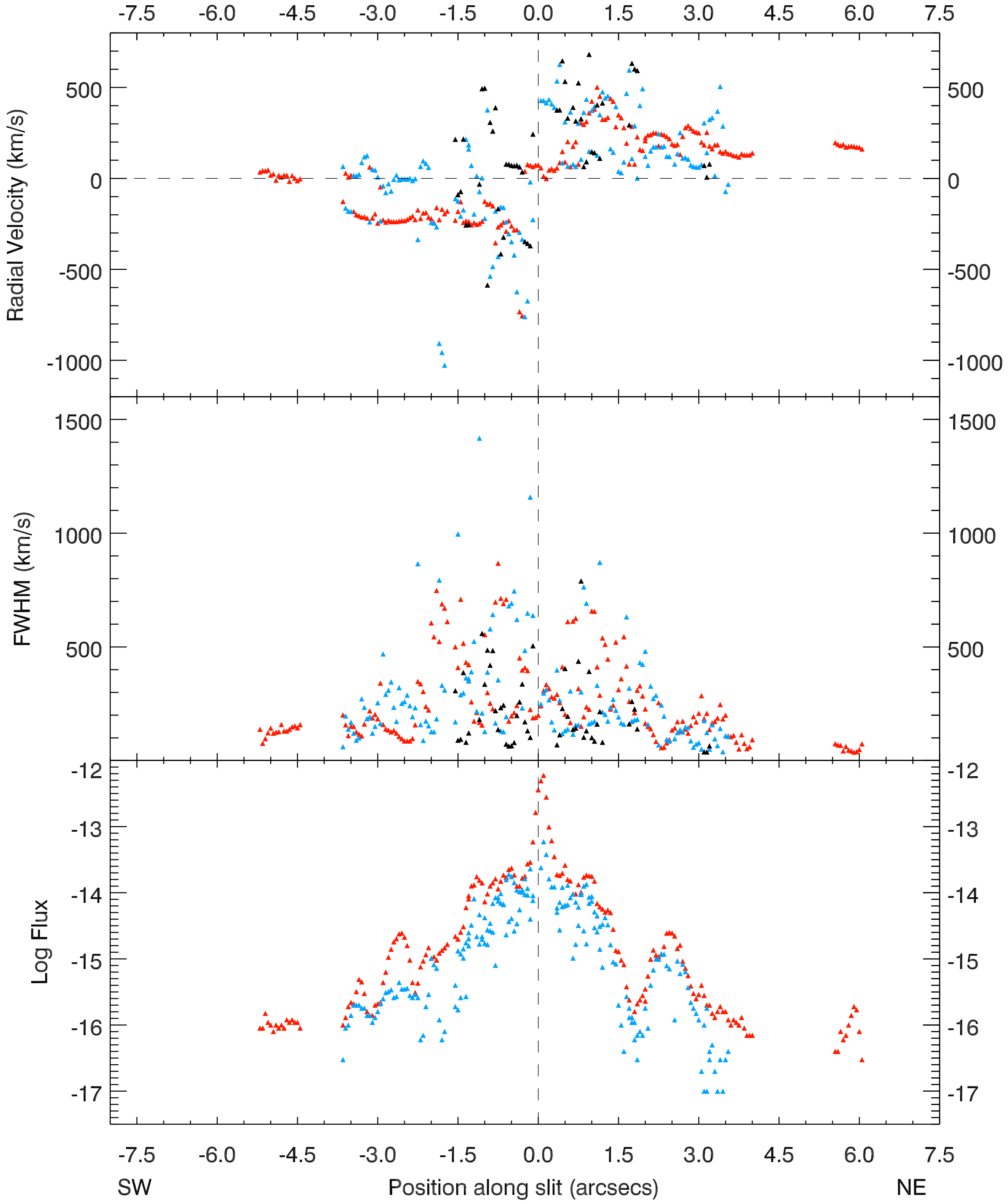

Figure 4.1: Slit 1 multi-colored plots showing the components present in the emission clouds at each position for NGC 4151. The colors represent high(red), medium(blue), and low(black) flux levels respectively. Radial velocities are given relative to systemic, and fluxes are in ergs $s^{-1}cm^{-2}Å^{-1}$ per cross-dispersion pixel. All graphs share a common abscissa of position in arcseconds from the nucleus. The FWHM is not corrected for instrumental resolution.

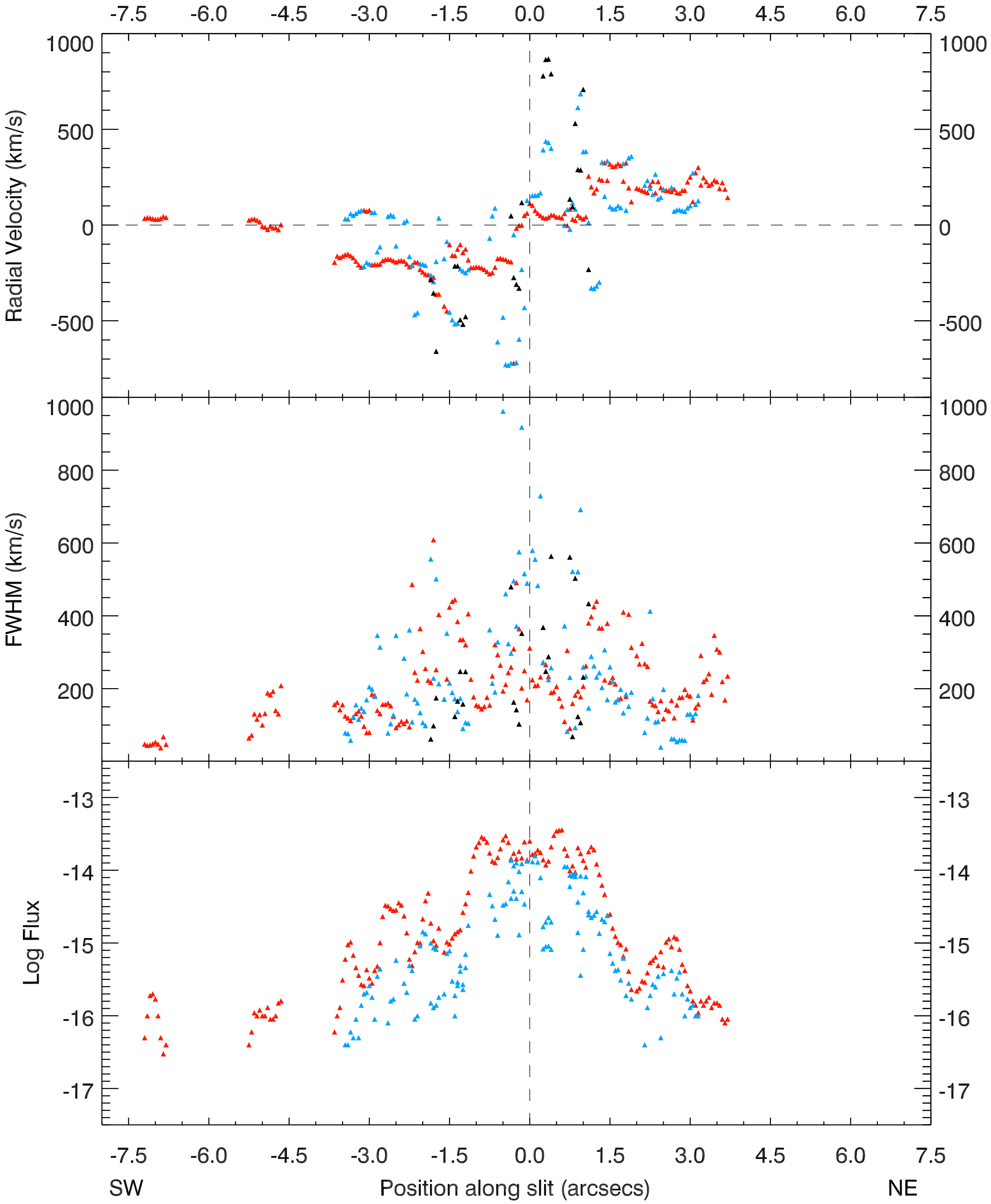

Figure 4.2: Plots of radial velocity, FWHM, and flux of slit 2 against position along the slit of NGC 4151. The different colors represent the different kinematic components as in Figure 4.1.

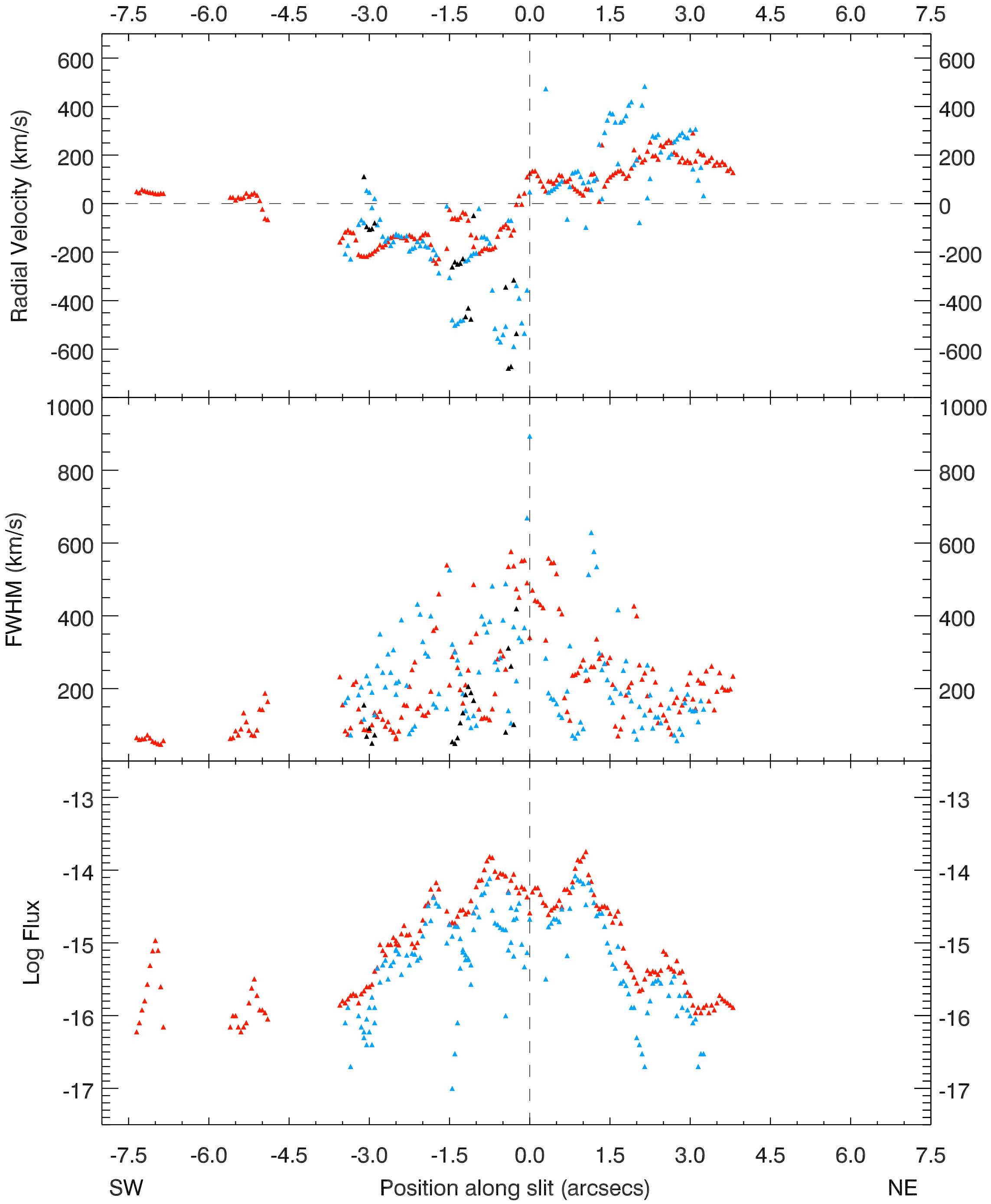

Figure 4.3: Plots of radial velocity, FWHM, and flux for slits 3 of NGC 4151. The colors depict the usual separation of flux levels as in Figure 4.1.

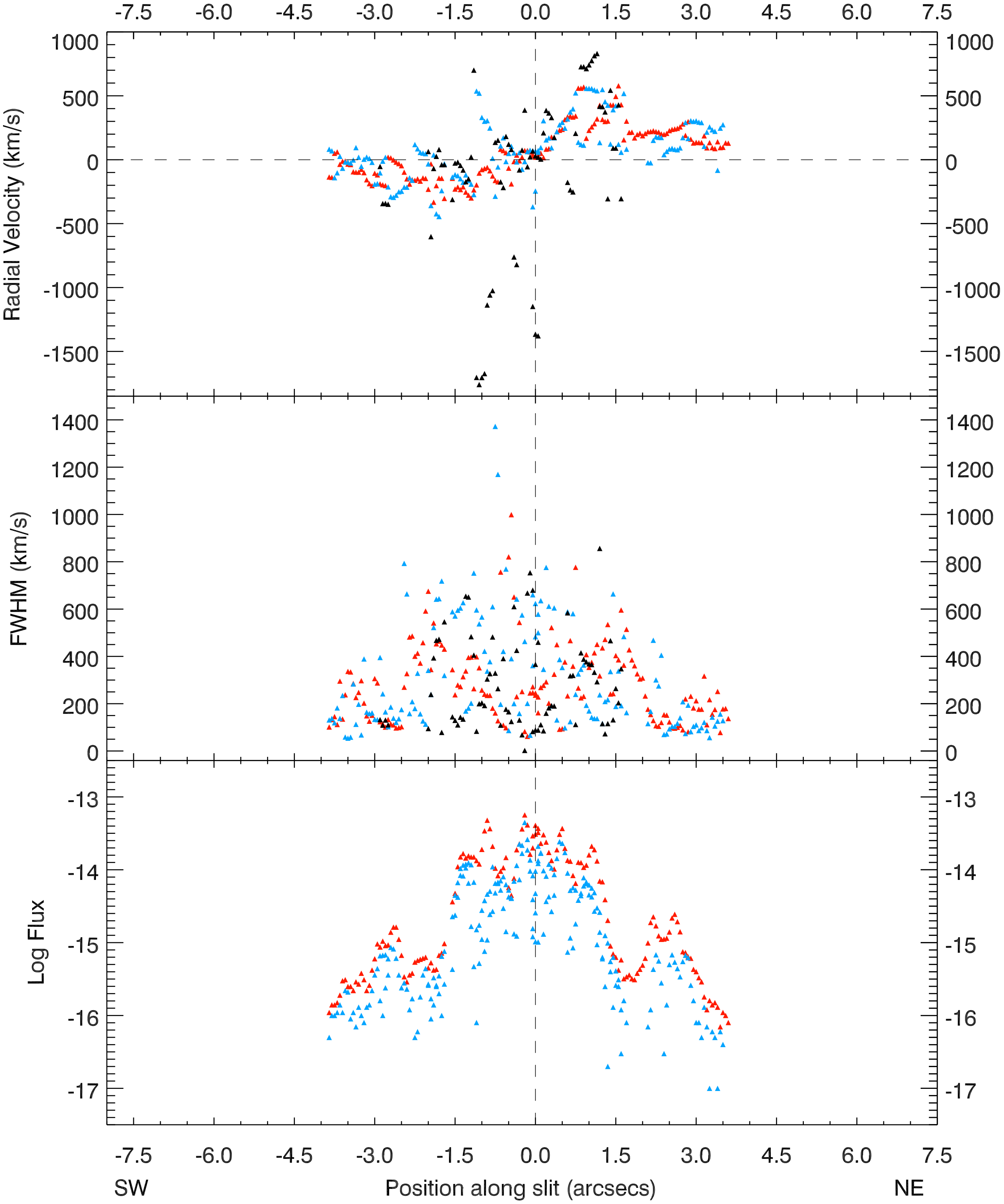

Figure 4.4: Plots of radial velocity, FWHM, and flux of slit 4 of NGC 4151 against position along the slit. The different colors represent the different kinematic components as in Figure 4.1.

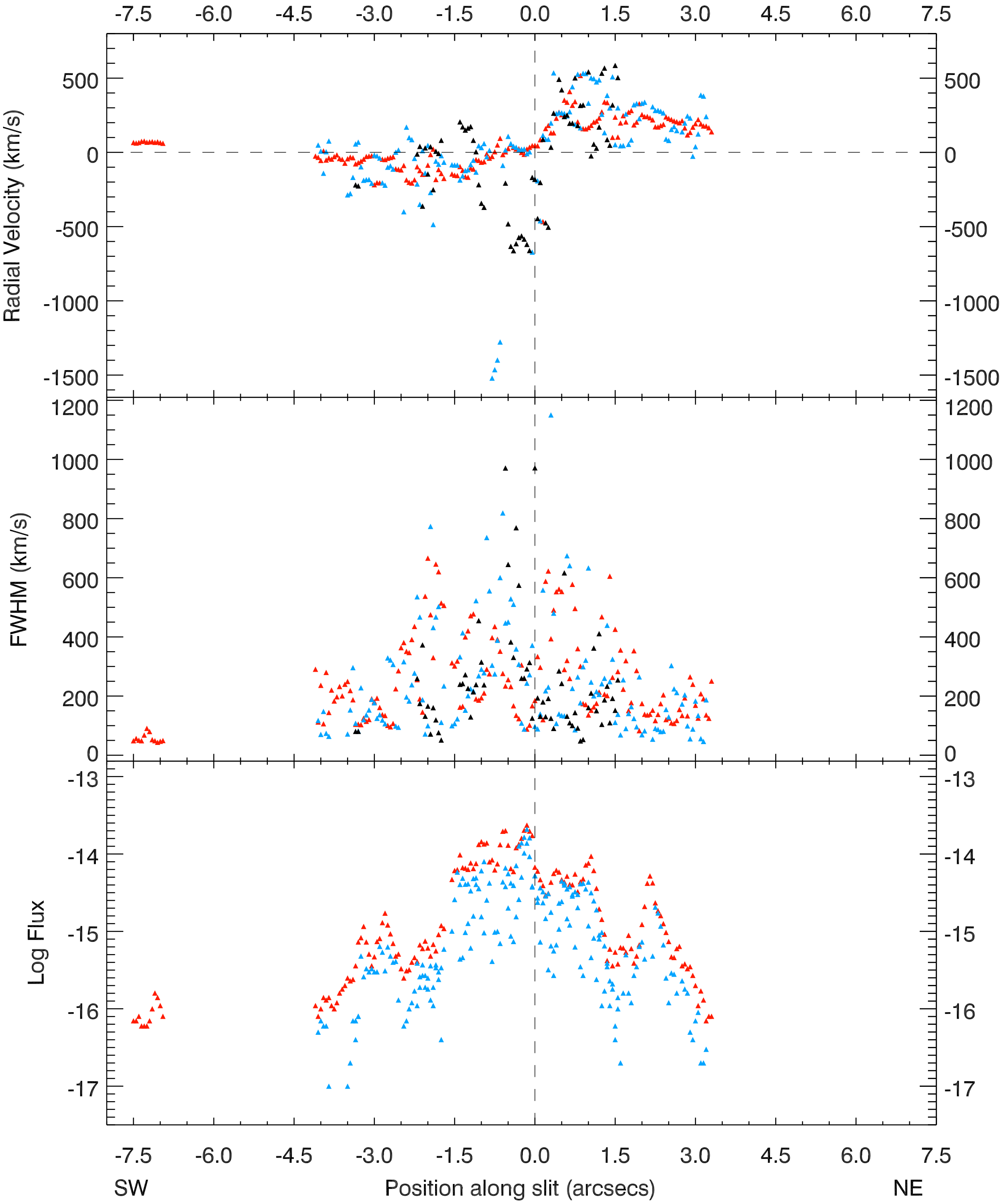

Figure 4.5: Plots of radial velocity, FWHM, and flux of slit 5 of NGC 4151 against position along the slit. The different colors represent the different kinematic components as in Figure 4.1.

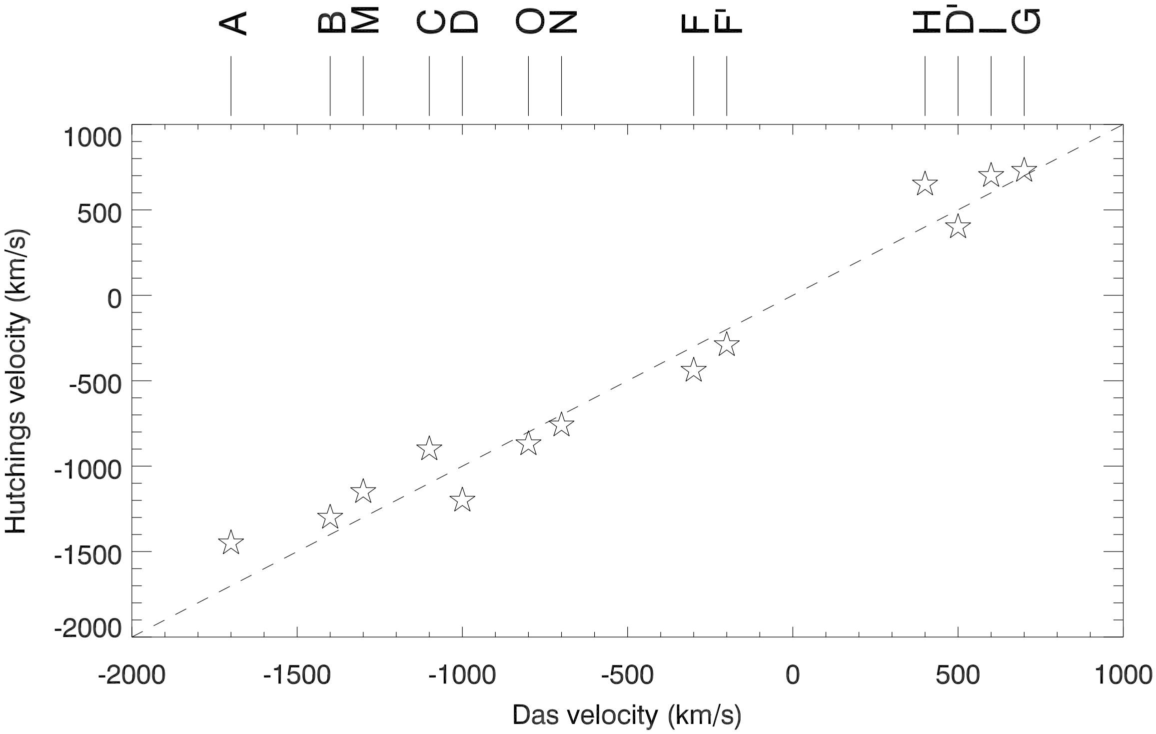

Figure 4.6: Comparison between our velocities and those of Hutchings et al. (1999). We found most of their knots; exceptions were knots E and J.

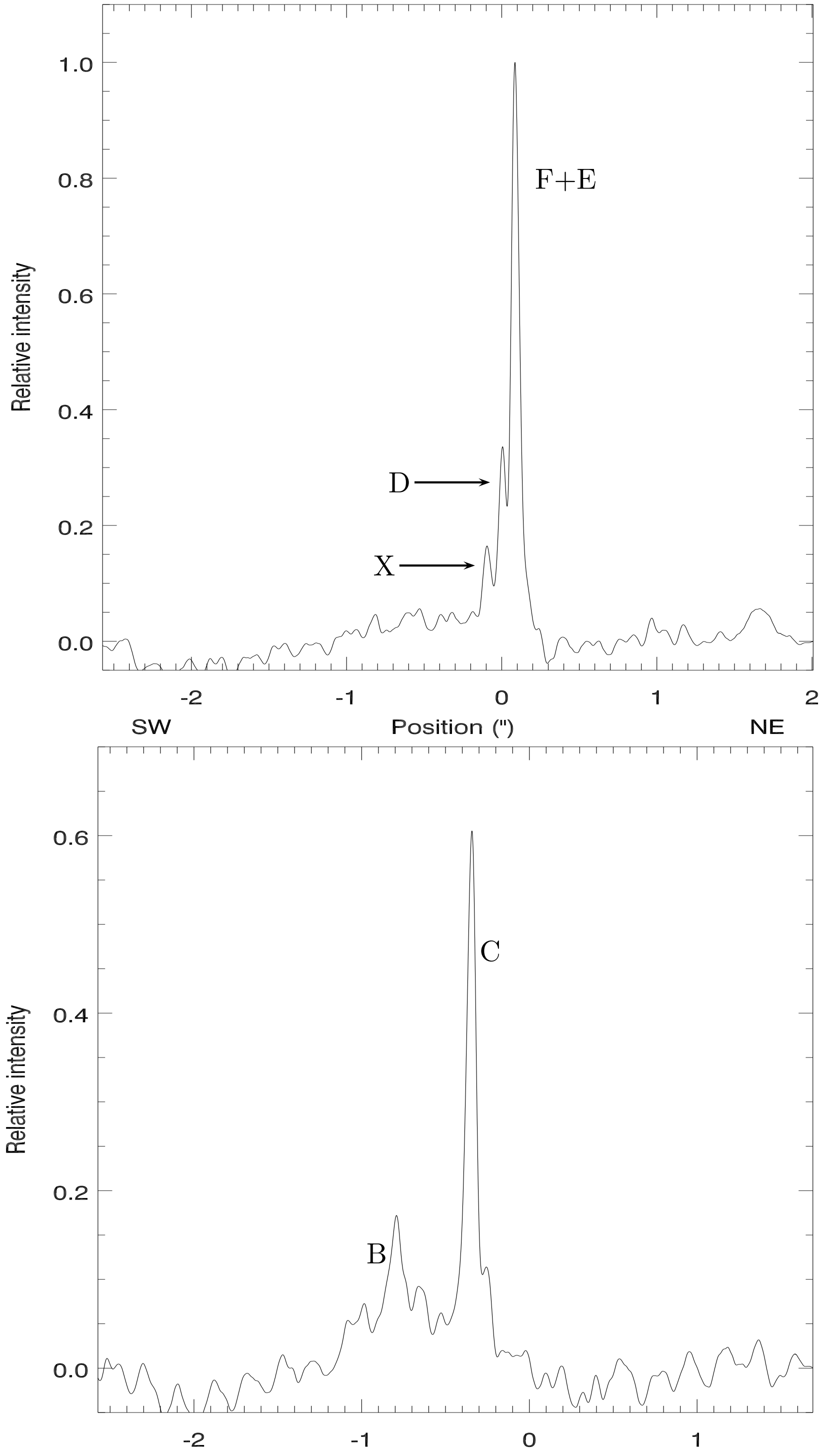

Figure 4.7: Plots showing the bright radio intensity of slits 1 (top) and 2 (bottom) of NGC 4151. The brightest peak in slit 1 is radio knot F+E, the second brightest coincides with the SMBH (knot D). Slit 2 contains a bright peak that corresponds to radio knot C.

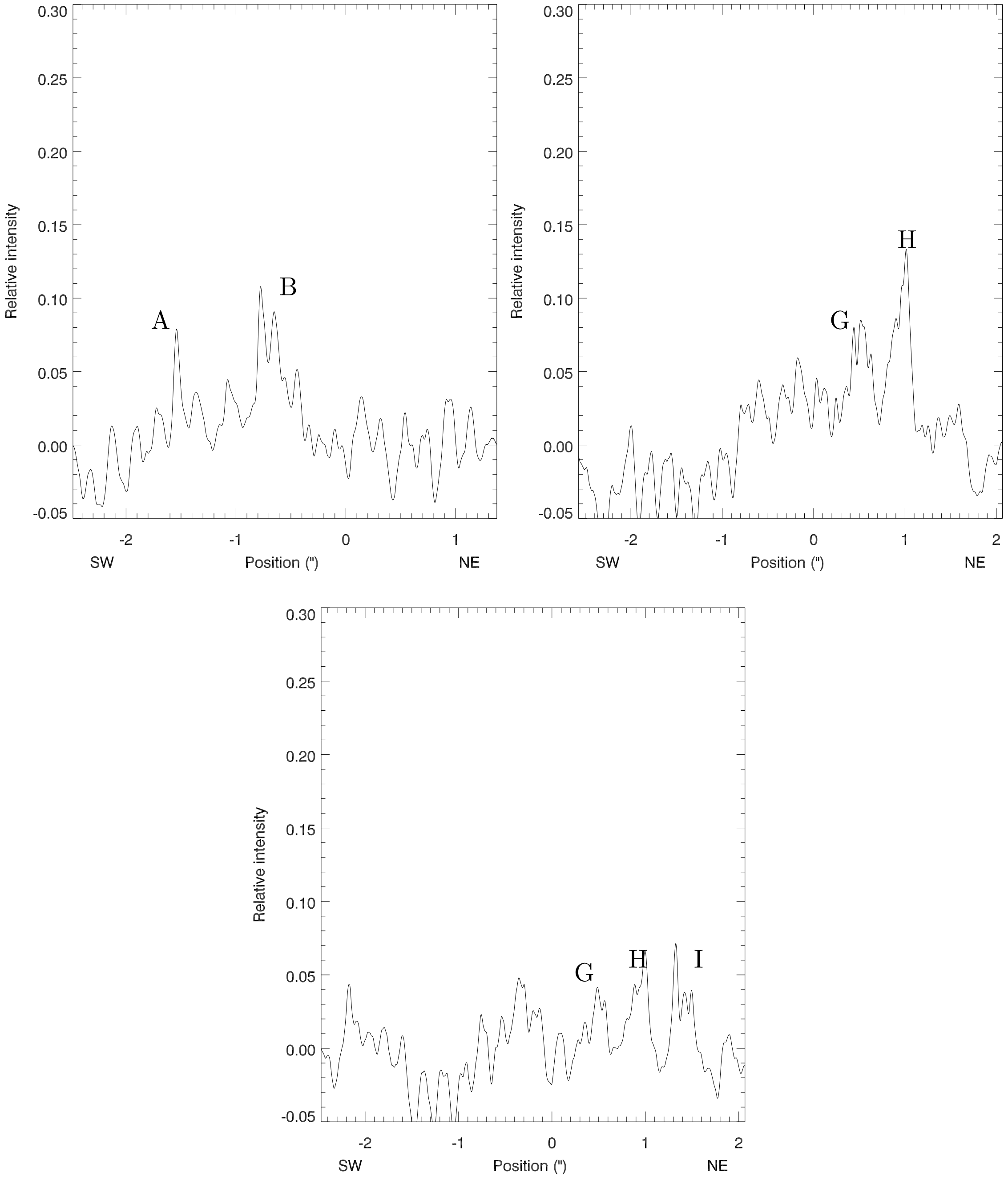

Figure 4.8: Plots showing the radio intensities of slits 3–5, ordered from left to right then top to bottom, of NGC 4151. The radio fluxes are weak in slits 3 and 4, and indistinguishable from the noise in slit 5.

4.2 Graphical Results for NGC 1068

Figures 4.9–4.16 show the kinematic components in plots of radial velocities, FWHM, and fluxes as functions of projected position from the center of each respective slit. The colors represent the different components as explained previously. In all the radial velocity plots, data points near zero velocity in the range $2''$–$10''$ are in the plane of the galaxy, as indicated also by their low FWHM. These points do not play any role in our modeling and are shown only for completeness. The fluxes generally decrease away from the SMBH, with two spikes, one at $\sim 3\farcs5$ and one at $\sim 8''$, indicating the presence of more gas at these locations. The FWHM does not present any discernible trends in any of the colors except for a slight decrease away from the SMBH. In contrast to the observed radial velocities in NGC 4151, the velocities in NGC 1068 show both redshifts and blueshifts on both sides of the nucleus. However, like NGC 4151, the velocities do show an increasing trend to about $1\farcs5$ in the northeast, followed by a decrease in velocity. There are fewer data points in the southwest and the velocities in most slits are generally lower there, but there is still some indication that the velocities are increasing, then decreasing with position, as shown in Figure 4.12 and somewhat in Figure 4.16.

The extracted radio intensities along the respective slits are plotted in Figures 4.17 and 4.18. The peaks in the radio intensities correspond to the bright compact radio knots seen in Figure 2.14. The disturbance to the [O III] clouds will be checked at locations near the radio peaks, where the radio emissions are most powerful.

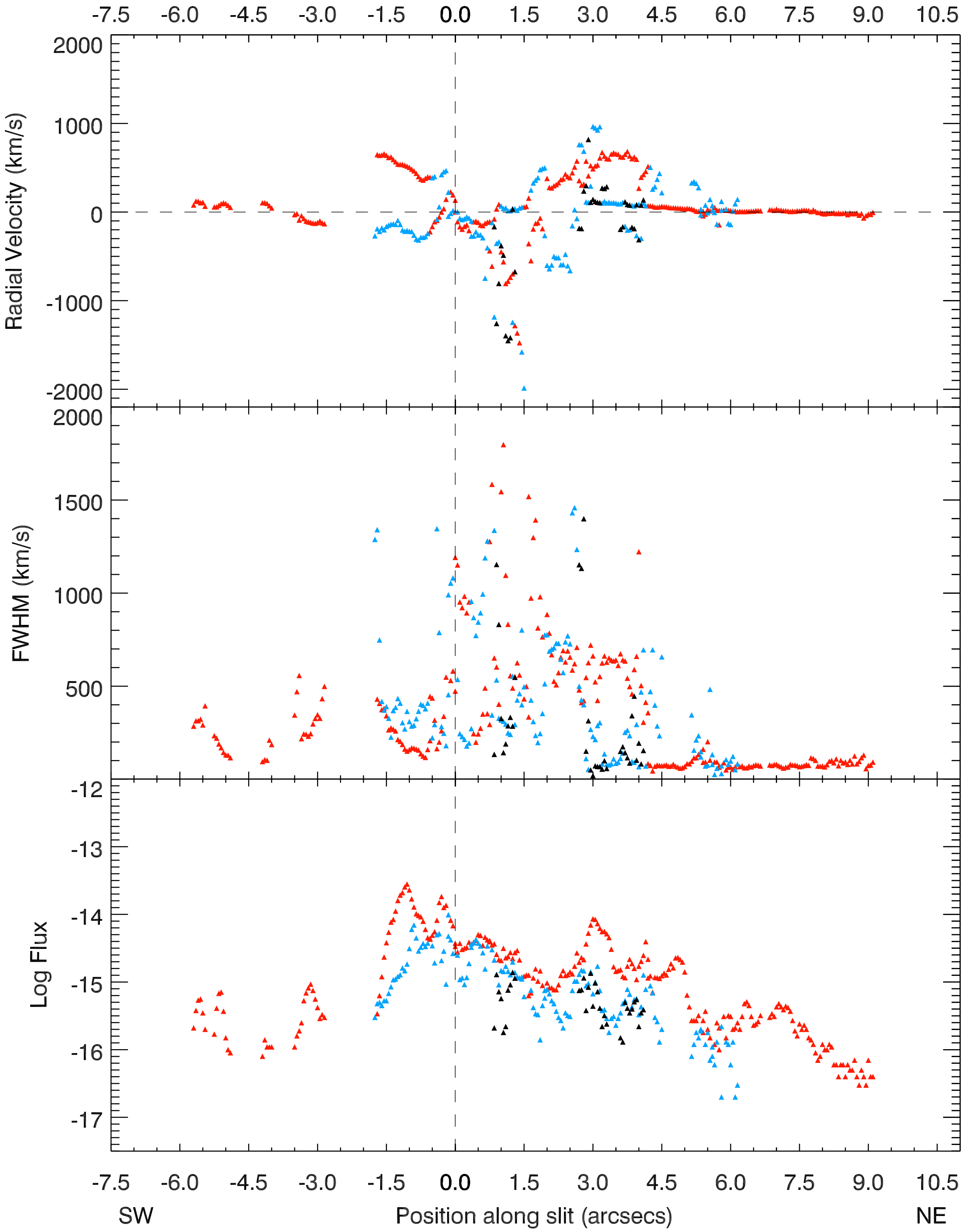

Figure 4.9: Slit 1 multi-colored plots showing the components present in the emission clouds at each position. The colors represent high(red), medium(blue), and low(black) flux levels respectively. Radial velocities are given relative to systemic, and fluxes are in ergs $s^{-1}cm^{-2}\text{Å}^{-1}$. All graphs share a common abscissa of position in arcseconds from the nucleus. The FWHM is not corrected for instrumental resolution.

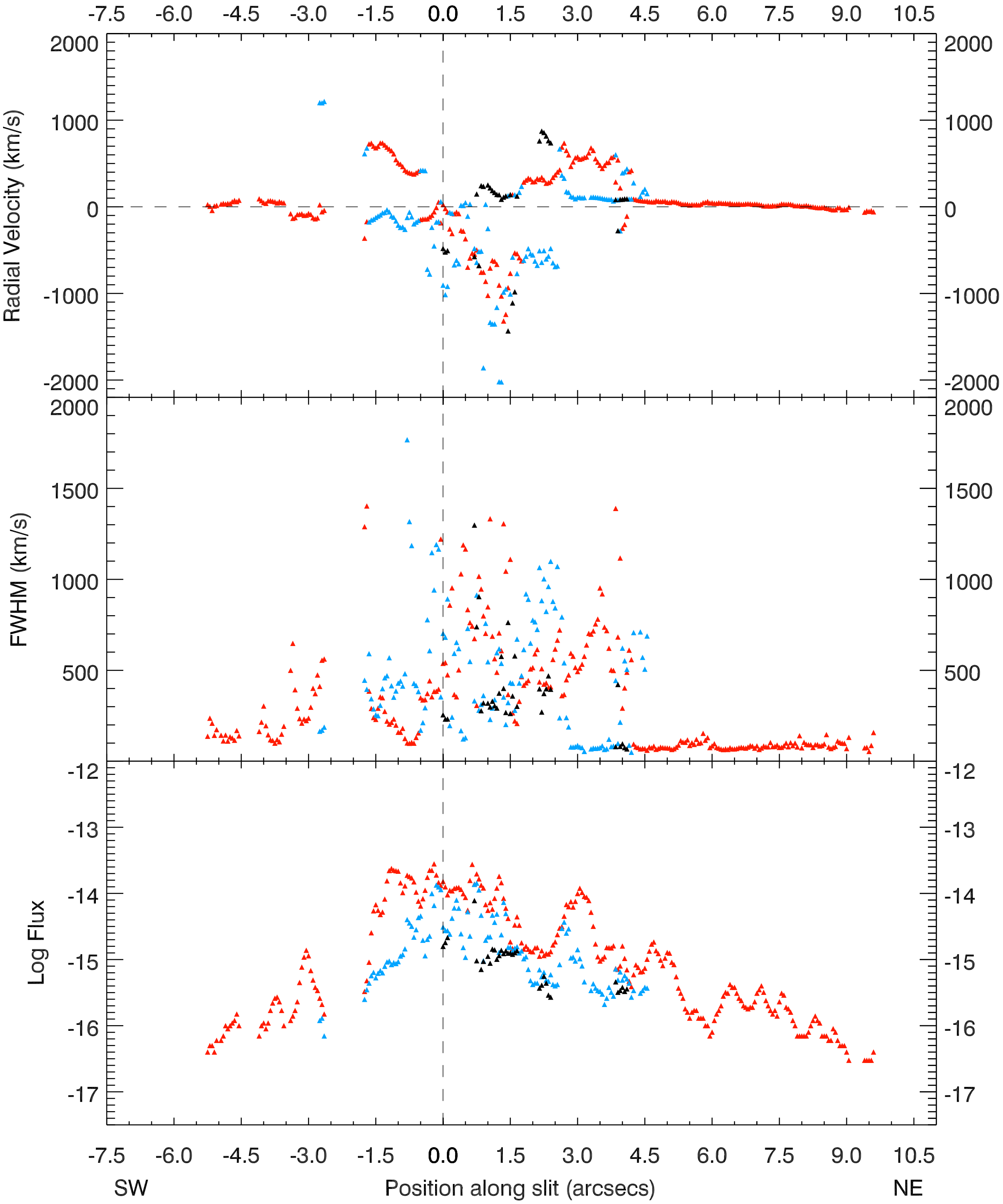

Figure 4.10: Plots of radial velocity, FWHM, and flux of slit 2 against position along the slit. The different colors represent the different kinematic components as in Figure 4.1.

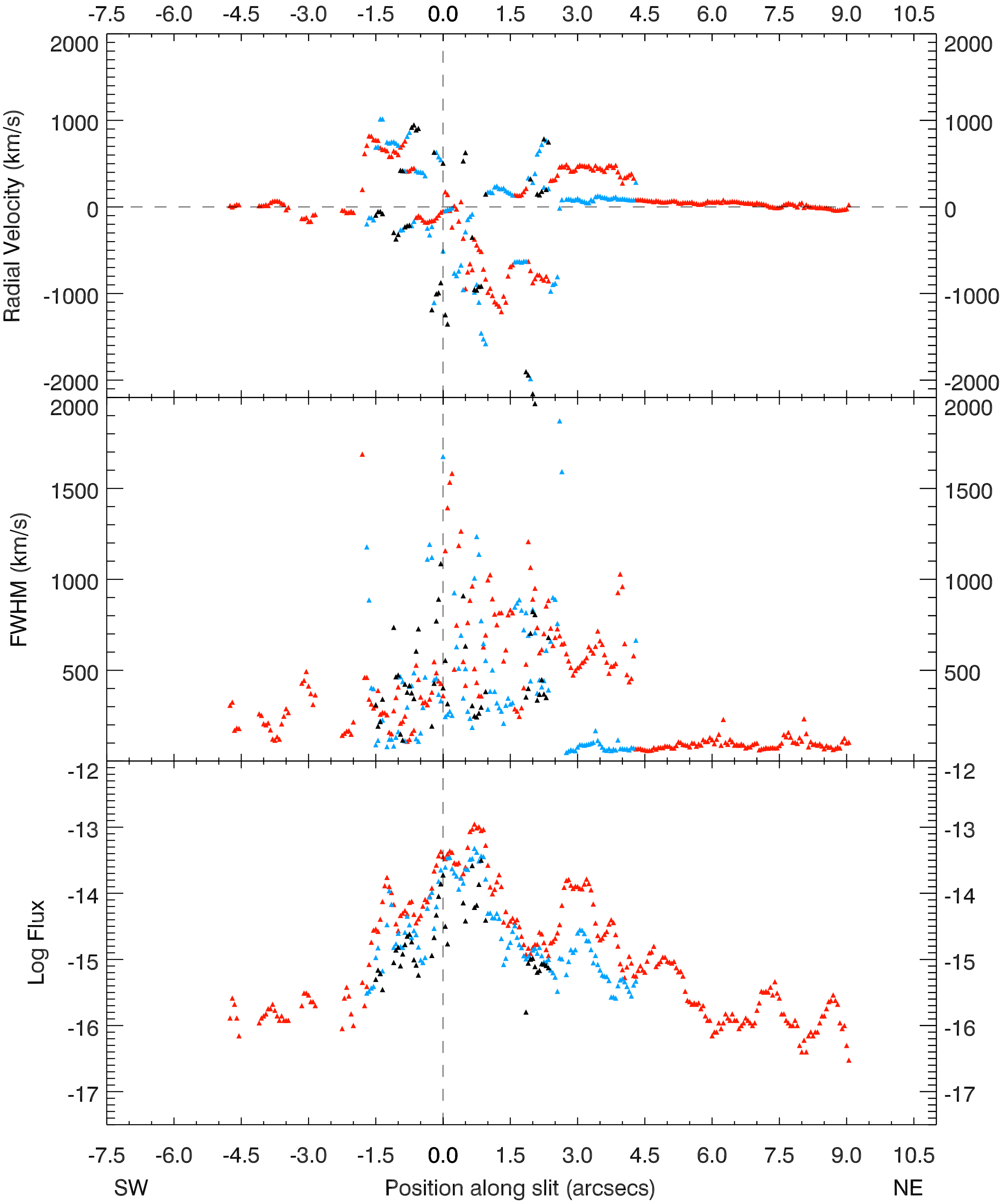

Figure 4.11: Plots of radial velocity, FWHM, and flux for slits 3. The colors depict the usual separation of flux levels as in Figure 4.9.

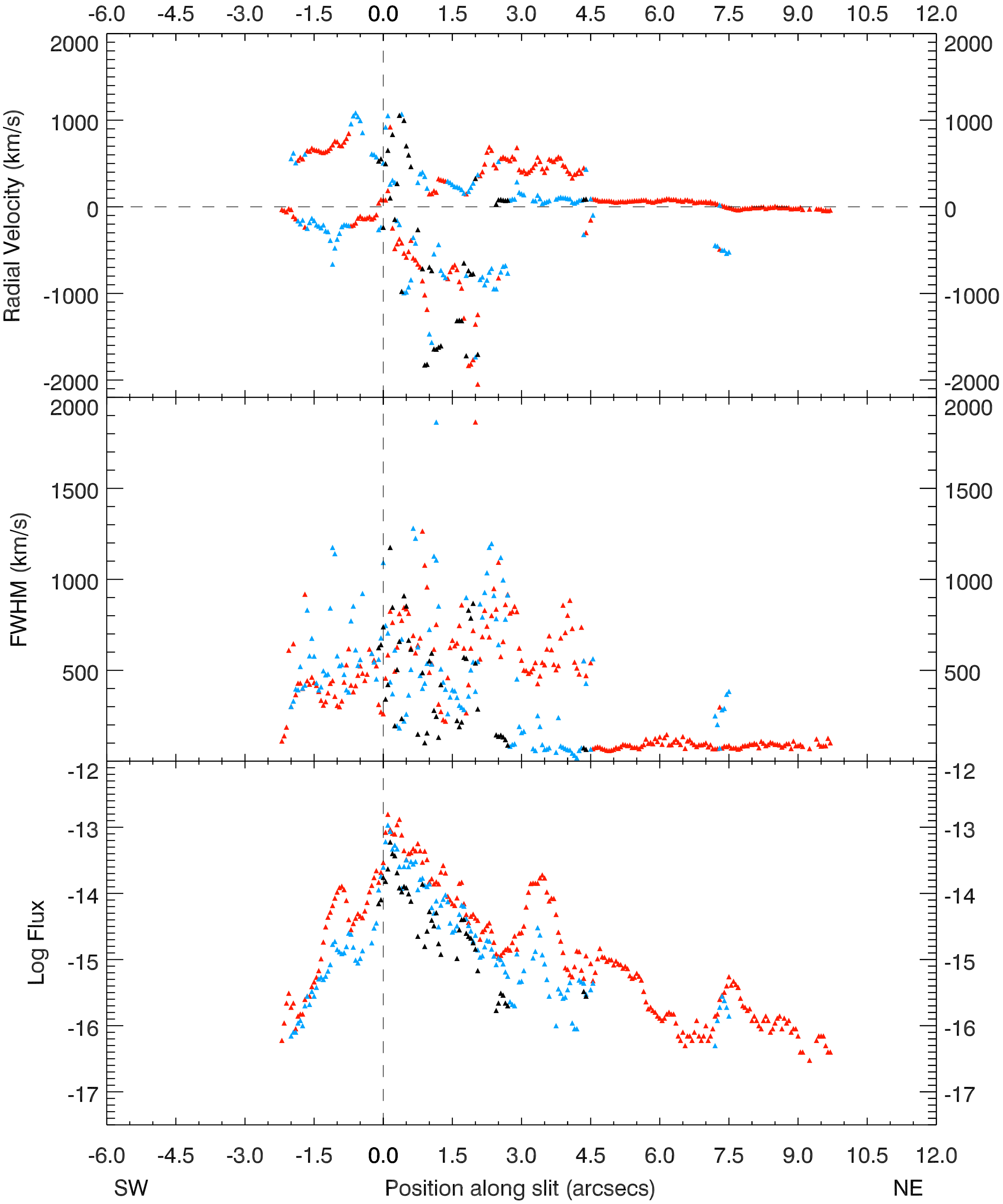

Figure 4.12: Plots of radial velocity, FWHM, and flux of slit 4 against position along the slit. The different colors represent the different kinematic components as in Figure 4.9.

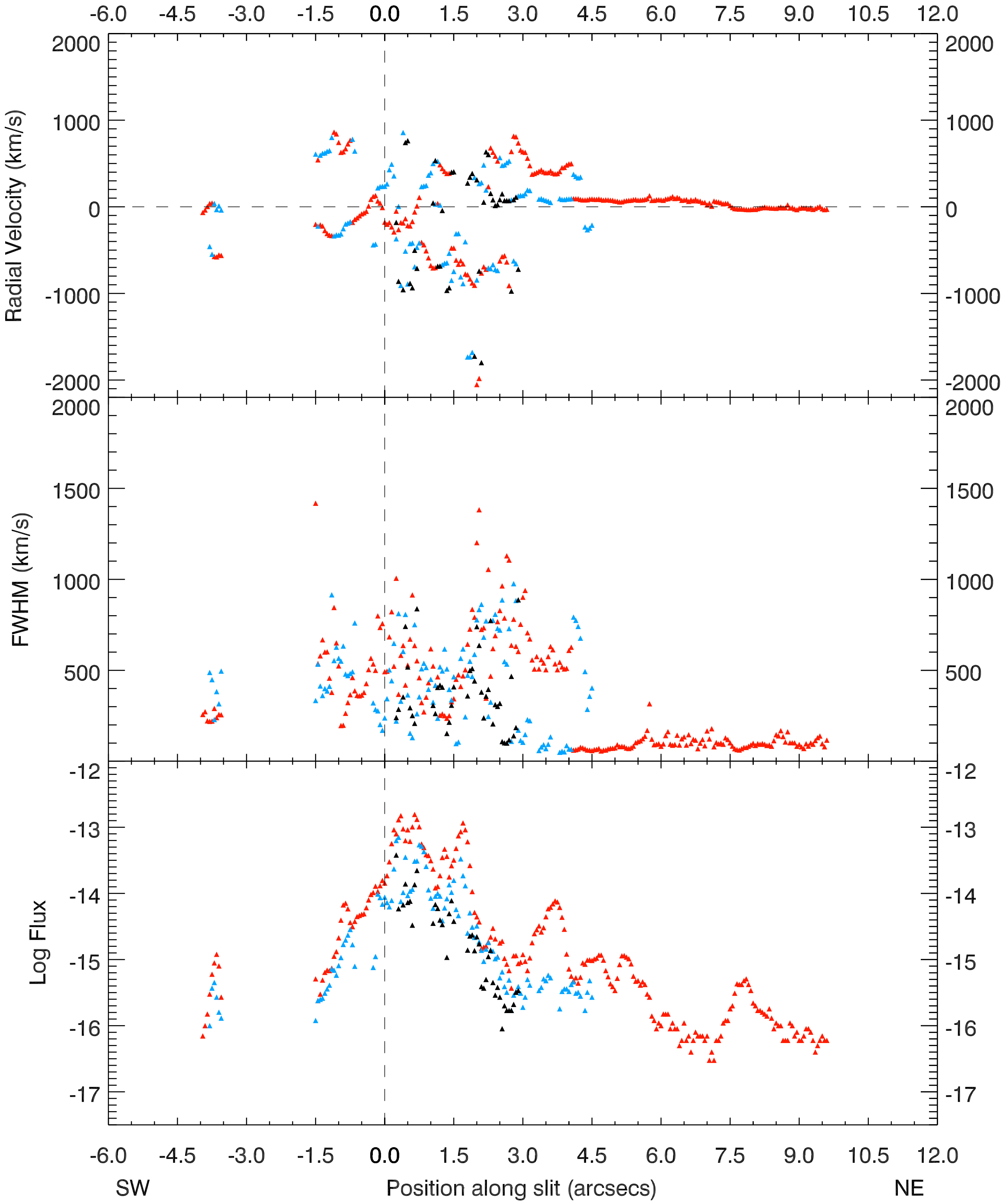

Figure 4.13: Plots of radial velocity, FWHM, and flux of slit 5 against position along the slit. The different colors represent the different kinematic components as in Figure 4.9.

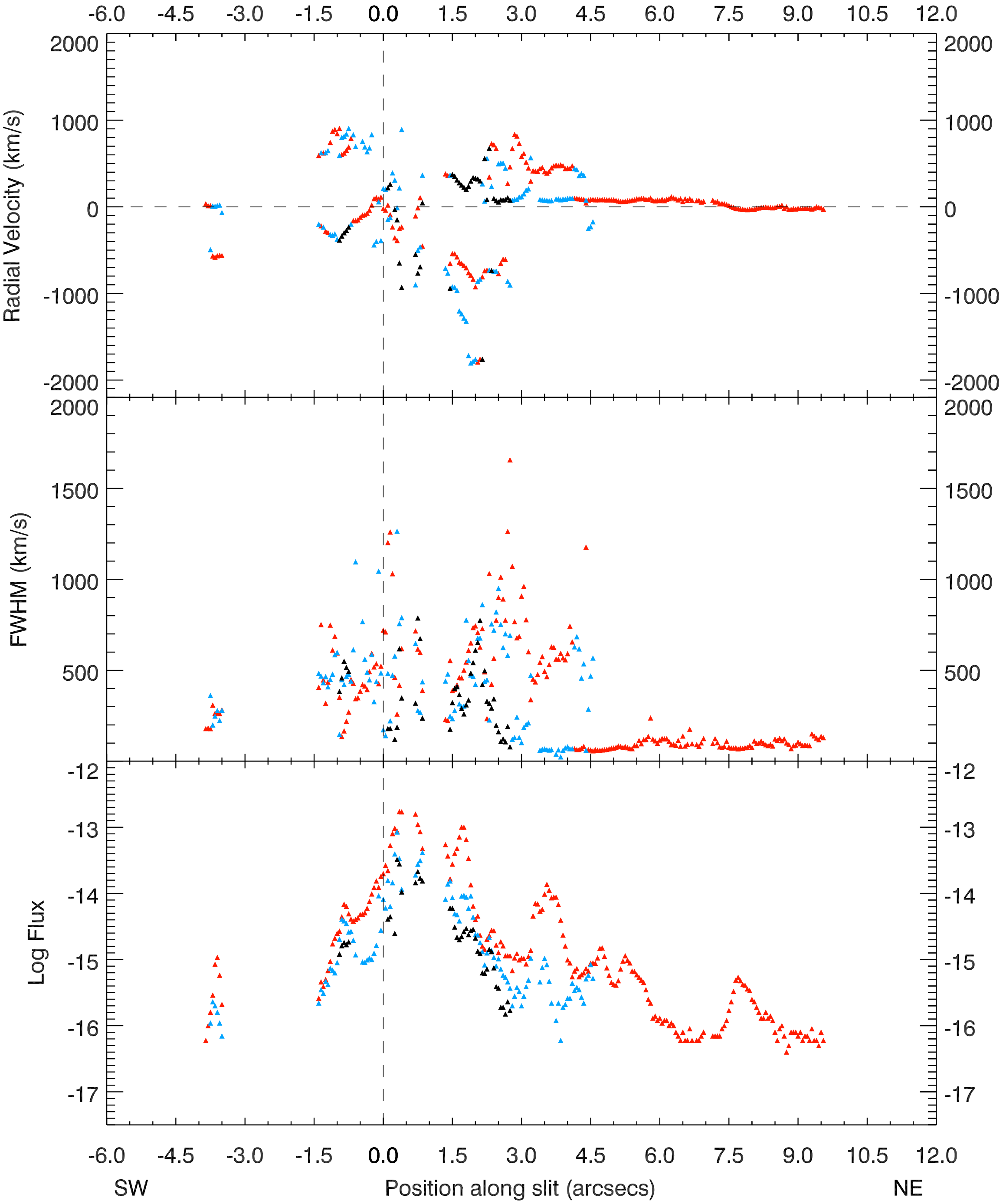

Figure 4.14: Plots of radial velocity, FWHM, and flux of slit 6 against position along the slit. The different colors represent the different kinematic components as in Figure 4.9.

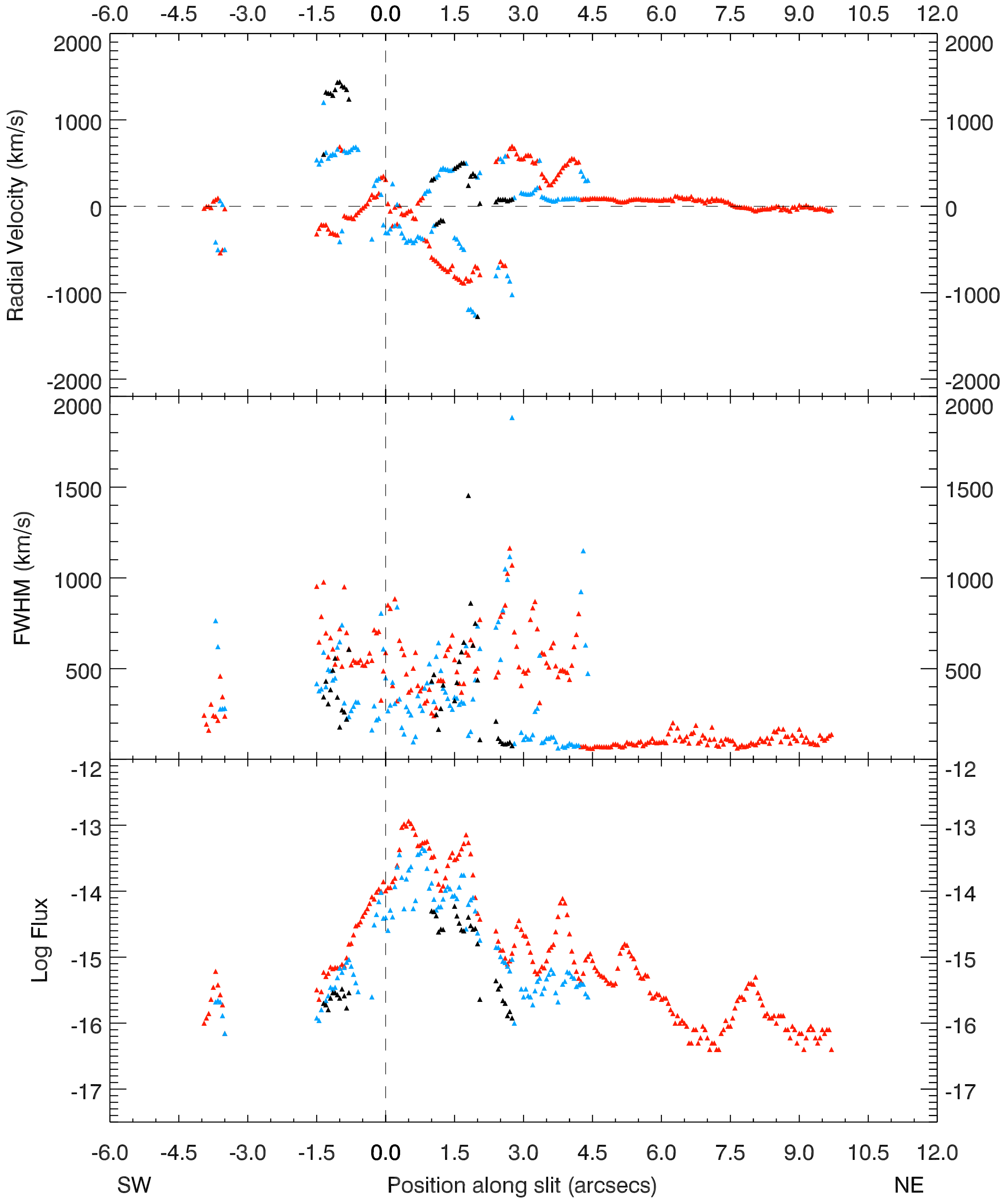

Figure 4.15: Plots of radial velocity, FWHM, and flux of slit 7 against position along the slit. The different colors represent the different kinematic components as in Figure 4.9.

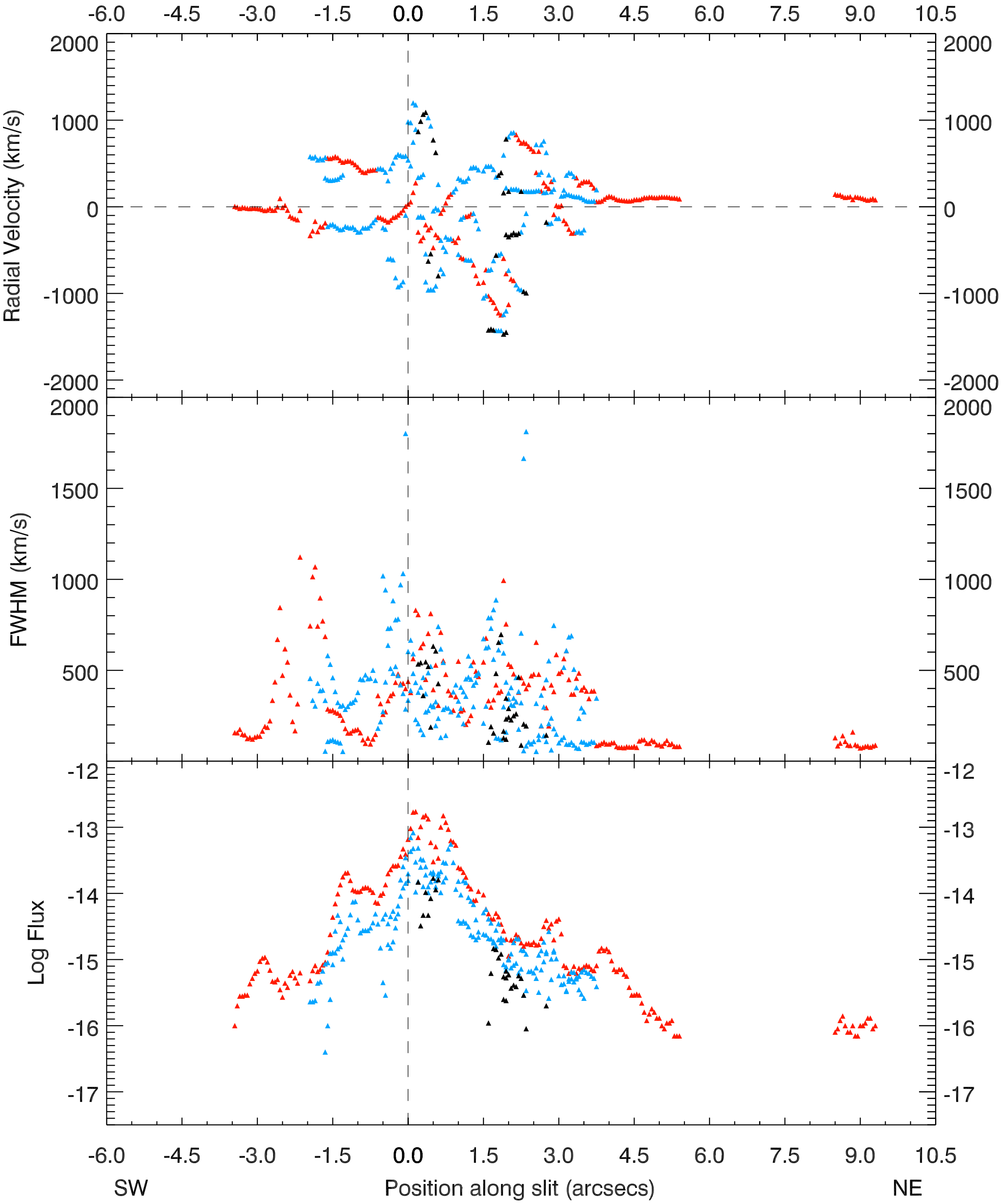

Figure 4.16: Plots of radial velocity, FWHM, and flux of slit 8 against position along the slit. The different colors represent the different kinematic components as in Figure 4.9.

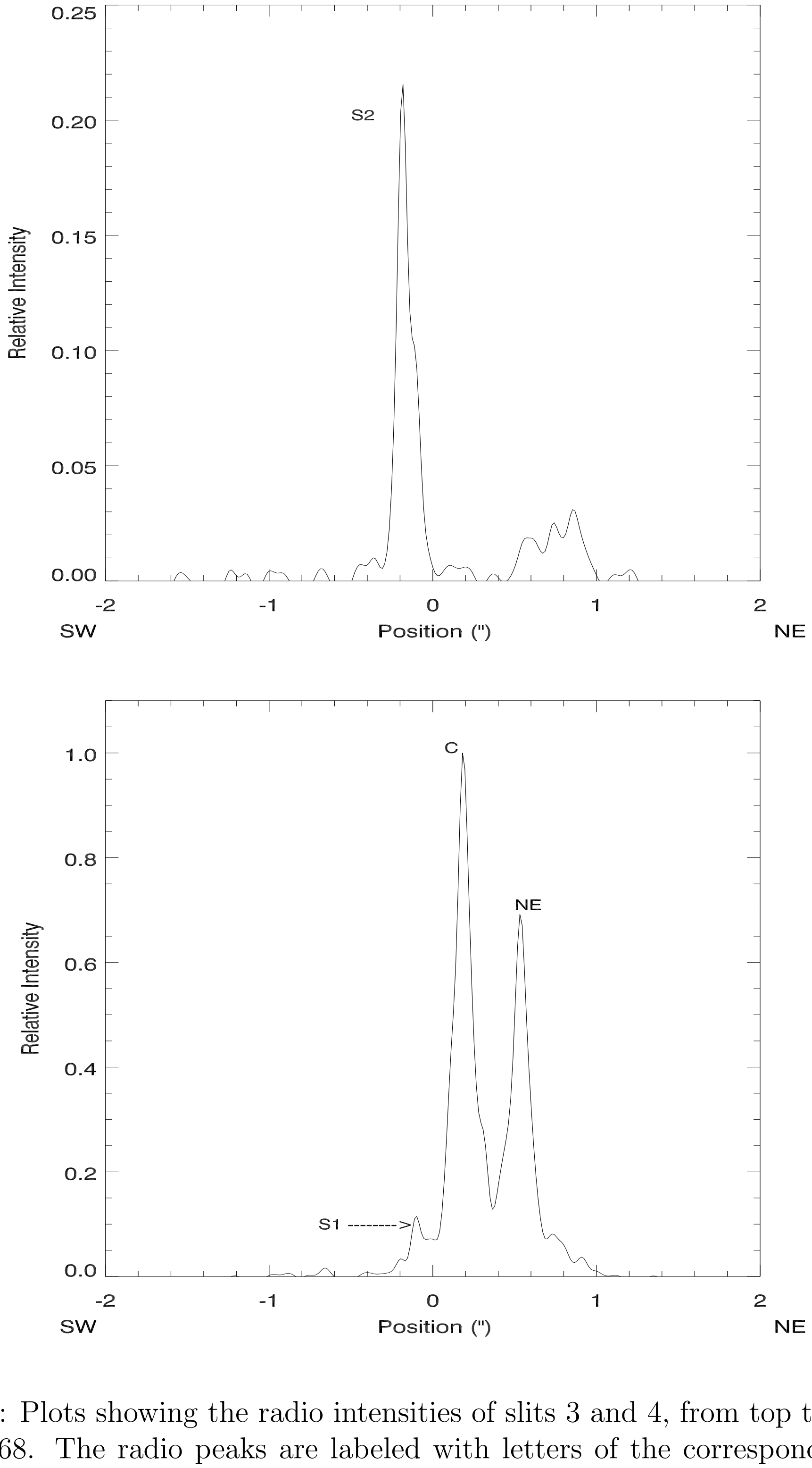

Figure 4.17: Plots showing the radio intensities of slits 3 and 4, from top to bottom, of NGC 1068. The radio peaks are labeled with letters of the corresponding radio knots as in Figure 3.6. The intensities are normalized to the peak value in slit 4.

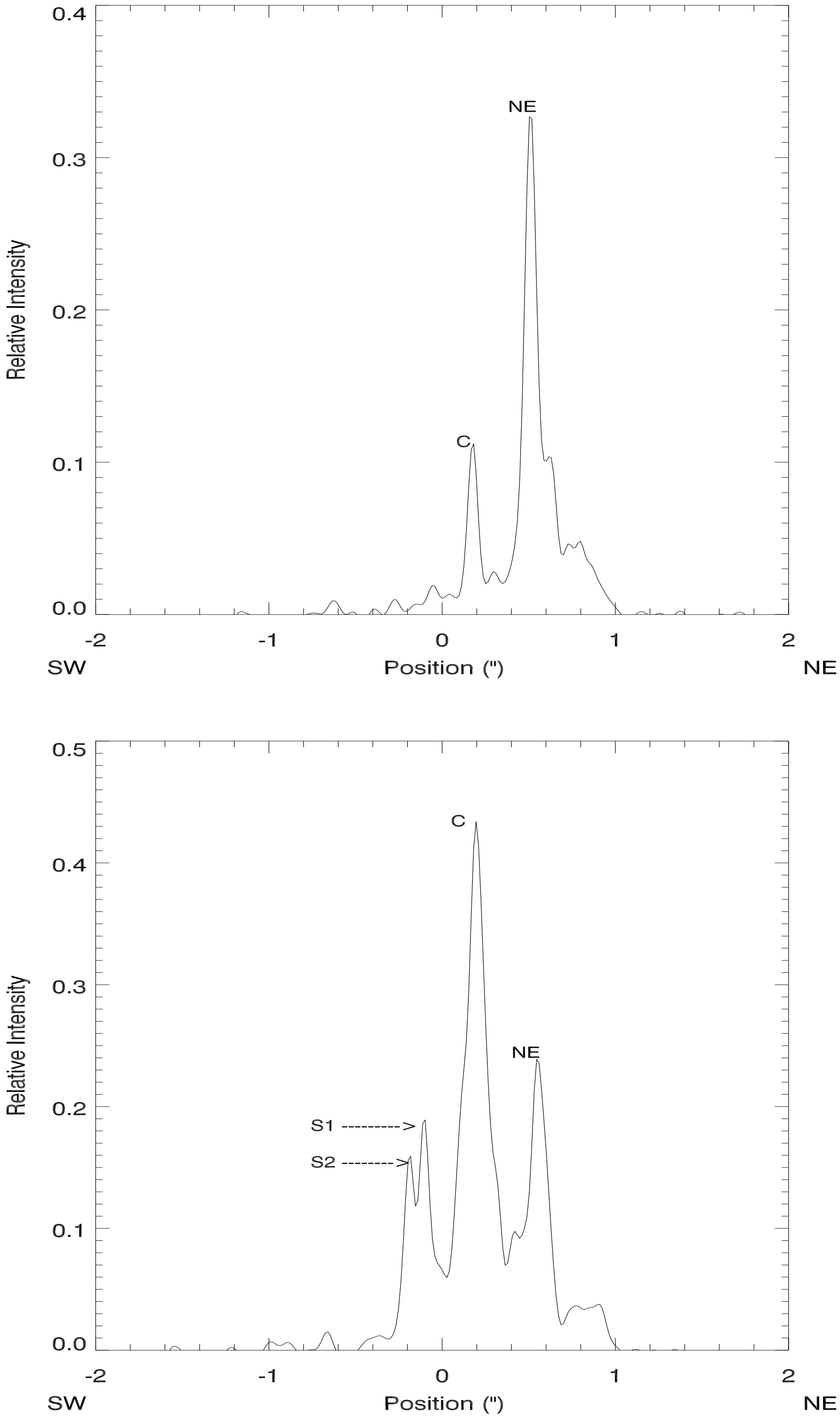

Figure 4.18: Plots showing the radio intensities of slits 5 and 8, from top to bottom, of NGC 1068. The radio peaks are labeled with letters of the corresponding radio knots as in Figure 3.6. The intensities are normalized to the peak value in slit 4.

– 5 –

Models

5.1 General Assumptions

The models that we generate to match the observations give kinematic fits to the radial velocities. They also provide some clues to the overall morphology of the NLR, such as inclination and position angle, and the true velocities of the outflowing clouds, but they do not define or explain the physical processes that govern the NLR. These kinematic models are the simplest to date that fit the data for both Seyfert 1s and 2s. The simplicity of the models stems from very basic assumptions concerning the characteristics of the NLR clouds, which are:

(1) The models assume a biconical geometry for the NLR, and the upper and lower cones are identical.

(2) The models assume that the biconical geometry is a result of confined illumination from the nucleus, due to a torus or some sort of obscuring material. The apex of the bicone then naturally starts at the nucleus defined by the SMBH.

(3) The models assume that the filling factor is 1 within the model geometry and 0 outside, because we do not know the location of a cloud along the LOS. This assumption gives a range of velocities along any LOS that a cloud can occupy. Since

our analysis is based on a forbidden line, [O III] λ5007, we assume that there is no absorption of this line within the bicone, although dust may actually absorb some of this emission (§6.4).

(4) The bicone edges are sharp, i.e. the inner and outer opening angles are sharply defined and there is no leakage of radiation outside or inside the bicone. Similarly the total length of the bicone is sharply defined, so that the model does not apply to clouds at greater distances.

5.2 Explanation of Model Parameters

The kinematic models described in this chapter are generated in a 3D geometry that depends on some basic input parameters. A fair understanding of the input parameters is necessary to fully comprehend the 3D aspect of the models. These parameters are listed in Table 5.1 and are discussed below. The cartoon in Figure 5.1 is used as a reference. The height of the bicone is defined as the distance from the nucleus to one end of the bicone, measured along the bicone axis. The inner and outer opening angles are measured from the bicone axis to the inner and outer edges of the bicone respectively. The inclination of the bicone is measured with respect to the plane of the sky. The upper cone is defined to be the one with a projected axis closest to north. If the upper cone is tilted towards the observer, the inclination is defined to be positive. The cartoon is shown representing a negative inclination. The position angle is the angle between North and the bicone axis projected unto the plane of the

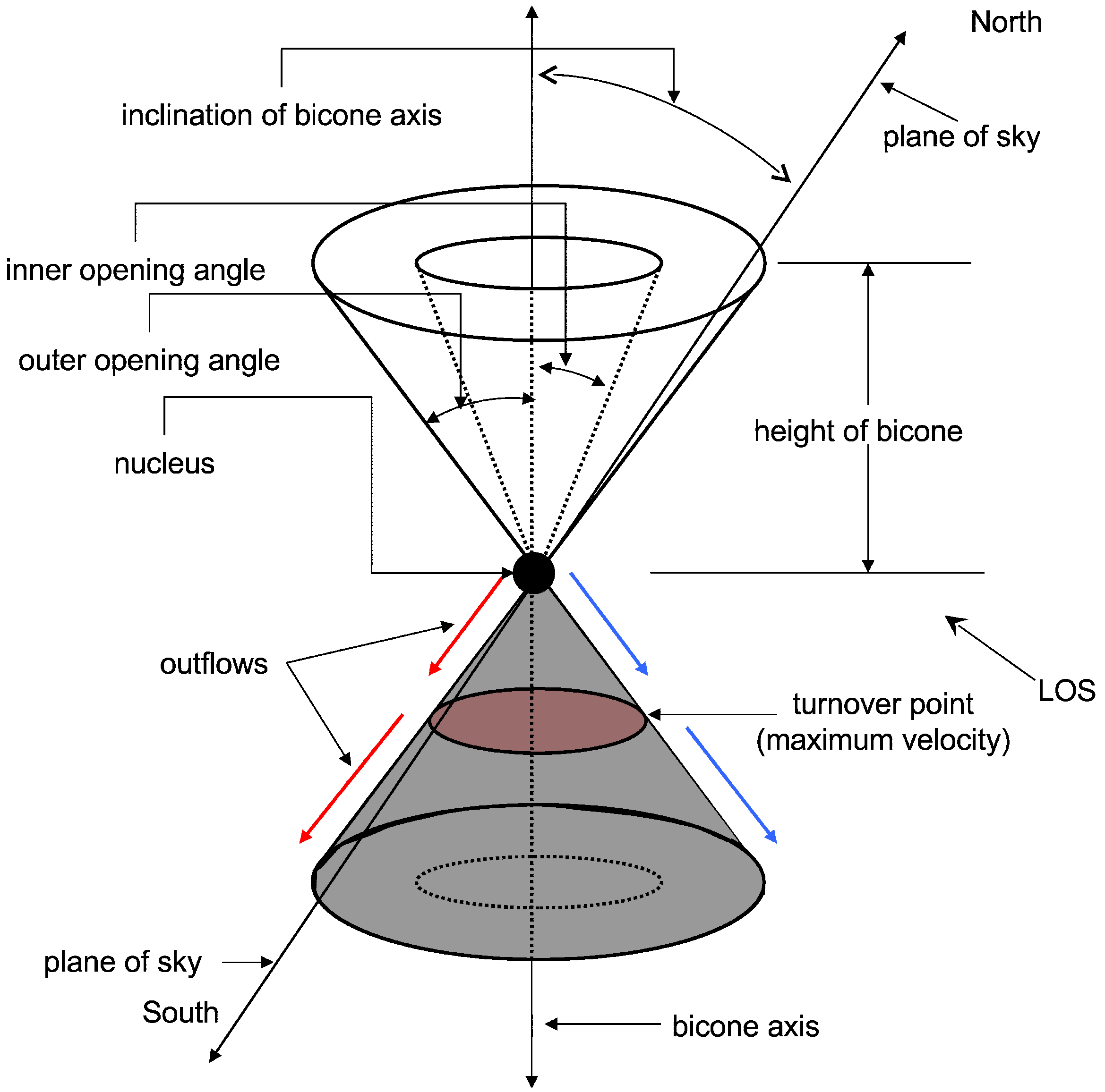

Figure 5.1: Figure that explains the parameters used to generate the kinematic models.

sky, measured in an eastward direction. We will present strong evidence that the NLR clouds are in outflow from the vicinity of the SMBH. We will also present evidence that the clouds are accelerated to a maximum velocity at a turnover point, and then decelerated back to the systemic velocity. The blue arrows in Figure 5.1 represent

Table 5.1: Definition of Model Parameters.

Parameter	Symbol
Height of bicone (pc)	z_{max}
Inner opening angle (deg)	θ_{inner}
Outer opening angle (deg)	θ_{outer}
Inclination of bicone axis (deg)	i_{axis}
Position angle of bicone axis (deg)	PA_{axis}
Maximum velocity [a]($\mathrm{km\,s^{-1}}$)	v_{max}
Turnover distance [a](pc)	r_{t}
Velocity law	v_{law}

[a] deprojected: i.e relative to the nucleus, not the observer

clouds with radial velocity components flowing in the direction towards the observer, hence blueshifted, and the red arrows represent redshifted clouds. The turnover point in this figure is defined by the location of the maximum velocity of the outflowing clouds. The turnover point is represented by the red 'disk' in the cartoon. The velocity laws used were of the form $v = kr^n$, where r was measured from the nucleus and k is some constant. We considered values of n that ranged from 0 to 2 and finally settled for a law with a value of 1 for n, which seemed to work best to represent the linear trend in the velocities shown in Figures 4.1–4.5 and Figures 4.9–4.16. Other values of n were already tried and found to be of poorer fit. Therefore, for the purposes of demonstration, we used the velocity law of the form $\mathrm{v = kr}$ for the accelerating phase of the gas, and $\mathrm{v = v_{max} - k^{'}(r - r_t)}$, for the decelerating phase. We called these two forms of the equation of outflow collectively the '*rlaw*'. The *rlaw*, also known as the 'Hubble flow' for the accelerating portion, seems to work best to fit the data.

5.3 Constructing the Models

5.3.1 Mapping Velocities on the Bicone

For this work we migrated from a 2D modeling scheme used in Crenshaw & Kraemer (2000b) and Crenshaw et al. (2000), to a 3D modeling scheme. Such transitions were made possible by friendlier and more efficient 3D programming codes in the IDL system. Also over a few years, advancements in computer architectures have enabled the handling of large amounts of data, yet have provided a dramatic increase in computational power and thus greatly reduced program runtime. The migration to 3D was particularly useful also for the visualization and interpretation of the models, as the reader can more easily picture and comprehend the biconical geometry

Construction of the models starts by filling in a cubic array with velocities for a given parameter set and velocity law. The process is done as follows. We start with a cubic array, whose dimension is specified by the resolution of the model; a default value of 100 is used. The dimensions of the array then becomes 100x100x100. For the sake of efficiency and short programming runtimes, this dimension will change slightly within the program to avoid wasted pixels that have undefined velocities. First we start with a bicone with its axis in the plane of the sky, i.e., at zero inclination. The Cartesian coordinates used here have the x-axis pointed towards the right, the z-axis pointed up, and the y-axis pointed away from the reader. The height of the bicone along the z-axis then becomes 100 pixels. If, for example, the height of the bicone was specified as 100 pc, then the scale of our model becomes 1 pc pixel^{-1}.

Table 5.2: Parameters used to generate Figure 5.2.

Parameters	$z_{\rm max}$ (pc)	$\theta_{\rm inner}$ (deg)	$\theta_{\rm outer}$ (deg)	$i_{\rm axis}$ (deg)	$PA_{\rm axis}$ (deg)	$v_{\rm max}$ ($\rm km\,s^{-1}$)	$r_{\rm t}$ (pc)
Values	200	30	40	0	0	2000	70

Next, a loop is constructed to identify every point in the array as belonging in the bicone or not. For example, point (50, 23, 81) was converted into standard polar representation (r, θ, ϕ) and then θ was tested to determine if it falls within the region as specified by our inner and outer opening angles. If this condition is met, the distance to the point r is first converted to parsec using the scale and the point is then assigned a velocity based on our simple velocity laws. This velocity is then stored in the array at point (50, 23, 81). For a 'Hubble flow' law, the constant of proportionality k is simply given by $k = v_{max}/r_t$, based on the two input parameters 'maximum velocity' and 'turnover point'. If θ falls outside of the bicone, the point is assigned a NaN (Not a Numerical) value. The testing and assigning of velocity for every point is continued until the array is filled up to the turnover point, after which our deceleration law, such as $\rm v = v_{max} - k^{'}(r - r_t)$, comes into effect until the end of the array is reached.

An example of such filled array is shown in Figure 5.2. This figure represents only one quarter of the top part of the bicone, and was generated with the input parameters listed in Table 5.2. The colors blue to red represent velocities 0–2000 $\rm km\,s^{-1}$ as shown in the color key at the bottom of the figure. Notice that maximum velocity occurs at

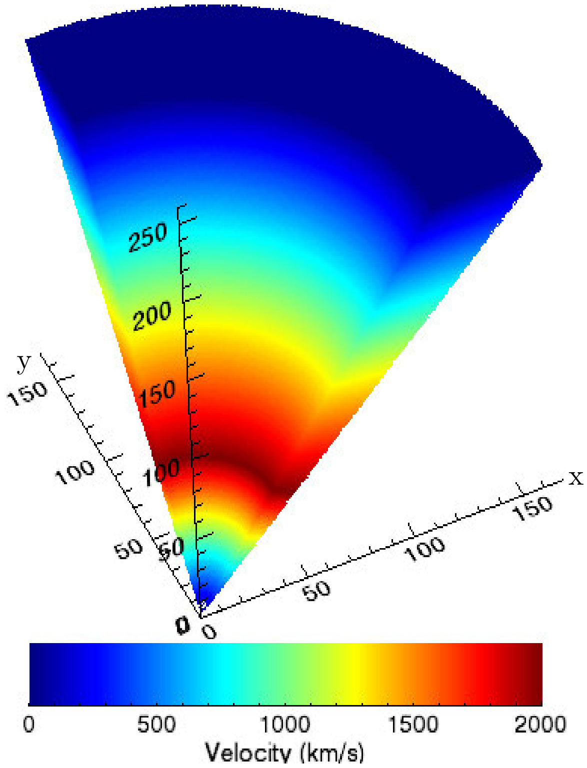

Figure 5.2: Diagram showing the velocity field on the first quadrant of the bicone. The blue-red color table was used to depict the velocity as a function of distance from the nucleus. This quadrant is used to construct the rest of the bicone, by multiple reflections.

the turnover point indicated by the bright red band around the partial bicone.

The axi- and mirror-symmetries of the bicone model allows us to construct the entire bicone from the first quadrant shown in Figure 5.2. The quadrant, if rotated around the z-axis, will produce the entire top half of the biconical geometry. The actual rotation is accomplished by multiple reflections about the xz and yz planes. The end product looks like Figure 5.3, which is now the top half of the bicone. One may be tempted at this stage to reflect the entire top half about the xy plane to produce the bottom cone, hence completing the geometrical bicone structure. While

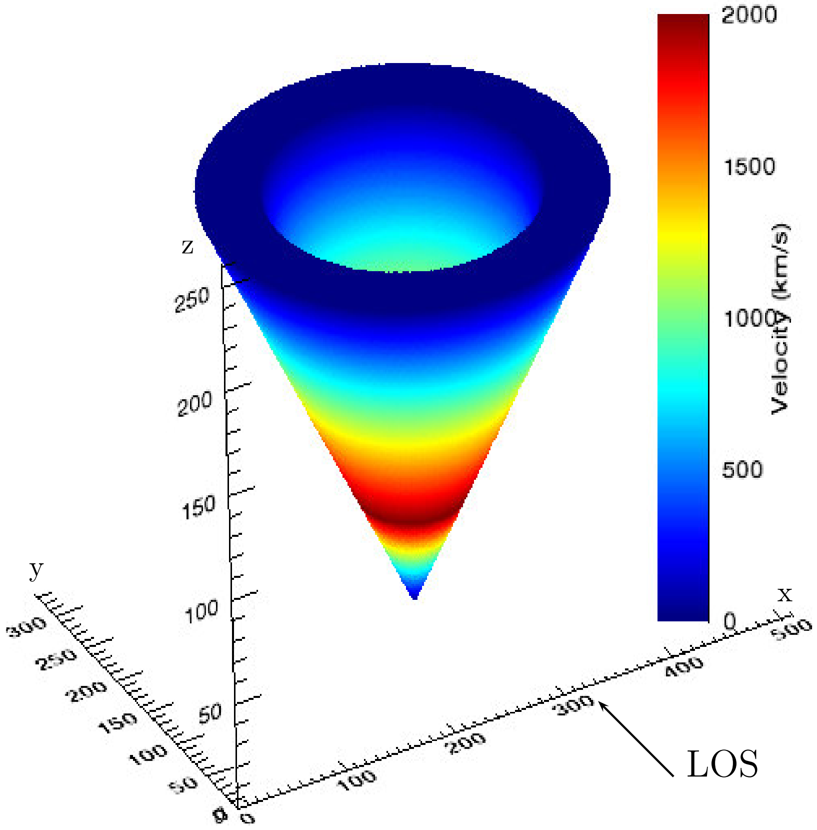

Figure 5.3: Diagram showing the radial velocity field on the top half of the bicone for an inclination of zero degrees. The bicone was constructed by a series of reflections about the xz and yz plane.

this approach is valid, it is more efficient to first project all velocities in the cone into radial velocities, and to then perform the reflection. The reason for this is that the radial velocities depend on the inclination of the bicone. A complete bicone occupies a large 3D array, hence operating on such an array overloads the random access memory (RAM) and the physical memory used by the central processing unit (CPU). Therefore we calculate the radial velocities first by considering the inclination input parameters, then we perform the necessary reflection to complete the bicone. Note that any rotation about the y-axis, as specified by the position angle input parameter, does not affect the radial velocities.

5.3.2 Finding Radial Velocities

The velocities assigned to the bicone in Figure 5.3 are converted to radial velocities depending on their coordinates by the simple conversion formula:

$$v_{radial} = v \sin\theta \sin\phi \tag{5.1}$$

The coordinate system used is defined in Figure 5.4. If there is a non-zero inclination input parameter, we first have to spin the cone by an amount given by the inclination before we apply Equation (5.1). Because the cone is embedded within the cubic array, we first need to translate its apex to the origin, then apply the inclination about the x-axis. The transformation of the axes by an inclination of i_{axis} is given by the following:

$$x' = x \tag{5.2}$$

$$y' = y\cos(i_{\mathrm{axis}}) - z\sin(i_{\mathrm{axis}}) \tag{5.3}$$

$$z' = y\sin(i_{\mathrm{axis}}) + z\cos(i_{\mathrm{axis}}) \tag{5.4}$$

After rotation, the new spherical coordinates are computed from (x', y', z') and the velocities at point (x, y, z) are then transformed to radial velocities by the usual formula as in Equation (5.1). After all the points have been transformed this way, the radial velocity field on the upper cone looks like that shown in Figure 5.5 with no in-

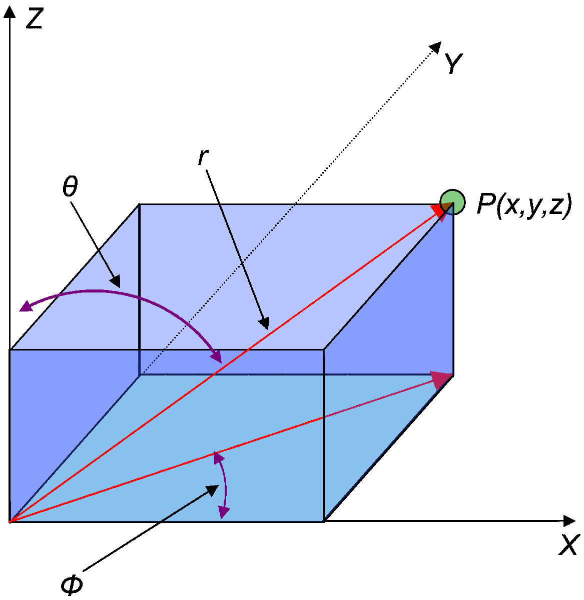

Figure 5.4: Cartoon showing the setup of the coordinate system used in constructing the bicone model. The LOS is along the Y axis, going into the picture.

clination and Figure 5.6 with a 20° inclination. The maximum velocity in Figure 5.5 is now shown in projection as 1278 $\mathrm{km\,s^{-1}}$ instead of 2000 $\mathrm{km\,s^{-1}}$ as in Figure 5.3. Also a comparison between Figures 5.5 and 5.6 will show that the due to the inclination toward the observer, the velocity of the front side of the cone increased in blueshift from -1278 $\mathrm{km\,s^{-1}}$ to ~ -1700 $\mathrm{km\,s^{-1}}$, while the velocity of the back side of the cone decreased in redshift side from 1278 $\mathrm{km\,s^{-1}}$ to $\sim$ 700 $\mathrm{km\,s^{-1}}$. Due to the symmetry of the bicone, the radial velocities shown in the front and back half of Figure 5.5 are identical in magnitude but opposite in direction.

The bottom half of the bicone can now be generated by the same use of symmetry: a reflection about the xy plane, followed by a reflection about the yz plane, and followed by a change in the radial velocity sign. The complete geometrical bicone model is displayed in Figure 5.7, which shows the front (top) and back (bottom) half

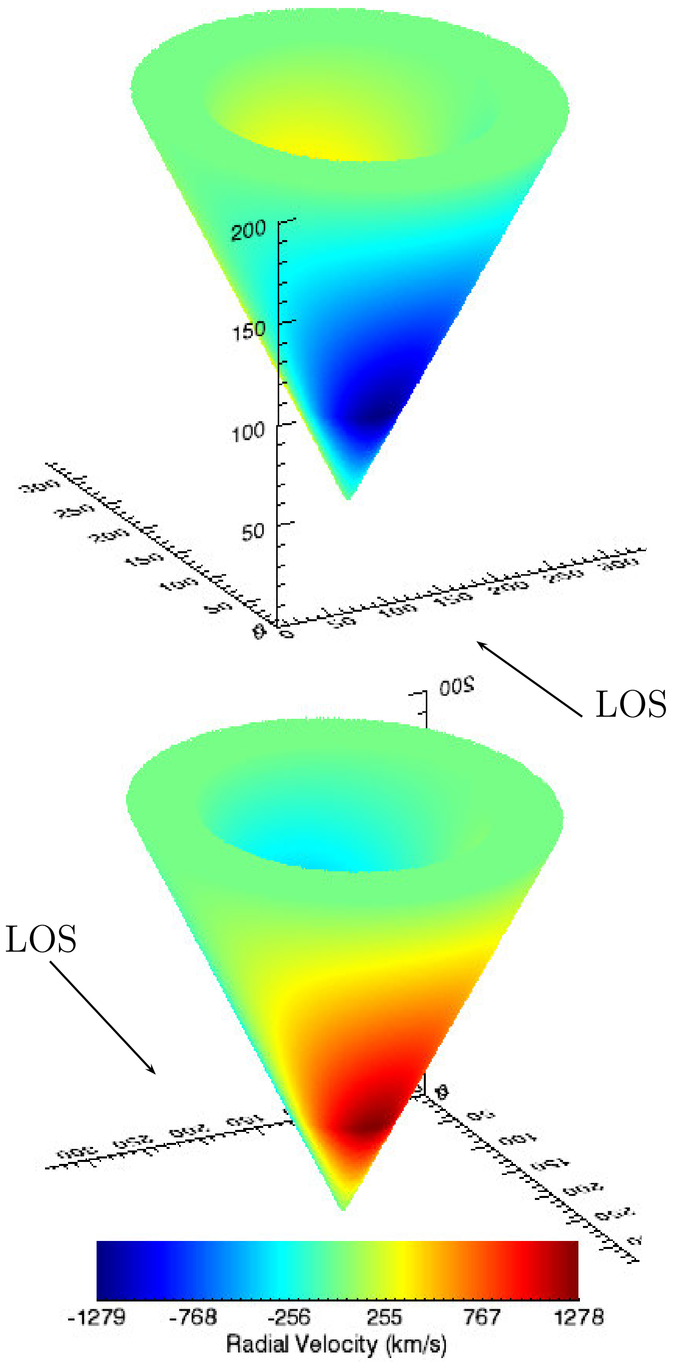

Figure 5.5: Diagram that shows the radial velocity field on the bicone as would have been measured by an observer looking at Figure 5.3. The front side of the bicone is shown here on top, the back side is shown below. The LOS is shown by the arrows.

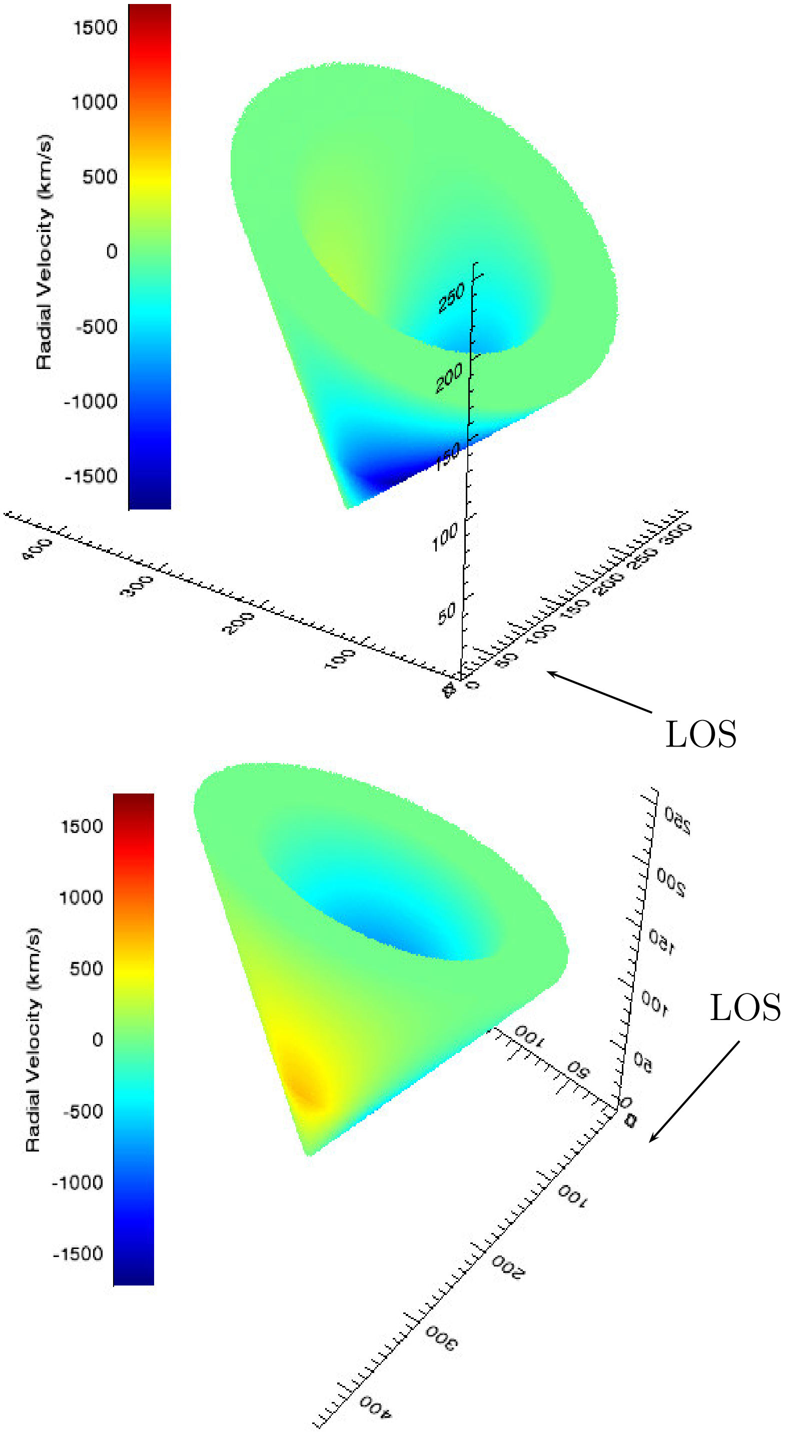

Figure 5.6: Figure showing the front (top) and back (bottom) half of a radial velocity field on an inclined bicone. Note that the blueshift has increased, while the redshift has decreased, in velocity.

of the model. The darkest blue and red colors in the model represent the turnover point, where the [O III] gas is at its maximum velocity, after which it decreases back to near systemic velocity. As expected, without any inclination, the velocities above and below the apex of the bicone are symmetrical. These velocities become asymmetrical if the bicone is inclined about the x-axis. To see this effect, a 30° inclined bicone is shown in Figure 5.8. Notice that the blueshifts are more predominant in the upper half of the bicone, while the redshifts are higher in the bottom. The situation reverses if one applies a negative inclination to the bicone.

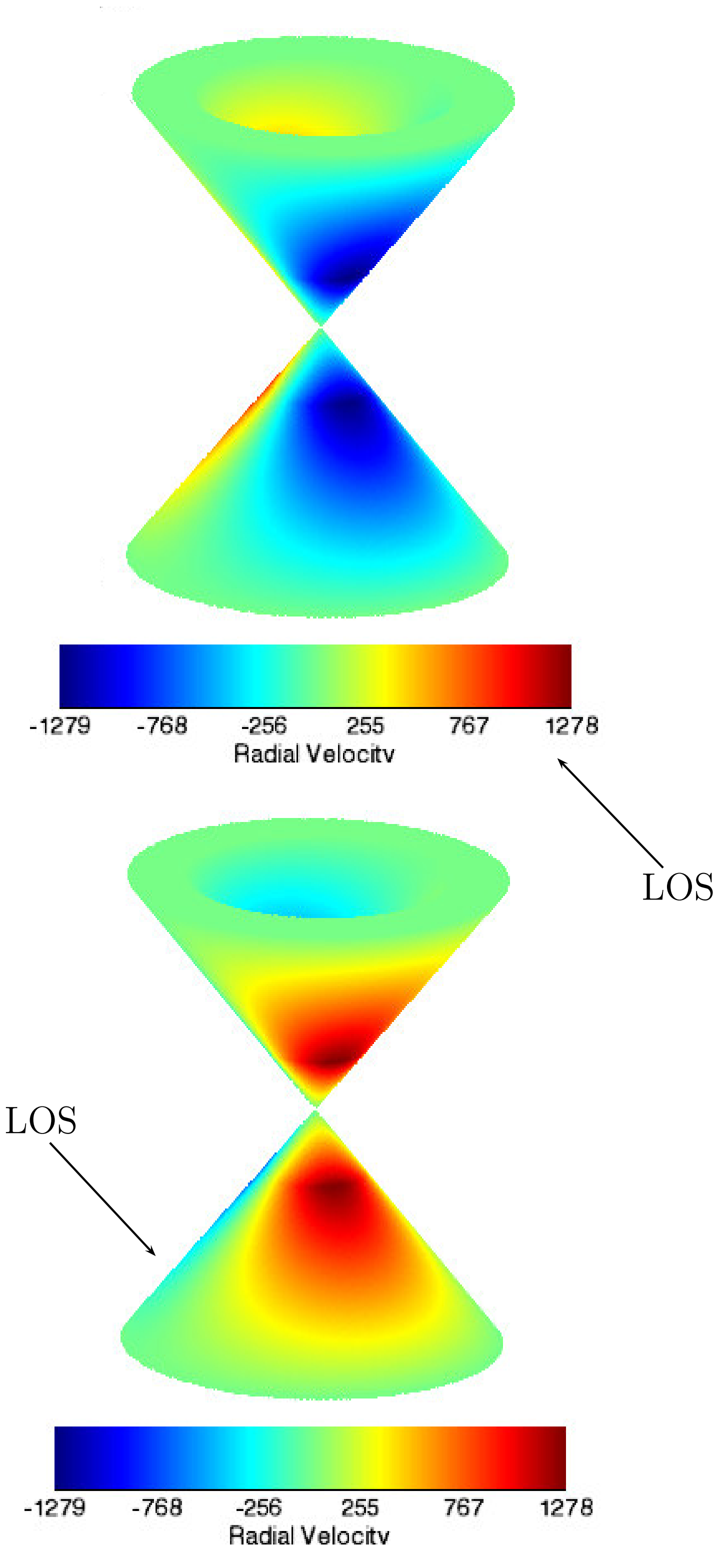

Figure 5.7: Diagram that shows the front (top) and back (bottom) half of a complete bicone model mapped with a radial velocity field.

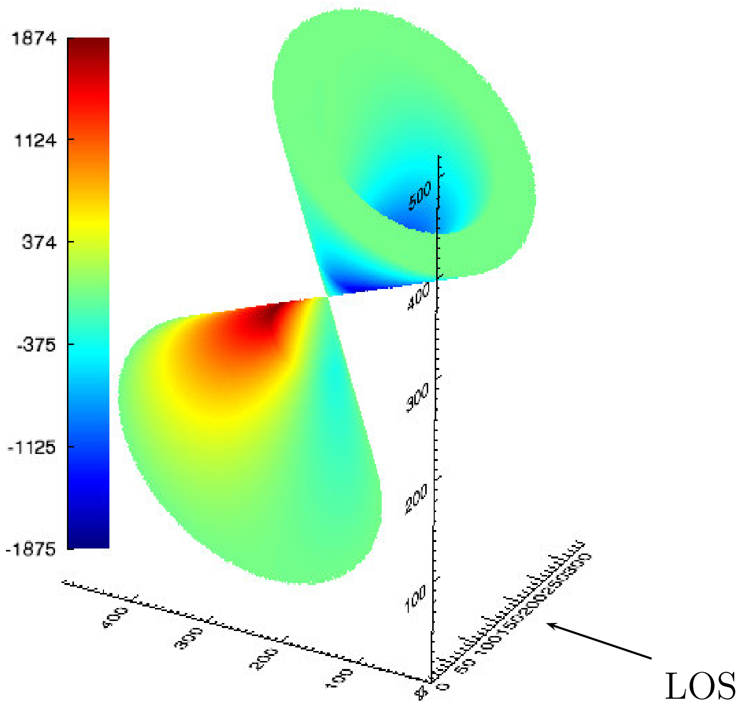

Figure 5.8: Diagram showing the radial velocity field on an inclined bicone from an angle off to the left.

5.4 Extraction of Slits

Before we can compare the models with data, we need to simulate what the velocities in the model slits would look like. Therefore we need to extract sample slits from the bicone models and make plots of their velocities against positions. The slit extraction procedure is outlined below. We start with a sample bicone model. Without loss of generality we will reuse the models generated with input parameters from Table 5.2. After the model is generated, we identify the slit positions, widths, and orientations in the sky and extract a sub-array from the bicone based on the slit criteria. The extracted array contains all the radial velocity values representative of that slit.

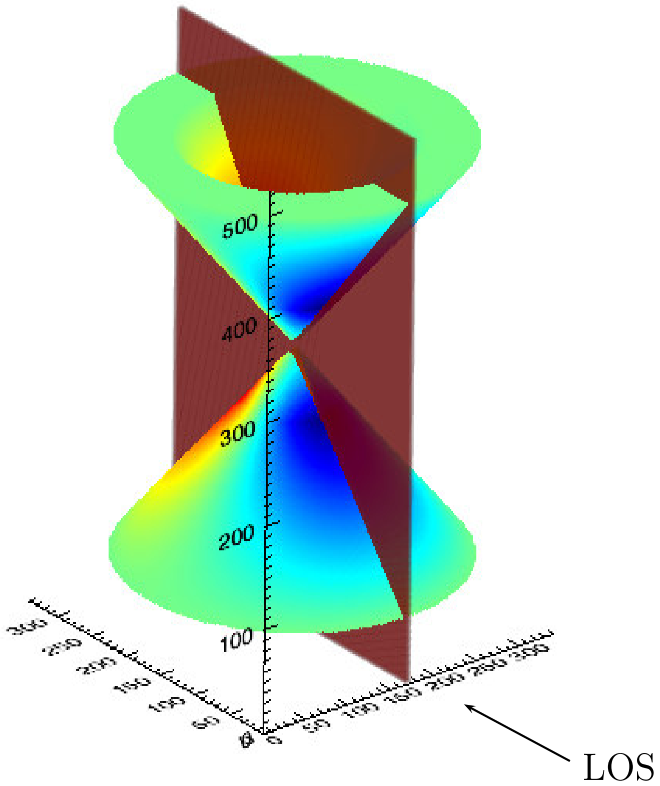

Figure 5.9: Figure showing a plane which represents a slit for extraction from the bicone. The plane is a few pixels wide, equivalent to a $0\farcs2$.

An example of a slit for extraction is shown in Figure 5.9. The light red plane represents a slit intercepting the bicone along the LOS and an observer would measure all velocities along that plane. The slit plane can be rotated to sample the model at any position angle with respect to the projected bicone axis. Here in Figure 5.9, we show a slit that is perfectly aligned with the bicone axis. The cross section of the bicone along the plane is extracted and shown in Figure 5.10. The radial velocities are shown in the usual red-blue colors that represent redshifts and blueshifts respectively, and an observer will be looking along the plane in the direction of the arrow. For comparison with the radial velocities from the data, we then sample

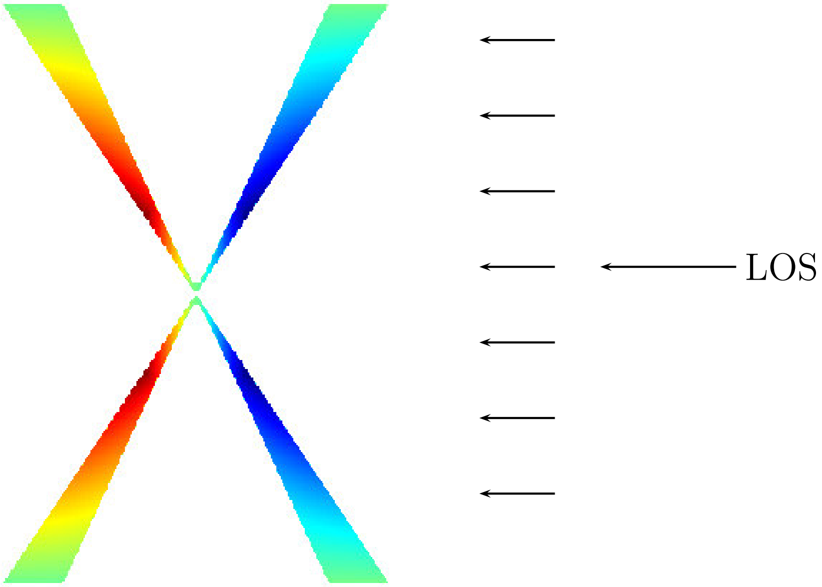

Figure 5.10: Figure showing the cross section of the plane which has been extracted from Figure 5.9. The colors represent the usual radial velocities. The minimum and maximum velocities were sampled along the slit at each point represented by the arrows. The sampling was done much more finely than shown by the arrows.

the radial velocities from the model slit of Figure 5.10 along the vertical direction as indicated by the arrows, and plot them against positions in arcseconds. The algorithm for this sampling is simple. Instead of referencing every point/velocity in this plane, we search instead for the minimum and maximum velocities along the LOS at each position along the vertical edge of the plane. The range of velocities are then plotted as an 'outline' as shown in the first panel in Figure 5.11. The second panel in the figure simply shows a filled-in shaded version of the first, a technique employed to save computing time. The turnover point in the velocities is represented by the 'knee' in the figure; compare to the deep red-blue colors in Figure 5.10. Note that the thickness of the shaded region is not the same as the thickness of the bicone, but is the range of

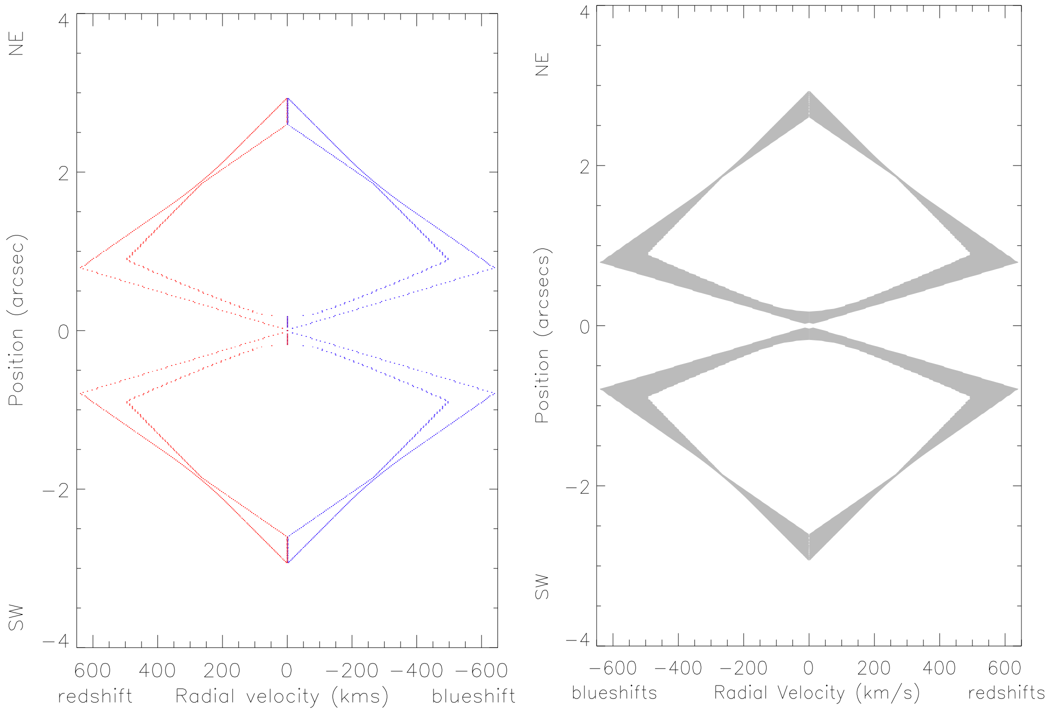

Figure 5.11: Left: Figure showing the plot of the extracted radial velocities from the previous figure. Only the minimum and maximum velocities per position is extracted and plotted. The observer is looking in from the blueshifted side.
Right: The same figure with the rest of the velocities filled to give the shaded effect. This trick saves a lot of computing time.

velocities along the LOS at each position. The model representing the final stage for comparison to the data is shown in Figure 5.12. The figure is the same as Figure 5.11 but with the axes swapped. This representation is following the convention used in previous kinematical modeling papers (Crenshaw et al. 2000; Crenshaw & Kraemer 2000b).

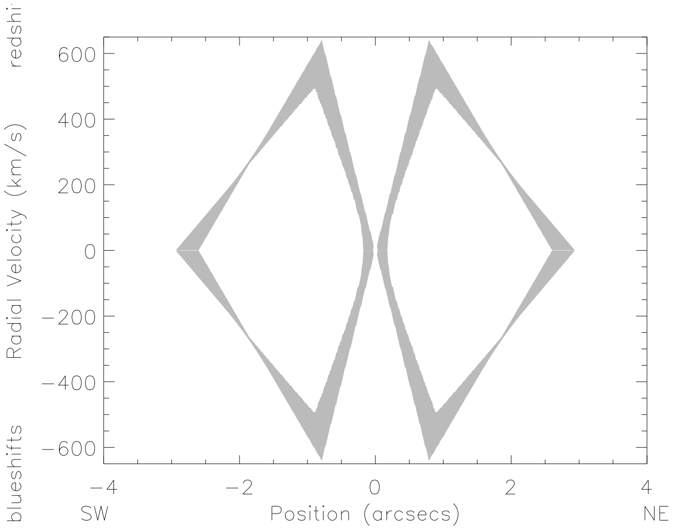

Figure 5.12: Figure showing the model radial velocity plot of the extracted radial velocities from Figure 5.10, similar to Figure 5.11 but with the axes reversed following the convention used in earlier papers. This is the final stage in the modeling whereby we compare data and model slits.

5.5 Fitting the Models to Data

Sections 5.3–5.4 show how we generate the models for comparison to the data. The entire process beginning from Figure 5.2 and finally ending at Figure 5.12 constitutes one run of the program with one parameter set. Table 5.2 for example represents one parameter set. In one run we can extract all the required slits for a particular galaxy and compare the radial velocities in them to the data simultaneously. The comparison at present is done by eye. There is no efficient statistical algorithm to compare the model and data. Several statistical tests have been tried in previous attempts with the results being unfruitful, because the statistical process generated too much wasted shaded regions. We will attempt no such test in this presentation. Starting input parameters to generate the models were taken from Crenshaw & Kraemer

Table 5.3: Parameters used to generate Figure 5.13.

Parameters	z_{max} (pc)	θ_{inner} (deg)	θ_{outer} (deg)	i_{axis} (deg)	PA_{axis} (deg)	v_{max} ($\mathrm{km\,s^{-1}}$)	r_{t} (pc)
Values	200	30	40	30	20	1000	200

(2000b) and Crenshaw et al. (2000) for NGC 1068 and NGC 4151 respectively. The starting input parameters by no means bias the final best-fit results, as the choice of input parameters are independent of final best-fit ones, as will be shown in the next chapter. For the actual comparison, we use the model radial velocity shaded plot as in Figure 5.12 and over-plot radial velocities identical to the ones shown in Figures 4.1–4.5 and Figures 4.9–4.16. An example of a data-model comparison is shown in Figure 5.13. This figure was generated with parameters shown in Table 5.3 and showed an example of a 'bad' fit for slit 1 of NGC 1068. Most of the data points lie outside the shaded region. In such a case, we reran the modeling process and tweaked the input parameters to improve the fit. The process of model fitting is summarized as follows:

1) The best fit model parameters are obtained when model slits enclose the maximum number of data points within a minimum shaded region and also match the trend (i.e. the increasing and decreasing velocity) in the data reasonably well.

2) Models should be consistent across all slits for a galaxy; i.e., input parameters cannot change across individual slits.

3) The shaded regions in the models should not necessarily contain all data points,

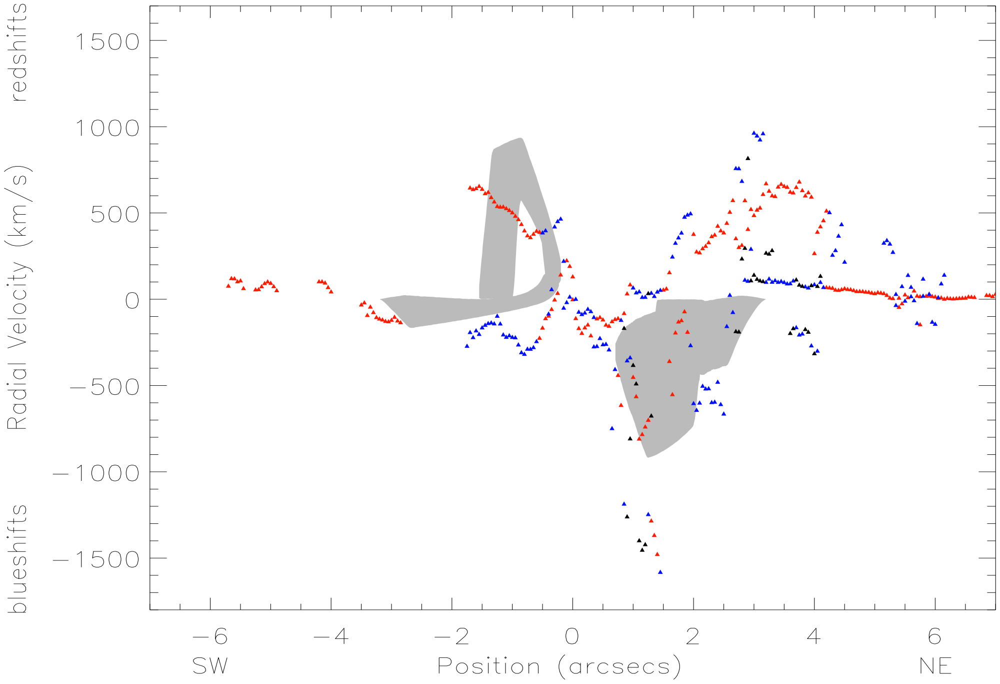

Figure 5.13: An example of a bad fit for slit 1 of NGC 1068. Most of the data points fall outside the shaded region. The colors represent the different flux components.

since some points are most likely not in the NLR and hence not in the bicone geometry. For example the points in Figure 5.13 at ∼ 0 $\mathrm{km\,s^{-1}}$ in radial velocity between ∼ 2–7″ are most likely emission from the host galactic disk.

4) If a fit is found to be unsuitable, the parameters are adjusted intuitively, and the entire process of generation, slit extraction, velocity sampling, and plotting undergoes repeated runs until we determine an acceptable match to the data.

5) Errors for a fit are not quantitatively defined, because the model fitting itself is not quantitatively defined. Therefore the errors are subjective and are defined as a range of values over which each input parameter can vary without significantly affecting the fit. The inclination of the bicone axis is the most important parameter

because it determines the Seyfert type. Because of this, we will vary the inclination, and make adjustments to the rest of the parameters to offset any resulting changes. If for example the best fit model parameter set is $[z_{\rm max}, \theta_{\rm inner}, \theta_{\rm outer}, i_{\rm axis}, PA_{\rm axis}, v_{\rm max}, r_{\rm t}]$, then if we can vary $i_{\rm axis}$ over the range [a, b], with the rest of the parameters changing while maintaining a good fit, then the error in $v_{\rm max}$ becomes $^{+(v_b - v_{\rm max})}_{-(v_{\rm max} - v_a)}$, where $[v_a, v_b]$ is the range in $v_{\rm max}$ that maintains a good fit. Similarly the error for $i_{\rm axis}$ would be $^{+(i_b - i_{\rm axis})}_{-(i_{\rm axis} - i_a)}$, where i_a and i_b are the extrema of i_{axis} while maintaining a good fit. Errors are developed for the rest of the parameters accordingly.

– 6 –

Kinematic Results

The process outlined in the previous chapter was applied to data for both NGC 4151 and NGC 1068. We did multiple program runs until we were satisfied with a best fit parameter set for each galaxy. The results for those fits are presented in this chapter. A brief outline of the model fitting process is shown to explain to the reader how the process works. We will vary some of the parameters and discuss reasons for changes, if any, to the input parameters until we converge upon the best-fit set. We will start with the center slit of NGC 4151, slit 1, and show how the choices of parameters in fitting slit 1 affect the outcome of the fit on a step by step basis. We start with an initial parameter set estimated from the observations, and vary the parameters appropriately with visual justification to show in the end that our best-fit set is not too different from that derived in the previous study of Crenshaw et al. (2000). After we have determined the best fit, we will vary the most important parameter, the inclination, and track the changes in the rest of the parameters to get a feel for the errors involved in the fitting (see §5.5). Finally, we will show for each galaxy the bicone model that has been generated with our best-fit parameters, and how it would appear in the sky to an observer. The procedure for fitting the data of NGC 1068 is identical to that for NGC 4151, so we will not show the fitting and error processes for

NGC 1068; only its final models will be shown together with the errors. The radio comparison is also done in this chapter and the results for both galaxies are presented here, following their model fitting.

6.1 Methodology

We will start the process of fitting the kinematics of NGC 4151 with an estimate of the initial input parameters (see Figure 5.1 for reference). The maximum height of the bicone can be estimated from the top plots of Figures 4.1–4.5. Emission-line gas can be seen up to $\pm \sim 6''$, which corresponds to $z_{max} = 372$ pc. Because the data in the northeast side are mostly redshifted, and the southwest side contains mostly blueshifted points, the inclination of the bicone is negative by our definition. Seyfert 1s are proposed to have large inclinations relative to the plane of the sky, so we start with $i_{axis} = -30^\circ$ for the inclination of the bicone axis. The data suggest a maximum absolute radial velocity of about 700 $\mathrm{km\,s^{-1}}$. In de-projection, this velocity will increase, but we will use $v_{max} = 700\ \mathrm{km\,s^{-1}}$ for now. The velocity appears to turn over close in, at about $1''$, which corresponds to $r_t = 62$ pc. Again this distance appears in projection to the observer, so it will necessarily be larger in the model. The outer opening angle cannot be much greater than the inclination, as this will introduce redshifts and blueshifts for both northeast and southwest parts of the bicone. For an initial guess, we do not have a good constraint on the inner opening angle, so we will start with a thick bicone, and if needed, decrease the inner opening angle to decrease the velocity spread. For now we use $\theta_{inner} = 10°$ and $\theta_{outer} = 40°$. The position angle of the bicone axis is constrained by the appearance of the [O III] image in Figure 2.1. This parameter, according to the figure, cannot vary by more than 5–7°, a conservative estimate, and it is initially taken to be the same value as the position angle of the slit. Therefore we will use $PA_{axis} = 57.8°$, which might change later. Clearly the data suggest a linear velocity law, so we will not model any other velocity laws now; however, to provide a comparative example, we will also show slit 1 fitted with the velocity law $\mathrm{v} = \mathrm{k}_1\sqrt{\mathrm{r}}$ and $\mathrm{v} = \mathrm{v}_{\mathrm{max}} - \mathrm{k}_2\sqrt{\mathrm{r} - \mathrm{r}_\mathrm{t}}$ $(\mathrm{r} \geq \mathrm{r}_\mathrm{t})$ for the accelerating and decelerating phases of the gas, respectively.

We will vary the input parameters until we obtain a good visual fit between the model (shaded regions) and the high and medium flux clouds (red and blue data points) since the low flux clouds may be affected by other processes. After running the model with the parameters from Table 6.1, the outcome is presented in Figure 6.1. In this figure, one can see extended shaded regions in the lower part of northeast quadrant, containing little data points. As suggested above, the outer opening angle should be less than the inclination. We can cut down some of the shaded regions in the figure by inclining the bicone axis more, to say −45°, or we can decrease the outer opening angle to say 25°. However the latter will limit us to a narrow range of opening angles. By increasing the inclination, we are also increasing the maximum redshifts and blueshifts in the northeast and southwest respectively, and therefore we can better fit the high veloc-

Table 6.1: Parameters used to generate the first run model for NGC 4151.

Parameters	z_{max} (pc)	θ_{inner} (deg)	θ_{outer} (deg)	i_{axis} (deg)	PA_{axis} (deg)	v_{max} ($\mathrm{km\,s^{-1}}$)	r_{t} (pc)
first run	372	10	40	−30	57.8	700	62

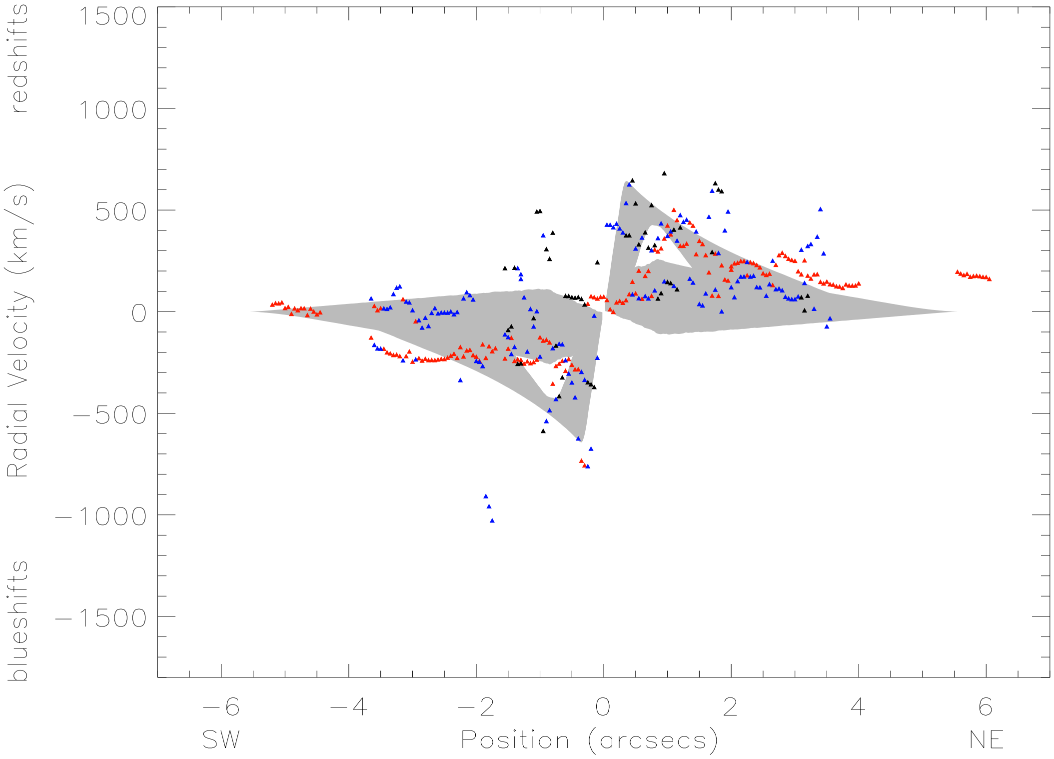

Figure 6.1: Figure showing the model outcome of the first run for slit 1 of NGC 4151, using the parameters from Table 6.1.

ity red points near (0,−800), (−3,−200), and (3,200). We try the two paths described above just to be thorough, decreasing the outer opening angle first. After the necessary adjustments, we use Table 6.2 to generate the model in Figure 6.2.

Table 6.2: Parameters used to generate the second run model for NGC 4151.

Parameters	$z_{\rm max}$ (pc)	$\theta_{\rm inner}$ (deg)	$\theta_{\rm outer}$ (deg)	$i_{\rm axis}$ (deg)	$PA_{\rm axis}$ (deg)	$v_{\rm max}$ ($\rm km\,s^{-1}$)	$r_{\rm t}$ (pc)
second run	372	10	25	–30	57.8	700	62

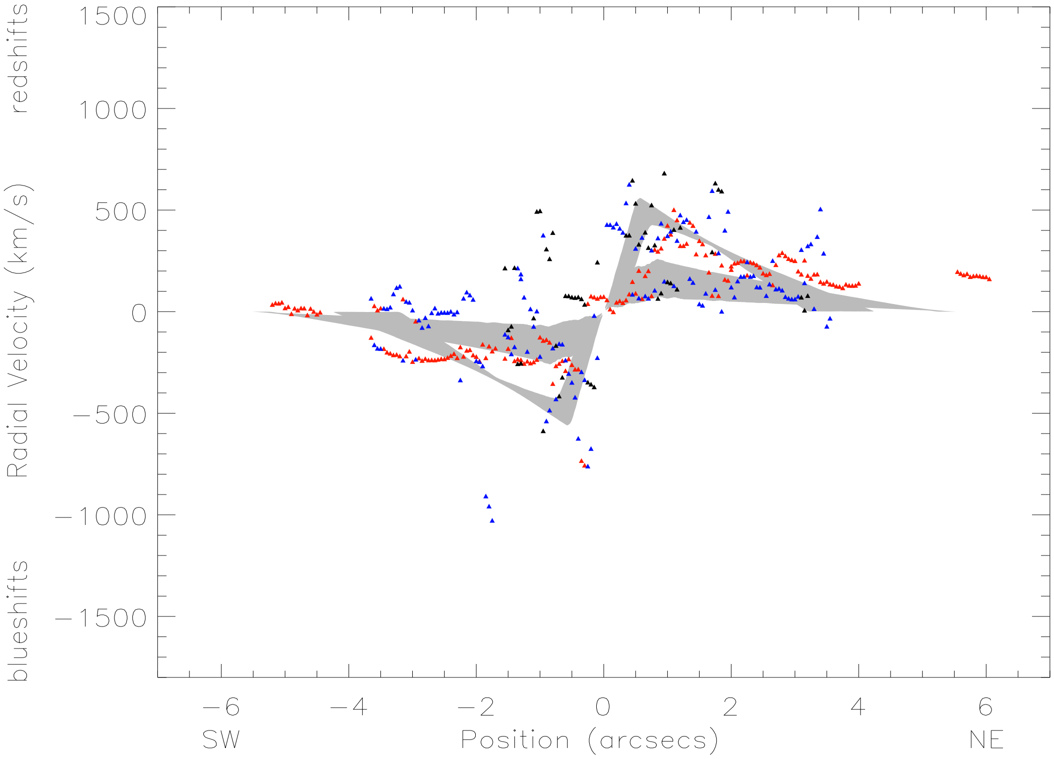

Figure 6.2: Figure showing the model outcome of the second run for slit 1 of NGC 4151, using the parameters from Table 6.2.

In Figure 6.2, the turnover point is difficult to fix, because on one hand, we need to decrease it to account for the high velocity points near ($-0\farcs5$, -800 $\rm km\,s^{-1}$). On the other hand we need to increase the turnover point to better match the turnover velocity near ($1''$, 500 $\rm km\,s^{-1}$). The only way to have turnover points differing is to incline the bicone, so that the front and back faces in each cone have different projections. So this branch in the modeling process is at a dead end. We move the outer opening angle back to 40°, and vary the inclination instead. Using parameters from Table 6.3, we generate the model shown in Figure 6.3.

Now if we increase the maximum extent of the bicone to $z_{max} = 400$ pc, we can possibly cover some of the red points near $-5''$, while also better fitting red points near $\pm\ 3''$. The turnover point needs to be a bit larger, $r_t = 80$ pc. Let us try increasing the maximum velocity a bit more to $v_{max} = 800\ \mathrm{km\,s^{-1}}$. Now decreasing the outer opening angle to say 35° will actually lift the shaded regions near $\pm\ 3''$, because this brings the outflow velocity vector closer to the LOS. Also let us decrease the total amount of shaded region by increasing the inner opening angle to $i_{inner} = 15°$. Table 6.4 lists the new adjusted parameters and the model rerun is shown in Figure 6.4.

If we incline the bicone too much in an effort to increase the maximum radial velocity, the maximum extent and turnover point of the bicone will eventually start to decrease in projection. At this stage, decreasing the thickness of the bicone by either increasing the inner opening angle or decreasing the outer opening angle will do us more harm than good. We still did not quite get all the red points near $\pm\ 3''$. We can try increasing the maximum extent of the bicone, the turnover point, and the inclination a bit. These all have the effect of ‘lifting’ the shaded regions near $\pm\ 3''$. The red points near $6''$ and $-5''$ are likely to be clouds in the galactic

Table 6.3: Parameters used to generate the third run model for NGC 4151.

Parameters	$z_{\rm max}$ (pc)	$\theta_{\rm inner}$ (deg)	$\theta_{\rm outer}$ (deg)	$i_{\rm axis}$ (deg)	$PA_{\rm axis}$ (deg)	$v_{\rm max}$ ($\rm km\,s^{-1}$)	$r_{\rm t}$ (pc)
third run	372	10	40	-45	57.8	700	62

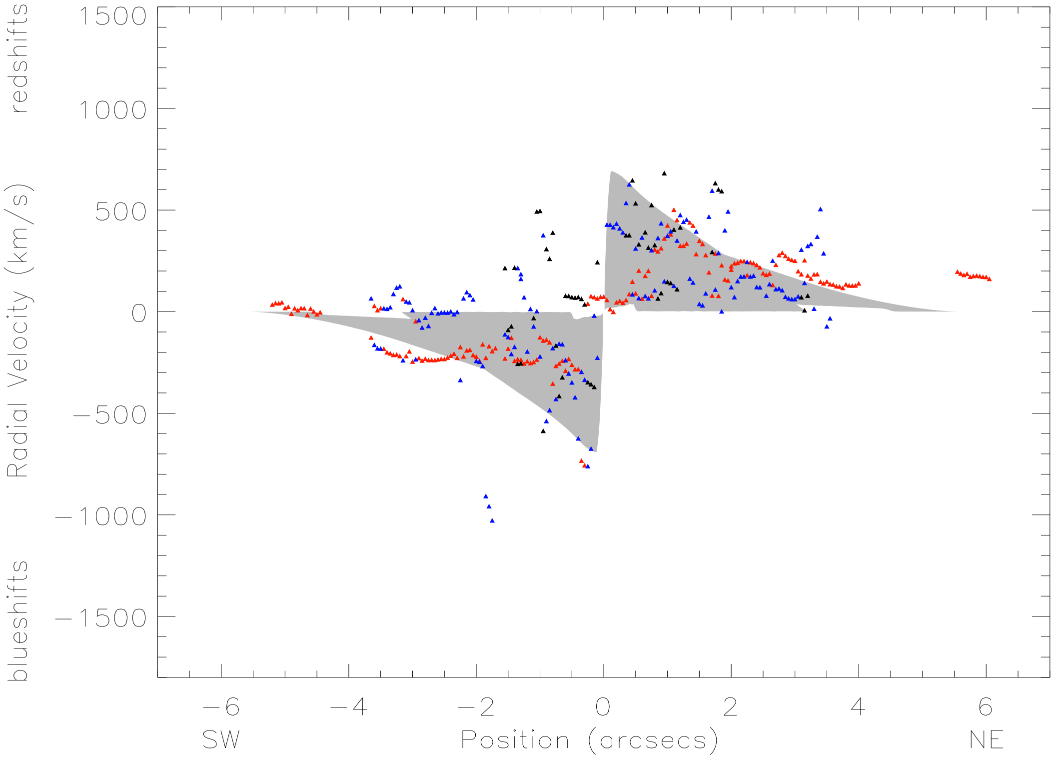

Figure 6.3: Figure showing the model outcome of the third run for slit 1 of NGC 4151, using the parameters from Table 6.3.

disk with normal rotational velocity, and are not fitted. In addition, we have ignored the low-flux (black) data points because they do not seem to fit the general outflow pattern in many cases. At this point the model fit is not bad given the simplicity of the assumptions, so it is now just a matter of ‘fine tuning’ the input parameters.

Table 6.4: Parameters used to generate the fourth run model for NGC 4151.

Parameters	$z_{\rm max}$ (pc)	$\theta_{\rm inner}$ (deg)	$\theta_{\rm outer}$ (deg)	$i_{\rm axis}$ (deg)	$PA_{\rm axis}$ (deg)	$v_{\rm max}$ ($\rm km\,s^{-1}$)	$r_{\rm t}$ (pc)
fourth run	400	15	35	-45	57.8	800	80

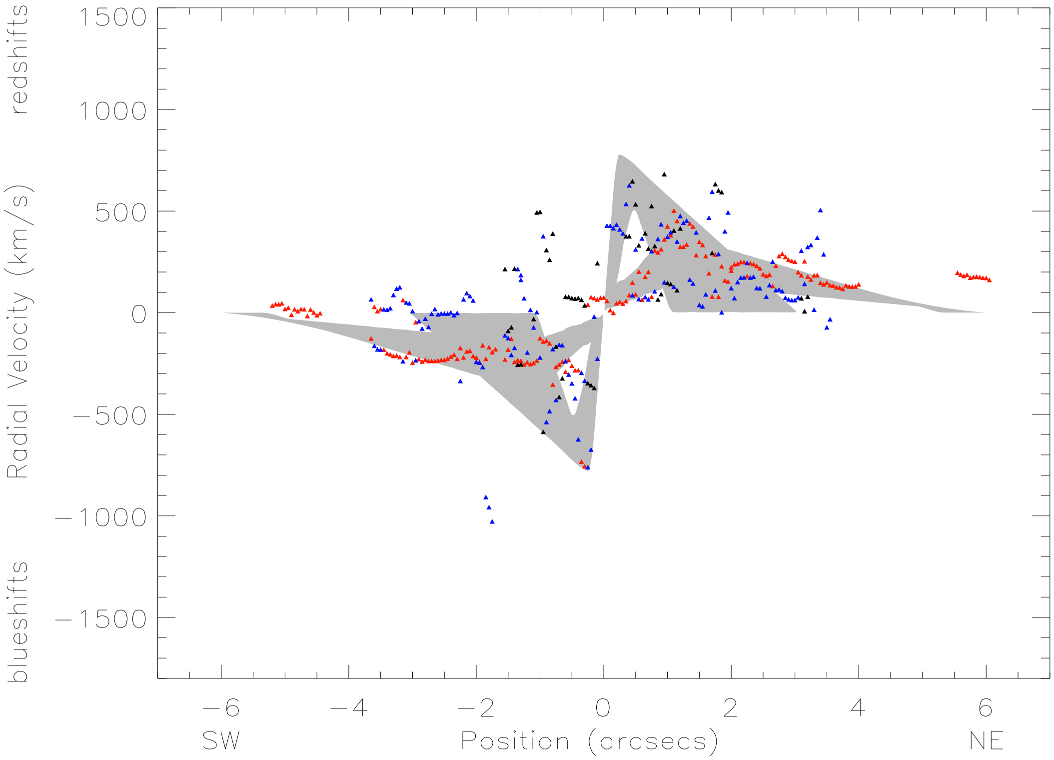

Figure 6.4: Figure showing the model outcome of the fourth run for slit 1 of NGC 4151, using the parameters from Table 6.4.

Table 6.5 has the adjusted input values and our best-fit model is shown in Figure 6.5.

Although we claim that this is our best fit model, the modeling process does not stop here. First we made sure that data from all the rest of the slits were consistent in this model. We did numerous runs with changing inclinations and other parameters

Table 6.5: Parameters used to generate the fifth run model for NGC 4151.

Parameters	z_{max} (pc)	θ_{inner} (deg)	θ_{outer} (deg)	i_{axis} (deg)	PA_{axis} (deg)	v_{max} ($\mathrm{km\,s^{-1}}$)	r_{t} (pc)
fifth run	450	15	35	-47	57.8	800	90

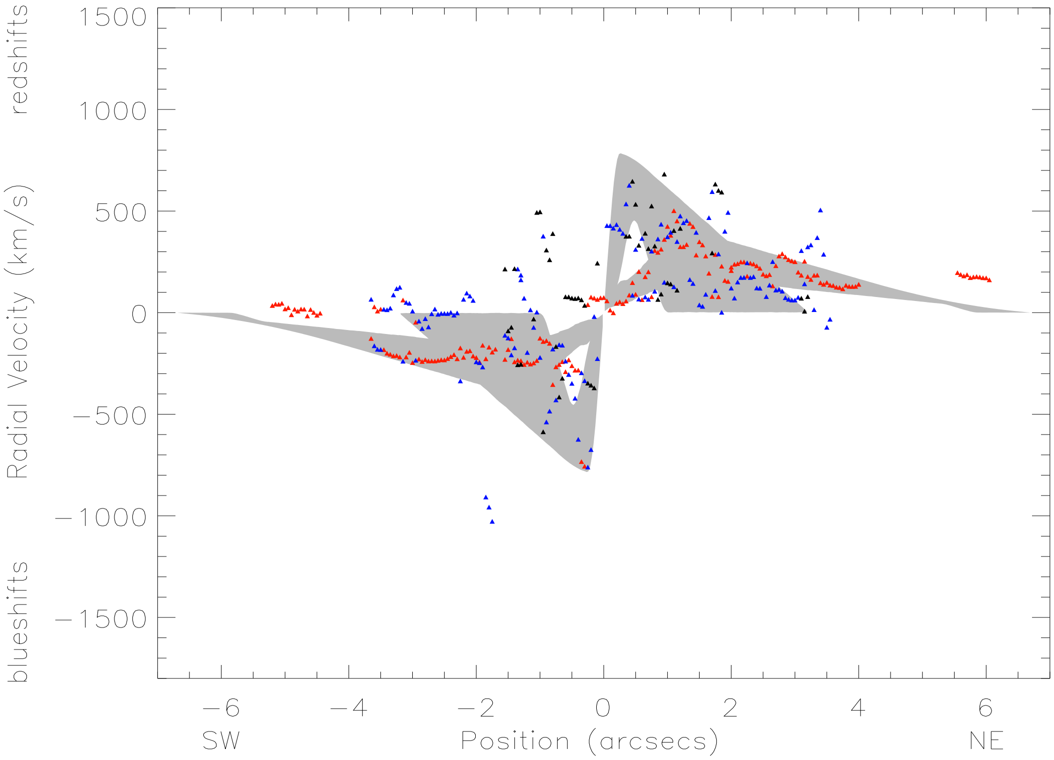

Figure 6.5: Figure showing the model outcome of the fifth run for slit 1 of NGC 4151, using the parameters from Table 6.5.

to get a handle on the errors in our best fit in Figure 6.5. We start the error evaluation process by varying the inclination as much as possible, while varying the rest of the parameters to maintain a good fit. Care must be taken not to enlarge the shaded regions too much, as a good fit is determined by the least shaded area covering the most data points. We found that for any inclination not in the range $-50 \leq i_{axis} \leq -40$, the rest of the parameters cannot compensate to result in a good fit. However, at $i_{axis} = -50°$ the parameters can be manipulated to give a reasonable fit to the data of slit 1. These parameters are shown in Table 6.6 and the resulting fit is shown in Figure 6.6. When the inclination varies to the other extreme to $i_{axis} = -40°$, the parameters all change to those in Table 6.7, with the resulting fit shown in Figure 6.7. Figure 6.6 represents the minimum shaded region for a fit, while Figure 6.7 represents a more conservative shading area for a fit, with our best-fit model lying somewhere in between. Therefore we claim that the errors for the parameters of the best-fit model are those outlined in Table 6.8, using the two extremum values from Tables 6.6 and 6.7. Note that one cannot simply choose any random parameter within their respective ranges and generate a good fit. One has to first choose an inclination within its range, then vary the rest of the parameters until a good fit (by eye) results.

Table 6.6: Parameters used to generate the error model with the largest possible inclination for NGC 4151.

Parameters	$z_{\rm max}$ (pc)	$\theta_{\rm inner}$ (deg)	$\theta_{\rm outer}$ (deg)	$i_{\rm axis}$ (deg)	$PA_{\rm axis}$ (deg)	$v_{\rm max}$ ($\rm km\,s^{-1}$)	$r_{\rm t}$ (pc)
error run	390	17	36	-50	57.8	800	130

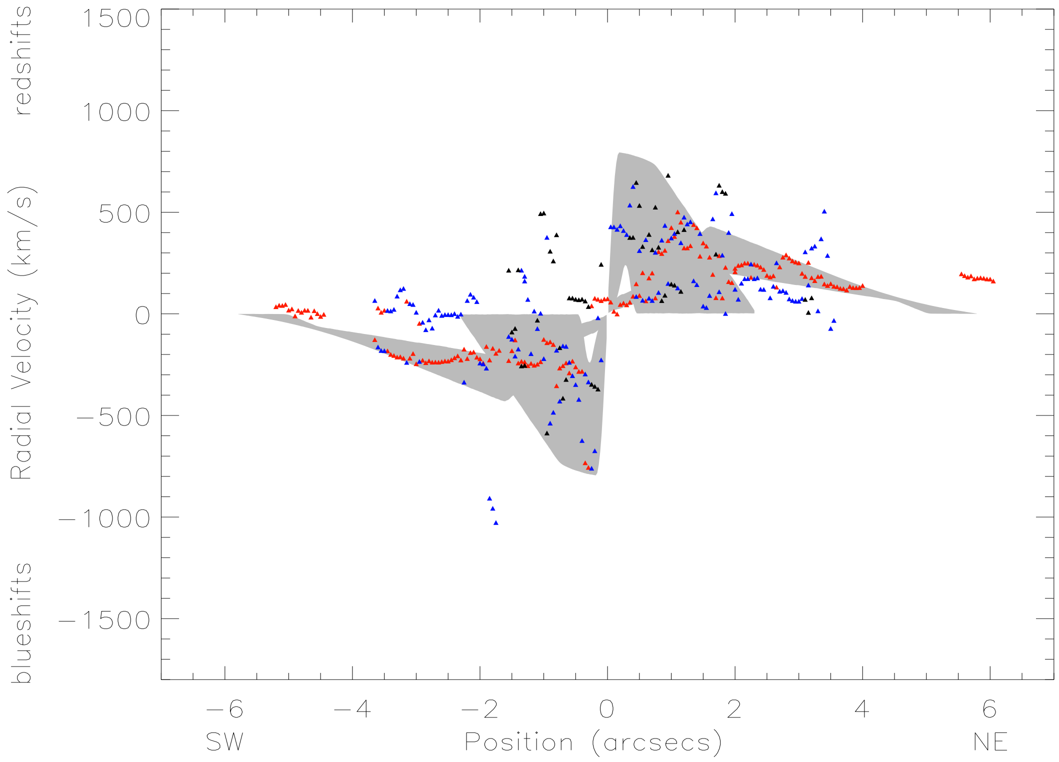

Figure 6.6: Figure showing the error model which include the largest possible inclination for slit 1 of NGC 4151, generated with parameters from Table 6.6.

Table 6.7: Parameters used to generate the error model with the smallest possible inclination for NGC 4151.

Parameters	$z_{\rm max}$ (pc)	$\theta_{\rm inner}$ (deg)	$\theta_{\rm outer}$ (deg)	$i_{\rm axis}$ (deg)	$PA_{\rm axis}$ (deg)	$v_{\rm max}$ ($\rm km\,s^{-1}$)	$r_{\rm t}$ (pc)
error run	450	13	33	−40	52	850	75

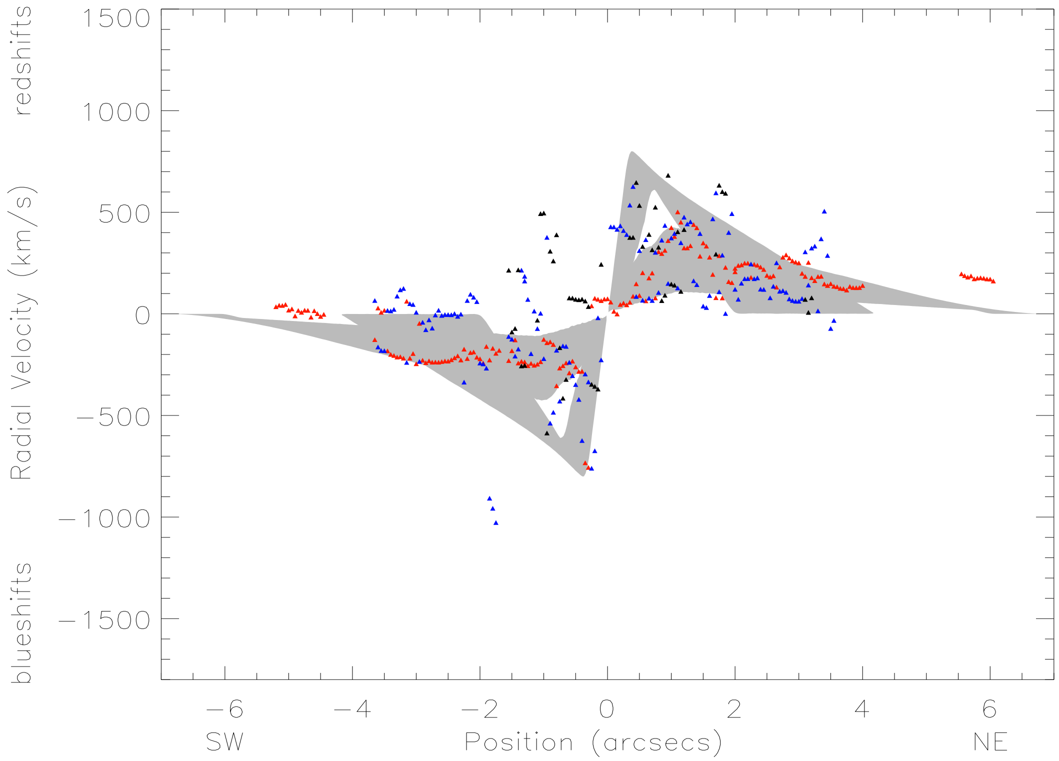

Figure 6.7: Figure showing the error model which include the smallest possible inclination for slit 1 of NGC 4151, generated with parameters from Table 6.7.

6.2 The Final Fits for NGC 4151

The final model parameters for NGC 4151 are presented in Table 6.8. For comparison, the fitting parameters from Crenshaw et al. (2000) are also presented. Following the deceleration trend of the knots in all five slits, the model suggests that the knots return to systemic velocity at a larger distance from the nucleus than previously found in the low-resolution STIS observation of Crenshaw et al. (2000). This work extends the bicone to a greater value than previously found, i.e. to 450 pc as opposed to 288 pc. The turnover point is much closer in, 96 pc compared to 162 pc, and our inner opening angle is only 15°, which makes our model less evacuated along the bicone axis, and thicker. The high luminosity knots seem to travel outward from the nucleus at lower inclination and were modeled previously as such; however, in this work we also incorporate medium and some low luminosity knots into the plots and hence our match suggests a larger inclination of −47°. The other parameters, i.e., the inner and outer opening angles, and the maximum velocity of the gas, show only minor differences between past and present work. The maximum velocity before turnover was increased to account for the fast moving medium luminosity clouds.

Table 6.8: Best-fit parameters and their errors for the NLR of NGC 4151.

Parameters	$z_{\rm max}$ (pc)	$\theta_{\rm inner}$ (deg)	$\theta_{\rm outer}$ (deg)	$i_{\rm axis}$ (deg)	$PA_{\rm axis}$ (deg)	$v_{\rm max}$ ($\rm km\,s^{-1}$)	$r_{\rm t}$ (pc)
This paper	450^{+10}_{-60}	15^{+2}_{-2}	35^{+1}_{-2}	-47^{+7}_{-3}	$57.8^{+5.8}_{-5.8}$	800^{+50}_{-10}	96^{+34}_{-21}
Previous paper[a]	288	20	36	−40	57.8	750	162

[a] Crenshaw et al. (2000)

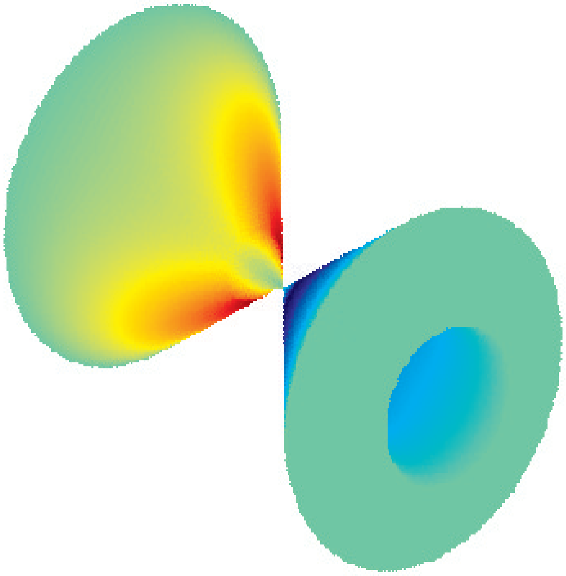

Figure 6.8: Figure showing the model orientation of the NLR of NGC 4151 as seen in the sky by an observer. The back side of the NE cone cannot be seen in this depiction. Deep red represents a radial velocity of 545 $\mathrm{km\,s^{-1}}$ and dark purple represents a radial velocity of 792 $\mathrm{km\,s^{-1}}$.

These clouds are accelerated to high speeds close to the nucleus and therefore play a major role in modeling the turnover point, which we found to be 96 pc. If we had used only the bright clouds (red points), then our turnover point would have been larger and similar to that of Crenshaw et al. (2000). A model representation of the NLR of NGC 4151 as seen in the sky by an observer is shown in Figure 6.8.

Figures 6.9–6.11 show all five slits with the models in shaded gray and the observed data points in colors. Zero position in slit 1 corresponds to the nucleus, while zero position in all other slits corresponds to a position in the center of the slit that is offset from the nucleus in the dispersion direction. These radial velocity plots show that the models match the bright and medium-flux clouds well. The northeast side is mostly redshifted, and the southwest side is mostly blueshifted, except for some low luminosity clouds (black points), and a few medium luminosity clouds (blue points), which exhibit an unusual flow pattern. These rogue clouds are shown by the arrows in the figures and we present an explanation for such odd flow pattern in a later section in this chapter. The second panel in Figure 6.9 shows a fit for slit 1 with the $\sqrt{r}$ *law* ($\mathrm{v = k_1\sqrt{r}}$ and $\mathrm{v = v_{max} - k_2\sqrt{r - r_t}}$). A closer inspection between the two panels of Figure 6.9 shows some differences in the fit, with the top panel being better.

The main points to note here concerning the model fits are summarized as follows. The model was intended to match the general trend of the data and not intended to be a perfect fit. The model fits the data well at least for slits 1, 2, and 4 (slits close to the SMBH). Slits 3 and 5 (slits away from the SMBH; see Figure 2.1) are not fit as well. There are points at $\sim 0''$ that are not picked up by the shaded region of our model. Its hard to tell if these points are in the host galactic disk or not, since they are not only low-velocity but also bright. Their fluxes and FWHM do not indicate any obvious feature to distinguish them from the rest of the NLR clouds. In general, the model suffers from the lack of velocity points near the SMBH due to the sharp apex of the bicone. This is because our model adheres to the current understanding of the unification theory; radiation is being squeezed from a point and escapes only in a preferred direction illuminating clouds in a biconical formation. This does not seem to be the case however, as the data in slits 3 and 5 show; there are points within $\pm\ 0''.5$ of the nucleus in these offset slits that are not covered by the model. This is a problem that is not specific to our models, because extended emission outside of the bicone can easily be seen in the direct [O III] image in Figure 2.1 (see also Collins et al. 2005; Schmitt et al. 2006).

The model inclination of −47° with an outer opening angle of 35° puts the entire bicone out of the plane of the sky, with the southwest side towards the observer and the northeast side away from the observer. Since the clouds are in outflow, this orientation forbids redshift in the bottom (southwest) and blueshifts in the top (northeast). However there are some low-flux data points shown by the arrows in Figures 6.9–6.11 that flow against the prediction of the model. We present arguments in the next section that these clouds may be in 'backflow', i.e., flowing along the biconical geometry but in the opposite direction as the outflowing clouds.

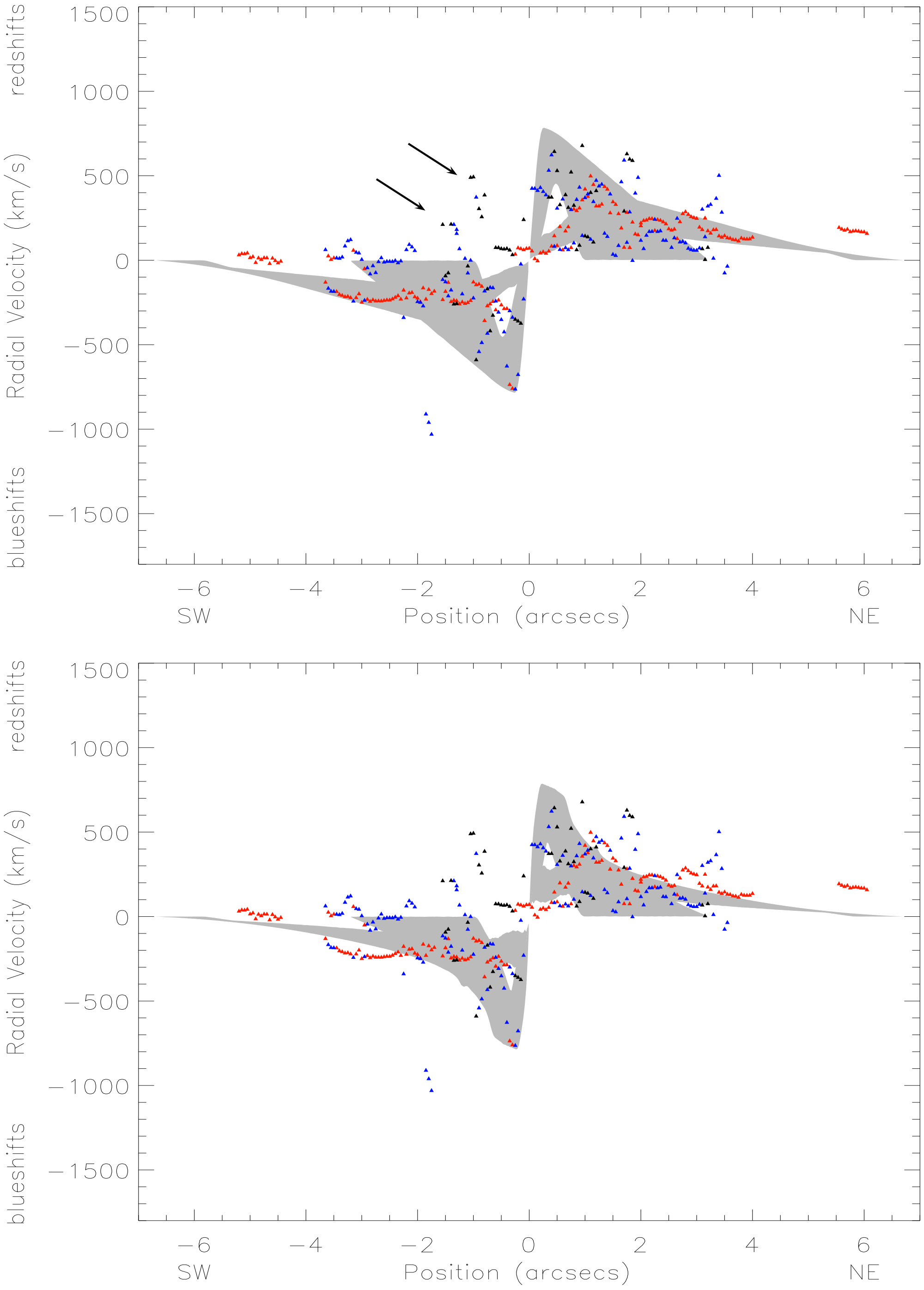

Figure 6.9: Top: The best-fit model for slit 1 of NGC 4151. The redshifted points in the southwest (arrows) are not fit by the model and possibly represent a different flow pattern. The red points near 6″ are likely clouds in the host galaxy.
Bottom: The best-fit model for slit 1 of NGC 4151, but with a velocity law of the form $\mathrm{v} = \mathrm{k}_1\sqrt{\mathrm{r}}$ up to the turnover point, and $\mathrm{v} = \mathrm{v}_{\mathrm{max}} - \mathrm{k}_2\sqrt{\mathrm{r} - \mathrm{r}_{\mathrm{t}}}$ after the turnover point.

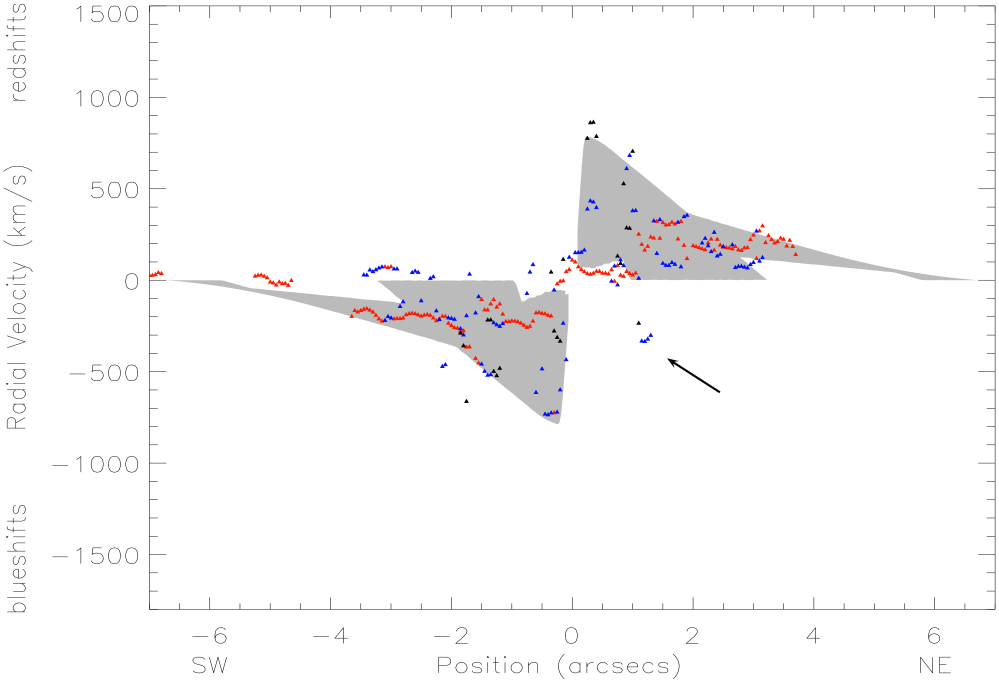

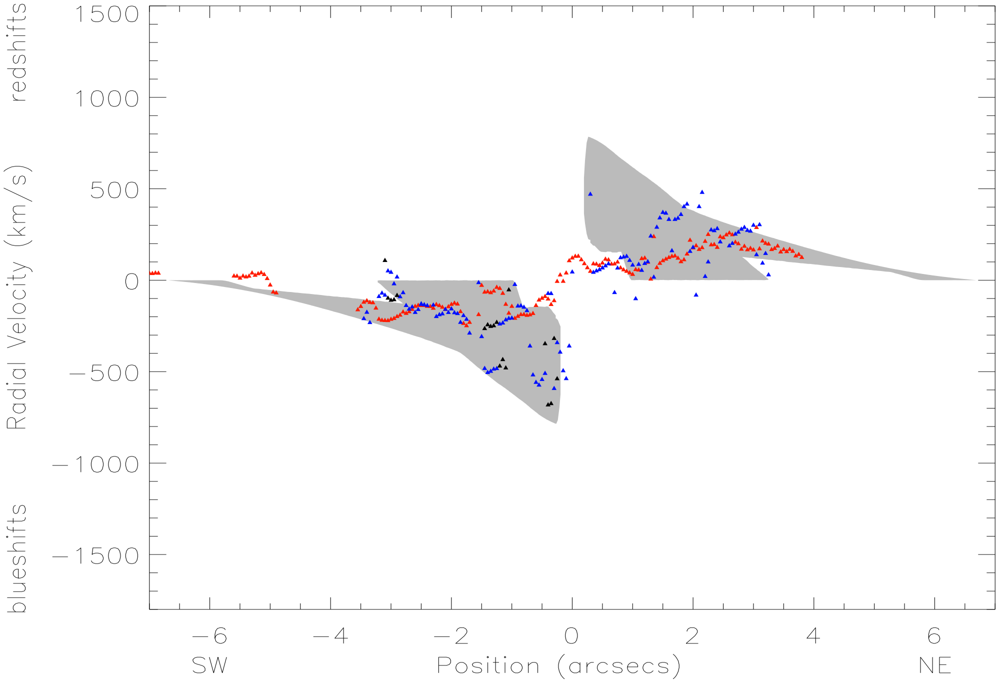

Figure 6.10: Top: The best-fit model for slit 2 of NGC 4151. As in slit 1 there are some blueshifted points in the unshaded regions at ∼ 1″.5 that were not fit (shown by the arrow).
Bottom: Figure showing the best-fit model for slit 3 of NGC 4151. As the slits move further away from the nucleus, the fit is poorer in the center, due to the sharp apex of the model bicone.

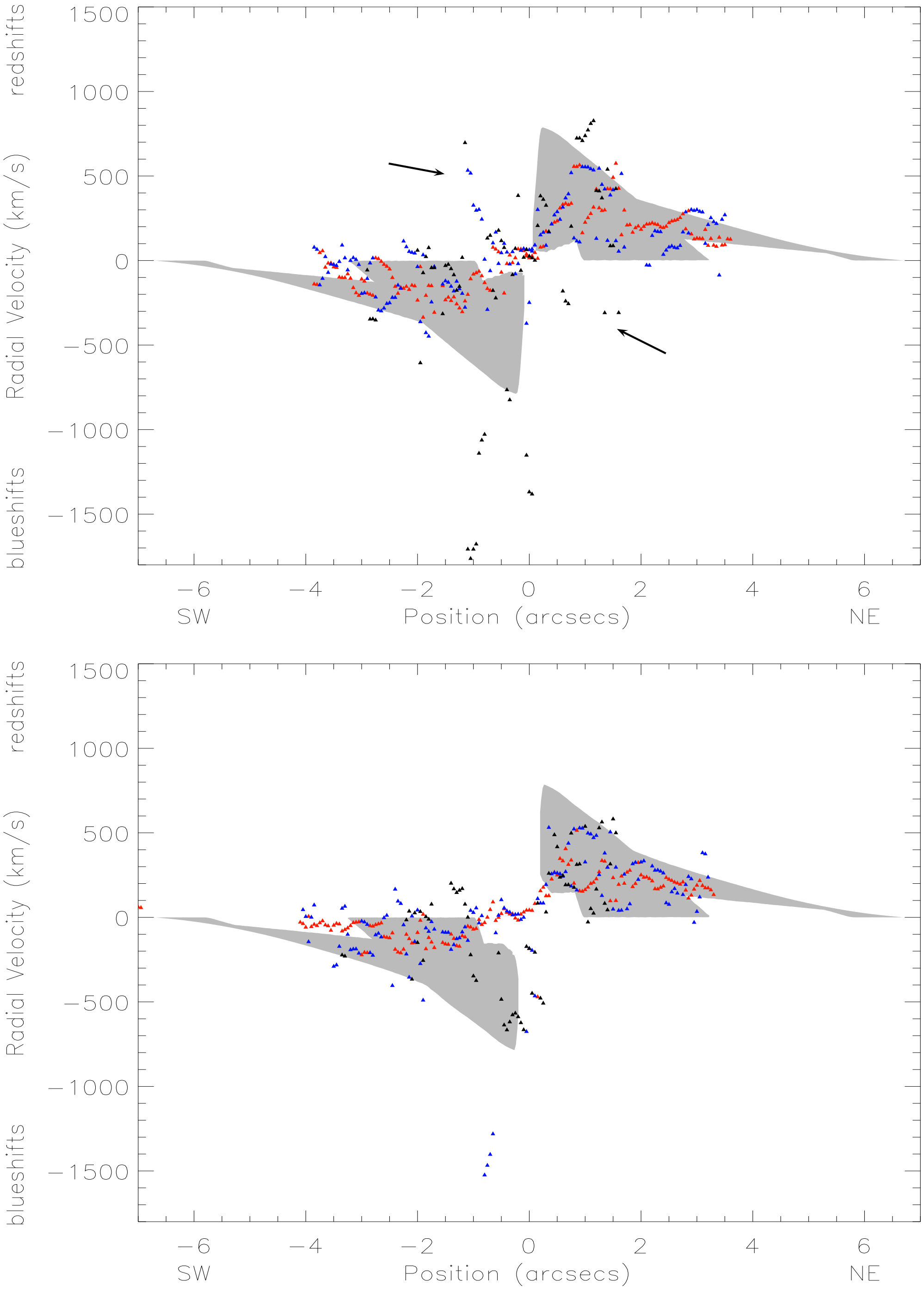

Figure 6.11: Top: The best-fit model for slit 4 of NGC 4151. The arrows show some clouds flowing in a different orientation than the model.
Bottom: Figure showing the best-fit model for slit 5 of NGC 4151. Points near the center of the slit are not fit very well, a shortfall of the apex model.

6.3 Backflow in NGC 4151

A possible scenario to explain the fainter clouds that do not fit the biconical outflow pattern, such as those shown by the arrows in Figures 6.9-6.11 is that of 'backflow' due to shocks caused by the outflowing bright clouds impacting on an ambient medium. The low-luminosity clouds could be flowing back along the bicone edges with a velocity that is proportional to the outflow velocity; that is, the higher the outflow velocity, the higher the backflow velocity. The top arrow in Figure 6.9 points to rogue clouds that might have resulted from fast outflowing gas in the near side of the southwest bicone, with the low-emission gas moving in the opposite direction of the general outflow, leaving a trail of clouds in the direction of the nucleus; see location b in Figure 6.12. The same argument holds for rogue clouds indicated by the bottom arrow in Figure 6.9. These backflows are likely a result of fast moving clouds outflowing in the far side of the bicone (d in Figure 6.12), since the velocities and positions there agree with those of the rogue clouds. The rogue clouds indicated by the arrow in Figure 6.10 can be geometrically associated with backflows resulting from outflowing clouds in the near side of the northeast bicone, where their positions and velocities coincide with those of the bright clouds at that location (a in Figure 6.12). Rogue clouds indicated by the bottom arrow in Figure 6.11 can also be explained by backflow caused by outflowing clouds in the near side of the northeast bicone because the velocities and positions of the rogue clouds are similar to those of the brighter clouds in that region. The argument loses some credibility, however, when we consider rogue

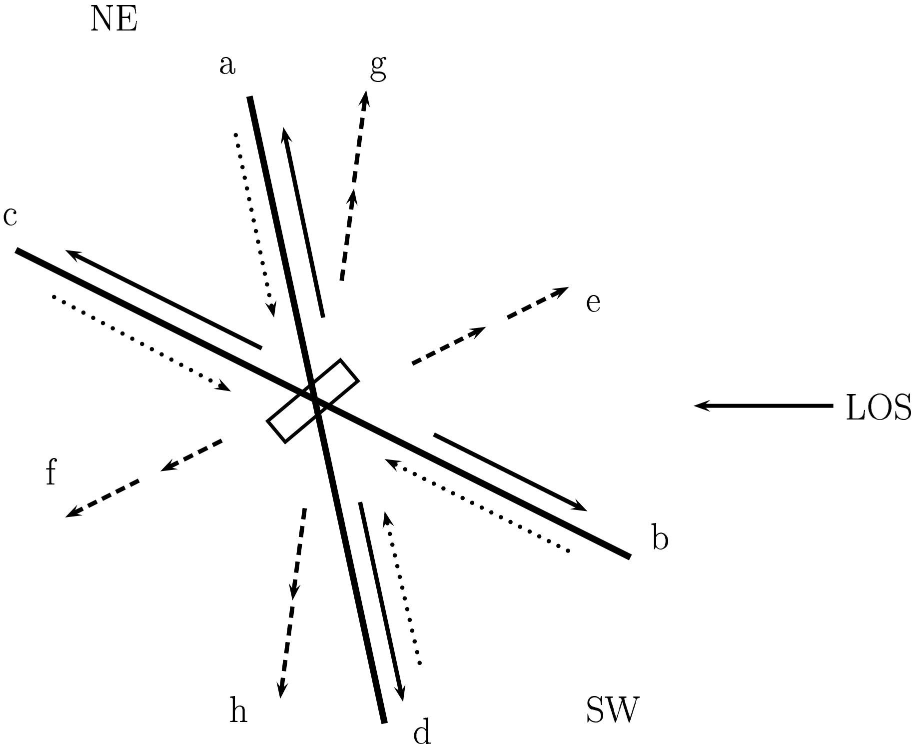

Figure 6.12: Possible flow patterns for the faint rogue clouds that do not fit our model. The solid lines are the bicone edges. The solid arrows represent normal outflow corresponding to the high- and medium-flux clouds, and the dotted and dashed arrows represent possible flow patterns for the rogue clouds. Note the line of sight (LOS) to the right, and bottom of the bicone tilted out of the plane of the sky, corresponding to 47° in our model. The box in the middle of the figure represents the torus. The largest opening angle is drawn here (cartoon not drawn to scale).

clouds pointed at by the top arrow of Figure 6.11. These high-velocity clouds seem to be geometrically associated with outflows from the near side of the southwest bicone (b in Figure 6.12), but there are no bright clouds in this region to contribute to the backflow behavior.

There is another possibility that can explain the unusual flow pattern of all the rogue clouds. The argument is that the rogue clouds are moving in an entirely different geometry, flowing away from the nucleus as shown in Figure 6.12 (locations e, f, g, and h). Note that backflows from a, b, c, and d are equivalent to projected velocities from locations g, f, e, and h, respectively. This geometric equivalent of the backflows is but one of the many ways in which the projected velocities agree, because the geometry could be positioned anywhere along the line of sight to yield the same projected velocities. We adopt the geometry whereby clouds emanate from the central nucleus, as this scenario seems to be the most plausible one. If that is the case, then the flows from locations e and f would be at a rather large angle (near 90°) with respect to the bicone axis. This would suggest that clouds are flowing close to the plane of the torus, which might explain their low fluxes. The problem with this scenario is that there are no means for the clouds to be ionized unless radiation is coming from holes in the torus. It is also not clear how these clouds would be accelerated without radiation or winds from the nucleus, as these clouds do indeed attain high velocities.

We prefer the first scenario, because the rogue clouds appear mostly at the positions of the turnover velocities of the bright clouds. This supports the idea that the bright clouds may be plunging into an ambient medium at the turnover point, causing the clouds to slow down and eventually return to ambient velocity, and at the same time producing the faint clouds through backflow.

6.4 The Final Fits for NGC 1068

Our fits to the kinematic data of NGC 1068 followed a similar procedure to that for NGC 4151. With our best fit parameters listed in Table 6.9, we generate a 3D representation of the NLR of NGC 1068 as it would appear in the sky to an observer, which is shown in Figure 6.13. Figures 6.14–6.17 show the best fit comparison plots for all eight slits. The model envelopes are in shaded gray and the data points in colors, and both data and model envelopes are plotted with positions relative to the center of the respective slits. Slits 5 and 6 cover the same region except for an offset along the slit. They were taken one year apart and show almost identical data points. The difference is seen mostly in the low and medium flux clouds, which can be attributed to our separation criteria for distinguishing the different kinematic components. These models were also done with our best fit parameters listed in Table 6.9. Previous model parameters found in Crenshaw & Kraemer (2000b) are also listed in that table for comparison. Our results are consistent with the earlier ones, except that in the newer results, we increase the maximum extent of the bicone and the maximum velocity at turnover point, consistent with the results of Cecil et al. (2002). In addition, the position angle of the bicone was changed from the previously accepted value of 15° (Evans et al. 1991) to 30°, consistent with values derived by Bergeron et al. (1989) and Pogge (1988). This change gave a coherent fit across all eight slits. The present bicone is thicker as well, as indicated by the smaller θ_{inner}.

Table 6.9: Parameters used to generate the best-fit models for NGC 1068, with the errors shown for each parameter.

Parameters	$z_{\rm max}$ (pc)	$\theta_{\rm inner}$ (deg)	$\theta_{\rm outer}$ (deg)	$i_{\rm axis}$ (deg)	$PA_{\rm axis}$ (deg)	$v_{\rm max}$ ($\rm km\,s^{-1}$)	$r_{\rm t}$ (pc)
This paper	460^{+30}_{-30}	19^{+3}_{-1}	40^{+2}_{-2}	5^{+3}_{-2}	30^{+5}_{-1}	2200^{+50}_{-200}	140^{+10}_{-20}
Previous paper[a]	306	26	40	5	15	1300	137

[a] Crenshaw & Kraemer (2000b)

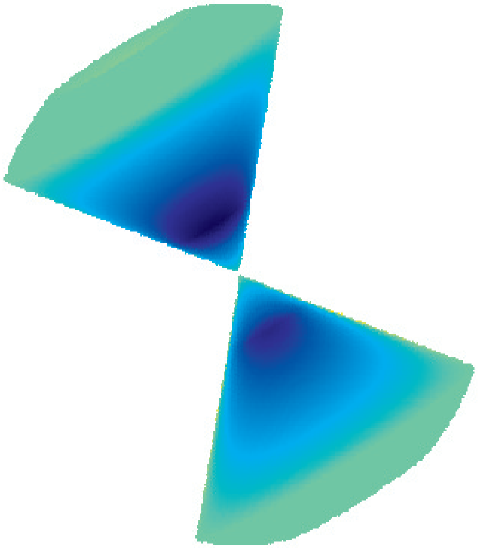

Figure 6.13: The kinematic model orientation of the NLR of NGC 1068 as seen in the sky by an observer. Deep purple represents a maximum blueshifted radial velocity of 1555 $\rm km\,s^{-1}$. The redshifted back face is not seen in this representation.

The fit to the bright and most medium flux clouds is good. Note that the long line of red points near zero velocity in the northeast are points in the host galaxy (in the ENLR), which were not fitted. These points are distinguished from the NLR clouds by their low FWHM as seen in Figures 4.9–4.16. These points are actually low absolute flux points detected with only one kinematic component per location. Because of this, our separation routine assigned the color red to these points, but clearly these points are not in any outflow pattern. There are also some faint clouds outside of the shaded region (hence outside of the bicone geometry) around $0''$ in all slits that are not fit. These again reflect the fact that the observed NLR is not a sharp bicone, as can be seen in the direct [O III] image in Figure 2.7. We present a possible explanation for these points in terms of the radio jet in the next section.

The trend in all slits is that the points accelerate then decelerate in approximately a linear fashion. The sparsity of points enclosed by, but not in, the shaded regions of Figures 6.14–6.17 is consistent with a hollow interior along the axis of the bicone. Slit 8 does not show this hollowed out area as do the rest of the slits, because it is placed at a position angle of 10°, at opposed to 38° for the rest of the slits. This slit lies along one edge of the bicone, therefore intercepting velocities continuously along the LOS. For all the slits, the data follow the models quite well in the northeast, even for slit 8, where the data seem to agree with the filled shaded configuration reasonably well.

The lack of data points in the southwest can be explained by the shielding of the bicone by the host galaxy, as shown in Figure 6.18. Our model predicts that the outer half-opening-angle of the bicone is 40°, with the northeast side inclined at 5° out of the plane of the sky. This decreases the opening angle of the southwest side relative to the plane of the sky by 5 degrees. The host galaxy is inclined by 40°, with the southwest side closer to us (de Vaucouleurs et al. 1991), thus effectively placing more material between us and the southwest side of the bicone. Both the northeast far side, and the southwest near side of the bicone are flowing in/near the galactic plane. Such interactions between the gases in the host galaxies and the ionizing radiation of the NLR bicones are responsible for carving out the morphology of the ENLR.

The main points to note here concerning the model fits are as follows:

(1) The near ‘continuous’ stretch of points at ~ 0 velocity in the northeast of slits 1–7 are points in the galactic disk as indicated by their low velocity and FWHM. There are also broken up chunks of galactic disk points $\leq -2''$ in the southwest in slits 1–3 and 5–8. We did not see any such points in Slit 4.

(2) The data points at position $\sim 0''$ are examples of the limitation of the model. The reason they are not fit is because our model was based on the constriction of radiation by a dense obscuring material, which resulted in the bicone tapering to an apex in the middle as shown in Figure 6.13. The NLRs of Seyferts do not appear to fit this simple picture.

(3) The lack of data in the southwest is probably due to extinction by dust in the host galaxy, similar to the case for Mrk 3 (Collins et al. 2005). However, this effect is not seen in NGC 4151 (Figure 6.19). According to the figure, data from the northeast side of the bicone should have been somewhat suppressed. However the observations show that the data points along this region are just as bright as the data from the southwest side, indicating the possibility of less dust, and hence less extinction in the host galaxy, consistent with the claim by Kraemer et al. (2000).

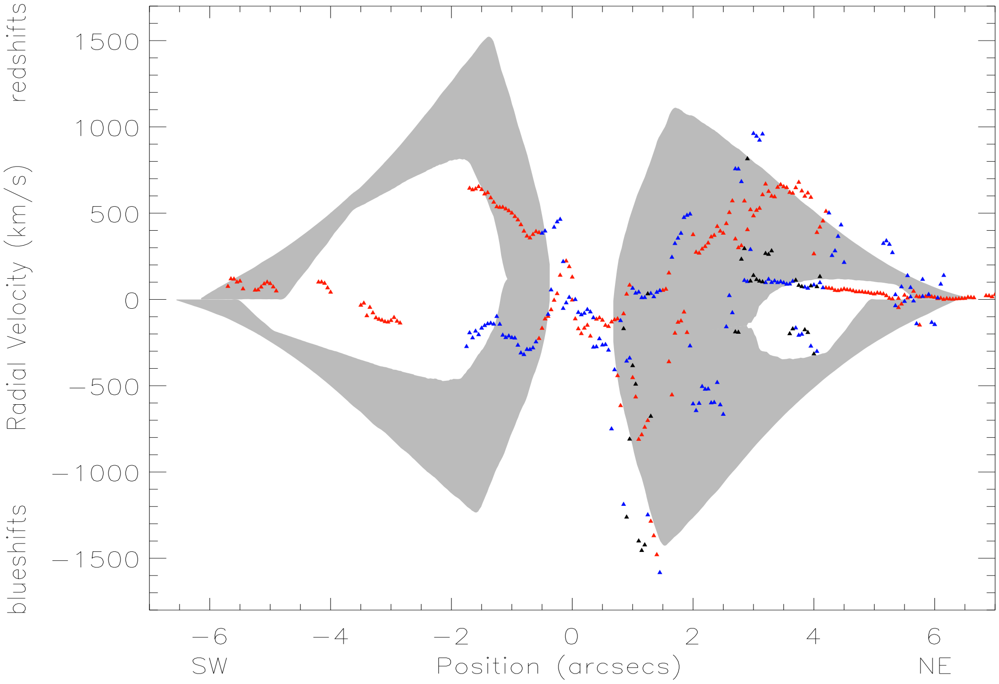

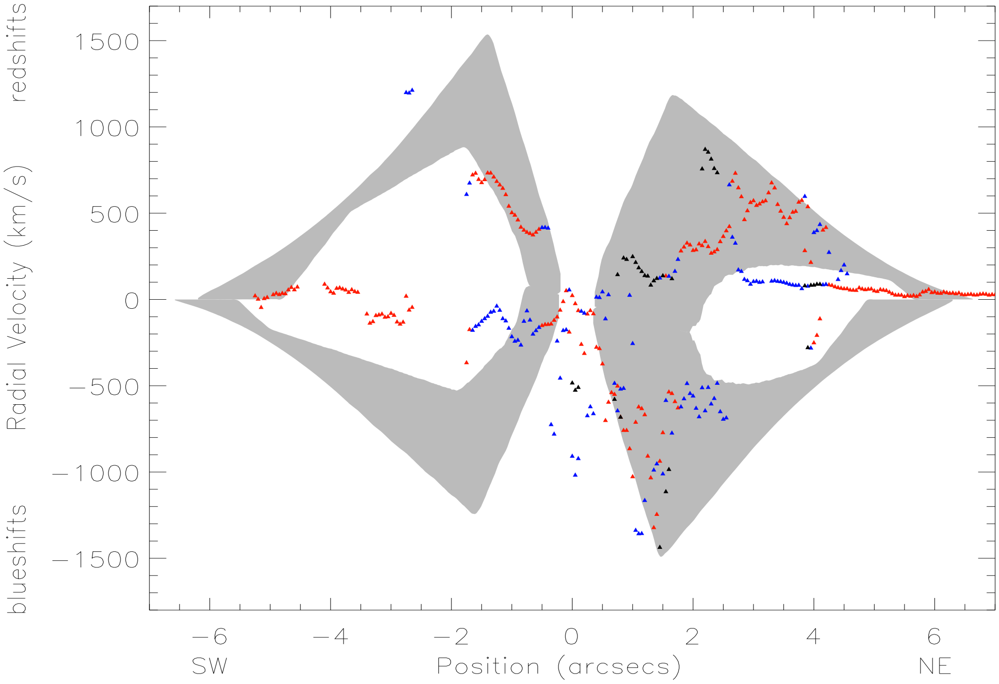

Figure 6.14: Top: Figure showing the best-fit model for slit 1 of NGC 1068. The 'continuous' stretch of points at ~ 0 velocity in the NE are points in the galactic disk. There are also broken up chunks of galactic disk points $\leq -2''$ in the SE. The data points at position $0''$ are examples of the limitation of the model.
Bottom: The best-fit model for slit 2 of NGC 1068. As in slit 1, galactic points are picked up in this slit in the NE and SE. There are some high velocity low and medium flux data points at position $\sim 0''$ that are not on the model.

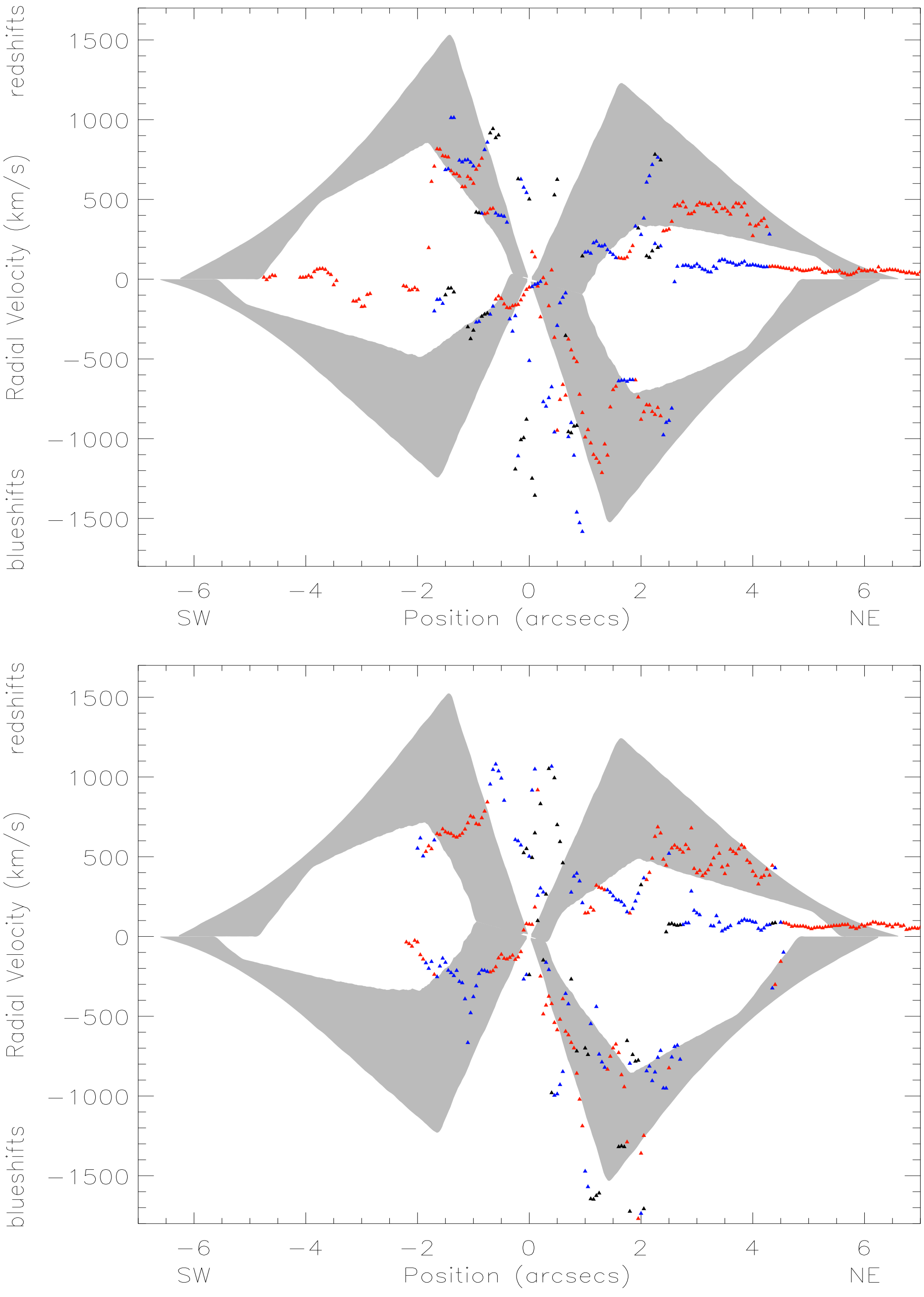

Figure 6.15: Top: The best-fit model for slit 3 of NGC 1068. The fit is better for slits near the bicone axis, but again the high velocity, low and medium flux components near 0″ are not fitted very well.
Bottom: The best-fit model for slit 4 of NGC 1068. The high velocity low and medium flux components are now mostly in redshift near 0″ and again they are not fitted well. We continue to pick up galactic disk points in the NE, but the disk points in the SE have diminished.

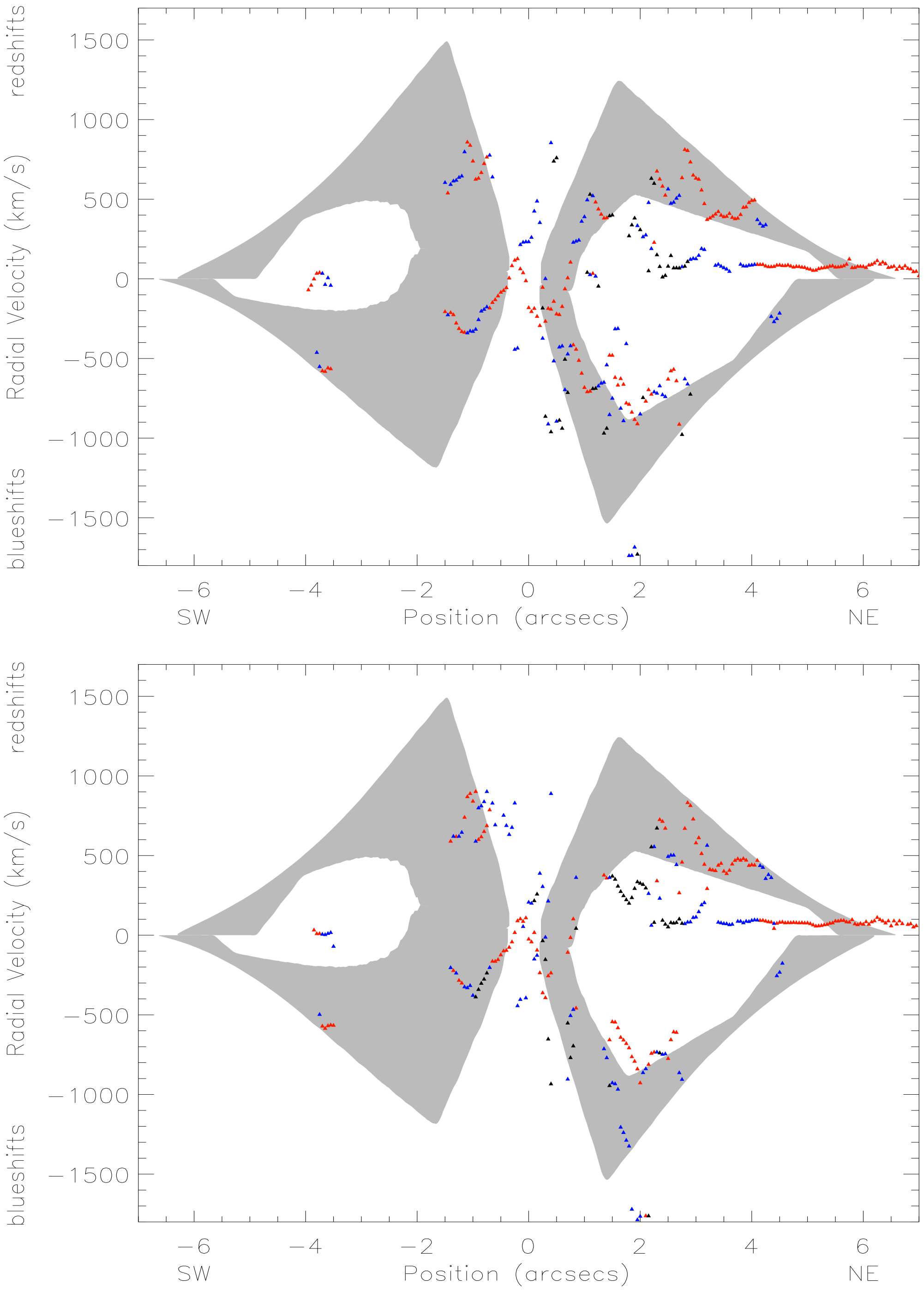

Figure 6.16: Top: The best-fit model for slit 5 of NGC 1068. The number of high velocity low and medium flux components has reduced near 0″, but there are some near 2″ that are poorly fit.
Bottom: The best-fit model for slit 6 of NGC 1068. Slit 6 covers the same region as slit 5. Notice the data points are generally the same, but not exactly so. The minor differences may be due to the measurement and separation processes employed.

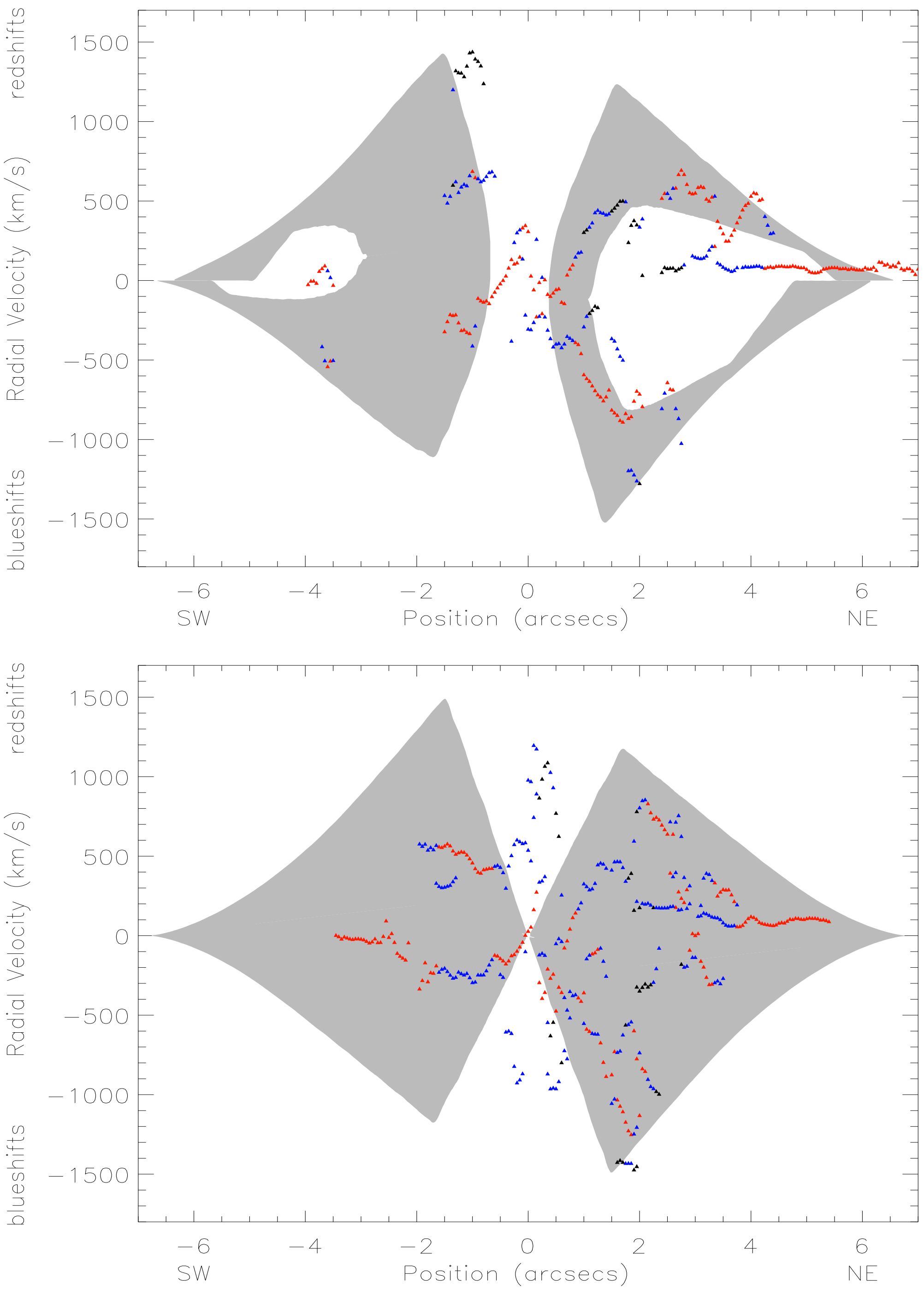

Figure 6.17: Top: The best-fit model for slit 7 of NGC 1068. The model did not fit points near 0″. This limitation is present in slits on either sides of the central bicone axis due to the tapering of the bicone model. As in slits 5 and 6, there are some galactic disk points in the SE, but the NE ones are more predominant.
Bottom: The best-fit model for slit 8 of NGC 1068. Slit 8 is at a different position angle than the rest of the slits and intercepts an edge on the bicone model, resulting in the filled in shaded region. Points near 0″ in blueshifts and redshifts are not fitted.

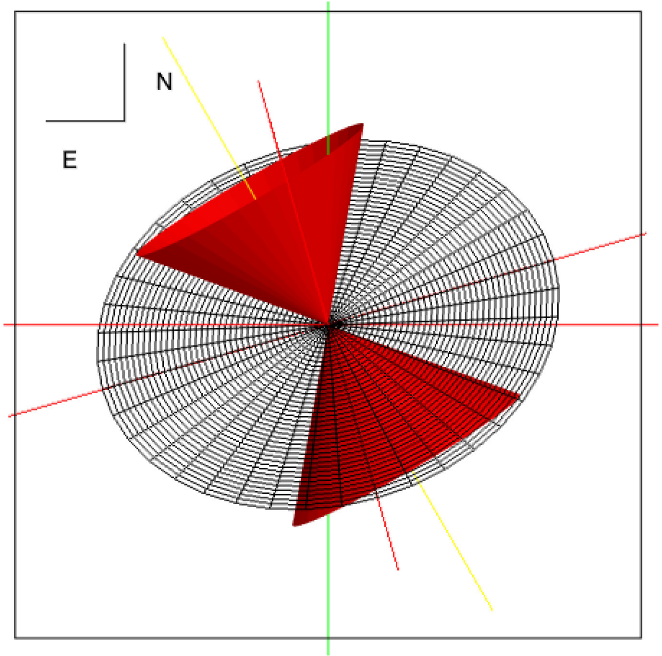

Figure 6.18: The orientation of the NLR with respect to the host galaxy of NGC 1068. Note that the southwest side of the NLR is being observed through the galactic disk, which will explain the lack of data points on this side of the slits. Figure provided by R. P. Deo.

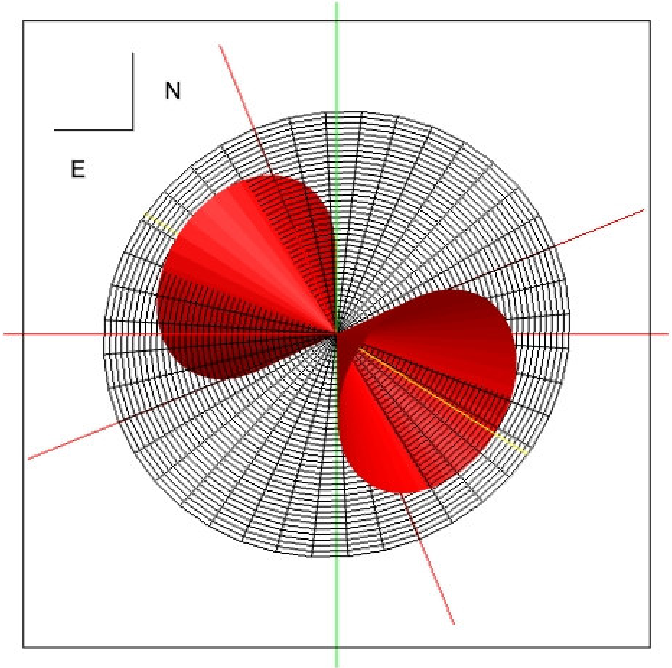

Figure 6.19: The orientation of the NLR with respect to the host galaxy of NGC 4151. Note that the northeast side of the NLR is being observed through the galactic disk, which should provide extinction along the LOS in this region. However this effect is not detected, contrary to the case for NGC 1068. Figure provided by R. P. Deo.

6.5 Effects of the Radio Jet

6.5.1 Inclination Effects

The jet/cloud comparison of NGC 4151 is not very straightforward because its NLR is inclined out of the plane of the sky. To look for equal-magnitude velocity splitting of the [O III] clouds at each position along the radio jet is not valid. The velocities intercepted along the LOS near a radio knot will not necessarily show redshifts and blueshifts of equal magnitude, as the cartoon in Figure 6.20 shows. If an observer is looking from the right of the figure, his LOS will intercept points on the bicone such as A, B, C, and D. If the radio jet, shown in blue, is transversely pushing clouds

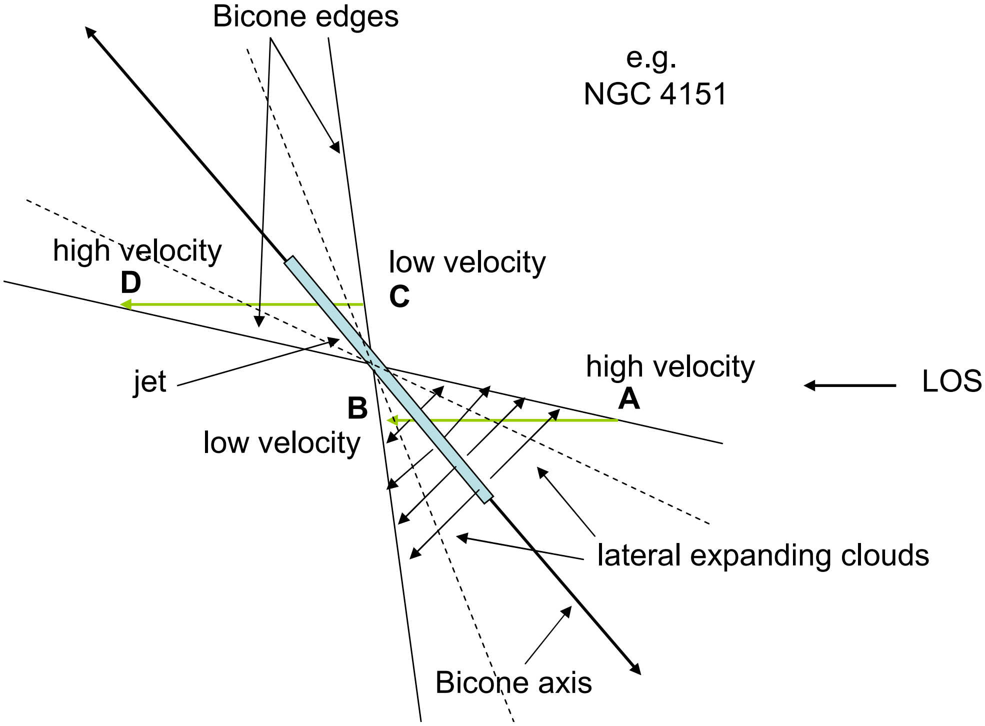

Figure 6.20: The uneven velocity splitting of the [O III] clouds due to projection effects of the inclined radio jet. See text for more details.

away from the axis, the velocities obtained at A and B will usually not be the same in magnitude. The velocity of the clouds at point A will be higher than that of point B, assuming for example that the clouds are increasing their velocity with distance from the jet axis. The same arguments hold for line-of-sight points C and D. This argument holds for Seyfert 1 galaxies in general where the inclination of the NLR bicone and radio jet axis is presumably large. However in the case of NGC 4151, the radio jet is aligned close to one of the outer edges of the bicone. In such a case the bicone edges appear closer together as shown by the dotted lines in Figure 6.20. This will effectively reduce the effect of the inclined jet and the observed radial velocities at points A and B will not differ in magnitude as much as when the jet flows down the center of the bicone axis.

Contrast the previous argument with Seyfert 2 galaxies, where the inclination of the jet is small, e.g. NGC 1068, and we have the scenario as shown in Figure 6.21. Now the radial velocities measured at points A and B should be the same in magnitude if the radio jet is pushing on the NLR clouds laterally. Velocities at points C and D will also be similar in magnitude. In this case the one-to-one comparison between radio knots and [O III] disturbance becomes easier, because one can look for redshifts and blueshifts of similar magnitude near the radio knots. The same cannot be said for Seyfert 1 galaxies.

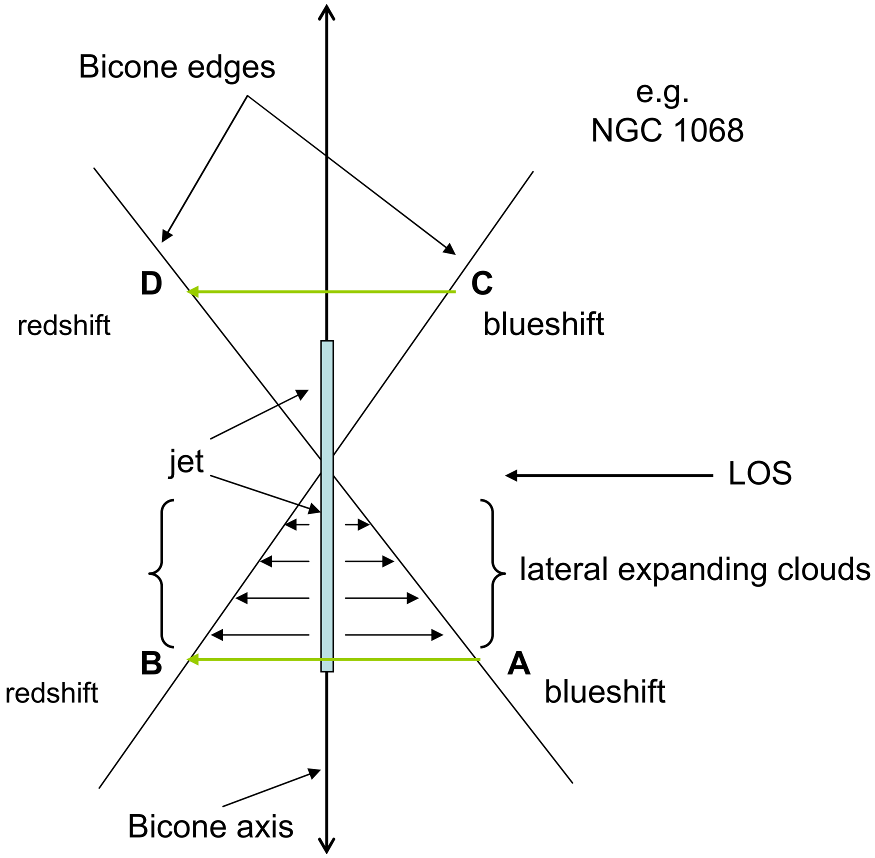

Figure 6.21: The even velocity splitting of the [O III] clouds due to the radio jet can be sought at positions near the radio knots. See text for more details.

6.5.2 Interaction with the Radio Jet in NGC 4151

We plotted the radio fluxes together with NLR radial velocities for each slit in NGC 4151, and these are shown in Figures 6.22–6.24. The radio knots are labeled with the letters next to them with the same labeling scheme as in Figure 3.3. In the top panel of Figure 6.22, there is splitting near radio knot F+E but the splitting extends across the knot and to the right where there is no significant radio. There is also velocity splitting going away from the radio knots D and X to the left. Clearly these large scale splittings cannot be caused by the radio knots. In the bottom panel of the figure, we see some disturbance near radio knot C, and somewhat near B. These smaller scale effects might be due to these knots. In the top plots of Figure 6.23, the velocity splitting is seen clearly above radio knots A and B, but not otherwise. This disturbance seems to be related to the two knots. In the bottom plots also, there seem to be strong correlation between the knots and the disturbance to the [O III] clouds, especially at knot H. In Figure 6.24, the effect of radio knot H is repeated and radio knot I shows disturbance also. There may be some effect due to radio knot G in both figures, but this is not very conclusive. Above the question marks, the velocity of the clouds is clearly disturbed, but there is no labeled radio knot at this position. The radio emission at this position is only slightly enhanced, and could be due to noise. However, there are also a number of cases of localized velocity disturbances (splitting) and no radio knot, for example, at $1''$ in slit 2 and at $-1''$ in slit 2.

The overall conclusion is that the velocities of the [O III] clouds may be disturbed at or near the positions of the radio knots. However the driving mechanism of the outflowing clouds cannot be attributed to the radio jet, since the velocity splitting is on a large scale and not localized to the positions of the radio knots. More importantly, Figure 6.20 shows that the transverse velocity model predicts blueshifts and redshifts of roughly equal magnitude in each cone. However, the observed trend in NGC 4151 is blueshifts in one cone and redshifts in the other. Thus the outflow theory is more suited to describe the kinematics of the NLR of NGC 4151 and probably Seyferts in general.

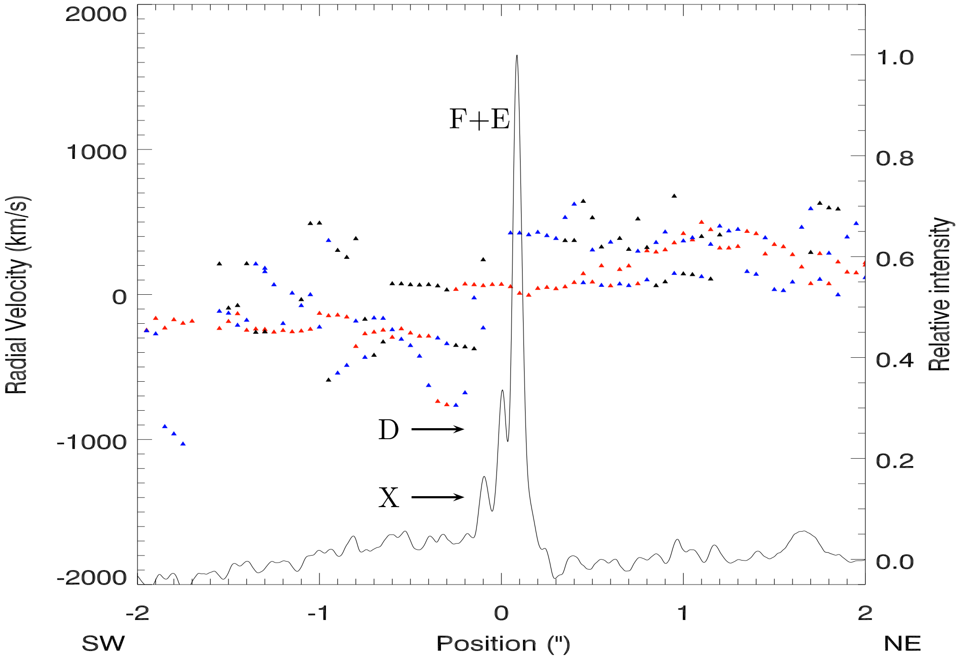

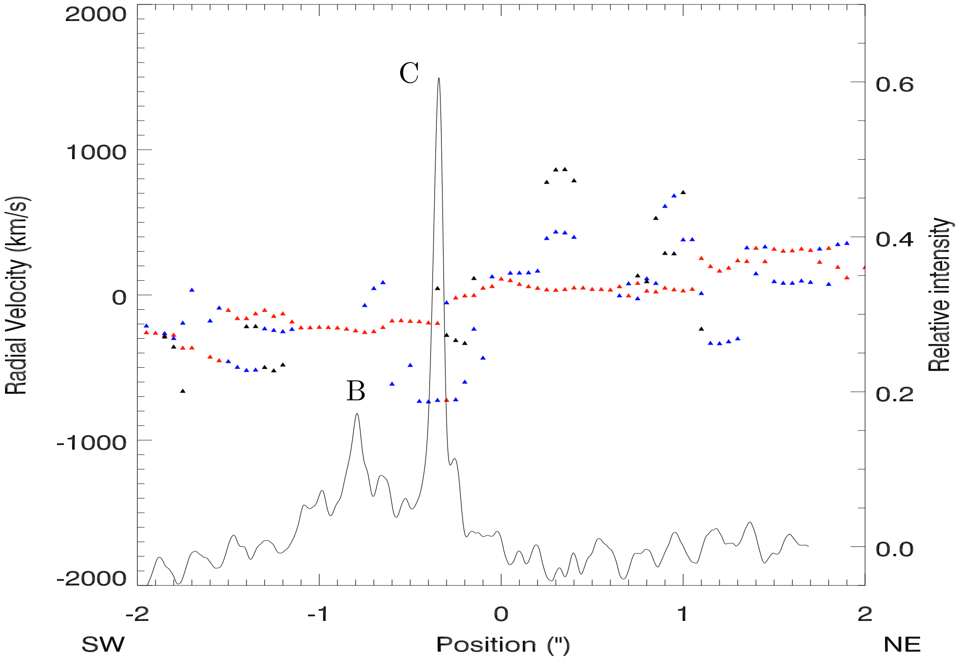

Figure 6.22: Top: Figure showing the radial velocity plot together with the radio intensities from $-2''$–$2''$ extracted from slit 1. There is extended splitting of the velocities near radio knot F+E and there is also some splitting near the smaller knots D and X.
Bottom: Figure showing similar plots as above but with slit 2. Note the splitting near radio knot C. There are some points above knot B also, but no clear splitting. See text for more details.

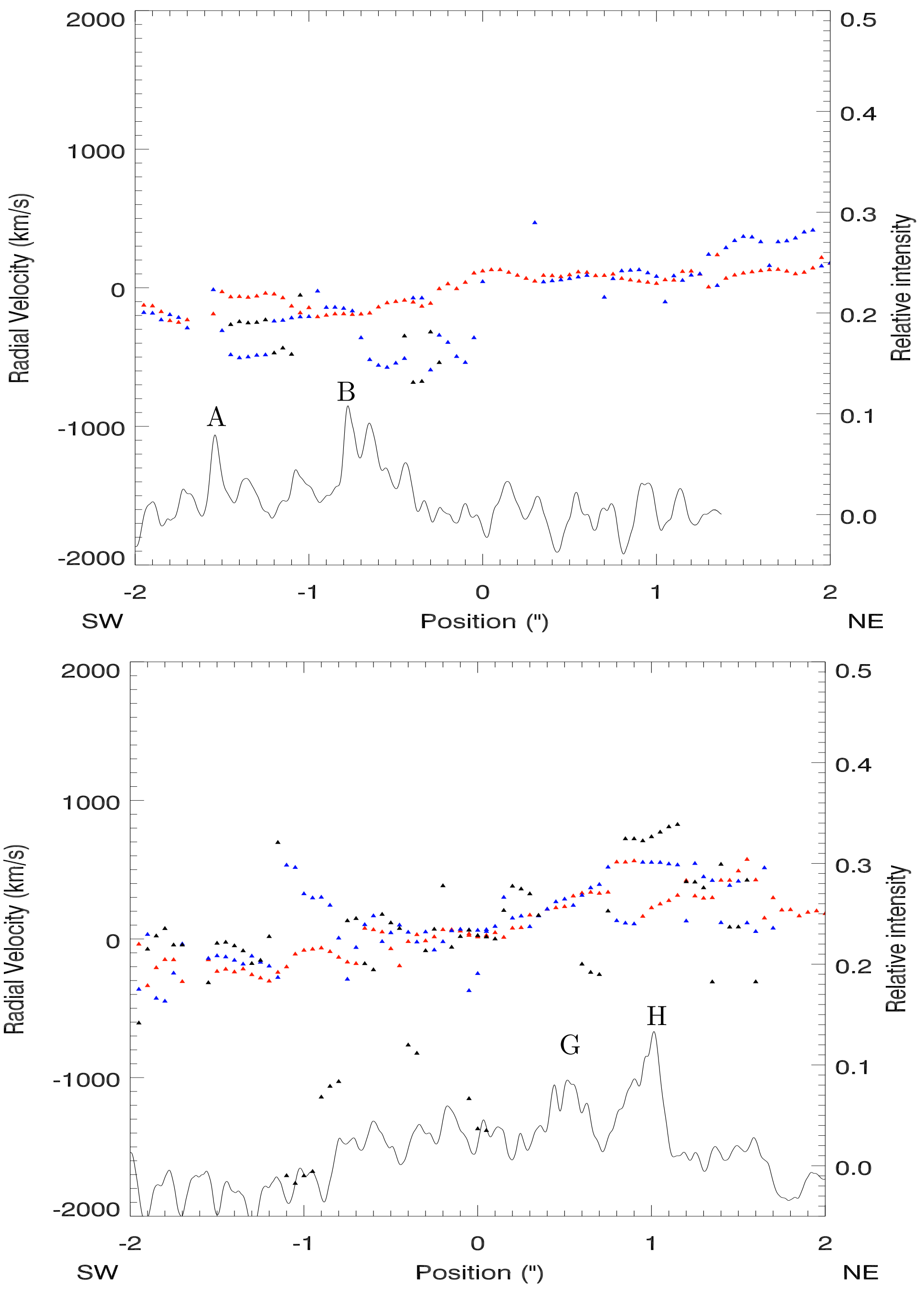

Figure 6.23: Top: Similar to Figure 6.22 but showing slit 3. Again there is some disturbance of the clouds near the strongest radio knots A and B.
Bottom: Radio intensities superposed on radial velocity plots of slit 4. There is clear splitting of the velocities near the highest radio peak H, but not so much for knot G.

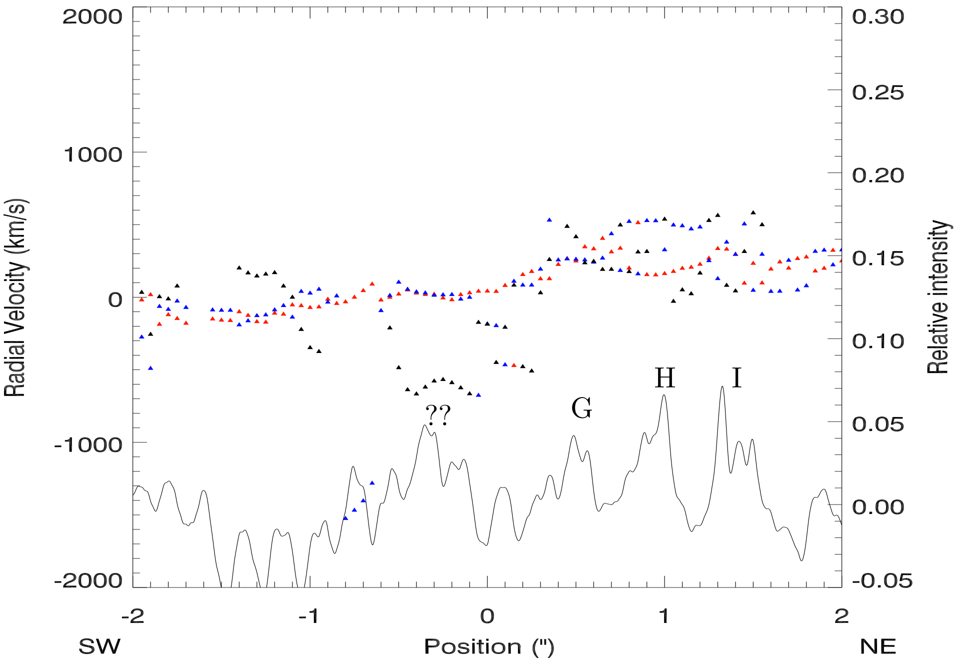

Figure 6.24: Radio intensities superposed on radial velocity plots of slit 5. Note the splitting of velocities near radio peaks H and I. The question marks indicate splitting of the velocities but no identifiable radio knot. See text for more details.

6.5.3 Interaction with the Radio Jet in NGC 1068

Figures 6.25–6.26 are plots of relative radio intensities along slits 3, 4, 5, and 8 respectively, together with [O III] radial velocities within $2''$ of the SMBH. In the top panel of Figure 6.25, the radio knot S2 does not seem to have any effect on the bright cloud velocities, i.e., the red points are not convincingly split into redshifts and blueshifts at S2. Furthermore the narrow range of the radio emission cannot account for the slowly but steadily increasing blueshifted velocity going from $0''.5$ to $-0''.5$. At radio knot S1 in the bottom panel of Figure 6.25, there seems to be splitting of the velocities, but this splitting extends all the way beyond $-0''.2$, where there is no radio emission. The splitting of the bright clouds continues after the radio knot in the northeast, going to the right. Similar scenarios apply to Figures 6.26; the bright clouds split in velocities, but not preferentially at the position of the radio knots. Instead, our models attribute this splitting of the radial velocities to radial outflow along a hollowed-out bicone.

The fainter clouds at the positions of the radio knots in Figures 6.25–6.26, however, portray a different picture. The green circles represent pairwise velocity splitting where the radio knots are strongest. The split velocities have approximately equal magnitudes in redshifts and blueshifts, and the splitting is seen only in the low and medium flux clouds. At radio knot C in Figures 6.25–6.26, we detected only redshifted velocities. The blue circles represent faint clouds for which there is no corresponding blueshifted velocity split. This could be due to the fact that the radio jet bends at this position.

One possible explanation for the pairwise splitting of the velocities is that of lateral expansion of the NLR clouds due to the radio jet as shown in the cartoon of Figure 6.27. The figure represents a schematic of this lateral expansion of the fainter clouds away from the radio jet/bicone axis. This flow, however, is restricted to clouds within a few tens of parsecs from the SMBH, along the region of the inner radio jet. The large scale outflow of the bright clouds cannot be accounted for by the radio jet, and needs a different acceleration process. The same arguments hold for NGC 4151, if one changes the inclination of the bicone and radio jet to $\sim -45^\circ$.

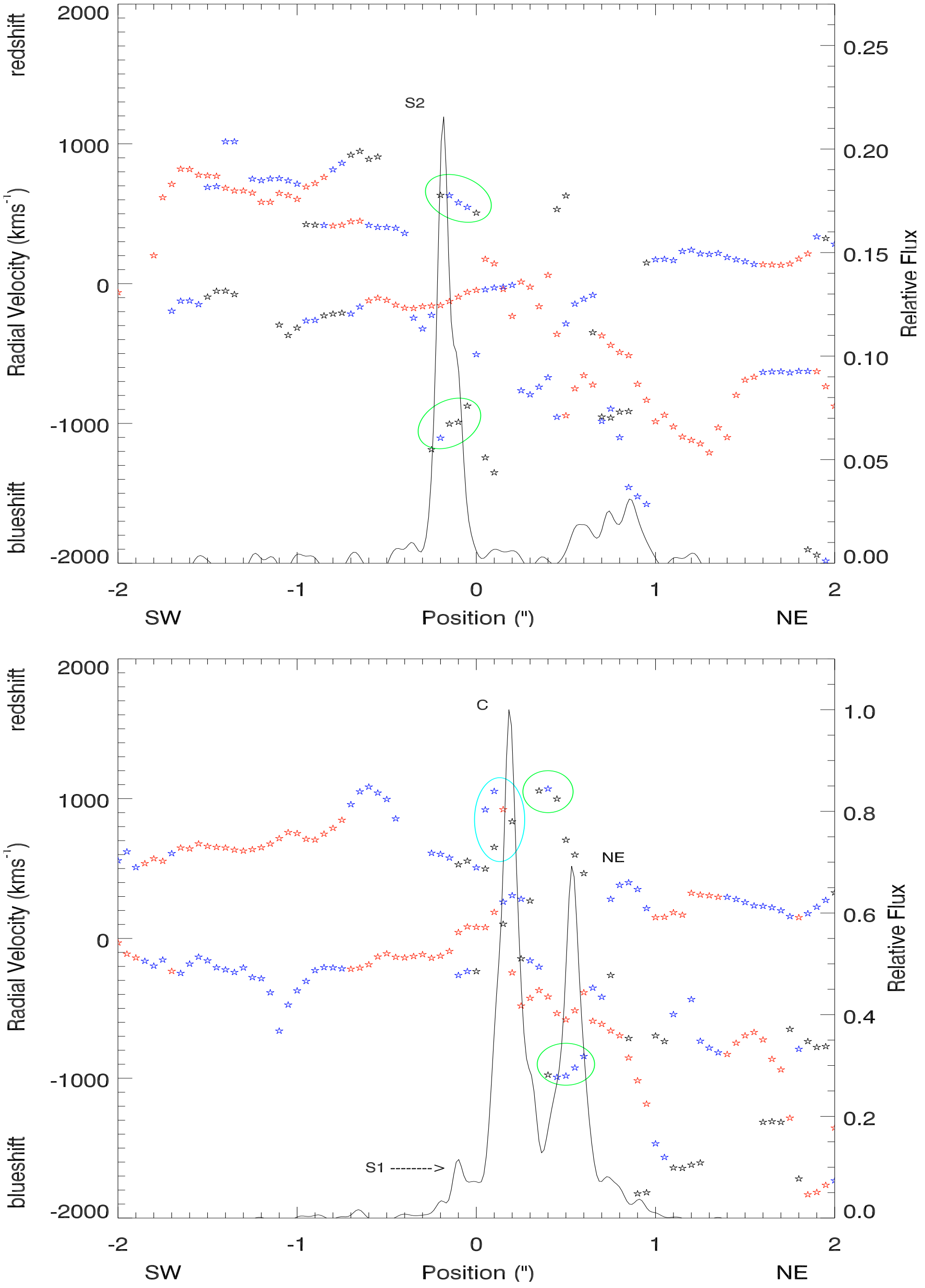

Figure 6.25: Top: Figure showing the radial velocity plot together with the radio intensities from $-2''$–$2''$ extracted from slit 3. The green ovals depict equal magnitudes velocity splitting of the fainter clouds at the radio knot S1. The blue ovals show some disturbance at radio knot C, but no splitting is seen at C.
Bottom: Figure showing similar plots as above but with slit 4. The splitting can be seen now at radio knot NE. Radio knot C does not seem to split the radial velocities.

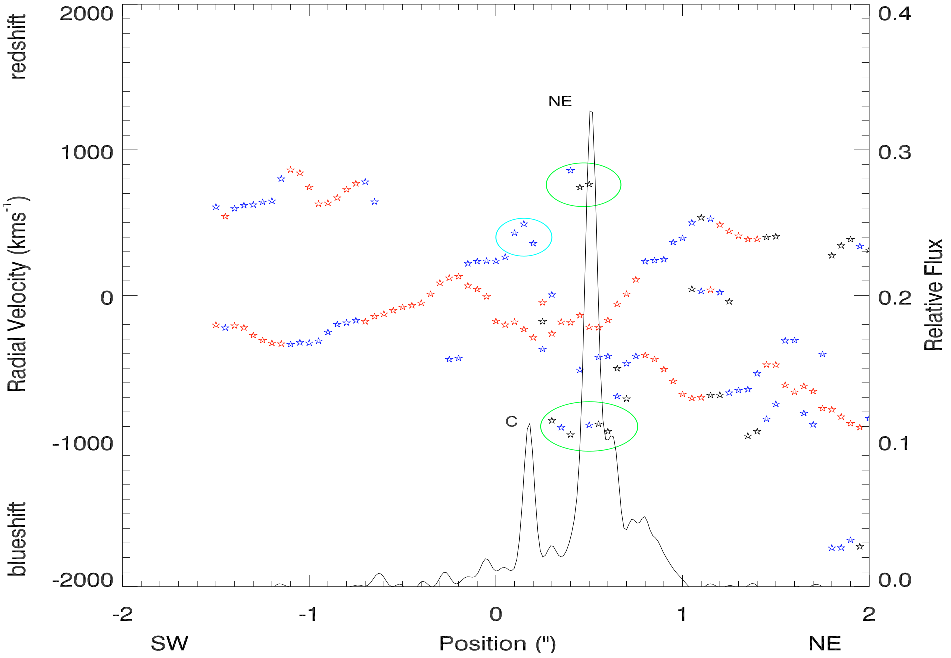

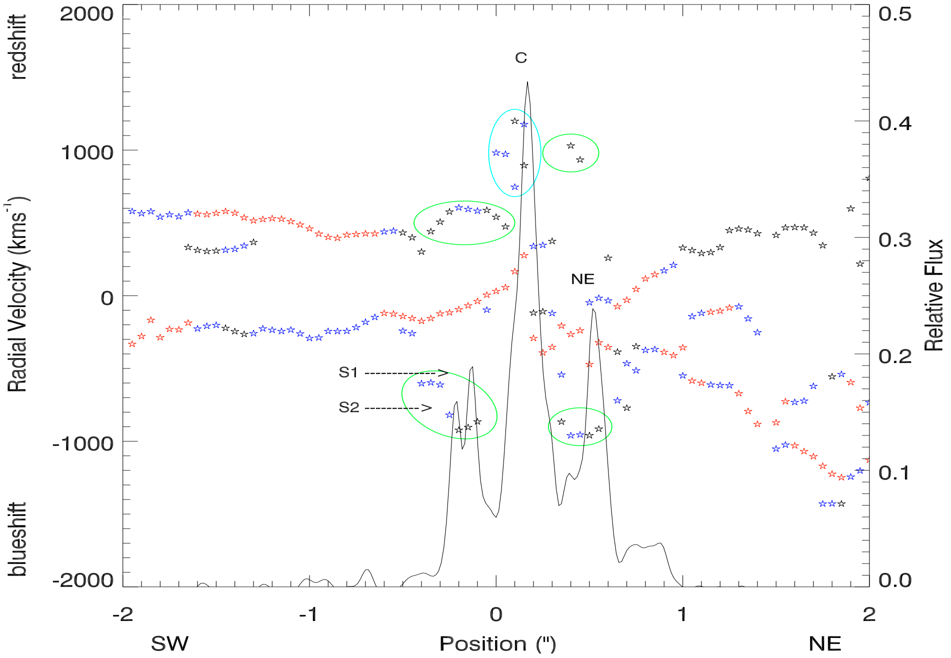

Figure 6.26: Top: Similar to Figure 6.25 but showing slit 5. The radio knot C is less intense and splitting is again seen at radio knot NE.
Bottom: Slit 8 with radio intensities superposed on radial velocity plots. Knots S1 and S2 show radial velocity splitting, so does NE, but not C. Note that only the fainter clouds are split.

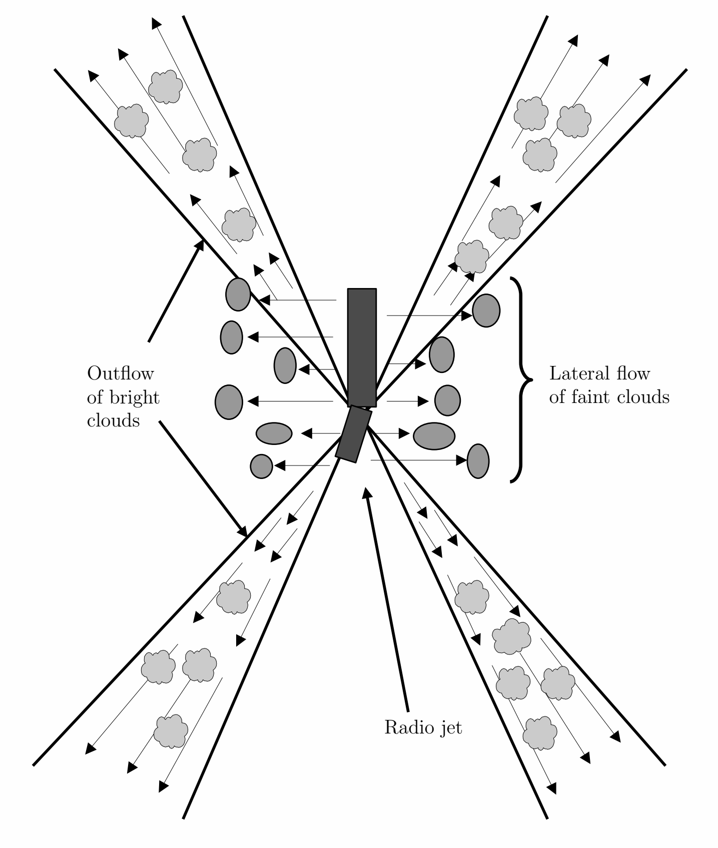

Figure 6.27: A schematic showing the lateral radio expansion driving the fainter clouds within proximity of the radio jet. The larger outflows are driven by some other mechanism, possibly by radiation line driving.

– 7 –

Dynamics of the NLR of NGC 1068

Previous work on the dynamics of the NLR were discussed in Chapter 2. Can we constrain the dynamics of the NLR in Seyfert galaxies with the detailed knowledge that we have gained from our kinematical studies? Here, we concentrate on the dynamics of the NLR in NGC 1068, since it has the best constraints. We will start with a simple construction of the enclosed mass function based on data from previous studies and eventually formulate a radiation pressure-gravity tug-of-war on the NLR clouds. The questions we will attempt to answer include the following:

1) If the NLR gas is in outflow, is radiation pressure really the best driving mechanism?

2) If the NLR gas is turning over its velocity and decelerating back to systemic, is gravity responsible for stopping the gas?

3) Can we fit the velocity profile of the data with a simple radiation-gravity law, or do we need to include another force (such as drag)?

The analysis below applies to NGC 1068 in particular, but has relevance to all Seyferts in general that show signs of gas outflow and gas deceleration. To test whether gravity is playing any role in stopping and turning back the gas velocity, we need to construct an accurate mass profile within $\sim$ 10,000 pc from the nucleus of

NGC 1068. With the mass profile in hand, we will test whether the gas kinematics are dominated by rotation. Such a test might prove fruitful for rotation in NGC 4151, which shows only redshifts in the northeast and only blueshifts southwest of the nucleus, but from a geometrical point of view, rotation of the gas will prove difficult to match the data of NGC 1068, which shows blueshifts and redshifts on each side of the nucleus. Next we plot the escape velocity with distance to see if the gas should escape or not from that point, given the velocities seen in the data, and whether or not the kinematics of the NLR can be dominated by gravitational infall. Then we concentrate on outflow, and determine if the deceleration of the gas can be attributed to the enclosed mass, regardless of the outward accelerating force. We then apply radiative line driving forces balanced by gravitational forces and compare the results to the observed velocity law of NGC 1068 derived from the kinematic models. Finally, we introduce a drag force due to an ambient medium on the NLR clouds, in addition to radiation pressure and gravity, to determine if it can improve the fit to either the accelerating or decelerating portions of the observed velocity curve.

7.1 Building the Mass Profile for NGC 1068

7.1.1 The Black Hole Mass

NGC 1068 is one of only a few AGN that shows an edge-on disk of H_20 maser emission close to the SMBH. The disk shows the signature of a rotational velocity curve, which can be used to determine the mass of the SMBH. Greenhill & Gwinn (1997) estimated the mass of NGC 1068 to be 1.5×10^7 $M_\odot$ within 0.65 pc, based on the velocity field of the H_20 maser emission observed with the VLBA and the VLA. We will therefore use this estimate for the mass of the SMBH.

7.1.2 The Bulge Mass

Since we are going out to $\sim$ 10,000 pc, which encloses the NLR and the ENLR clouds, we need an accurate assessment of the total mass within this region. At small distances ($\leq$ 1 pc), the SMBH is dominant, although in the case of NGC 1068, a concentrated stellar cluster is also providing substantial gravity close in. For an estimate of the bulge mass in NGC 1068, we rely on the work of Häring & Rix (2004). They found a tight correlation between black-hole mass and bulge mass for a sample of 30 galaxies, including NGC 1068. They determined the bulge mass by modeling the bulge with the Jeans equation[1] in spherical form. They assumed the bulge to be isotropic and spherically symmetric, which might lead to an overestimation of the bulge mass; however they also neglect any contribution from dark matter, which would tend to underestimate the bulge mass. Their value for the bulge mass in NGC 1068 is 2.3×10^{10} $M_\odot$ within a radius r = $3R_e$ (3 effective radii), where R_e = 3.1 ± 0.8 kpc, a value taken from the surface brightness deconvolution of Marconi & Hunt (2003). The effective radius R_e is defined to be such that half of the total light from the galaxy is predicted to be contained within the isophotal ellipse that has area

---

[1] The Jeans equation in spherical form is given by $\frac{d(\rho_* \sigma_r^2)}{dr} + 2\frac{\beta \rho_* \sigma_r^2}{r} = -\rho_* \frac{d\Phi_*}{dr}$, where r is the radius, ρ_* is the stellar mass density of the bulge, σ_r is the stellar radial velocity dispersion, β measures the anisotropy in the velocity, and Φ_* is the total potential due to the stars.

$\pi \mathrm{R}_e^2$ (Binney & Merrifield 1998).

Elliptical galaxies' and bulges' surface brightnesses can be well described by the empirical formula developed by de Vaucouleurs (1948)

$$I(R) = I_e e^{-7.6692[(\frac{R}{R_e})^{\frac{1}{4}}-1]}, \tag{7.1}$$

where $I_e = \mathrm{I}(R_e)$. In the 1980s–1990s, a family of stellar density curves emerged that modeled both elliptical galaxies and bulges well. These curves are of the form

$$\rho(r) = \frac{(3-\gamma)M}{4\pi} \frac{\eta}{r^\gamma (r+\eta)^{4-\gamma}}, \tag{7.2}$$

where η is a scaling radius and M is the total mass of the bulge (Dehnen 1993). The parameter γ determines different types of models, where the $\gamma = 2$ cases corresponds to previous density models by Jaffe (1983) and the $\gamma = 1$ cases to models by Hernquist (1990). These models, when integrated over a spherical volume, yield the following enclosed mass profile:

$$M(r) = \int_0^r 4\pi t^2 \rho(t) dt = \frac{4\pi(3-\gamma)M\eta}{4\pi} \int \frac{t^2 dt}{t^\gamma (t+\eta)^{4-\gamma}} = M \left(\frac{r}{r+\eta}\right)^{3-\gamma}. \tag{7.3}$$

For the special case when $\gamma = 1.5$, the density profile of Equation 7.2 yields a surface density distribution that closely matches the de Vaucouleurs surface brightness profile of Equation 7.1 to within 15% over nearly 4 decades in radius (Dehnen 1993). Therefore we adopt the following form of the mass function as the bulge profile

$$M(r) = M \left(\frac{r}{r+\eta}\right)^{1.5}. \tag{7.4}$$

We find a suitable value for η in Equation 7.4 by first defining the 'half-mass radius' $r_{\frac{1}{2}}$:

$$\frac{1}{2}M = M\left(\frac{r_{\frac{1}{2}}}{r_{\frac{1}{2}}+\eta}\right)^{\frac{3}{2}}, \tag{7.5}$$

which yields the following relation for η

$$\eta = r_{\frac{1}{2}}(2^{\frac{2}{3}} - 1). \tag{7.6}$$

Dehnen (1993) has found a simple approximation for $\frac{R_e}{r_{\frac{1}{2}}}$ that depends only slightly on γ. For a $\gamma \leq \frac{5}{2}$, he found that

$$\frac{R_e}{r_{\frac{1}{2}}} \approx (0.7549 - 0.00439\gamma + 0.00322\gamma^2 - 0.00182\gamma^3) \pm 0.0007. \tag{7.7}$$

Therefore we can find a value for η by using our choice for γ ($\gamma = 1.5$), by using R_e given above, and by using Equation 7.6. We find that $\eta \sim 2400$ pc. We also know that M(3R$_e$) = 2.3×10^{10} M$_\odot$, so that

$$M = 2.3 \times 10^{10}/\left[\frac{3 \times 3.1 \times 10^3}{3 \times 3.1 \times 10^3 + 2400}\right]^{1.5} = 3.2 \times 10^{10}\ \mathrm{M}_\odot. \tag{7.8}$$

The bulge mass distribution can finally be written as

$$M(r) = 3.2 \times 10^{10}\left(\frac{r_{pc}}{r_{pc}+2400}\right)^{1.5}\ \mathrm{M}_\odot. \tag{7.9}$$

7.1.3 The Nuclear Stellar Cluster Mass

It is known that NGC 1068 has a compact nuclear stellar cluster ∼ 140 pc in radius (Thatte et al. 1997; Crenshaw & Kraemer 2000a), which contributes significant mass to the total mass profile of the NLR of NGC 1068. Therefore this mass must be taken into account when deriving the mass profile. Thatte et al. (1997) found a mass of 6.8×10^{8} $\mathrm{M}_\odot$ within $1''$ of the SMBH of NGC 1068, assuming a virialized, isotropic, and isothermal distribution of the stars. They used the stellar velocity distribution (σ_*) found in Dressler (1984), a value of $143 \pm 5\ \mathrm{km\,s^{-1}}$ at $\sim 1''$, to calculate the total dynamical mass within $1''$ of the nucleus of NGC 1068.

$$M_{dyn} = \frac{2\sigma_*^2 R}{G}, \tag{7.10}$$

where $R = 1'' \approx 72$ pc for NGC 1068. This mass includes contributions from the stellar cluster, the nucleus, and the bulge within a radius of 72 pc. Therefore to find just the mass from the stellar cluster, we took out the rest of the mass contribution from the total mass.

$$M_{sc,\,72} = M_{dyn,\,72} - M_{smbh} - M_{bulge,\,72} \tag{7.11}$$

Making the various substitutions we have

$$M_{sc,\,72} = 6.8 \times 10^{8} - 1.5 \times 10^{7} - 3.2 \times 10^{10} \left(\frac{72}{72 + 2400}\right)^{1.5} = 5.1 \times 10^{8}\ \mathrm{M}_\odot. \tag{7.12}$$

Based on the radial surface brightness profile presented in Figure 4 of Thatte et al. (1997), Beckert & Duschl (2004) computed a power law consistent with the form $S_*(r) \propto r^{-1}$ to fit the data. They claim that if the profile traces the stellar mass distribution, then they would expect that the mass profile would have the form $\mathrm{M}_*(r) \propto r$, given a spherical, isothermal distribution of stars in the cluster. Using their distribution we can estimate the stellar mass function based on the condition

$M_{sc,72} = 5.1 \times 10^8$ M$_\odot$ $= kr$, so that $k = \frac{5.1\times10^8}{72} = 7.1 \times 10^6$ M$_\odot$ pc^{-1}. The stellar cluster mass function is therefore

$$M_{sc}(r) = 7.1 \times 10^6 r_{pc} \ \mathrm{M}_\odot. \tag{7.13}$$

Finally the total enclosed mass function for the NLR of NGC 1068 is given by $M_{tot}(r) = M_{smbh} + M_{bulge} + M_{sc}$ or

$$M_{tot}(r) = 1.5 \times 10^7 + 7.1 \times 10^6 r_{pc} + 3.2 \times 10^{10} \left(\frac{r_{pc}}{r_{pc} + 2400}\right)^{1.5} \ \mathrm{M}_\odot. \tag{7.14}$$

Here we have assumed that the cluster and bulge mass profiles extend all the way inward to the SMBH, which may overestimate the mass close in. However, the SMBH dominates within ~ 2 pc, as shown in the next section. Beyond the observed extent of the stellar cluster, we assumed that $M_{sc}(r)$ is a constant. Finally, we did not include a contribution from the disk of NGC 1068, since the galactic potential is dominated by the large bulge to at least 1000 pc, which is well beyond the extent of the NLR.

7.2 Dynamics Based on Gravity

A figure representing the total mass enclosed within r_{pc} is shown in Figure 7.1. The mass profiles for each contribution, the SMBH, bulge, and cluster are also shown in the figure. Close in toward the nucleus, the nuclear stellar cluster dominates up to its entire extent, while the bulge takes over from there. The black hole mass dominates at ≤ 2 pc. The kink in the total mass curve at ~ 140 pc is because the stellar cluster was cut off abruptly at this location. We could have modeled the cluster to assume

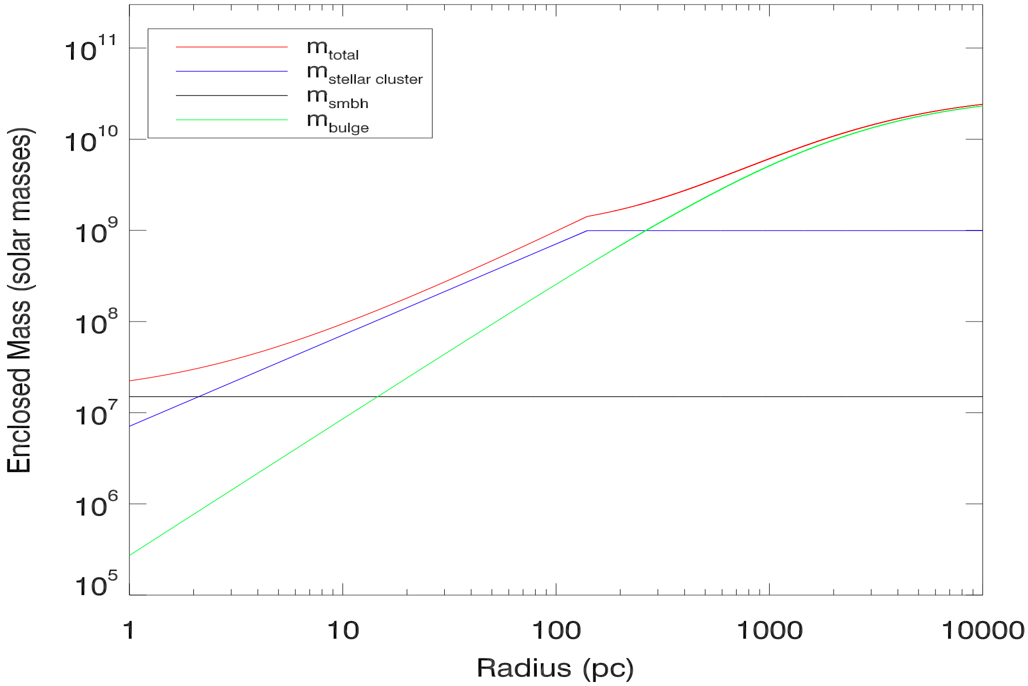

Figure 7.1: Figure showing the total enclosed mass profile of NGC 1068 in orange color. The individual contributions to the total mass is shown in blue (stellar cluster), green (bulge), and black (SMBH). The stellar cluster was modeled to have an extent of 140 pc.

an exponential drop-off after 140 pc, but this would not have contributed much to the gravitational force exerted by the total mass.

7.2.1 Rotation

With the total mass profile we calculate the circular rotational velocity and plot its function with distance as shown in Figure 7.2. The rotation velocity only depends on the enclosed mass at radius r_{pc}, and is given by the formula below

$$V(r) = \sqrt{G \frac{M(r_{pc})}{r_{pc}}} \ \mathrm{km\,s^{-1}}. \tag{7.15}$$

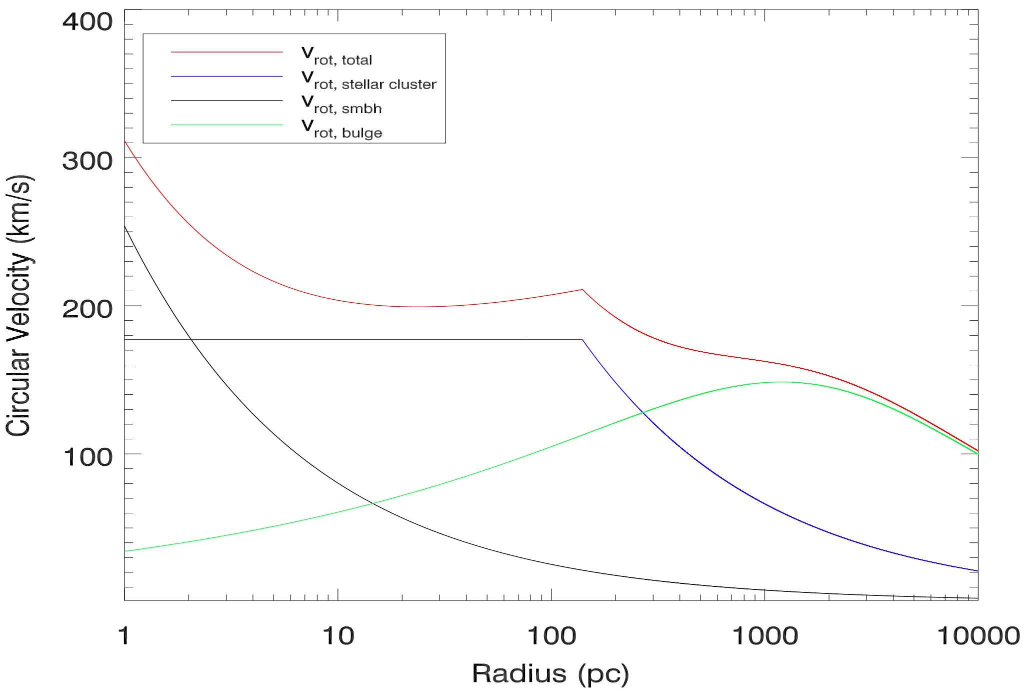

Figure 7.2: Figure showing the total rotational velocity profile of the NLR of NGC 1068 in orange color. The individual contributions to the velocity is shown in colors similar to that of Figure 7.1.

For demonstration purposes, we show the rotational velocities as if only each mass component was present, as well as the velocity for the total mass profile. The rotational velocity profile indicates to us that rotation cannot dominate the kinematics of the NLR of NGC 1068 because many observed data points exhibit large velocities (≥ 1000 km s^{-1}), whereas the rotation curve represents much lower velocities. Again the stellar cluster dominates the velocities up to ~ 300 pc.

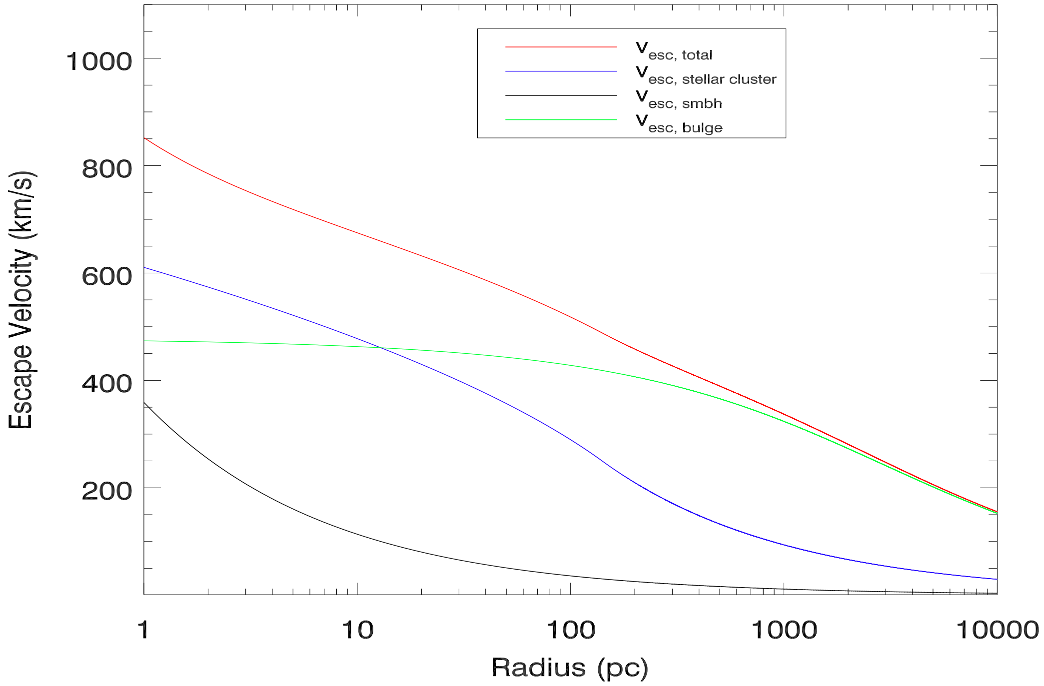

Figure 7.3: Figure showing the escape velocity as a function of distance for the NLR of NGC 1068. The individual contributions to the escape velocity is shown in colors similar to that of Figure 7.1.

7.2.2 Escape and Infall Velocity

The escape velocity at a given distance r_{pc} is calculated numerically from the formula

$$V(r) = \sqrt{\int_r^\infty 2G\frac{M(t)}{t^2}dt} \ \mathrm{km\,s^{-1}}, \tag{7.16}$$

based on the enclosed mass function, and is plotted in Figure 7.3. According to our kinematic model, the maximum velocity at the turnover radius $r_t = 140$ pc is 2000 $\mathrm{km\,s^{-1}}$; therefore Figure 7.3 tells us that the NLR clouds should have escaped after 140 pc, where the escape velocity is only ~ 500 $\mathrm{km\,s^{-1}}$. In the data however, clouds at 140 pc are at much higher velocity than escape velocity; yet after the turnover point, the clouds start to decrease their velocity and return to systemic. Thus, some force other than gravity is causing the clouds to decelerate at r $\geq$ 140 pc. The infall velocity profile is equivalent to the escape velocity profile, except that the velocity vector is now directed inward. Therefore gravitational infall also cannot account for the faster moving clouds at 140 pc.

7.2.3 Gravitational Drag

To test the importance of the force of gravity alone on slowing down the outflowing NLR clouds, we give the clouds a maximum velocity at the turnover point and let gravity do the rest. In other words, we assume that there is no outward driving force after the turnover point and let the clouds coast under the force of gravity. The top panel of Figure 7.4 shows that with a maximum velocity $\geq$ 1000 $\mathrm{km\,s^{-1}}$ at 140 pc, there is little deceleration with radius. However, with maximum velocities $\leq$ 300 $\mathrm{km\,s^{-1}}$ gravity can slow the clouds down to rest, as seen in the bottom panel of Figure 7.4. The maximum velocities in the NLRs of some Seyfert galaxies are on the order of $\sim$ 400 $\mathrm{km\,s^{-1}}$ (Ruiz et al. 2005), and gravitational deceleration may be important in these cases. The kinematic model of NGC 1068, however, shows maximum velocities of up to $\sim$ 2000 $\mathrm{km\,s^{-1}}$, clearly out of the reach of gravitational deceleration. Gravity alone cannot slow down the outflowing clouds in this case and there must be some other force or forces involved.

To compound the problem, suppose we let radiation or some other force push on the gas while gravity is trying to pull it back. In this case the gravitational

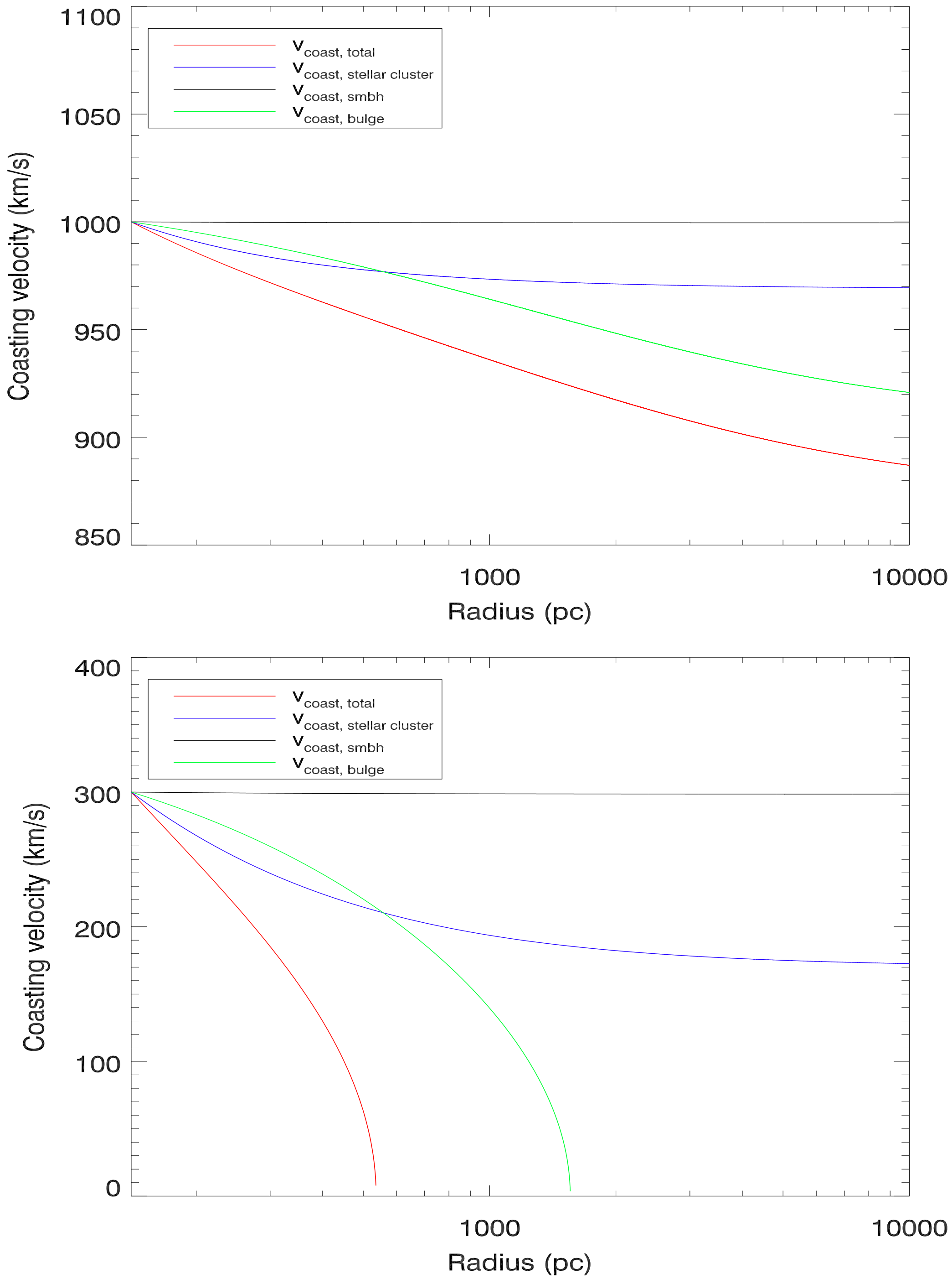

Figure 7.4: Figure showing how velocity slows down with distance for an initial launch at 140 pc with 1000 km s^{-1} (top) and 400 km s^{-1}(bottom) for the clouds in NGC 1068. The clouds barely slow down out to 10,000 pc when launch with 1000 km s^{-1}. However, gravity was able to slow down the clouds down when they were launched with 300 km s^{-1}. The colors represent the mass contributions of Figure 7.1.

deceleration will be even less. However, to satisfy our curiosity, we generate a line-driven radiation model, with gravity competing to slow the gas down. This will eventually lead us in the direction of including a drag force to complete the analysis.

7.3 Radiation-Gravity Formalism

The various mechanisms to push the gas out from close to the nucleus include a radiation pressure driven wind, a thermally driven wind, or a magneto-hydrodynamic (MHD) wind (Crenshaw et al. 2003). The latter two methods are discussed in more detail in Everett (2005) and Everett & Murray (2006), and were summarized in §1.6.2.2. However, no dynamical model to date has led to a satisfactory description of the kinematics in NGC 1068 or NGC 4151. The radiation driven wind mechanism is most efficient when the momentum imparted to the gas is due to line-driving (bound-bound transitions); bound-free and free-free electron transitions (Thomson scattering) can also drive the gas out, but less efficiently when the gas is ionized (Chelouche & Netzer 2001). The radiation force is dependent on the ionization state of the gas, with lower ionization states more efficient due to the greater availability of electrons in the bound states. If dust is mixed in with the NLR gas, then it will compete with the gas in absorbing ionizing photons and hence radiation pressure on the dust can become an important contributor to the velocities of the outflowing gas in the NLR (Dopita et al. 2002). If the dust grains are electrically charged, they can drag the ionized gas along to similar velocities as the dust. In this section we ignore the effects of dust, which would only increase the force multiplier. Thus we consider a radiation driving mechanism coupled with the effects of gravity to find the velocity profile of the NLR gas.

7.3.1 Building the Velocity Equation

We start with the acceleration due to radiation on a point mass, with the Thomson scatterer as the driving mechanism.

$$a(r) = \frac{force}{mass} = \frac{L \sigma_T \mathcal{M}}{4 \pi r^2 c m_p}, \tag{7.17}$$

where a is the acceleration, L is the bolometric luminosity of NGC 1068, σ_T is the Thomson scattering cross section for the electron, r is the radius, c is the speed of light, m_p is the mass of the proton, and $\mathcal{M}$ is the force multiplier. As mentioned above, to really drive the gas out efficiently, we need to incorporate other sources of opacity such as bound-bound and bound-free opacity in addition to those from Thomson scattering. These additional opacities are included via the force multiplier, $\mathcal{M}$ in Equation 7.17, which is primarily a function of ionization parameter[2] U for a given spectral energy distribution (SED) (Crenshaw et al. 2003, and references therein).

The acceleration due to gravity per mass is simply given by

$$a(r) = -\frac{GM(r)}{r^2}, \tag{7.18}$$

---

[2] The ionization parameter U is defined as $U = \frac{\int_{\nu_0}^{\infty} \frac{L_\nu}{h\nu} d\nu}{4 \pi r^2 n_H c} = \frac{\#\text{ of ionizing photons}}{\#\text{ H atoms}}$ at the ionized face of the clouds, where $h\nu_0 = 13.6$ eV and n_H is the hydrogen number density.

where $M(r)$ is the total enclosed mass within r parsecs, and G is the known universal gravitational constant. Putting Equations 7.17 and 7.18 together we have

$$a(r) = \frac{L\sigma_T\mathcal{M}}{4\pi r^2 c m_p} - \frac{GM(r)}{r^2}. \tag{7.19}$$

Now we will have to rewrite the acceleration in terms of velocity as a function of radius, and then solve for $v(r)$.

$$a = \frac{dv}{dr} = \frac{dr}{dt}\frac{dv}{dr} = v\frac{dv}{dr}. \tag{7.20}$$

Therefore we can now write Equation 7.19 as a simple separable differential equation

$$vdv = \frac{L\sigma_T\mathcal{M}}{4\pi r^2 c m_p}dr - \frac{GM(r)}{r^2}dr. \tag{7.21}$$

Substituting for the constants in Equation 7.21 and converting to appropriate units of $\mathrm{km\,s^{-1}}$ and pc, then integrating and setting the initial velocity to zero yields the following form for $v(r)$

$$v(r) = \sqrt{\int_{r_1}^{r}\left[6840 L_{44}\frac{\mathcal{M}}{t^2} - 8.6\times 10^{-3}\frac{M(t)}{t^2}\right]dt}, \tag{7.22}$$

where L_{44} is luminosity in units of 10^{44} ergs $\mathrm{s^{-1}}$ and $M(r)$ is in units of $M_\odot$. The constraints on the luminosity and the force multiplier are presented in the next section.

7.3.2 Physical Constraints on the NLR of NGC 1068

Since NGC 1068 is a Seyfert 2 galaxy, we cannot measure its luminosity directly. From Pier et al. (1994), the total luminosity of NGC 1068 is given by

$$L_{bol} = 2.2\times 10^{11}\left(\frac{f_{refl}}{0.01}\right)^{-1}\left(\frac{D}{22Mpc}\right)^{2} L_\odot, \tag{7.23}$$

where f_{refl} is the fraction of nuclear flux observed as scattered radiation, D is the distance to NGC 1068, and $L_{\odot}$ is the solar luminosity. The most uncertain term in Equation 7.23 is f_{refl}. Pier et al. (1994) have summarized a range of values for f_{refl} that have been determined previously by several authors. The range in f_{refl} spans a few orders of magnitude, from 0.001–0.05. They claimed that the best estimate came from Miller et al. (1991), who had determined a value for f_{refl} to be 0.015, based on observations of [O III] and broad $H\beta$ luminosity and their ratio. Pier et al. (1994) concluded that f_{refl} is probably within a factor of a few of 0.01, hence we have adopted a value for f_{refl} of 0.015 because it is the "best" estimate and close to the average value adopted by Pier et al. (1994). We already know the distance to NGC 1068 as 14.4 Mpc so the bolometric luminosity of NGC 1068 is given by

$$L_{bol} = 2.2 \times 10^{11} \left(\frac{0.015}{0.01}\right)^{-1} \left(\frac{14.4}{22Mpc}\right)^{2} L_{\odot} = 2.4 \times 10^{44}\ \mathrm{erg\,s^{-1}}, \qquad (7.24)$$

a value which could be uncertain by a factor of 0.3–15, depending on f_{refl}.

The emission lines arising from the NLR gas are best fitted with a two component photoionization model at each position, based on *HST*/STIS long-slit spectra (Kraemer & Crenshaw 2000b). According to Kraemer & Crenshaw, the ionization state of the gas ranges from $U \sim\ 10^{-1.5}$–$10^{-3.0}$ for the two components but seems to vary little with distance. Using U and the SED for NGC 1068, Kraemer (private communication) found the force multiplier to vary from $\mathcal{M} \approx 500$–6000 for the front face (ionized face) of the clouds, based on CLOUDY models (Ferland & Osterbrock 1986). The mass function was derived in previous sections, and $L_{44} = 2.4$, so we can now numerically solve Equation 7.22 for $v(r)$. The results are presented in the next section.

7.3.3 Radiation and Gravity Results

Equation 7.22 has only two parameters that we can vary to find the velocity v as a function of distance r: the launch radius r_1, and the force multiplier $\mathcal{M}$. We plotted $v(r)$ for NGC 1068 for various combinations of launch radii and force multipliers of the gas. The graphs of Figure 7.5 show that with a launch radius of $r_1 = 1$ pc, the velocity of the gas increases with force multiplier, but quickly reaches a terminal velocity and never slows down, even out to $\sim$ 10,000 pc. This is not a surprise, as

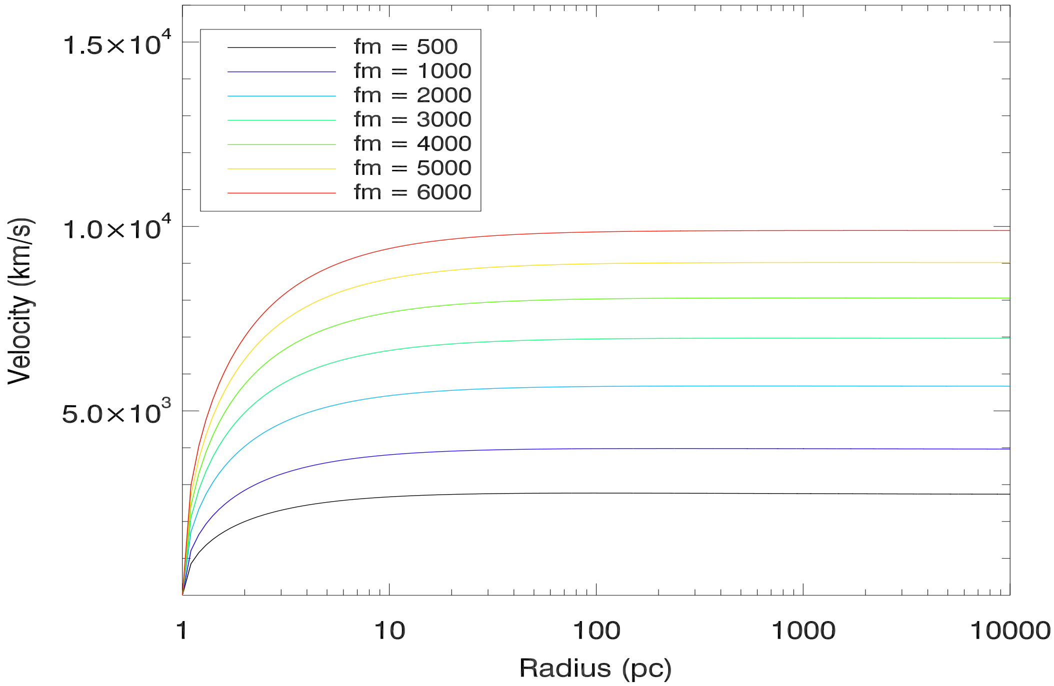

Figure 7.5: Figure showing the velocity profiles for several force multipliers with the gas launched at $r_1 = 1$ pc. None of the curves show a significant decrease in velocity up to 10,000 pc.

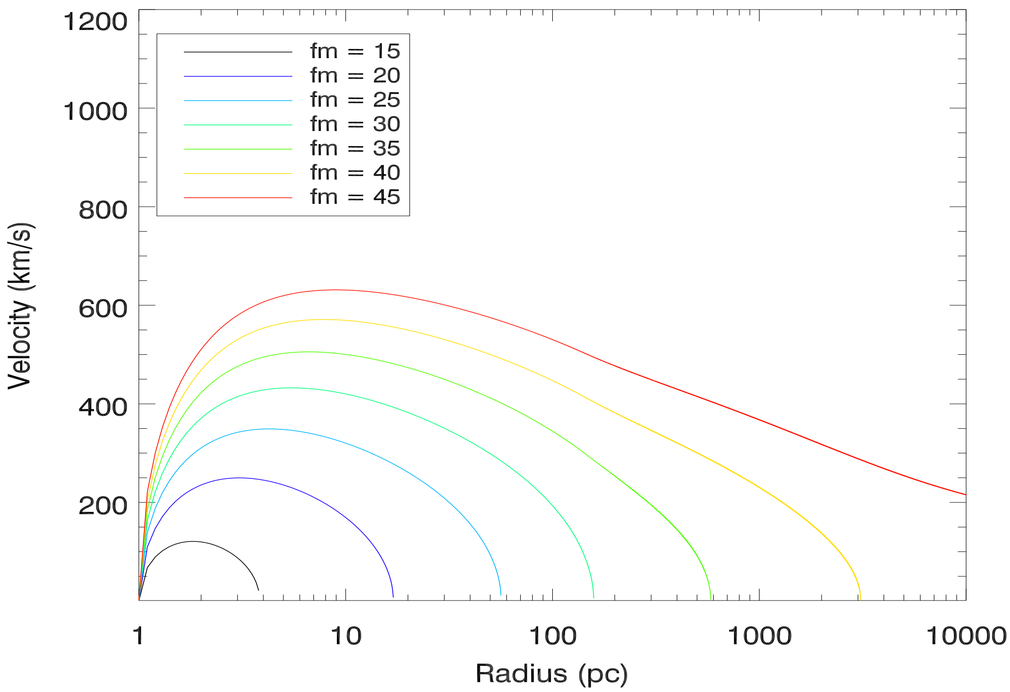

Figure 7.6: Figure showing the velocity profiles for several lower force multipliers with the gas launched at $r_1 = 1$ pc. Curves with force multipliers less than 40 turn over before reaching 10,000 pc, although their maximum velocities do not fit the data of NGC 1068.

previous plots had shown that the mass is not enough to slow down the high-velocity clouds. In addition, the maximum velocities for $\mathcal{M} \geq 500$ are too high compared to the observations, indicating that we must increase the launch radius r_1.

The physical constraints on the NLR gas suggested that the force multiplier is larger than 500. However, we generated plots for $\mathcal{M}$ smaller than 500 to see whether or not gravity can slow the clouds down, if the clouds are launched from 1 pc. In Figure 7.6, we see that with force multipliers less than 40, gravity does slow the clouds down, but that the maximum velocities are too low to fit the data of NGC 1068. Such velocity profiles can prove useful for Seyferts with lower outflow velocities in their

NLRs, such as NGC 4151 and Mkn 3.

We next fix the force multiplier to the lowest value of 500 (because higher values of $\mathcal{M}$ will be even more problematic to slow down the clouds) and vary the launch radius. These plots are presented in Figure 7.7. The maximum velocity falls below the observed values at $r_1 \geq 2$ pc, and the final velocity does not return to zero until we reach large launch radii. As the launch radius increases to ~ 32 pc, the maximum attainable velocity of the outflowing clouds decreases, and the enclosed mass is finally able to turn the velocity around. However by that time, the maximum velocity is too low to serve any real purpose. Also, the launch radius and the maximum distance

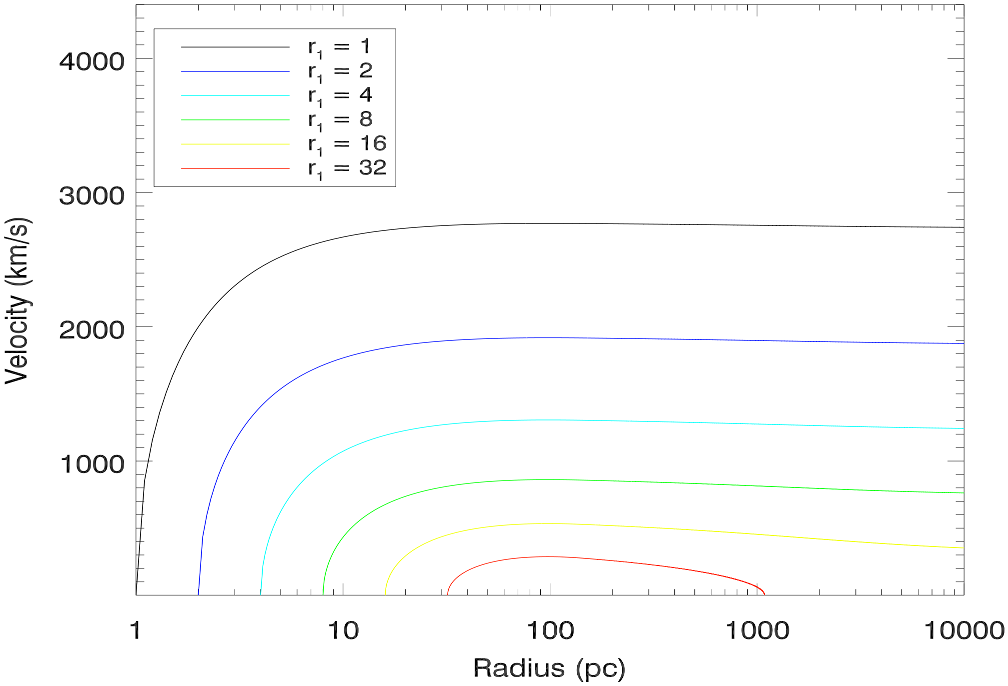

Figure 7.7: Figure showing the velocity profiles for several different launch radii all modeled with a constant force multiplier of 500. The red curve was able to turn over and return to systemic at $\sim$ 1000 pc. The maximum velocity and maximum distance reached do not fit the data.

of outflow are too large to fit the data. Clearly these curves cannot fit the observed NLR velocities of NGC 1068.

7.4 Radiation, Gravity, and Drag Forces

The radiation-gravity interaction on the NLR clouds of NGC 1068 fails to reproduce its velocity profile. For reasonable parameters, the velocity increases quickly close to the nucleus and mostly remains constant over large distances regardless of launch radius. The maximum outflow velocity is rather sensitive to launch radius and decreases with increasing r_1 but the clouds' velocity never turns over and decreases. Fine-tuning r_1 and $\mathcal{M}$ outside of the range of reasonable parameters can lead to a deceleration profile, but the resulting velocity profile and amplitude does not match the observed trend. Therefore we conclude that there must be additional forces at play in the NLR to account for the velocity profile that we see in the data. One such force that could explain the trend in the data is drag, whereby the clouds are slowing down in a more diffuse, hotter, and higher ionization medium (Crenshaw & Kraemer 2000b).

7.4.1 Deceleration due to Drag

The drag force exerted on a cloud by an ambient medium is

$$F_{drag,\,cloud} = \rho_{med}(v_{cloud} - v_{med})^2 A_{cloud}, \tag{7.25}$$

where ρ_{med} is the mass density of the ambient medium, v_{cloud} and v_{med} are the velocities of the cloud and medium respectively, and A_{cloud} represents the cross sectional area of a cloud (Everett & Murray 2006). For simplicity, we assume the clouds to be spherical with mass $m_{cloud} = \frac{4}{3}\pi R_{cloud}^3 \rho_{cloud}$, where R_{cloud} is the radius of a cloud, and ρ_{cloud} is its mass density. The acceleration on the clouds due to drag is then

$$a_{drag,\,cloud} = \frac{\rho_{med}(v_{cloud} - v_{med})^2 \pi R_{cloud}^2}{\frac{4}{3}\pi R_{cloud}^3 \rho_{cloud}} = \frac{m_p n_{med}}{m_p n_{cloud} R_{cloud}} \frac{3}{4} \left(v_{cloud} - v_{med}\right)^2, \quad (7.26)$$

where n is the hydrogen number density and m_p is the mass of the proton. In our case, we assume that the velocity of the ambient medium is zero and the radius of the cloud remains constant. Therefore with $v_{med} \approx 0$ we can write

$$a_{drag,\,cloud} = -\frac{n_{med}}{N_{H,\,cloud}} \frac{3}{4} v_{cloud}^2, \quad (7.27)$$

where $N_{H,\,cloud}$ ($\approx n_{cloud} R_{cloud}$) is the hydrogen column density of the cloud, and the minus sign represents deceleration. Combined with the radiative and gravitational acceleration of Equation 7.19, the total acceleration on the clouds becomes

$$a_{tot} = \frac{L \sigma_T \mathcal{M}}{4\pi r^2 c m_p} - \frac{GM(r)}{r^2} - \frac{n_{med}}{N_{H,cloud}} \frac{3}{4} v_{cloud}^2, \quad (7.28)$$

and in differential form is

$$v dv = \frac{L \sigma_T \mathcal{M}}{4\pi r^2 c m_p} dr - \frac{GM(r)}{r^2} dr - \frac{n_{med}}{N_{H,cloud}} \frac{3}{4} v^2 dr. \quad (7.29)$$

Substituting the various constants and converting to units of pc and $\mathrm{km\,s^{-1}}$, we have the following inseparable differential equation to solve

$$\frac{dv(r)}{dr} = 3420 L_{44} \frac{\mathcal{M}}{v(r) r^2} - 4.3 \times 10^{-3} \frac{M(r)}{v(r) r^2} - 2.3 \times 10^{-2} \frac{n_{med}}{N_{20}} v(r), \tag{7.30}$$

where $N_{20} = \frac{N_H}{10^{20}\mathrm{cm}^{-2}}$.

7.4.2 Constraints on Cloud and Medium Densities for NGC 1068

Both NGC 1068 and NGC 4151 show evidence for highly ionized gas extended throughout their NLRs, based on Chandra X-ray Observatory images (Ogle et al. 2000, 2003). Thus, we assume an ambient medium that is highly ionized, with ionization parameter $U \approx 10$. The ionization parameter, which is inversely related to the density and radius, can be written as follows

$$U \propto \frac{L_{ion}}{r^2 n_H}. \tag{7.31}$$

Therefore if the ambient and the NLR clouds see the same luminosity at a particular distance r_{pc} from the source, we can write

$$n_{med} = n_{cloud} \frac{U_{cloud}}{U_{med}}. \tag{7.32}$$

Kraemer & Crenshaw (2000b) provided good constraints on the parameters on the right side of Equation 7.32. The densities of the NLR clouds are almost constant out to large distances from the nucleus with a typical value of $n_{cloud} \approx 10^4$ cm^{-3} for clouds with $U \approx 10^{-3}$. If we substitute these estimates in Equation 7.32, we will have a typical estimate for n_{med} as follows

$$n_{med} = 10^4 \frac{10^{-3}}{10} = 1 \text{ cm}^{-3}. \tag{7.33}$$

Kraemer & Crenshaw found column densities for the NLR clouds in the range $N_H = 10^{19}$–10^{21} cm^{-2}, which corresponds to $N_{20} = 0.1$–10. We already know that $\mathcal{M}$ can take values from 500–6000, so Equation 7.30 can now be solved numerically for $v(r)$ with various values of the launch radius (r_1), force multiplier ($\mathcal{M}$), and the column density of the clouds (N_{20}). We used Mathematica v5.2, which employs the most efficient choices among various flavors of Runge-Kutta algorithms, to solve for $v(r)$. The results are presented in the next section.

7.4.3 Radiation, Gravity and Drag Results

Figure 7.8 represents several plots with a force multiplier of 500 and varying column density of the NLR gas. The figure shows that when launched at 1 pc, the gas accelerates to a maximum velocity in the first few parsecs, then slows down again. The velocity slows down faster with increasing drag forces, as measured by decreasing column densities of the gas. However the point of maximum velocity is too close in to match the data, which has a turnover velocity at $\sim$ 140 pc. The curve with column density $N_{20} = 3$ shows gradual deceleration out to $\sim$ 500 pc, but its maximum velocity is slightly too high. Any other curve has either too high velocity at turnover or the velocity drops too quickly. Note that the velocity of the data we are trying to match has $\sim$ 2000 km s^{-1} at a turnover of $\sim$ 140 pc for NGC 1068. With force

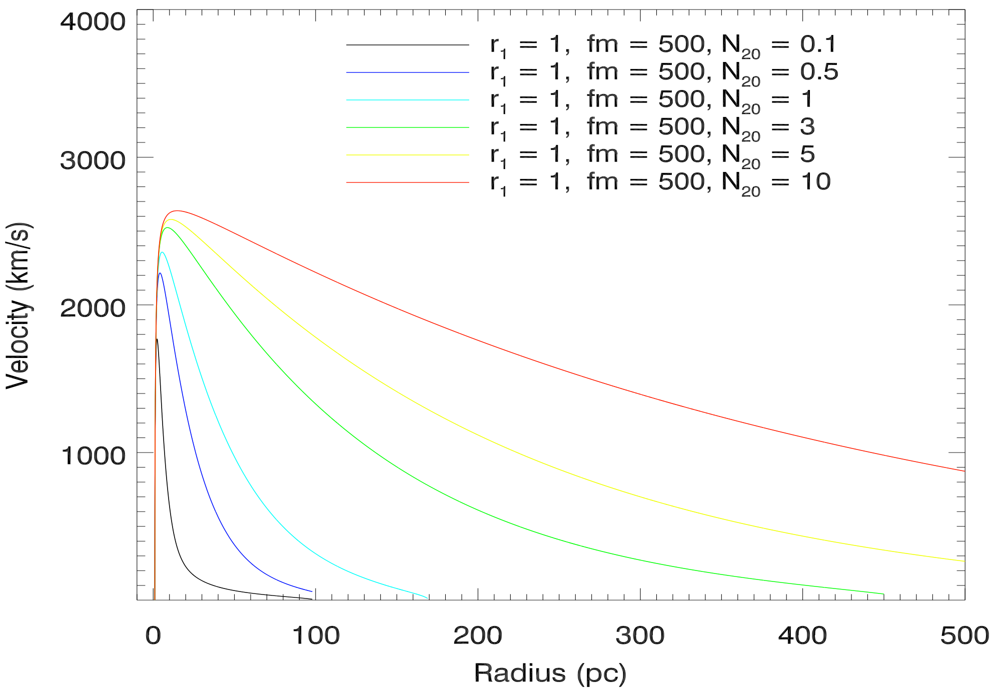

Figure 7.8: The velocity profiles for force multiplier 500 and a constant launch radius of 1 pc. The different colors are defined by different input parameters as shown in the key.

multipliers higher than 500, the same trend is seen in the velocity model, as depicted in Figure 7.9. Again, the curve that seems best to match the deceleration in the data is with column density $N_{20} = 3$. The rest of the curves decelerate too quickly or too slowly. In addition, for all the curves in Figure 7.9, the velocities are much too high to match the data. The major problem with all of these curves is that the velocity turnover point is much closer to the nucleus than 140 pc.

Another way to decrease the overall velocity is to increase the launch radius, and this was done in the following two plots. In Figures 7.10 and 7.11, the maximum velocity increases with force multiplier, but the overall velocities are lower than those

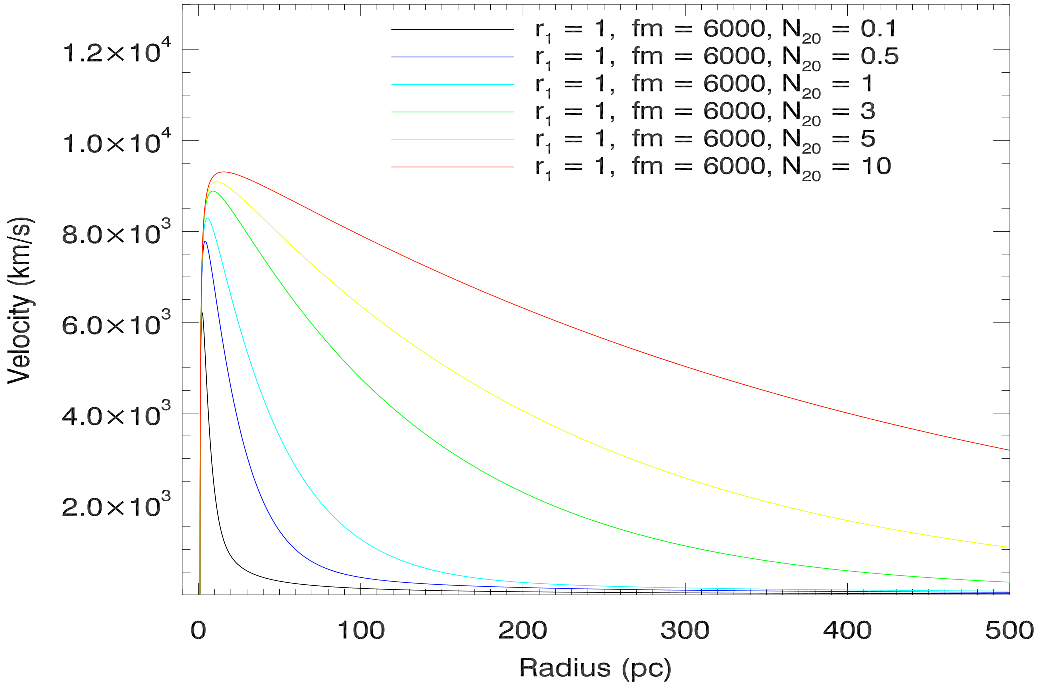

Figure 7.9: The velocity profiles for force multiplier 6000 and a constant launch radius of 1 pc. The different colors are defined as shown in the key.

of the previous two plots where the clouds are launched at 1 pc. On the other hand, the turning point increases by a factor of 5 as we increase the launch radius from 1 to 10 pc. However the turnover point is still too low to fit the data well. In order to have a good fit, we first need to maximize the launch radius and then tweak the force multiplier and column density to get the closest match to data as possible.

The resolution in our data is $\sim$ 10 pc and we should not launch much beyond this distance since we see clouds close to the SMBH with near zero velocity. Therefore, in Figure 7.12, we present a plot for a launch radius of $r_1 = 20$ pc and with a force multiplier of 6000. The maximum velocity reached is $\sim$ 1700 $\mathrm{km\,s^{-1}}$ with $N_{20} = 10$. The best curve to represent the data seems to be the one with $N_{20} = 3$, whose

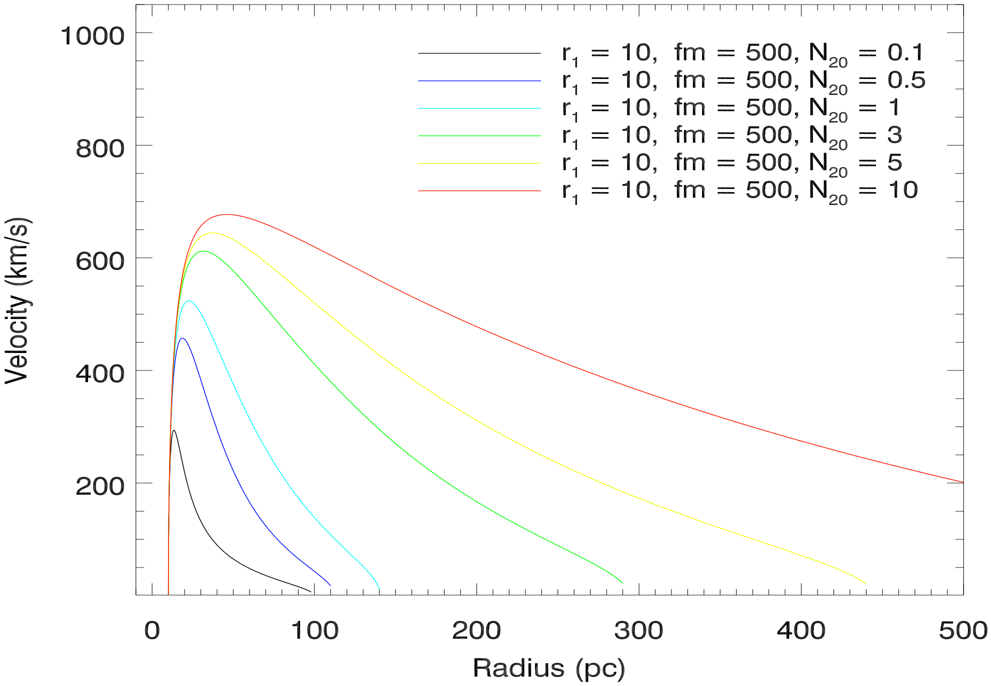

Figure 7.10: The velocity profiles for force multiplier 500, but with a larger launch radius of 10 pc. The different colors are defined as shown in the key.

maximum velocity is $\sim$ 1500 $\mathrm{km\,s^{-1}}$, although the turnover point at $\sim$ 60 pc is still too low according to our kinematic model. Furthermore, we have had to tweak the launch radius and force multiplier to very specific values, such that only a narrow range of the observed values gives a reasonably decent fit. However, to directly test this velocity profile, we generate biconical models similar to our previous kinematic models, to determine whether a more dynamical velocity law, other than the simple linear law, can reasonably match the data.

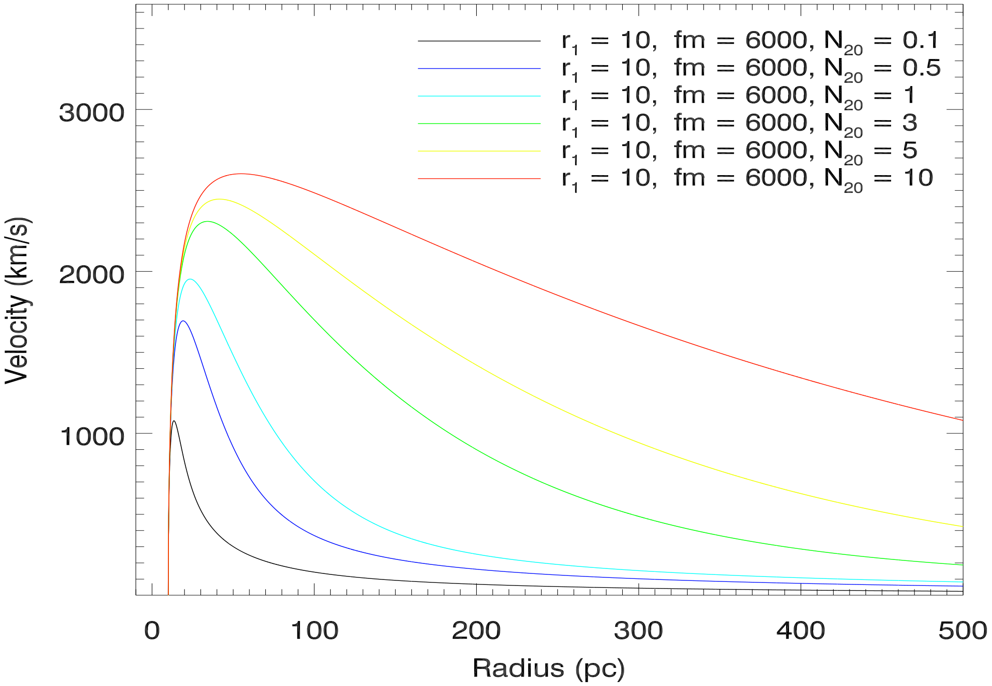

Figure 7.11: The velocity profiles with force multiplier 6000 and a constant launch radius of 10 pc. The different colors are defined as shown in the key.

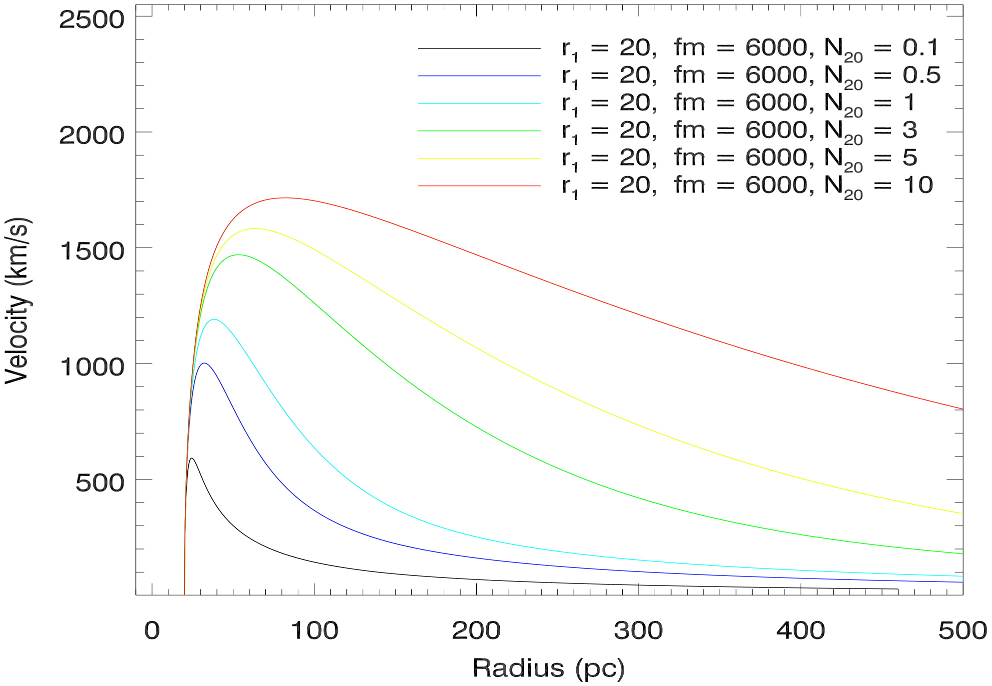

Figure 7.12: The velocity profiles for force multiplier 6000 and a constant launch radius of 20 pc. The different colors are defined as shown in the key.

7.4.4 Dynamical Fit

A model with the new velocity law of Equation 7.30 is presented in Figure 7.13, using the input parameters from Table 7.1, and using the best-fit curve from Figure 7.12, with $N_{20} = 3$ and $n_{med} = 1$. The model represents a poor fit to the data from slit 4 (the center slit) of NGC 1068. This was expected from looking at the previous velocity plots, as the turnover point was too low, the launch radius was a bit large, and the velocity profile did not resemble our kinematically derived linear profiles. We have varied the input parameters from Table 7.1, but this makes very little improvement. The turnover point, starting distance, and maximum velocity of the bicone cannot be varied without changing the drag parameters, as these are implicitly defined in Equation 7.30. The thickness of the bicone can be increased to accommodate more data points, but the bicone will show lots of unnecessary shaded regions. Changing the maximum extent of the bicone z_{max} will have absolutely no effect on the shaded region, except interrupting the shaded regions before or continuing them beyond $\pm$ $6''$. That leaves us with only two parameters to vary, the inclination of the bicone axis, and its position angle in the sky, and these two alone cannot fix the model.

7.4.5 Remarks on Accelerating the Clouds

With radiation pressure driving the NLR clouds, their velocities will accelerate very quickly, within a few parsecs of the nucleus, assuming the clouds are indeed launched close in. With the introduction of the drag forces, the overall velocities are lowered, but even so the velocities reach maximum too quickly. The data suggest that the

Table 7.1: Parameters used to generate the drag model shown in Figure 7.13.

Parameters	$z_{\rm max}$ (pc)	$\theta_{\rm inner}$ (deg)	$\theta_{\rm outer}$ (deg)	$i_{\rm axis}$ (deg)	$PA_{\rm axis}$ (deg)	v_{law}
	450	10	40	5	57.8	Equation 7.30

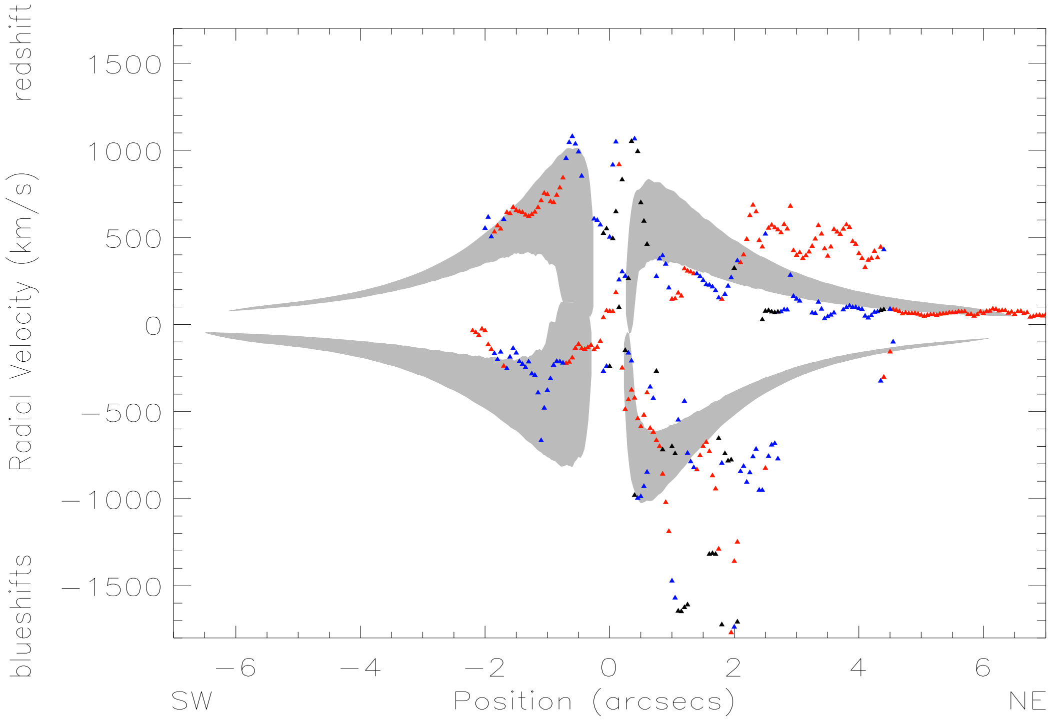

Figure 7.13: The model of slit 4 generated with input parameters from Table 7.1, and the best-fit velocity profile of Figure 7.12 with $N_H = 3$. Clearly this model is a poor match to the data.

clouds are gradually increasing their velocities to a maximum at about 140 pc. This gradient in the velocity cannot be simply accounted for by radiative forces driving the clouds. It seems therefore, that radiation pressure may not be the only driving mechanism for the NLR clouds, or that other forces are involved to steer the clouds to that particular gradient. The velocity profile shown in the data resembles one with a linear or 'Hubble flow' law. The inclusion of a drag force only serves to reduce the overall high velocities due to radiation driving, but the maximum velocities are reached very close to the nucleus, too close to match the data effectively.

7.4.6 Remarks on Decelerating the Clouds

Gravitational forces alone cannot stop the fast moving clouds observed in the NLR of NGC 1068. With velocities as high as 1500 $\mathrm{km\,s^{-1}}$ at 140 pc, the clouds should have escaped the NLR. To compound the problem, when radiation forces are added, the clouds are boosted even more! Yet we see clouds that are slowing down and gradually reaching systemic velocity. Therefore, the data suggest that there is a powerful force dragging on the clouds to slow their velocity.

The drag force that we introduce can have a significant effect on the clouds' velocities. We can conclude therefore that the drag forces are a strong competitor to the radiative forces, strong enough to bring the clouds to a halt even close to the nucleus, depending on the column densities of the outflowing clouds and the densities of the ambient medium. However the overall velocity profiles generated with radiative, gravitational, and drag forces do not match the data for NGC 1068. Assuming that the mass profile of NGC 4151 is similar to the one for NGC 1068, it will prove difficult to match its observed velocity profile, because the same linear trends are seen in the velocity of the outflowing clouds. The same can be said for Mkn 3 (Ruiz et al. 2001).

– 8 –

Discussion

We have undertaken a study of the kinematics and dynamics of the NLRs of the Seyfert 1 galaxy NGC 4151 and the Seyfert 2 galaxy NGC 1068, with the help of excellent datasets obtained from STIS aboard the *Hubble Space Telescope*. Previous ground-based studies using integrated emission-line profiles and previous spaced-based studies using the FOC on *HST* were useful, but were limited to low angular and spectral resolutions, respectively, which resulted in many interpretations that could explain the NLR kinematics equally well. STIS allowed us for the first time to identify and map multiple kinematic components in the NLR emission line gas, resulting in radial velocity profiles of high accuracy. These kinematic components, when separated by relative fluxes, were found to trace out somewhat different kinematic flows, as discussed below. Our most important result is to confirm previous claims that outflow dominates the kinematics of the NLR in Seyfert galaxies.

For the first time, we have been able to map the kinematics of the entire NLR at unprecedented angular and spectral resolutions using multiple long-slit observations with STIS. Angular resolutions of $0\farcs1$ along and $0\farcs2$ across each slit, and a spectral resolution of 30 $\mathrm{km\,s^{-1}}$, allowed us to identify, discriminate, and map the velocities of the gas at a spatial resolution of ~ 10 pc within a few hundred parsecs of the SMBH.

8.1 Kinematic Results and Implications

We have developed improved 3D kinematic models with better visualization and faster runtime than previous models to fit the velocities of the outflowing gas in the NLRs. These models and the STIS datasets resulted in much more detailed kinematic maps of the NLRs in NGC 4151 and NGC 1068, compared to previous studies based on STIS observations at low spectral resolution (~ 300 km s^{-1}) (Crenshaw & Kraemer 2000b; Crenshaw et al. 2000). Our models were able to match the general trend of radial velocities in the NLRs of both types of Seyfert galaxies, indicating a common accelerating and decelerating mechanism for the gas residing within a few hundred parsecs of the central SMBH. These biconical outflow models are the simplest geometrical constructs to date that can match both Seyfert types by simply manipulating the input parameters, the most effective one being the inclination of the bicone axis. Important implications based on the kinematic fits to the data of NGC 4151 and NGC 1068 are as follows.

1) Of practical importance are the inclinations of the bicone axes of NGC 4151 and NGC 1068, which are consistent with the Seyfert types as implied by the unified model of Seyfert galaxies. The inclination for the bicone axis of NGC 1068 is 5°, placing the obscuration near the observer's LOS and blocking nuclear photons, consistent with a Seyfert 2 interpretation. The low inclination of NGC 1068 predicted by our models is consistent with the presence of H_20 masers (Gallimore et al. 2001) in a nearly edge-on disk surrounding the large central mass (SMBH). This implies that the masers might

be an inward extension of the torus and/or an outward extension of the accretion disk. The inclination of the bicone axis of NGC 4151 fits the data with a value of −47° out of the plane of the sky, placing the LOS of the observer well away from the plane of the central torus or obscuring source. From Table 6.5, the 47° inclination and a further 35° half-opening outer angle of the bicone, puts the outer bicone edge 8° away from the LOS of the observer. This implies that we are technically viewing the NLR of NGC 4151 outside of the bicone. However, this result is consistent with a Seyfert 1 interpretation if the bicone has fuzzy boundaries, which would result from a torus atmosphere (Krolik & Kriss 2001) or a dusty wind (Emmering et al. 1992). Support for such an idea comes from evidence that the torus is clumpy, and that the number of clumps in the line of sight decreases with increasing polar angle from the torus plane (Nenkova et al. 2002; Elitzur & Shlosman 2006). A view through the atmosphere of the patchy torus is also consistent with the high column of absorption measured along the LOS by Kraemer et al. (2001). These kinematic studies of the NLRs of NGC 4151 and NGC 1068 also offer a way to determine the inclination of the accretion disk, if we assume that this disk is perpendicular to the bicone axis.

2) The biconical morphologies of the NLRs of NGC 4151 and NGC 1068 with respect to their host galactic disks could explain the blue asymmetries of emission lines previously seen in ground based data. For NGC 4151, where the southwest bicone is mostly above the galactic disk, and the northeast bicone is mostly behind the disk (see Figure 6.19), the redshifted points are likely attenuated by more dust

along the LOS, compared to the blueshifted points, hence the blue asymmetry. The effect is not so pronounced in NGC 1068 due to the orientation of the galactic disk (see Figure 6.18), but the redshifted points in the back half of the bicone will intercept more galactic dust along the LOS, which will attenuate the redshifted points more than the blueshifted points in the front half.

3) In both NGC 4151 and NGC 1068, there were some fainter kinematic components that did not follow the general outflow pattern of our biconical models. In NGC 4151 for example, some of the faint clouds may be flowing back along the bicone edges with speeds proportional to the outflow speeds. This behavior is seen in multiple slits and multiple quadrants of the bicone geometry, indicates either the backflow effect is real or that these clouds are flowing in an entirely different geometry than the bright NLR clouds. The backflow effect, if present in NGC 1068, was not seen. This effect would be difficult to detect in NGC 1068, because both redshifts and blueshifts are present in both the northeast and southwest parts of the bicone.

Some of the fainter clouds in NGC 1068 and NGC 4151 close to the SMBH also fell outside of our model velocity-position boundaries due to geometrical constraints. This is because in our model, gas outflow emanates from a point-like apex and goes in opposite directions along the bicones. These faint clouds therefore may not be in outflow along the bicones, but may be flowing laterally away from the jet/bicone axis as discussed in the next section.

4) Another constraint on the outflowing NLR clouds is the opening angles of the

bicone, particularly the inner opening angle. The fact that this quantity is not 0° implies that the bicone is evacuated along the bicone axis. This has been previously seen and quantified in Crenshaw et al. (2000) and Crenshaw & Kraemer (2000b) for both galaxies. The present study confirms that NLR gas is absent along the bicone axis, or that ionizing radiation is not reaching this region. One explanation is that the radio jet might be preventing the accumulation of gas along the jet axis by clearing a channel through them. However radio images show that the jet axis is sometimes misaligned with the bicone axis, as in the case of NGC 4151 (Figure 3.4), or sometimes the jet is bent from collision with a NLR cloud (Capetti et al. 1999), as in the case of NGC 1068 (Figure 3.7), making this explanation less likely.

5) In both galaxies under study, our kinematic models confirm a common velocity trend in the outflowing NLR gas. The gas increases its velocity with distance from the SMBH, reaches a maximum velocity at a turnover point, and decelerates its velocity back to systemic in a linear fashion. This pattern in the velocities on the NLR gas can be seen in other Seyfert galaxies, for example Mkn 3 (Ruiz et al. 2001). The turnover points for NGC 4151, NGC 1068, and Mkn 3 are comparable (96 pc, 140 pc, 80 pc respectively), and the maximum extent of their bicones are also comparable (450 pc, 460 pc, 300 pc respectively), implying a common accelerating and decelerating mechanism of the gas. Based on the dynamics and radio jet interactions on the NLR clouds, we argued that this accelerating and decelerating mechanism remains elusive at present.

8.2 The Radio Jet Interaction and Implications

High resolution radio maps ($0''.014$ pixel^{-1}) were provided by Jack Gallimore for NGC 1068 (Gallimore et al. 2004) and by Caroll Mundell for NGC 4151 (Mundell et al. 2003). These maps allowed us to make a detailed comparison between the positions of the radio knots and the positions of the [O III] λ5007 radial velocities of the NLR clouds. In both galaxies, the comparison indicates that the radio knots cannot be the main driving mechanism within the biconical geometry that we see in the NLR clouds. There were radial velocity splittings in the bright clouds far away from the radio knots, indicating other driving forces. In addition the splitting of the bright NLR clouds showed a smooth transition across the radio knots, and remained undisturbed in the vicinity of the knots. However, the velocities of some of the fainter NLR clouds are seen to split into two components near positions of the bright radio knots. The radio jet seems therefore to split the velocities of the faint clouds perpendicular to the jet axis. In the case of NGC 4151, due to the large inclination of its jet axis, the velocity splittings may not be symmetrical in magnitudes of redshifts and blueshifts, but for NGC 1068, whose jet axis inclination is small, the velocity splittings are symmetrical in magnitudes of redshifts and blueshifts. This implies that the radio jet could be important in driving localized regions of fainter NLR clouds, and could also explain the absence of a sharp apex in the data. These fainter clouds may be caused by the radio jet pushing clouds laterally away from the jet axis (as originally claimed by Pedlar et al. 1989; Taylor et al. 1992; Axon et al.

1998; Capetti et al. 1999, and references therein). Close to the nucleus therefore, the fainter clouds may be blown-off bits of torus material, and could be responsible for filling in the otherwise sharp apex seen in our 3D models. These clouds could be faint because they are ionized by a weaker continuum from scattered light or holes in the torus, or they are ionized by some other process such as shocks (Schmitt et al. 2006).

8.3 Dynamics of the NLR and Implications

We developed a dynamical outflow model for the NLR of NGC 1068 because it has the best observational constraints. In the process of developing the model, we tested various scenarios whereby the NLR gas is being driven by rotation, infall, or outflow, and whether or not gravity alone can slow the clouds down. An important aspect of the modeling process involved the development of the mass profile within 10,000 pc of the SMBH. Such a cumulative mass profile that involves the masses of the SMBH, the nuclear stellar cluster, and the bulge, was previously lacking, although estimates of the masses of individual components existed previously.

With an accurate assessment of the mass, a rotation profile for the NLR gas was calculated, which resulted in a poor match to the observations. In addition, infall velocity profiles were estimated in an attempt to match the data; these were also found to be of poor fit. Therefore the NLR gas is not dominated by either rotation or infall, leaving outflow as the only viable alternative. Certainly the gas is not escaping the region as the data show, implying other forces are at work in molding the biconical flow pattern that we see.

We attempted to match the decelerating clouds by assuming an initial projectile velocity and letting gravity do the rest. Our calculations showed that using our current mass profile and velocity at the turnover point in the data (~ 1500 km s^{-1} at 140 pc), the clouds showed no indication of slowing down under gravity alone. If we introduce radiative forces on the clouds, the problem only becomes worse.

We next modeled the clouds' velocities by launching at 1 pc and let radiation pressure and gravity act on the clouds. We found that the predicted acceleration of the clouds was much faster than observed, and the predicted deceleration was negligible, unless we used an unrealistically large launch radius ≥ 60 pc, in which case the maximum velocity at turnover point became too low to fit the data. Because the clouds do slow down in the data, this implies that there are other forces dragging on the NLR clouds, which motivated us to introduce one such decelerating force, whereby the clouds are interacting with an ambient medium.

Together with radiation pressure and gravity, we included an additional drag force due to a hot ambient medium, to see if we could bring the velocity back to systemic within 400 pc, and thereby match the data. Although we could slow the clouds with realistic parameters, the overall predicted velocity profile does not match the data well. Again, the accelerating phase of the model was too quick to match the more slowly accelerating NLR gas. When the gas is launched close to the nucleus (≤ 1 pc), the maximum velocity reached was too high to fit the data. Launching at increasing distances from the SMBH drops the maximum velocity to observed values, but the predicted turnover point never seems to reach the observed value of 140 pc, even when we launch the gas from large launch radii.

The deceleration in our models, due mostly to the drag force, is not linear with distance, but varies with v^2 of the NLR clouds, while the decelerating trend seen in the data seems more linear, as fit by our kinematic models. Average values for the column densities of the NLR gas seem to work best to reduce the speeds of the clouds within 400 pc regardless of the values used for the force multipliers and launch radii, which just tend to increase or decrease the maximum velocity of the gas at turnover point. Although drag forces can slow the clouds down within the accepted range seen in the data, the predicted acceleration, turnover point, and deceleration of the gas do not match the data as well as our empirical kinematic models.

Our kinematic models showed that the outflowing NLR gas can be best matched by an initially increasing and then a decreasing linear velocity law. Radiation pressure, which seems to be the dominant source for accelerating the gas, does not fit the accelerating profile seen in the data, because with radiation line driving, the clouds accelerate too quickly and too close to the SMBH. The drag force, which seems like a strong candidate to decelerate the gas, does not fit the linear trend seen in the data. So what then really drives and stops the NLR gas? We still do not know the answers to these questions, but we do think we know what it cannot be. Given our assumptions, neither the radio jet nor the radiative force give reasonable fits to the data, and drag does its job in slowing down the clouds, but does not yield the approximate linear trends in velocity. Infall and rotation certainly do not work, and we confirm that outflow is by far the most likely option for the NLR clouds, although the dynamics are still poorly understood.

8.4 Future Studies

The kinematics of the NLRs of Seyfert galaxies seem to be fitted by simple velocity laws and simple geometrical figures, but the physical processes at work to generate such simple flows eludes us. A simple answer to explain the flow pattern is still sought after, because it is difficult to picture why a complex set of interactions among many different forces can explain the simple velocity pattern that is observed in the NLRs of these Seyfert galaxies. Future studies would be worthwhile to obtain more observational constraints using the wealth of long-slit G430M STIS spectra of other Seyfert galaxies already in the *HST* archives. In particular, analysis of objects at different inclination angles might help us to further constrain our kinematic models. We have not yet modeled a Seyfert galaxy at high inclination ($\sim 90°$), which could provide a critical test of our kinematic model.

We would also like to try different kinematic models, involving different geometrical configurations, such as 'hour-glass' shape flow patterns rather than biconical ones. A moderate yet important driver of the fainter NLR clouds is the radio jet. We saw that the jet is responsible for splitting the velocities of the clouds at least near the bright radio knots, giving rise to the non-apex like flow that we see. Therefore, it is not impossible to imagine that the jet could play a more dominant role in other Seyfert galaxies in producing the flow patterns seen in their NLRs. This needs to be thoroughly tested in future studies.

In other scenarios, the velocity flow could be non-radial, where the clouds change their velocity vectors. In an extreme case, changes in the directions of the velocity vectors might provide an alternate explanation for the apparent radial acceleration and deceleration that we see. One of the problems that lingers is, what is keeping these parsec-sized clouds together, while they flow over large distances? One explanation is that these clouds may be embedded in strong magnetic fields, and therefore essentially flowing along these field lines, which could also result in the clouds' changing velocity vectors. These kinds of dynamical studies need to be considered in the future, if we want to solve the riddle of the outflowing clouds in the NLRs of Seyfert galaxies.

References

Antonucci, R. R. J. 1983, Nature, 303, 158

Antonucci, R. R. J., & Miller, J. S. 1985, ApJ, 297, 621

Arribas, S., Mediavilla, E., & Garcia-Lorenzo, B. 1996, ApJ, 463, 509

Axon, D. J., Marconi, A., Capetti, A., Maccetto, F. D., Schreier, E., & Robinson, A. 1998, ApJ, 496, L75

Baade, W., & Minkowski, R. 1954, ApJ, 119, 206

Beckert, T., & Duschl, W. J. 2004, A&A, 426, 445

Bell, M. B., & Seaquist, E. R. 1980, ApJ, 238, 818

Bergeron, J., Petitjean, P., & Durret, F. 1989, A&A, 213, 61

Binney, J., & Merrifield, M. 1998, Galactic Astronomy (Princeton, NJ : Princeton University Press, 1998.)

Bland-Hawthorn, J., Gallimore, J. F., Tacconi, L. J., Brinks, E., Baum, S. A., Antonucci, R. R. J., & Cecil, G. N. 1997, Ap&SS, 248, 9

Bowen, I. S. 1928, ApJ, 67, 1

——. 1936, Rev. Mod. Phys., 8, 55

Brinks, E., Skillman, E. D., Terlevich, R. J., & Terlevich, E. 1997, Ap&SS, 248, 23

Campbell, W. W., & Paddock, G. F. 1918, PASP, 30, 68

Capetti, A., Axon, D. J., Macchetto, F. D., Marconi, A., & Winge, C. 1999, ApJ, 516, 187

Capetti, A., Macchetto, F. D., & Lattanzi, M. G. 1997, ApJ, 476, L67

Carral, P., Turner, J. L., & Ho, P. T. P. 1990, ApJ, 362, 434

Carroll, B. W., & Ostlie, D. A. 1996, An Introduction to Modern Astrophysics (Reading, MA: Addison-Wesley)

Cecil, G., Bland, J., & Tully, R. B. 1990, ApJ, 355, 70

Cecil, G., Dopita, M. A., Groves, B., Wilson, A. S., Ferruit, P., Pécontal, E., & Binette, L. 2002, ApJ, 568, 627

Chelouche, D., & Netzer, H. 2001, MNRAS, 326, 916

Claussen, M. J., & Lo, K.-Y. 1986, ApJ, 308, 592

Collins, N. R., Kraemer, S. B., Crenshaw, D. M., Ruiz, J., Deo, R., & Bruhweiler, F. C. 2005, ApJ, 619, 116

Crenshaw, D. M., & Kraemer, S. B. 2000a, ApJ, 532, 247

——. 2000b, ApJ, 532, L101

Crenshaw, D. M., Kraemer, S. B., & George, I. M. 2003, ARA&A, 41, 117

Crenshaw, D. M. et al. 2000, AJ, 120, 1731

Das, V. et al. 2005, AJ, 130, 945

Das, V., Crenshaw, D. M., Kraemer, S. B., & Deo, R. P. 2006, AJ, 132, 620

de Vaucouleurs, G. 1948, Annales d'Astrophysique, 11, 247

de Vaucouleurs, G., de Vaucouleurs, A., Corwin, H. G., Buta, R. J., Paturel, G.,

& Fouque, P. 1991, Third Reference Catalogue of Bright Galaxies, Vol. 1-3, XII (Springer-Verlag Berlin Heidelberg, New York), 2069

Dehnen, W. 1993, MNRAS, 265, 250

Dopita, M. A., Groves, B. A., Sutherland, R. S., Binette, L., & Cecil, G. 2002, ApJ, 572, 753

Dopita, M. A., & Sutherland, R. S. 1995, ApJ, 455, 468

Dressler, A. 1984, ApJ, 286, 97

Elitzur, M., & Shlosman, I. 2006, ApJ, in press (astro-ph/0605686)

Emmering, R. T., Blandford, R. D., & Shlosman, I. 1992, ApJ, 385, 460

Evans, I. N., Ford, H. C., Kinney, A. L., Antonucci, R. R. J., Armus, L., & Caganoff, S. 1991, ApJ, 369, L27

Evans, I. N., Tsvetanov, Z., Kriss, G. A., Ford, H. C., Caganoff, S., & Koratkar, A. P. 1993, ApJ, 417, 82

Everett, J. E. 2005, ApJ, 631, 689

Everett, J. E., & Murray, N. 2006, submitted to ApJ

Fath, E. A. 1908, Lick Observatory Bulletin, 5, 71

Ferland, G. J., & Osterbrock, D. E. 1986, ApJ, 300, 658

Galliano, E., Alloin, D., Granato, G. L., & Villar-Martín, M. 2003, A&A, 412, 615

Gallimore, J. F., Baum, S. A., & O'Dea, C. P. 1996a, ApJ, 464, 198

——. 1997, Nature, 388, 852

——. 2004, ApJ, 613, 794

Gallimore, J. F., Baum, S. A., O'Dea, C. P., & Pedlar, A. 1996b, ApJ, 458, 136

Gallimore, J. F., Henkel, C., Baum, S. A., Glass, I. S., Claussen, M. J., Prieto, M. A., & Von Kap-herr, A. 2001, ApJ, 556, 694

Greenhill, L. J., & Gwinn, C. R. 1997, Ap&SS, 248, 261

Greenstein, J. L., & Schmidt, M. 1964, ApJ, 140, 1

Groves, B. A., Cecil, G., Ferruit, P., & Dopita, M. A. 2004, ApJ, 611, 786

Häring, N., & Rix, H.-W. 2004, ApJ, 604, L89

Heckman, T. M. 1980, A&A, 87, 152

Heckman, T. M., Miley, G. K., van Breugel, W. J. M., & Butcher, H. R. 1981, ApJ, 247, 403

Hernquist, L. 1990, ApJ, 356, 359

Ho, L. C., Filippenko, A. V., & Sargent, W. L. W. 1994, in IAU Symp. 159: Multi-Wavelength Continuum Emission of AGN, ed. T. Courvoisier & A. Blecha, 275–278

Hubble, E. P. 1926, ApJ, 64, 321

Hutchings, J. B. et al. 1999, AJ, 118, 2101

——. 1998, ApJ, 492, L115

Jaffe, W. 1983, MNRAS, 202, 995

Kaiser, M. E. et al. 2000, ApJ, 528, 260

Khachikian, E. Y., & Weedman, D. W. 1974, ApJ, 192, 581

Kinney, A. L., Antonucci, R. R. J., Ward, M. J., Wilson, A. S., & Whittle, M. 1991, ApJ, 377, 100

Koski, A. T. 1978, ApJ, 223, 56

Kraemer, S. B., & Crenshaw, D. M. 2000a, ApJ, 532, 256

——. 2000b, ApJ, 544, 763

Kraemer, S. B. et al. 2001, ApJ, 551, 671

Kraemer, S. B., Crenshaw, D. M., Hutchings, J. B., Gull, T. R., Kaiser, M. E., Nelson, C. H., & Weistrop, D. 2000, ApJ, 531, 278

Kriss, G. A. et al. 1992, Bulletin of the American Astronomical Society, 24, 751

Krolik, J. H., & Kriss, G. A. 2001, ApJ, 561, 684

Krolik, J. H., & Lepp, S. 1989, ApJ, 347, 179

Krolik, J. H., & Vrtilek, J. M. 1984, ApJ, 279, 521

Lattanzi, M. G., Capetti, A., & Macchetto, F. D. 1997, A&A, 318, 997

Macchetto, F., Capetti, A., Sparks, W. B., Axon, D. J., & Boksenberg, A. 1994, ApJ, 435, L15

Marconi, A., & Hunt, L. K. 2003, ApJ, 589, L21

Mathews, W. G., & Veilleux, S. 1989, ApJ, 336, 93

Miller, J. S., Goodrich, R. W., & Mathews, W. G. 1991, ApJ, 378, 47

Mulchaey, J. S., Koratkar, A., Ward, M. J., Wilson, A. S., Whittle, M., Antonucci, R. R. J., Kinney, A. L., & Hurt, T. 1994, ApJ, 436, 586

Mundell, C. G., Pedlar, A., Baum, S. A., O'Dea, C. P., Gallimore, J. F., & Brinks, E. 1995, MNRAS, 272, 355

Mundell, C. G., Wrobel, J. M., Pedlar, A., & Gallimore, J. F. 2003, ApJ, 583, 192

Murayama, T., Mouri, H., & Taniguchi, Y. 2000, ApJ, 528, 179

Muxlow, T. W. B., Pedlar, A., Holloway, A. J., Gallimore, J. F., & Antonucci, R. R. J. 1996, MNRAS, 278, 854

Nelson, C. H., Weistrop, D., Hutchings, J. B., Crenshaw, D. M., Gull, T. R., Kaiser, M. E., Kraemer, S. B., & Lindler, D. 2000, ApJ, 531, 257

Nenkova, M., Ivezić, Ž., & Elitzur, M. 2002, ApJ, 570, L9

Neufeld, D. A., Maloney, P. R., & Conger, S. 1994, ApJ, 436, L127

Ogle, P. M., Brookings, T., Canizares, C. R., Lee, J. C., & Marshall, H. L. 2003, A&A, 402, 849

Ogle, P. M., Marshall, H. L., Lee, J. C., & Canizares, C. R. 2000, ApJ, 545, L81

Oke, J. B. 1965, ApJ, 141, 6

Osterbrock, D. E. 1978, Proceedings of the National Academy of Science, 75, 540

Osterbrock, D. E., Koski, A. T., & Phillips, M. M. 1975, ApJ, 197, L41

Osterbrock, D. E., & Parker, R. A. R. 1966, ApJ, 143, 268

Parker, E. N. 1965, Space Science Reviews, 4, 666

Pedlar, A., Howley, P., Axon, D. J., & Unger, S. W. 1992, MNRAS, 259, 369

Pedlar, A., Kukula, M. J., Longley, D. P. T., Muxlow, T. W. B., Axon, D. J., Baum, S., O'Dea, C., & Unger, S. W. 1993, MNRAS, 263, 471

Pedlar, A., Meaburn, J., Axon, D. J., Unger, S. W., Whittle, D. M., Meurs, E. J. A., Guerrine, N., & Ward, M. J. 1989, MNRAS, 238, 863

Peterson, B. M. 1997, An Introduction to Active Galactic Nuclei (Cambridge University Press)

Pier, E. A., Antonucci, R., Hurt, T., Kriss, G., & Krolik, J. 1994, ApJ, 428, 124

Pogge, R. W. 1988, ApJ, 328, 519

Rhee, J. H., & Larkin, J. E. 2000, ApJ, 538, 98

——. 2005, ApJ, 620, 151

Ruiz, J. R., Crenshaw, D. M., Kraemer, S. B., Bower, G. A., Gull, T. R., Hutchings, J. B., Kaiser, M. E., & Weistrop, D. 2001, AJ, 122, 2961

——. 2005, AJ, 129, 73

Schmidt, M. 1963, Nature, 197, 1040

Schmitt, H. R., Donley, J. L., Antonucci, R. R. J., Hutchings, J. B., & Kinney, A. L. 2003a, ApJS, 148, 327

Schmitt, H. R., Donley, J. L., Antonucci, R. R. J., Hutchings, J. B., Kinney, A. L., & Pringle, J. E. 2003b, ApJ, 597, 768

Schmitt, H. R., & Kinney, A. L. 1996, ApJ, 463, 498

Schmitt, H. R., Kraemer, S. B., Crenshaw, D. M., & Hutchings, J. B. 2006, in The X-ray Universe 2005 (ESA), proceedings, in press

Schulz, H. 1990, AJ, 99, 1442

Seyfert, C. K. 1943, ApJ, 97, 28

Slipher, V. M. 1917, Lowell Observatory Bulletin, 1, 59

Storchi-Bergmann, T., Mulchaey, J. S., & Wilson, A. S. 1992, ApJ, 395, L73

Tadhunter, C., & Tsvetanov, Z. 1989, Nature, 341, 422

Taylor, D., Dyson, J. E., & Axon, D. J. 1992, MNRAS, 255, 351

Thatte, N., Quirrenbach, A., Genzel, R., Maiolino, R., & Tecza, M. 1997, ApJ, 490, 238

Veilleux, S. 1991, ApJ, 369, 331

Veilleux, S., Shopbell, P. L., & Miller, S. T. 2001, AJ, 121, 198

Visvanathan, N. 1969, ApJ, 155, L133

Vrtilek, J. M. 1983, Ph.D. Thesis

——. 1985, ApJ, 294, 121

Walker, M. F. 1968, ApJ, 151, 71

Wilson, A. S., Braatz, J. A., Heckman, T. M., Krolik, J. H., & Miley, G. K. 1993, ApJ, 419, L61

Winge, C., Axon, D. J., Macchetto, F. D., Capetti, A., & Marconi, A. 1999, ApJ, 519, 134